Electronic Thesis and Dissertation Repository

1-30-2020 2:30 PM

Calcium signaling and pathogenesis of dysferlin C2 domains

Yuning Wang, *The University of Western Ontario*

Supervisor: Gary S. Shaw, *The University of Western Ontario*

A thesis submitted in partial fulfillment of the requirements for the Doctor of Philosophy degree in Biochemistry

© Yuning Wang 2020

Recommended Citation

Abstract

Failure to repair injured sarcolemmal membranes leads to muscular dystrophy, a degenerative disorder that results in increasing weakness and gradual wasting of skeletal muscles. Mutations in the gene encoding dysferlin are causative for limb girdle muscular dystrophy type 2B (LGMD2B) and Miyoshi myopathy (MM) forms of the disease. Dysferlin is a Ca^{2+}-sensitive membrane repair protein involved in trafficking of proteins and vesicles around injured membranes in skeletal muscle cells. It is a cytosolic-facing, membrane bound protein composed of seven intermittently spaced C2 domains (C2A-C2G). Dysferlin activity is mediated by the Ca^{2+}-dependent actions of the C2 domains. The main goals of this thesis were to characterize the structure, dynamics and Ca^{2+}-binding mechanisms of the C2 domains, and assess the impact of pathogenic substitutions on the C2 domains.

First, the dynamics of the C2A domain in both Ca^{2+}-free and Ca^{2+}-bound state was comprehensively probed using NMR spectroscopy, which revealed a remarkable flexibility change in the loop region upon Ca^{2+} binding. The Ca^{2+}-binding properties of the C2A domain was studied on the basis of the crystal structure of the Ca^{2+}-bound C2A, which determined the stoichiometry, binding sites and affinities. Further, mutagenesis study revealed the important role of the electrostatic potential contributed by non-Ca^{2+}-coordinating residues, which provides novel insights into the mechanism of Ca^{2+} binding to the dysferlin C2A domain as a link for membrane repair.

To understand the consequences of pathogenic mutations, three substituted C2A proteins were generated and analyzed. It was demonstrated that there is dramatic decrease in stability resulted from the substitutions. The unfolding or improper folding of the substituted C2A domain is predicted to be responsible for impaired dysferlin function in the membrane repair process, and consequently the wasting of skeletal muscles in muscular dystrophy patients.

Finally, proteins encompassing the C2B and C2C domains of dysferlin were designed and generated using a combination of computational and experimental methods. The precise domain boundaries of the C2B and C2C domains were determined, which will provide useful information for the further characterization of dysferlin structure.

Summary for Lay Audience

The cell membrane separates the interior of cells from the outside environment and helps maintain the well-being of cells. However, when cells are subject to physical tearing (which happens frequently), the membrane can be damaged, leading to the damage of the equilibrium of cell. This is why a membrane repair system mediated by proteins is required for cell survival. Proteins are biological molecules that can perform an array of functions within living organisms. Each protein has its specific three-dimensional structure, and the function is directly related to the structure.

One protein that regulates cell membrane repair is dysferlin. Abnormalities of dysferlin caused by gene mutations lead to muscle diseases with detrimental consequences. In cells, dysferlin functions with the help of calcium ions. Calcium ions play a vital role in the physiological processes of organisms and cells, usually by selectively and reversibly binding to partner proteins. This binding causes changes of the protein structure, thereby activating the protein function. Thus, knowing when and how calcium ions bind to dysferlin is important to the understanding of its functions, and the mechanisms of inherited muscle diseases.

In this thesis, the 3-D structure of a calcium-binding region in dysferlin was determined by biophysical techniques. Not only the calcium-binding sites within this region were clearly observed at atomic level, how calcium changes the dysferlin structure was also elucidated. It was discovered that this structural change is directly related to the function of dysferlin

in membrane repair. Furthermore, we were able to artificially generate the abnormal forms of dysferlin protein when gene mutation occurs. We found that some properties of dysferlin were altered. This helps the analysis for the cause of function loss in membrane repair, that subsequently leads to muscle diseases. Finally, an additional region of dysferlin was explored, which may have a distinct role in regulating the function of dysferlin.

This work represents an important step forward in fully explaining the mechanisms of membrane repair by dysferlin. The structural and biochemical study here will have a significant impact on the understanding of related diseases and the development of drug therapeutics in the future.

Dedication

For my parents, Jingtao and Qixia, who have always shown unconditional love, support and encouragement.

Acknowledgements

First and foremost, I would like to thank my supervisor, Dr. Gary Shaw, for taking a chance on me as a graduate student and for all of his guidance, encouragements, and insightful comments throughout the years. I have learned so much and I truly couldn't have asked for a better supervisor.

Thanks to Kathy Barber for being a wonderfully organized and approachable lab manager as you have helped a great deal. Thanks to all of the past and present Shaw lab members: Karen, Richard, Tara, Jake, Aisha, Rachel, Roya, Anne, and Liliana. You have made this lab a great place to work. Thanks for the laughter and priceless memories. I consider myself lucky for making so many friends.

Thanks to everyone who have helped with this research project. To my advisory committee, Dr. Hong Ling and Dr. Murray Junop, thank you for your constructive discussions during our many meetings. I also thank Lee-Ann Briere and Paula Pittock for their expertise and helping me design my experiments and analyze data.

Finally, to my family and friends, thank you from the bottom of my heart for all of your love and support. Thanks to my good friends, Ke and Xiaoling, for making me laugh and always being there for me. To my parents Qixia and Jingtao, for always showing big hearts and encouraging me to pursue my dream. Thank you — with love always.

Co-authorship Statement

Chapter 2

The gene corresponding to the dysferlin C2A domain (C2A) containing residues 1-130 was generously donated by Dr. S. van der Maarel (Leiden University). The crystal structure of the Ca^{2+}-free C2A domain presented in **Figure 2.1 C** was solved by Dr. Pascal Mercier, Dr. Liliana Santamaria-Kisiel, and Chantal Forristal. Mass spectrometry data in **Figure 2.2** were collected at the Biological Mass Spectrometry Laboratory (Western University) by Paula Pittock.

Chapter 3

The accurate concentration of the stock solution of $CaCl_2$ was analyzed by the Biotron Experimental Climate Change Research Centre (Western University). Dr. Roya Tadayon performed the crystallography experiments and solved the structure of the Ca^{2+}-bound C2A domain presented in **Figure 3.1**. The LineShapeKin program used for NMR line-shape simulation shown in **Figure 3.5** was developed and shared by Dr. Evgenii Kovrigin (University of Notre Dame).

Chapter 4

The mutagenesis of $C2A^{V67D}$, $C2A^{V67A}$, $C2A^{V67T}$, and $C2A^{V67N}$ was performed by Dr. Valentina Taiakina.

Chapter 5

The computational modeling of the dysferlin structure presented in **Figure 5.2** was performed and kindly shared by Dr. Lance Stewart and Dr. David Baker (University of Washington). Mass spectrometry data in **Figure 5.6** were collected at the Biological Mass Spectrometry Laboratory (Western University) by Paula Pittock.

Chapter 6

Perspectives are this author's only.

Table of Contents

List of Figures

List of Tables

List of Abbreviations

AD	Alzheimer's disease
ALS	amyotrophic lateral sclerosis
ATP	adenosine triphosphate
Ca^{2+}	calcium ion
$CaCl_2$	calcium chloride
cADPR	cyclic ADP ribose
CD	circular dichroism
CaV	voltage-gated Ca^{2+} channel
D_2O	deuterium oxide
Da	daltons
DAG	diacylglycerol
DSS	2,2'-dimethyl-2-silapentane-5-sulfonate
DTT	dithiothreitol
E. coli	Escherichia coli
EDTA	ethylenediaminetetraacetic acid
ER	endoplasmic reticulum
ESI	electrospray ionization
FF	fast flow
GndHCl	guanidinium chloride
GST	glutathione S-transferase
HPLC	high performance liquid chromatography
HSQC	heteronuclear single quantum coherence

Hz	hertz
ICP	inductively coupled plasma atomic emission spectrometry
IP$_3$	inositol-1,4,5-trisphosphate
IP$_3$R	inositol-1,4,5-trisphosphate receptor
IPTG	isopropyl β-D-thiogalactopyranoside
ITC	isothermal titration calorimetry
K$_d$	dissociation constant
kDa	kilodaltons
KH$_2$PO$_4$	potassium dihydrogen phosphate
LGMD	limb-girdle muscular dystrophy
MES	2-(N-morpholino) ethanesulfonic acid
MgCl$_2$	magnesium chloride
MM	Miyoshi myopathy
MOPS	3-(N-morpholino)-propanesulfonic acid
MW	molecular weight
NAADP	nicotinic acid dinucleotide phosphate
Na$^+$	sodium ion
NaCl	sodium chloride
Na$_2$HPO$_4$	disodium hydrogen phosphate
NH$_4$Cl	ammonium chloride
NMR	nuclear magnetic resonance
PAGE	polyacrylamide gel electrophoresis
PCR	polymerase chain reaction
PIP$_2$	phosphatidylinositol 4,5-bisphosphate

PLC	phospholipase C
PMCA	plasma membrane calcium ATPase
ppm	parts per million
RTK	receptor tyrosine kinases
SDS	sodium dodecyl sulfate
SERCA	sarco-endoplasmic reticulum calcium ATPase
SR	sarcoplasmic reticulum
SUMO	small ubiquitin-like modifier
TEV	tobacco etch virus
Tris	tris(hydroxymethyl) aminomethane
T2	transverse relaxation
TEV	tobacco etch virus
TCEP	tris(2-carboxyethyl)phosphine
TRP	ligand-gated channel
WT	wild type
Ala (A)	alanine
Arg (R)	arginine
Asn (N)	asparagine
Asp (D)	aspartic acid
Cys (C)	cysteine
Gln (Q)	glutamine
Glu (E)	glutamic acid
Gly (G)	glycine

His (H)	histidine
Ile (I)	isoleucine
Leu (L)	leucine
Lys (K)	lysine
Met (M)	methionine
Phe (F)	phenylalanine
Pro (P)	proline
Ser (S)	serine
Thr (T)	threonine
Trp (W)	tryptophan
Tyr (Y)	tyrosine
Val (V)	valine

Chapter 1

Introduction and Background

1.1 Calcium signaling in cells

Historically, calcium was first found to be essential for heart contraction by Sydney Ringer in 1883 (Ringer, 1883). An inadvertent use of tap water led to the astonishing finding that isolated rat hearts contracted perfectly in tap water, but failed to beat in distilled water. Ringer quickly realized that the contraction was attributed to residual calcium ions (Ca^{2+}), which was present at 38.3 parts per million, in the tap water supplied by London New River Water Company,. Although calcium was already known to be one of the most abundant elements in the skeleton and teeth, this unexpected finding recognized the important role of calcium as a fundamental carrier of chemical signals. In the 1940s, the concept of "calcium signaling" became prevalent, when Heilbrunn (Heilbrunn, 1940) and Bailey (Bailey, 1942) found that Ca^{2+} ions caused contraction of frog muscles and stimulated the ATPase activity of myosin. Since then, calcium has been identified to be involved in nearly every aspect of body activities.

The calcium signaling system operates in a variety of ways to regulate cellular processes that function over a wide dynamic range. In cells, a 20,000-fold gradient is maintained between the intracellular (~100 nM) and extracellular (mM) concentrations (Clapham, 2007; Tsien, 1981). The flow of Ca^{2+} in and out of the cells has to be precisely controlled

by specialized calcium pumps and channels at any moment in time. The internal stores of Ca^{2+} reside within the membrane systems of the endoplasmic reticulum (ER) or the sarcoplasmic reticulum (SR) of muscle cells. Cytosolic Ca^{2+} ions act as "secondary messengers" combined with a variety of effectors to stimulate and mediate numerous Ca^{2+}-dependent cellular processes including exocytosis, metabolism, transcription and proliferation. Berridge et al. divided the calcium signalling network into four functional steps (Berridge et al., 2000) (**Figure 1.1**):

1) Signalling is triggered by a stimulus that generates various Ca^{2+}-mobilizing signals. The stimuli bind to a variety of cell-surface receptors, such as G-protein-linked receptors and receptor tyrosine kinases (RTK), and generate signals, including inositol-1,4,5-trisphosphate (IP_3), cyclic ADP ribose (cADPR) and nicotinic acid dinucleotide phosphate (NAADP). These signals determine whether Ca^{2+} can activate channels on the plasma membrane and intracellular organelles.

2) The signals activate the ON mechanisms that feed Ca^{2+} into the cytoplasm. The ON mechanisms depend on Ca^{2+} channels that control the entry of external Ca^{2+} or the release of Ca^{2+} from internal stores. Ca^{2+} channels include voltage-gated Ca^{2+} channel (CaV) and ligand-gated channel (TRP) located on the plasma membrane, and IP_3R channel spanning on the membrane of ER.

3) Ca^{2+} functions as a messenger to stimulate various Ca^{2+}-sensitive processes. A wide variety of Ca^{2+} binding proteins respond to the Ca^{2+} release into the cytoplasm and activate numerous cellular processes.

4) Finally, the OFF mechanisms, composed of pumps and exchangers, remove Ca^{2+} from the cytoplasm to restore the resting state. OFF mechanisms pump Ca^{2+} out of
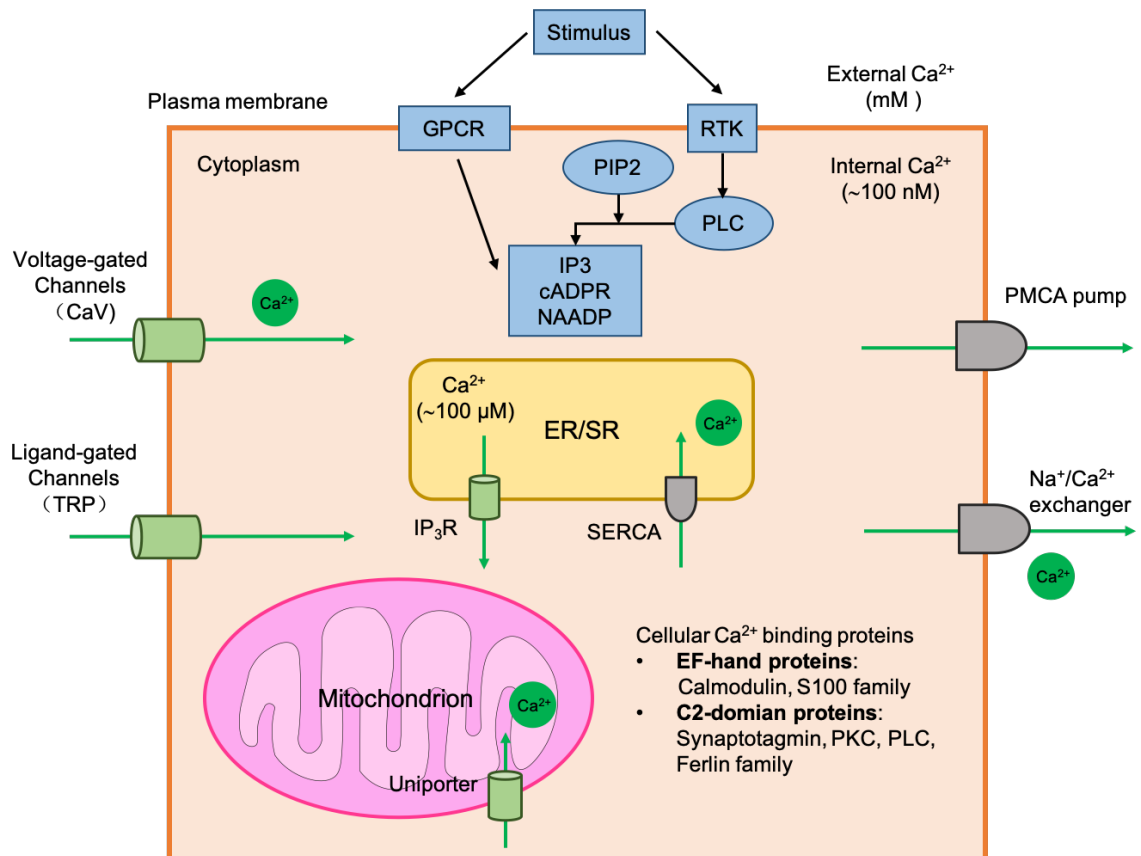
Figure 1. 1 Ca^{2+} signaling in cells.

A 20,000-fold gradient is maintained between the intracellular (~100 nM) and extracellular (mM) concentrations. Ca^{2+}-mobilizing signals (blue), including IP$_3$, cADPR and NAADP, are generated by stimuli acting through cell-surface receptors. ON mechanisms (green) include Ca^{2+} channels on plasma membrane and ER/SR, which control the entry of external Ca^{2+} or the release of Ca^{2+} from internal stores. The Ca^{2+} released into the cytoplasm by these ON mechanisms activates different Ca^{2+} binding proteins, which augment a wide range of cellular processes. A uniporter transmembrane complex transports Ca^{2+} into mitochondria. OFF mechanisms (grey) pump Ca^{2+} out of the cytoplasm: the Na$^+$/ Ca^{2+} exchanger and PMCA pump Ca^{2+} out of the cell, and the SERCA pumps it back into the ER/SR.

the cytoplasm once Ca^{2+} carried out its signaling functions. The plasma membrane Ca^{2+}-ATPase (PMCA) pumps and Na^+/Ca^{2+} exchangers extrude Ca^{2+} out of the cell and the sarco-endoplasmic reticulum ATPase (SERCA) pumps return Ca^{2+} back into the internal stores.

In the third step, calcium takes on the role of a near universal signaling molecule recognized by numerous calcium-binding proteins in eukaryotes, prokaryotes and even viruses (Permyakov, 2009; Permyakov and Kretsinger, 2011; Zhou et al., 2009). The calcium ion, with an ionic radius of 0.99 Å, can accommodate 4 - 12 oxygen atoms in its primary coordination sphere, with 6 - 8 being most common (Clapham, 2007). Calcium binding proteins use the oxygen atoms of carboxyl and carbonyl groups to coordinate binding to Ca^{2+}. The majority of calcium-binding sites in proteins consist of seven oxygen atoms surround Ca^{2+} at ~2.5 Å in a pentagonal bipyramid configuration (Strynadka and James, 1989) (**Figure 1.2**). It is worth mentioning that not all oxygen ligands in the Ca^{2+} coordination sphere are provided by amino acid residue side chains; main-chain carbonyl oxygen atoms and water molecules also participate (Katz et al., 1996). Hundreds of cellular proteins have adapted to selectively and reversibly bind Ca^{2+} through specific motifs. The binding occurs over a million-fold range of affinities (nM to mM) and the distinctive nature of each Ca^{2+}-mediated pathway is closely associated with this broad range of affinities. Substitutions or abnormalities in proteins involved in Ca^{2+} signaling can lead to a diverse array of diseases, including muscular dystrophy, congestive heart failure, diabetes, hypertension, maniac depression, cancers, and neurodegenerative diseases including Alzheimer's disease and amyotrophic lateral sclerosis (ALS) (Brini et al., 2014; Missiaen
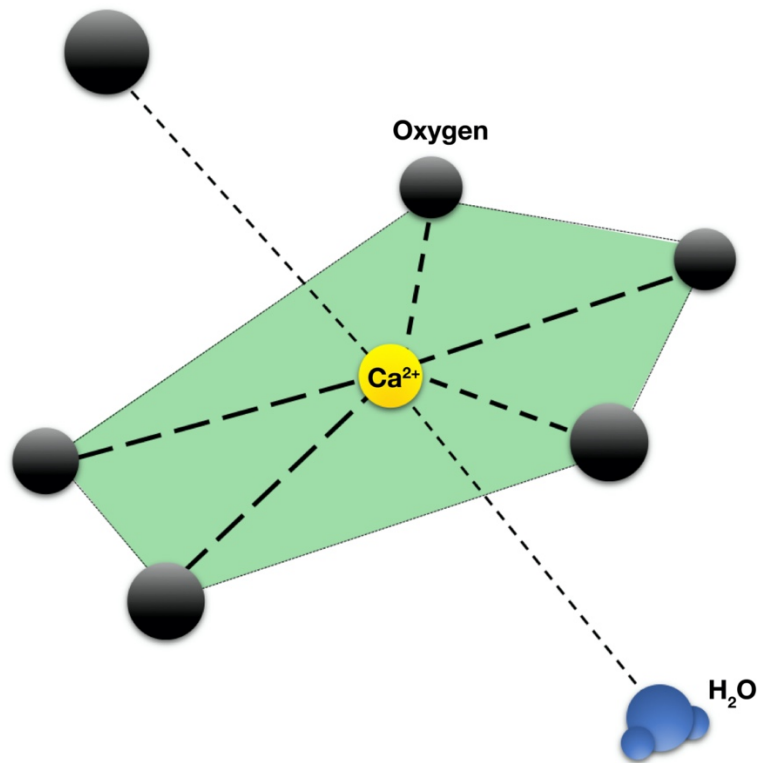
Figure 1. 2 Ca²⁺ coordination sphere.

Ca^{2+} is normally coordinated by seven oxygen atoms (five in the plane of the green pentagon and two perpendicular to the plane, thus forming a bipyramidal pentagon). All oxygen ligands in the Ca^{2} coordination sphere are provided by amino acid residue side-chain and main-chain oxygen atoms, as well as water molecules.

et al., 2000; Stewart et al., 2015). For example, disruption of the gene for calpain III, a calcium-dependent protease, causes limb girdle muscular distrophy type 2A; Defects in the genes for the PMCA pumps have been found to lead to hearing deficits (Carafoli, 2002).

Two major calcium binding motifs within cellular proteins have been extensively studied: EF-hand (eg. calmodulin, S100 family) and C2 domains (eg. synaptotagmin, PKC, ferlin family). Both mediate intracellular Ca^{2+} signals and direct diverse physiological events. The EF-hand motif is the most common Ca^{2+}-binding motif found in proteins. The EF-hand motif usually consists of 30 amino acids that fold into a helix-loop-helix structure. Its structure resembles a right hand fist, with the index finger and thumb extended. The loop between the helices comprises ~12 conserved residues that can coordinate a Ca^{2+} ion. Binding of calcium to this globular domain leads to a dramatic conformational change from "closed" to "open," exposing a hydrophobic surface that permits the interaction with target proteins in a Ca^{2+}-regulated manner. Calmodulin is the best known EF-hand protein: it has four EF-hand binding motifs, and the molecular mechanism by which it decodes the Ca^{2+} signal has been clarified. It interacts with hundreds of proteins in the cell, and acts as a regulator or an effector molecule in a wide variety of cellular functions (Ikura, 1996).

1.2 C2 domains

The C2 domain was originally discovered as the second of two conserved domains in classical protein kinase C (PKCs) responsible for calcium-dependent membrane binding. The C2 domain was proposed to be responsible for Ca^{2+} regulation of PKC, on the basis of

the finding that the kinase activity and phospholipid binding of PKC were known to be Ca^{2+} dependent, whereas the isoform lacking the C2 domain failed to exhibit Ca^{2+} dependent activities (Ono et al., 1989). Subsequent studies have revealed the existence of homologous C2 domains in a large number of proteins, which are widely distributed in all cell types in eukaryotes. Identification of the C2 domain in synaptotagmin (Perin et al., 1990) and cytosolic phospholipase A2 (cPLA$_2$) (Clark et al., 1991) found that they both bind to phospholipids and natural cell membranes in a Ca^{2+}-dependent manner, which is also a shared feature of protein kinase C (Bazzi and Nelsestuen, 1987, 1990; Brose et al., 1992). These findings led to the belief that the C2 domain was involved in Ca^{2+}-dependent membrane binding. Moving forward, a number of C2 domains within different proteins have been isolated and structurally characterized. Most of them are involved in signal transduction, lipid modification, membrane trafficking, activation of GTPases, and control of protein phosphorylation (Zhang and Aravind, 2010), including synaptotagmins (Fernandez et al., 2001; Shao et al., 1998), rabphilin-3A (Biadene et al., 2006), cPLA$_2$ (Perisic et al., 1998a) and so on.

To date, more than 100 structures of C2 domains have been solved by NMR (nuclear magnetic resonance) spectroscopy and X-ray crystallography. Characterization of the structures has confirmed that the C2 domain is an independently folded module of about 130 residues, and revealed a common fold that C2 domains share: an eight-stranded antiparallel β-sandwich consisting of a pair of four-stranded β-sheets connected by highly variable loops (Rizo and Südhof, 1998). Two types of topology are found in C2 domains: (i) the synaptotagmin-like variants also referred to as the type I topology and (ii) the PLC-

like variants, also known as the type II topology. The arrangement of β-strands in C2 domains of type II topology constitutes a circular permutation of type I C2 domains. Strand 1 of the type I C2 domains occupies the same position as the eighth strand of the type II C2 domains. In **Figure 1.3**, the N and C termini are at the top of the C2 domain in the type I topology but at the bottom of the type II topology. Having one or the other topology does not appear to be a determinant for the domain's function and it is unclear why C2 domains occur in two topologies (Corbalan-Garcia and Gómez-Fernández, 2014).

1.3 Ca^{2+} binding properties of C2 domains

The Ca^{2+}-binding sites of canonical C2 domains are composed of three variable loops located at one side of the domain (top) (**Figure 1.3**). Both side chains and the backbones of the loop residues are involved in coordination of multiple Ca^{2+} ions. The Ca^{2+}-binding sites are formed primarily by conserved aspartate residues and the carboxylate or carbonyl groups of other residues. Up to four Ca^{2+}-binding sites were identified to be possible in a C2 domain depending on the residues that are present on the loop (Ubach et al., 1998). In most cases, five highly conserved aspartate residues coordinate two or three Ca^{2+} ions. Taking the C2A domain of synaptotagmin as an example, there are five aspartate residues (D172, D178, D230, D232 and D238) in loops 1-3 that contribute to the coordination spheres of three Ca^{2+} ions via their carboxylate groups. Four of these residues (D172, D230, D232 and D238) simultaneously coordinate more than one Ca^{2+} ion. Additional residues on the loops also provide ligands for Ca^{2+} coordination, including the side chain of S235 and main chain oxygen of L171 and F231(Ubach et al., 1998). It is not clear why a C2 domain binds to multiple Ca^{2+} ions. One hypothesis is that multiple binding sites could be

8
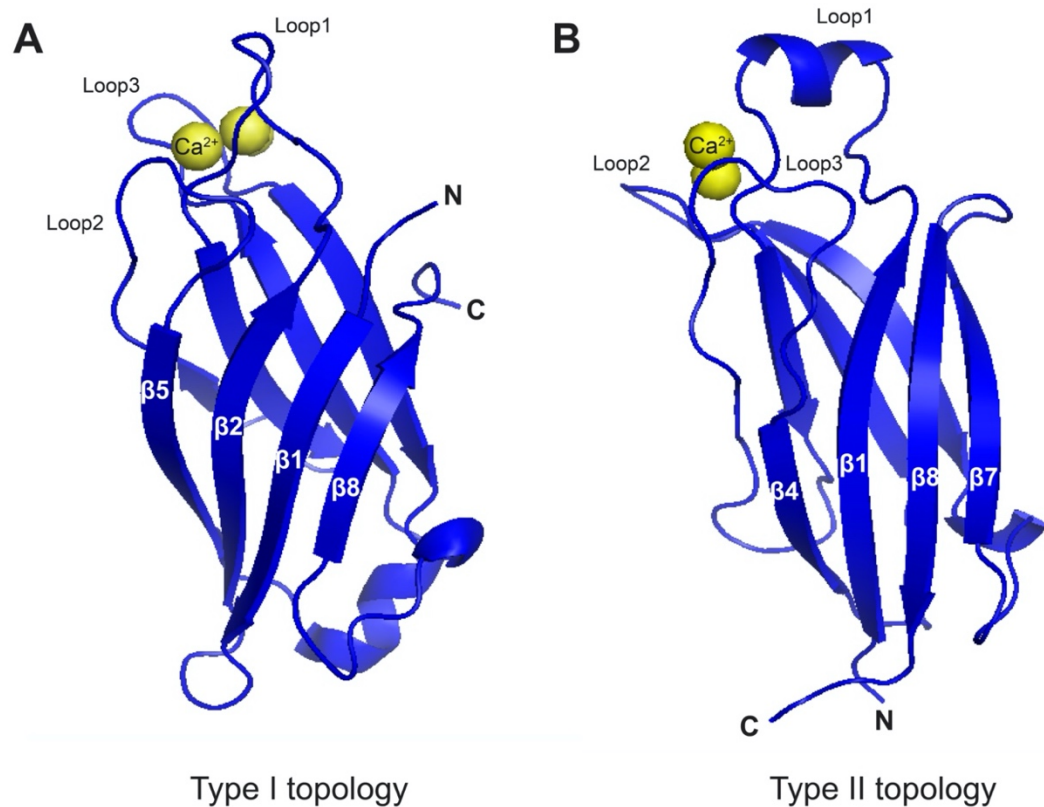
Figure 1. 2 Two topologies of C2 domain.

Cartoon diagrams of the structure of the type I and type II topology of C2 domains [left: synaptotagmin 5 C2A domain, PDB: 5H4Y; right: cytosolic phospholipase A2 (cPLA$_2$) C2 domain, PDB: 1RLW]. Bound Ca^{2+} ions are shown as yellow spheres and the localization of the three Ca^{2+} binding loops (Loop 1-3) are marked. Note that due to the circular permutation, the β1 strand in topology I overlaps with β8 strand in topology II, leaving the N- and C-terminals near the top of the domain in type I and at the bottom in type II.

advantageous by providing positive cooperativity to facilitate the Ca^{2+} binding, thereby generating a narrower activation threshold as observed for cooperative Ca^{2+} binding to many proteins of the EF-hand class (Linse and Forsén, 1995).

Although C2 domains share a high degree of structural homology and conserved residues for Ca^{2+} coordination (**Figure 1.4**), the Ca^{2+} binding mode varies from one C2 domain to another, in terms of binding stoichiometry and affinities. First, different numbers of Ca^{2+} ions have been found to occupy the Ca^{2+}-binding sites in different C2 domains, ranging from zero to four. For instance, the C2A domains of otoferlin (Helfmann et al., 2011) is unable to bind Ca^{2+} for having an unconventional loop 1, which is significantly shorter and flatter compared to the Ca^{2+} binding C2 domains. The C2 domain of protein kinase C-delta (PKCδ) (Pappa et al., 1998) has also been shown to be Ca^{2+} insensitive, due to lack of conserved aspartate residues necessary for Ca^{2+} coordination. In contrast, two Ca^{2+} ions bind to the cPLA$_2$ C2 (Perisic et al., 1998a), synaptotagmin-7 C2A (Voleti et al., 2017) and myoferlin C2A domains (Harsini et al., 2019) and three Ca^{2+} ions bind to synaptotagmin 1 C2B (Cheng et al., 2004) and phospholipase C-δ1 C2 domain (Essen et al., 1997). Four Ca^{2+} ions are observed to bind to the loop regions in the crystal structure of the C2 domain of perforin (Yagi et al., 2015) (**Figure 1.5**). Secondly, Ca^{2+} exhibits a wide range of binding affinities to different binding sites in C2 domains. Taking synaptotagmin 1 C2B domain as an example, the dissociation constants (K_d) measured for the three Ca^{2+} binding sites are 54 μM, 530 μM and >2 mM by NMR spectroscopy (Fernández-Chacón et al., 2001), and 119 μM, 465 μM and 1.7 mM by ITC (Radhakrishnan et al., 2009). In comparison, the C2 domain of plant phospholipase Dβ shows a single high affinity site with a K_d of 0.8 μM
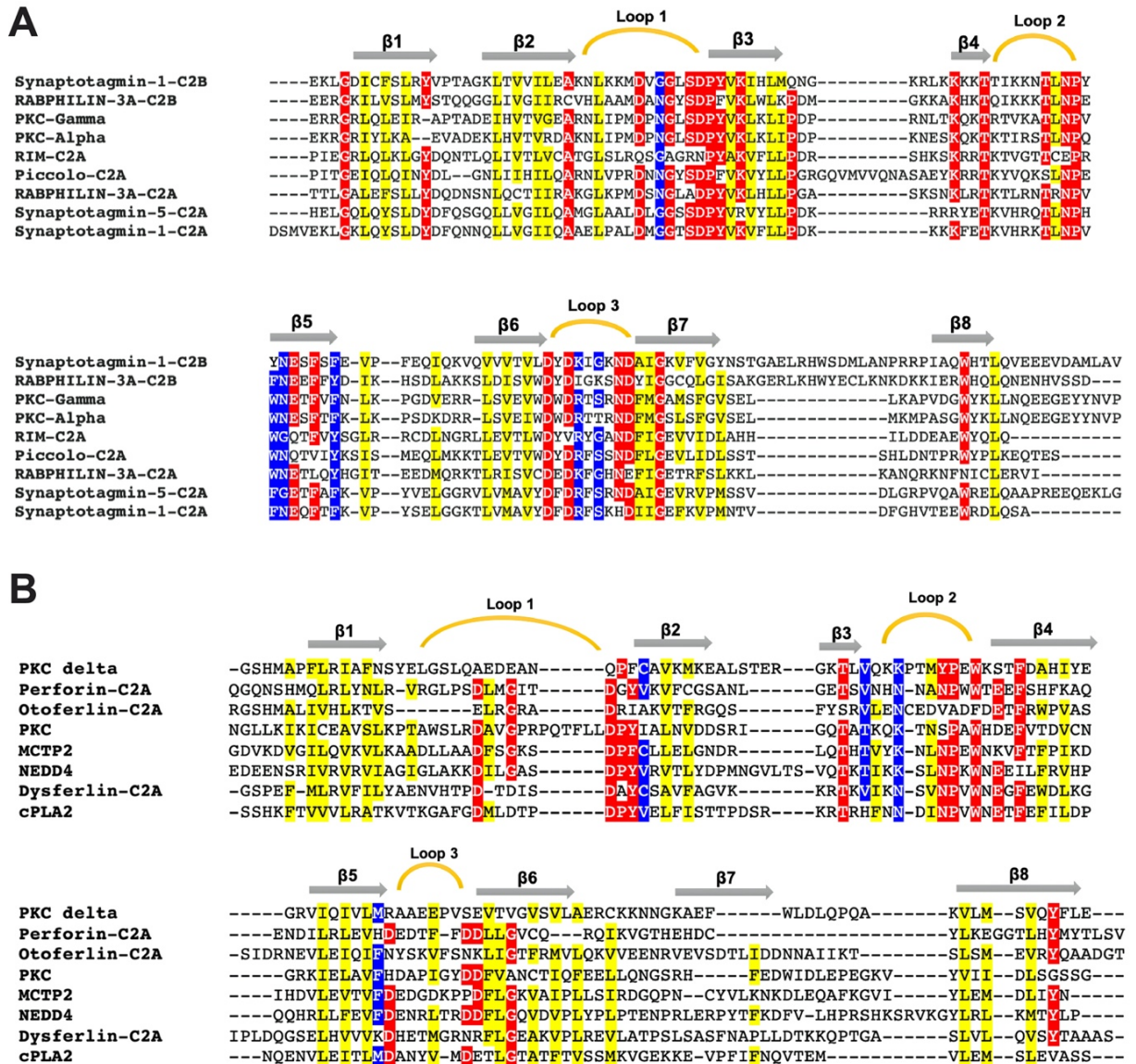
Figure 1. 3 Sequence alignments of selected C2 domains.

(A) Alignment of type I topology C2 domains. **(B)** Alignment of C2 domains that have type II topology. Residues that very highly conserved are highlighted in white with a red background. Residues that appear to be partially but still highly conserved are highlighted in white with a blue background. Hydrophobic residues are highlighted in yellow. The secondary structure domains (β-sheets and Ca^{2+}-binding loops) are indicated on the top of the sequences.
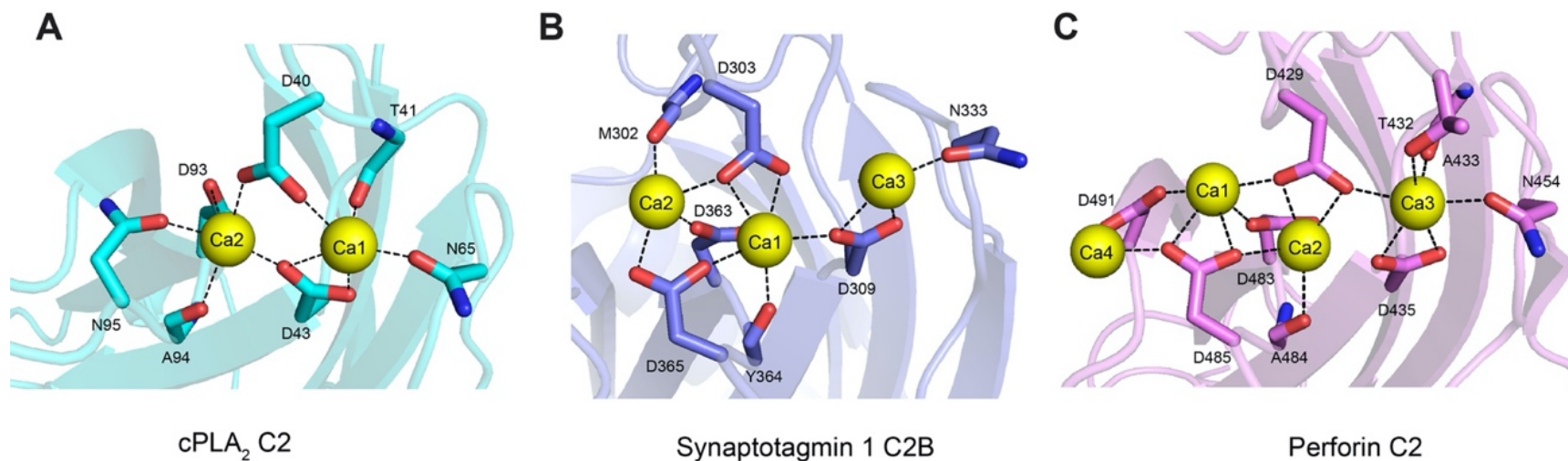
Figure 1. 4 Comparison of the Ca^{2+} binding modes of C2 domains.

(A) Two Ca^{2+} ions are bound to cPLA$_2$ C2 domain (cyan) (PDB: 1RLW)**. (B)** Three Ca^{2+} ions bind to synaptotagmin 1 C2B domain (blue) (PDB: 1UOV) . **(C)** Four Ca^{2+} ions are identified to bind to the loops of perforin C2 domain (pink) (PDB: 4Y1T). Bound Ca^{2+} ions are shown as yellow spheres and Ca^{2+} binding loops (Loop 1-3) are marked. Side chains and main chains of residues involved in Ca^{2+} coordination, contributing with oxygen atoms (red) are represented by sticks.

(Zheng et al., 2000). Moreover, C2 domains also demonstrate different Ca^{2+} dependencies for binding to phospholipids and other proteins, even for the same family of C2-containing proteins. All of the C2A-domains from the synaptotagmin proteins interact with syntaxin 1 in a Ca^{2+} dependent manner but synaptotagmins 1, 2, and 5 require Ca^{2+} concentrations of >0.2 mM, whereas synaptotagmins 3 and 7 bind at <1 µM Ca^{2+} (Li et al., 1995).

It is also worth mentioning that, it is not totally reliable to predict the Ca^{2+} binding manner of a C2 domain solely based on the sequence analysis. The position of variable loops, which provides the proper spatial orientation of residues for Ca^{2+} binding, is difficult to predict due to the high dynamics of the region. Secondly, Ca^{2+}-binding sites cannot simply be located from the sequence because the coordination of Ca^{2+} ions is also dictated by backbone carbonyl groups and water molecules. Therefore, direct structural characterization of C2 domains is of great significance on defining the Ca^{2+} binding mechanisms at the atomic level.

How does Ca^{2+} binding modulate the structure and activity of C2 domains? Unlike the Ca^{2+}-induced large structural rearrangement in EF-hand proteins (Ikura, 1996), Ca^{2+} binding does not seem to introduce big conformational changes of the C2 domain backbone: subtle rotations of some side chains upon Ca^{2+} coordination were witnessed in a number of studies (Grobler et al., 1996; Shao et al., 1996, 1998; Verdaguer et al., 1999). For example, as a consequence of Ca^{2+} binding to PLC- δ1, the only structural change occurs in the carboxylate oxygens of Asp 653 and Asp 708 at the binding sites, which move closer to each other by 0.8 Å. Binding of Ca^{2+} also has been shown to structurally stabilize the

secondary structure of C2 domains, and this is characterized by a variety of techniques, such as differential scanning calorimetry (DSC), infrared spectroscopy and thermal denaturation (García-García et al., 1999; Torrecillas et al., 2003, 2004).

Most importantly, it is broadly considered that the key role of Ca^{2+} binding to C2 domains is the electrostatic switch that changes the electrostatic potential of the loop region for favorable interaction with membranes. This model was initially proposed for the C2A domain of synaptotagmin 1 (Shao et al., 1997): upon Ca^{2+} binding, the zwitterionic environment of the loop region drastically changes, becoming largely positive, thereby triggering synaptic vesicle exocytosis. Later, electrostatic potential calculations of different C2 domains showed that Ca^{2+} markedly changes the potential of the loop regions, thereby facilitating the association to negatively charged or zwitterionic membranes (Murray and Honig, 2002).

1.4 Membrane binding properties of C2 domains

As mentioned above, one major function of proteins that contain C2 domains is targeting membrane surfaces as a consequence of Ca^{2+}-binding. A number of studies have demonstrated that C2 domains display different phospholipid selectivity. For example, the C2 domains of synaptotagmins and protein kinases C (PKC) family bind to acidic phospholipids such as phosphatidylserine (PS) and phosphatidylinositol (PI) (Corbalán-García et al., 1999; Fernandez et al., 2001; Fukuda et al., 1996; Medkova and Cho, 1998), whereas the C2 domains of cPLA2α and plant phospholipase D target neutral

phosphatidylcholine (PC) (Nalefski et al., 1998, 2001; Stahelin et al., 2003; Zheng et al., 2000). Furthermore, C2 domains also exhibit lipid specificity in a Ca^{2+}-dependent manner: studies have shown that at a Ca^{2+} concentration required for transmitter release (~100 μM) , the C2B domain of synaptotagmin 1 switches the specificity of binding from phosphatidylinositol-3,4,5-trisphosphate to phosphatidylinositol-4,5-bisphosphate (Schiavo et al., 1996). This lipid selectivity property may have a direct relation with the specific function a C2 domain carries as cell membranes present various and dynamic composition of lipids (Tucker et al., 2004).

To further explain these diverse lipid binding features of C2 domains, the binding mechanisms have to be elucidated. Effort by extensive studies has established the consensus that C2 domain binding to the membrane uses a combination of electrostatic and hydrophobic interaction. For a majority of membrane-binding C2 domains, the phospholipid binding site is related to the Ca^{2+}-binding region, and the residues on the surface of the Ca^{2+}-binding loops likely determine their lipid-binding manners. First, some C2 domains have been shown to bind anionic lipids via the cationic residues present on the loop region through non-specific electrostatic interaction irrespective of the presence of Ca^{2+} (Davletov and Sudhof, 1993; Fukuda et al., 1994). In contrast, a number of other C2 domains bind to their target phospholipids in a Ca^{2+}-dependent manner. As described earlier, Ca^{2+} binding changes the electrostatic potential of the loop region of many C2 domains and the resulting positively charged surface drives the interaction with anionic phospholipids, exemplified by the synaptotagmin C2A domain and PKCβ C2 domain (Murray and Honig, 2002; Striegel et al., 2012).

Structural characterization of the lipid binding sites of C2 domains has provided more insights on the binding mechanisms. An early determination of the three-dimensional structure of the C2 domain of PKCα in complex with Ca^{2+} and 1,2-dicaproyl-sn-phosphatidylserine (DCPS) showed that the phosphoryl group of the phosphoserine completes the coordination sphere of a Ca^{2+} ion (Verdaguer et al., 1999). In this case, Ca^{2+} acts as a bridge tethering the C2 domain and phospholipid (**Figure 1.6 A - B**). Additional binding sites were identified in the following ternary complex of Ca^{2+}-bound PKCα with either 1,2-diacetyl-*sn*-phosphatidyl-L-serine (DAPS) or 1,2-dicaproyl-*sn*-phos-phatidic acid (DCPA). The glycerol moiety of the phospholipid is hydrogen-bonded with residues Arg216 and Arg249 in loop 1; the serine head group interacts with Pro188 and Asn189 in loop 1 (Ochoa et al., 2002). This interplay between Ca^{2+} ions, phospholipid molecules and residues in C2 domains was subsequently supported by a number of studies on other C2 domains (Bittova et al., 1999; Hirano et al., 2019; Malmberg et al., 2003).

More recently, the X-ray crystal structure of cytosolic PLA2α (cPLA2α) C2 domain bound to 1,2-dihexanoyl-sn-glycero-3-phosphocholine (DHPC) was solved in the presence of Ca^{2+} (Hirano et al., 2019). In contrast to the two bound Ca^{2+} ions reported in the lipid-free structure (Dessen et al., 1999; Perisic et al., 1998a), an additional Ca^{2+} ion was observed to coordinate in the PC-bound structural complex by bridging residue N65 and the DHPC phosphoryl group. This finding expanded our views on the Ca^{2+}-dependent lipid binding mechanism of C2 domains. Indeed, most of the structural characterizations of C2 domains with Ca^{2+} are conducted in the lipid-free condition. It is possible that there is participation
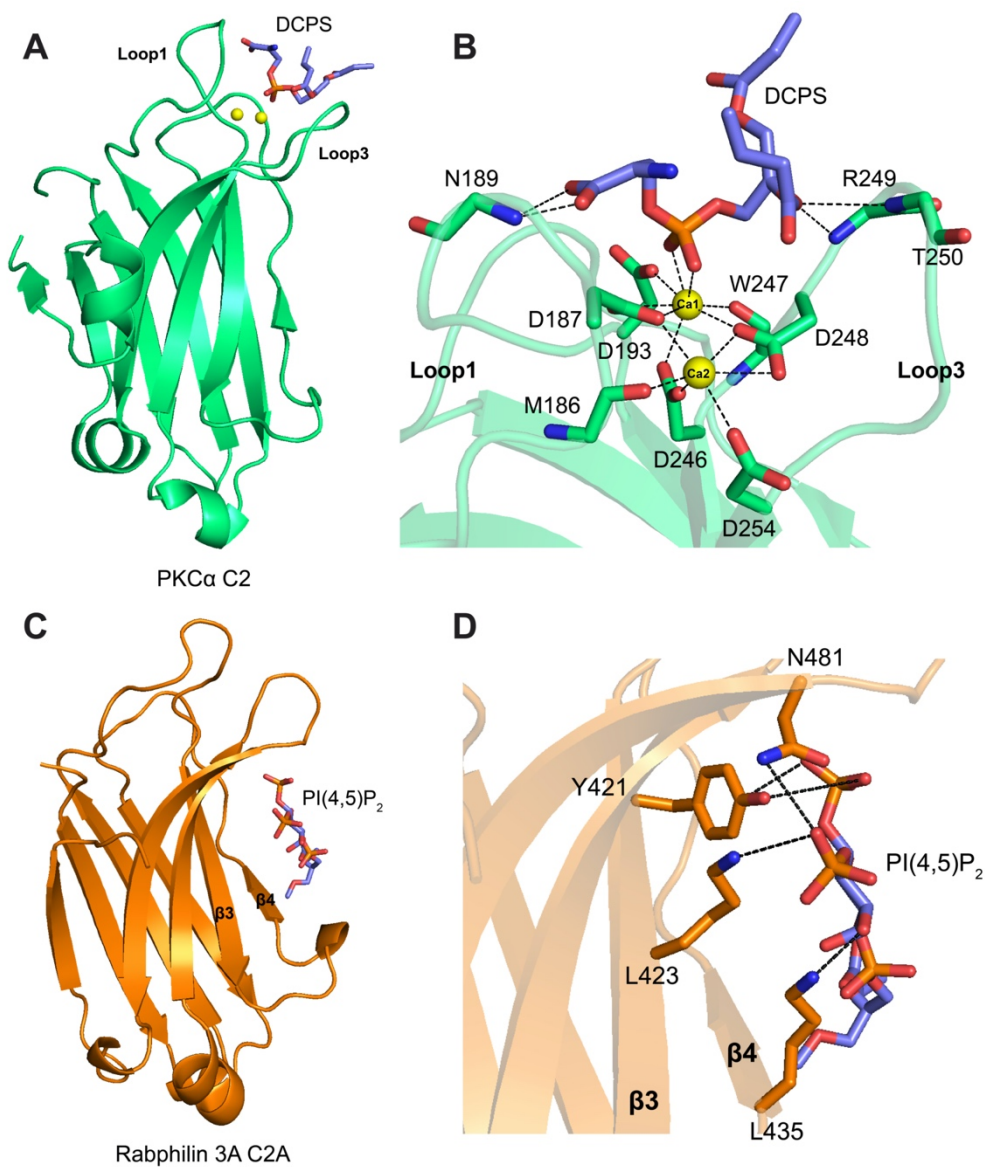
Figure 1. 5 Two lipid binding modes of C2 domain.

(A) Overall structure of the C2 domain of PKCα in complex with Ca^{2+} and DCPS (PDB: 1DSY) showing the lipid binding site overlaps with the Ca^{2+}-binding region. Bound Ca^{2+} ions are shown as yellow spheres. **(B)** Close-up view of the lipid binding site demonstrating the phosphoryl group completes the coordination sphere of a Ca^{2+} ion (Ca1). **(C)** The rabphilin 3A C2A-PI(4,5)P_2 complex (PDB: 4NS0), showing the β sheet groove interacts with the phospholipid. **(D)** Close-up view of the β3–β4 groove, indicating the interactions between the C2A domain and the PI(4,5)P_2 ligand. The C2 domain contacting residues and the corresponding ligands are represented in sticks and explicitly labeled. Bonds are shown as dashed lines in black.

of extra Ca^{2+} ions when C2 domains target membranes, which might help explain the existence of unoccupied Ca^{2+}-binding sites in many C2 domains.

Moreover, the crystal structures of PKCα with DAPS and DCPA showed the presence of a second binding site for phospholipids in the vicinity of the lysine-rich cluster from the β3 and β4 strands. The concave surface with positive charges suited to interact with the anionic lipids (Ochoa et al., 2002). This interaction was further confirmed by the crystal structure of PKCα C2 domain in complex with Ca^{2+} and PtdIns(4,5)P_2, where PtdIns(4,5)P_2 binds specifically to the β3-β4 groove, forming direction interactions with four lysines as well as two aromatic residues. Mutations of these residues were shown to cause severely impaired plasma membrane localization of PKCα. Structure-based sequence alignment has revealed high conservation of aromatic and cationic residues in the β3-β4 among many C2 domains, including synaptotagmins 1, 4, 7 and 13, rapbhilin 3A, PI3K-C2α, piccolo and RIM1, 2 (Corbalan-Garcia and Gómez-Fernández, 2014). This model was further supported by the crystal structures of the C2A domain of rabphilin 3A and synaptotagmin 1 in complex with PtdIns(4,5)P_2 and IP3, which show that a collection of residues surrounding the polybasic cluster are essential to hold the phosphoinositide in order to induce Ca^{2+}-dependent vesicle clustering (Guillen et al., 2013) (**Figure 1.6 C - D**). The finding that phospholipids specifically interact with the lysine-rich cluster in addition to the Ca^{2+} binding region, suggests that C2 domain may be regulated by a dual-target mechanism. However, how these two targets combine in nature is not clear yet.

1.5 Ca^{2+}-mediated membrane repair

Eukaryotic cells are not protected by a hardened and impermeant cell wall like bacterial cells. The loss of a cell wall leads to an unprotected lipid bilayer membrane, which is more vulnerable to mechanical and chemical stress. Consequently, plasma membrane disruption occurs frequently especially in mechanically active tissues, such as skeletal and cardiac muscles and skins (Clarke Mark S. F. et al., 1995; McNeil and Ito, 1990; McNeil and Khakee, 1992). By using histochemical techniques to detect membrane damage in rat muscle fibers, it was shown that membrane wounding occurs far more frequently after eccentric exercise than the unexercised rat (McNeil and Khakee, 1992). Fortunately, membrane repair mechanisms have evolved in eukaryotic cells to reseal membrane breaches. The wounded cell is able to survive when an effective repair response is triggered that restores membrane integrity.

In fact, early in the 1920s, studies on the embryonic fate of egg fragments already demonstrated that metazoan cells could survive rupture of their surface membranes (Wilson, 1925). Several decades later, Chambers & Chambers and Heilbrunn discovered that healing of injured cells required the presence of physiological levels of Ca^{2+} (Chambers and Chambers, 1961; Heilbrunn, 2013). They observed that, in the presence of Ca^{2+}, cells displayed a rapid (seconds) reaction to a wound. This consisted of the disappearance of certain cytoplasmic vesicles at the disruption site and the simultaneous appearance there of an enlarged vesicle population. They also inferred that cytoplasm would begin and continue to spill out of the wounded cell in the absence of Ca^{2+}. In the presence of Ca^{2+}, the wounded cell clearly recovered. The critical role of Ca^{2+} as an

activating trigger for membrane repair has been universally accepted since then and evidently supported by a myriad of other studies.

Pioneering studies of cell membrane repair mainly were performed on sea urchin eggs and revealed that repair of the disruptions is mediated by Ca^{2+}-regulated exocytosis. Using confocal microscopy, researchers visualized Ca^{2+}-dependent exocytosis during membrane resealing by a mechanism similar to neurotransmitter release: when a sea urchin egg was wounded with a laser beam, rapid and localized exocytosis followed Ca^{2+} influx at the wound site (Bi et al., 1995; Steinhardt et al., 1994). It was then proposed that exposure of cytoplasm to high Ca^{2+} caused by a puncture of the fibroblast or sea urchin egg surface results in massive fusion of internal vesicles with each other and with the plasma membrane. These fusion reactions proceed rapidly until a patch of membrane continuous with the plasma membrane has formed, preventing further Ca^{2+} entry (Terasaki et al., 1997). Subsequent studies identified lysosomes as the Ca^{2+}-regulated exocytic compartments responsible for plasma membrane repair based on the observation of specific markers of lysosomes aggregating on the surface of injured epithelial and myoblasts cells (Reddy et al., 2001; Rodríguez et al., 1997). Instead of the traditional view that lysosomes are the final sites of accumulation of internalized macromolecules, it is believed now that lysosomes also behave as secretory vesicles, fusing with the plasma membrane in response to Ca^{2+} entry (Andrews, 2000). Ca^{2+}-dependent lysosomal exocytosis was later shown to occur in injured muscle fibers (Corrotte et al., 2013; Lennon et al., 2003).

All these findings together have established a broadly accepted mechanism to explain cell membrane repair - the "lipid patch" model. This model proposes that, a disrupted membrane causes diffusion of Ca^{2+} from the extracellular space and creates a zone of high Ca^{2+} around the disruption site. In response to the Ca^{2+} influx, protein-carrying repair vesicles (lysosomes) are targeted to the disruption site, where they accumulate and fuse with one another and the plasma membrane. Fusion of the repair vesicles with the plasma membrane puts a membrane patch across the membrane disruption, thereby resealing the disrupted plasma membrane (**Figure 1.7**).

Consistent with the critical role of Ca^{2+} in cell membrane repair, a number of Ca^{2+}-sensor proteins have been identified to be involved in resealing in various cell types, including SNARE proteins, synaptotagmins, S100A10, annexins, calpains and Ferlins. Most Ca^{2+} sensor proteins contain one or more Ca^{2+}-binding domains, such as a C2 domain or an EF-hand motif. Taking synaptotagmins for example, as mentioned above, synaptotagmins are a group of transmembrane proteins that contain two C2 domains in their cytosolic regions (Davletov and Sudhof, 1993). Synaptotagmins 1 and 2 are conventionally known for triggering the Ca^{2+}-activated fusion of neurotransmitter-containing vesicles through interaction with SNARE machinery in neural synaptic vesicle exocytosis (Bommert et al., 1993; Brose et al., 1992; Elferink et al., 1993; Schiavo et al., 1997). Later, synaptotagmin 1 was shown to be required for membrane repair in severed axons of squid and crayfish giant axons (Detrait et al., 2000). In addition, synaptotagmin 7, ubiquitously expressed in mammalian cells, was found to be critical for membrane resealing in embryonic fibroblasts (Chakrabarti et al., 2003). Fibroblasts taken from synaptotagmin 7-deficient mice
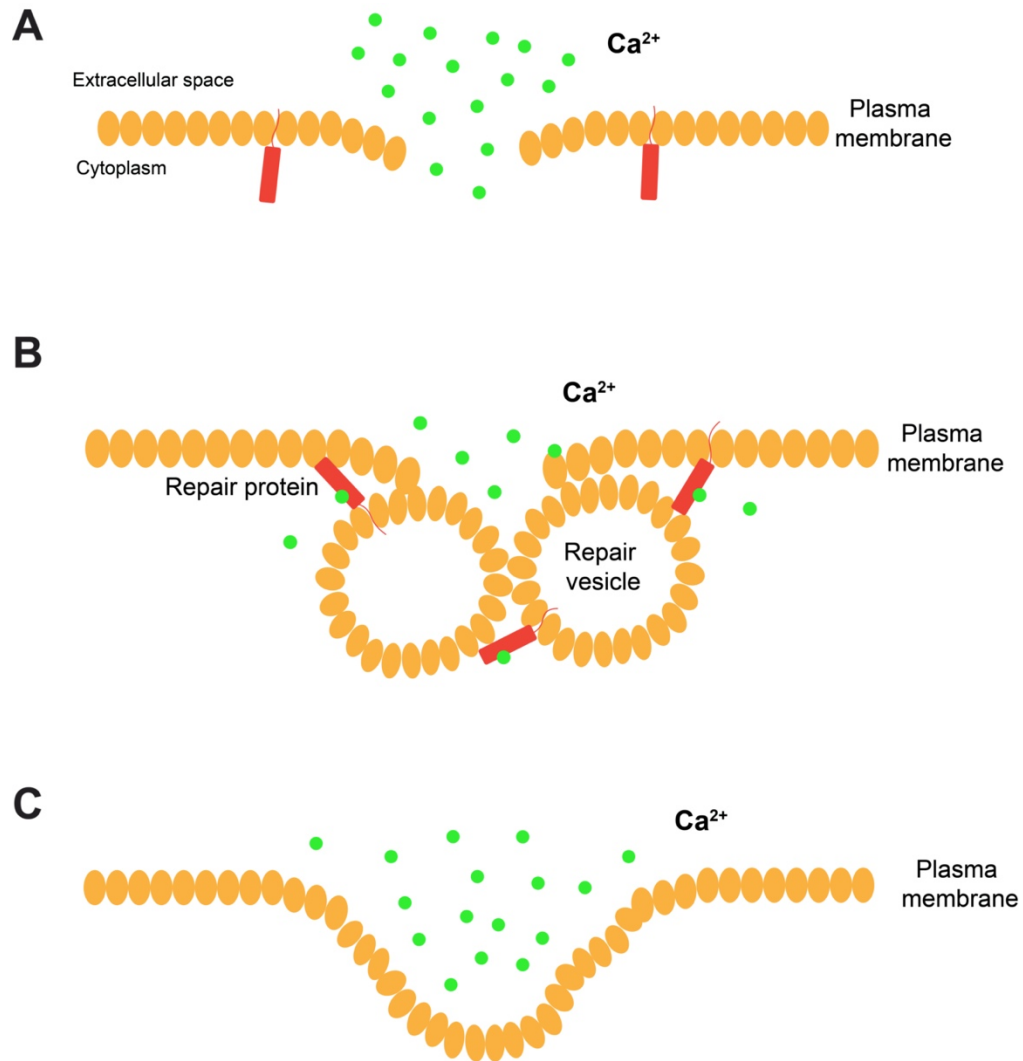
Figure 1. 6 Schematic diagram of the lipid patch model of plasma membrane repair.

(A) A disrupted membrane causes diffusion of Ca^{2+} from the extracellular space and creates a zone of Ca^{2+} calcium around the disruption site. **(B)** Ca^{2+} activates repair proteins and protein-carrying repair vesicles are targeted to the disruption site, where they accumulate and fuse with one another and the plasma membrane in the presence of localized high levels of Ca^{2+}. **(C)** Fusion of the repair vesicles with plasma membrane puts a membrane patch across the membrane disruption and thereby reseals the disrupted plasma membrane and prevents further Ca^{2+} entry.

demonstrated defective lysosomal exocytosis and decreased capacity to reseal their plasma membrane, resulting in extensive fibrosis in the skin and skeletal muscle.

Similar to synaptotagmins, a variety of proteins have been shown to be part of the membrane repair components, aside from the traditionally recognized functions of theirs, such as S100A10, annexins, and MG53 (Cai et al., 2009a; Koerdt and Gerke, 2017; Rezvanpour et al., 2011). Are there any proteins that have been identified to be specific and exclusive for membrane repair-based fusion events? Dysferlin seems to be the one.

1.6 Dysferlin and muscular dystrophy

In 1998, a novel gene was identified in skeletal muscle cell as the cause of two forms of inherited muscular dystrophy (Bashir et al., 1998; Liu et al., 1998). This gene shows homology to the *Caenorhabditis elegans* (*C. elegans*) spermatogenesis factor *fer-1*. The proposed name "dysferlin" combines the role of the gene in producing muscular dystrophy with its *C. elegans* homology. *Fer-1* is a spermatogenesis factor that is specifically expressed in primary spermatocytes of *C. elegans*. In spermatids, mutations in *fer-1* cause infertility by impairing the fusion of large vesicles with the plasma membrane (Achanzar and Ward, 1997; Ward et al., 1981). Given the structural and sequence homology between dysferlin and *fer-1*, it was postulated that dysferlin might also be a vesicle-associated membrane protein involved in the docking and fusion of vesicles in the skeletal muscle cells. Soon after the identification of dysferlin, several new genes showing protein structure and sequence similarity to dysferlin were identified, including myoferlin and otoferlin

23

(Britton et al., 2000; Yasunaga et al., 1999). Therefore, a new family of mammalian proteins was discovered and named "Ferlin". All ferlin proteins, including dysferlin, contain a variable number of C2 domains, accessory domains and a single C-terminal transmembrane spanning helix domain (Peulen et al., 2019).

In 2003, Bansal et al. made the fundamental discovery that dysferlin played an essential role in Ca^{2+}-dependent sarcolemma resealing. They showed that dysferlin-null mice developed a progressive muscular dystrophy, compared to the normal muscle cells, where membrane patches enriched in dysferlin can be detected in response to injuries. Further, increased entry of fluorescence dye into the muscle cells after a laser-induced disruption at plasma membrane was observed for the wounded muscle in the absence of Ca^{2+}, and dysferlin-null muscle, indicating disruptive muscle fibers could not be resealed without participation of Ca^{2+} or dysferlin (Bansal et al., 2003). Subsequently, the role of dysferlin in membrane repair was confirmed and extended by several other groups. For example, fusion and accumulation of dysferlin-containing vesicles and with lysosomes in response to muscle cell wounding was detected by live-cell imaging (McDade and Michele, 2014), supporting the "lipid patch" hypothesis for membrane repair mechanism described above.

However, the exact mechanism of dysferlin-mediated membrane repair is still unclear, and many steps involved in this process are unknown. One major mystery is the unique domain organization of dysferlin. Dysferlin is a 230 kD cytosolic-facing, membrane bound protein, which contains seven tandem C2 domains (C2A-C2G), two Fer domains (FerA and FerB) and a DysF domain (Sula et al., 2014) (**Figure 1.8 A**). Regarding the C2 domains of

dysferlin, it seems that they have distinct functions. For instance, the C2A domain was identified to bind phospholipids in a Ca^{2+}-dependent fashion, whereas other C2 domains showed weak and Ca^{2+}-independent binding (Therrien et al., 2009). It has been reported that the dysferlin C2A domain mediates the fusion of lysosomes with the plasma membrane (Han et al., 2012), and that it is also required for MG53-dependent accumulation of dysferlin at damage sites (Matsuda et al., 2012) (**Figure 1.8 B**). One study demonstrated that all seven dysferlin C2 domains interact with Ca^{2+} with various binding affinities ranging from micromolar to millimolar, and with different stoichiometry (Abdullah et al., 2014). Additionally, the C2B-C2C motif was proposed to mediate dysferlin expression at the plasma membrane, as well as its endocytic rate (Evesson et al., 2010). However, only the structure of the C2A domain of dysferlin has been reported (Fuson et al., 2014). There is very limited data regarding the structure and detailed Ca^{2+} binding mechanisms of other C2 domains. On the other hand, functions of Fer and DysF domains as well as the linker regions are also unidentified.

As mentioned, in humans, mutations in dysferlin are linked to two types of muscular dystrophy diseases: limb-girdle muscular dystrophy 2B (LGMD2B), a autosomal recessive degenerative myopathy, and Miyoshi muscular dystrophy (MM), a late-onset muscular dystrophy. Muscular dystrophy is a diverse group of inherited myogenic disorders, characterized by progressive loss of skeletal muscle strength and integrity, causing muscle weakness and wasting. Clinically, these diseases can present at any age from birth to middle years, resulting in severe morbidity and disability (Laval and Bushby, 2004). At the level of muscle pathology, muscular dystrophies are characterized by necrotic and regenerating

A

| C2A | C2B | C2C | FerA FerB | DysF | C2D | C2E | C2F | C2G | TM |

B
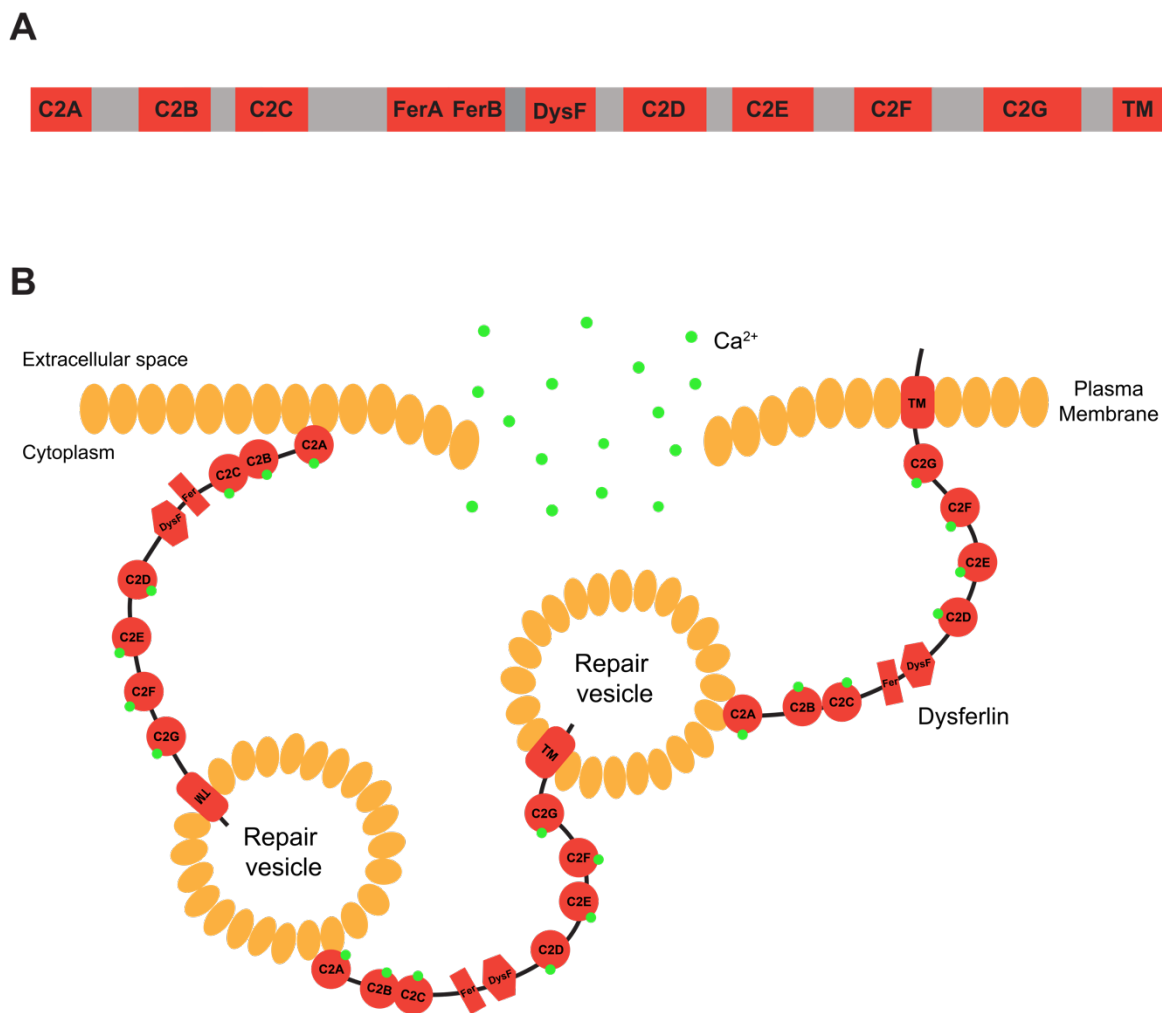
Figure 1. 7 Dysferlin domain organization and dysferlin-mediated membrane repair model.

(A) Domain organization for human dysferlin showing the seven C2 domains, two Fer domains, one DysF domain and a C-terminal transmembrane domain (red), connected by linker regions (grey). **(B)** Dysferlin is localized by its C-terminal transmembrane domain to cytoplasmic vesicles and the plasma membrane. On injury of the membrane, Ca^{2+} influx (green) raises the intracellular Ca^{2+} concentration locally, triggering the dysferlin-mediated patch repair response by binding to the C2 domains of dysferlin. Dysferlin molecules present on repair vesicles and the plasma membrane mediate docking and fusion of the patch, sealing the membrane breach, and preventing further influx of Ca^{2+} ions.

fibres, increase in fibre size variation, fibre splitting and centrally located myonuclei. Successive rounds of degeneration and regeneration of muscle fibres eventually result in necrosis and replacement of muscle with fatty and fibrous tissue (Laval and Bushby, 2004). Its most common form in children, Duchenne muscular dystrophy, affects approximately 1 in every 3,500 to 6,000 male births each year in the United States. To date, there are more than 30 forms of clinically distinctive muscular dystrophies, classified by the distribution of muscle degeneration, age of onset, rate of progression, severity of symptoms, and family history.

LGMD2B and Miyoshi myopathy (MM) are two autosomal recessive muscle diseases. LGMD2B is a predominantly proximal muscular dystrophy affecting the voluntary muscles, such as the arms, legs, fingers, toes, and facial muscles. The patients show normal mobility in childhood with a slowly progressive muscle weakness and wasting (Prelle et al., 2003). By contrast, Miyoshi myopathy is a predominantly distal muscular dystrophy with early involvement of muscles that are located away from the center of the body, such as those in the legs (Flachenecker et al., 1996).

More than 100 pathogenic mutations have been identified throughout the entire dysferlin gene including all seven C2 domains (Krahn et al., 2009). Clinical data have reported that the pathogenic dysferlin mutations affect the protein expression level in skeletal muscle, characterized by severely decreased or absence of dysferlin expression (Krahn et al., 2009; Nguyen et al., 2005). An amount of dysferlin $\leq 20\%$ has been shown to be pathogenic and always caused by primary dysferlin gene mutations (Cacciottolo et al., 2011). The V67D

substitution on the C2A domain was shown to impede the membrane repair process by diminishing phospholipid binding (Davis et al., 2002). Another substitution on the C2A domain, W52R, leading to Miyoshi myopathy (MM) (De Luna et al., 2007) inhibits the association with MG53 (Matsuda et al., 2012). The L344P substitution occurs within the linker between dysferlin C2B and C2C domains was demonstrated to change the tertiary conformation of C2B-C2C module (Woolger et al., 2017). Nevertheless, how these substitutions affect dysferlin expression and activities on the molecular basis still remains largely unknown.

Last but not least, *in vivo* studies (co-immunoprecipitation, pull-down assays, immunofluorescence, etc.) have made progress on identifying proteins that cooperate with dysferlin to regulate membrane fusion and provided new mechanistic insights into dysferlin function. For instance, dysferlin associates with annexins A1 and A2 in a Ca^{2+}-dependent and membrane injury dependent manner (Lennon et al., 2003); Caveolin-3 and calpain-3, two muscle specific proteins that are responsible for distinct forms of muscular dystrophy, have also been found to interact with dysferlin (Matsuda et al., 2001; Anderson et al., 2000). Patients deficient in caveolin-3 have been reported to exhibit a reduction or mislocalization of dysferlin, and patients deficient in dysferlin have reduced levels of calpain-3 (Anderson et al., 2000; Capanni et al., 2003). Dysferlin binding to SNAREs was identified in myoblast cell, revealing a function for dysferlin as a Ca^{2+} sensing SNARE-mediated membrane fusion events (Codding et al., 2016). Futhermore, dysferlin was shown to bind to AHNAK, a previously reported marker of enlargeosomes (Cocucci et al., 2004), through the C2A domain (Huang et al., 2007). AHNAK has also been reported to

participate in a ternary membrane repair complex with S100A10 and annexin A2 (Dempsey et al., 2012; Rezvanpour et al., 2011). Dysferlin with MG53 and caveolin-3 were shown to made up an essential component of the membrane repair machinery in striated muscle (Cai et al., 2009b). Additionally, the C2A domain of dysferlin was identified to be important for association with MG53. All these findings combined with multiple proteomic studies have suggested a multiprotein complex that includes dysferlin, AHNAK, annexin, S100A10, and MG53, and the C2A domain seems to play a critical role in interacting with other proteins (Leung et al., 2011; Morrée et al., 2010; Park et al., 2010). Thus, to uncover the mechanisms of membrane repair and related disorders, it is important to understand how the dysferlin-mediated membrane repair complex is assembled and how Ca^{2+} may play a regulatory role.

1.7 Scope of thesis

Dysferlin plays an essential role in muscle cell membrane resealing and abnormality of it leads to serious muscular dystrophy diseases. However, lack of information on the structures and Ca^{2+}-binding modes of the C2 domains of dysferlin does not allow a full understanding of the mechanisms of membrane repair. Although a crystal structure of the C2A domain was reported prior to the thesis (Fuson et al., 2014), it is unclear how the domain interacts with Ca^{2+}. The Ca^{2+}-binding site of the C2A domain is yet to be unveiled. Further, identification of other C2 domains in dysferlin remains ambiguous with respect to the domain boundaries and structural characterization. Limited data exists about the possible interdomain interaction and the modular topology of dysferlin. In addition, how

pathogenic substitutions affect the activities of dysferlin on the molecular basis still remains largely unknown.

Consequently, further biochemical and structural studies will be needed to answer the above questions. The objectives of this thesis were:

1) Determine the structure of the dysferlin C2A domain in the Ca^{2+}-free and Ca^{2+}-bound state. Assess the dynamics of the protein in the two states. (**Chapter 2 – 3**)

2) Investigate how calcium binds and modulates the dysferlin C2A domain in details. Compare the calcium binding mode with that of other C2 domain containing proteins. (**Chapter 3**)

3) Assess how some pathogenic substitutions in dysferlin C2 domains affect the domain structure and activity. (**Chapter 4**)

4) Characterize other C2 domains in dysferlin such as C2B and C2C domains and determine the precise domain boundaries. Explore the possible interdomain interactions. (**Chapter 5**)

To address these goals, a variety of biophysical and thermodynamic techniques were undertaken. Nuclear magnetic resonance (NMR) spectroscopy and X-ray crystallography were used to determine the structures of dysferlin C2A domain. The dynamic properties of the C2A domain were probed by NMR spectroscopy and circular dichroism (CD) spectropolarimetry, which revealed the flexibility of the dysferlin C2A domain as its unique feature. Isothermal titration calorimetry (ITC) was carried out to measure the thermodynamic properties of Ca^{2+} binding to the C2A domain. Based on the solved

structures and established Ca^{2+} binding properties of the C2A domain, impact of pathogenic mutations was then assessed on the molecular basis. Finally, to design and generate recombinant dysferlin C2B and C2C domains, a combination of biological and computational analyses were used. Together, these studies expand our knowledge of the Ca^{2+} signaling in dysferlin-mediated membrane repair, and pathogenesis of related diseases. The work also helps guide future strategies for investigating the tertiary folding of dysferlin.

1.8 References

Abdullah, N., Padmanarayana, M., Marty, N.J., and Johnson, C.P. (2014). Quantitation of the Calcium and Membrane Binding Properties of the C2 Domains of Dysferlin. Biophys. J. *106*, 382–389.

Achanzar, W.E., and Ward, S. (1997). A nematode gene required for sperm vesicle fusion. J. Cell Sci. *110*, 1073–1081.

Anderson, L.V.B., Harrison, R.M., Pogue, R., Vafiadaki, E., Pollitt, C., Davison, K., Moss, J.A., Keers, S., Pyle, A., Shaw, P.J., et al. (2000). Secondary reduction in calpain 3 expression in patients with limb girdle muscular dystrophy type 2B and Miyoshi myopathy (primary dysferlinopathies). Neuromuscul. Disord. *10*, 553–559.

Andrews, N.W. (2000). Regulated secretion of conventional lysosomes. Trends Cell Biol. *10*, 316–321.

Bailey, K. (1942). Myosin and adenosinetriphosphatase. Biochem. J. *36*, 121–139.

Bansal, D., Miyake, K., Vogel, S.S., Groh, S., Chen, C.-C., Williamson, R., McNeil, P.L., and Campbell, K.P. (2003). Defective membrane repair in dysferlin-deficient muscular dystrophy. Nature *423*, 168–172.

Bashir, R., Britton, S., Strachan, T., Keers, S., Vafiadaki, E., Lako, M., Richard, I., Marchand, S., Bourg, N., Argov, Z., et al. (1998). A gene related to Caenorhabditis elegans spermatogenesis factor fer-1 is mutated in limb-girdle muscular dystrophy type 2B. Nat. Genet. *20*, 37–42.

Bazzi, M.D., and Nelsestuen, G.L. (1987). Association of protein kinase C with phospholipid vesicles. Biochemistry *26*, 115–122.

Bazzi, M.D., and Nelsestuen, G.L. (1990). Protein kinase C interaction with calcium: a phospholipid-dependent process. Biochemistry *29*, 7624–7630.

Berridge, M.J., Lipp, P., and Bootman, M.D. (2000). The versatility and universality of calcium signalling. Nat. Rev. Mol. Cell Biol. *1*, 11–21.

Bi, G.Q., Alderton, J.M., and Steinhardt, R.A. (1995). Calcium-regulated exocytosis is required for cell membrane resealing. J. Cell Biol. *131*, 1747–1758.

Biadene, M., Montaville, P., Sheldrick, G.M., and Becker, S. (2006). Structure of the C2A domain of rabphilin-3A. Acta Crystallogr. D Biol. Crystallogr. *62*, 793–799.

Bittova, L., Sumandea, M., and Cho, W. (1999). A Structure-Function Study of the C2 Domain of Cytosolic Phospholipase A2 IDENTIFICATION OF ESSENTIAL CALCIUM LIGANDS AND HYDROPHOBIC MEMBRANE BINDING RESIDUES. J. Biol. Chem. *274*, 9665–9672.

Bommert, K., Charlton, M.P., DeBello, W.M., Chin, G.J., Betz, H., and Augustine, G.J. (1993). Inhibition of neurotransmitter release by C2-domain peptides implicates synaptotagmin in exocytosis. Nature *363*, 163–165.

Brini, M., Calì, T., Ottolini, D., and Carafoli, E. (2014). Neuronal calcium signaling: function and dysfunction. Cell. Mol. Life Sci. *71*, 2787–2814.

Britton, S., Freeman, T., Vafiadaki, E., Keers, S., Harrison, R., Bushby, K., and Bashir, R. (2000). The Third Human FER-1-like Protein Is Highly Similar to Dysferlin. Genomics *68*, 313–321.

Brose, N., Petrenko, A.G., Sudhof, T.C., and Jahn, R. (1992). Synaptotagmin: a calcium sensor on the synaptic vesicle surface. Science *256*, 1021–1025.

Cacciottolo, M., Numitone, G., Aurino, S., Caserta, I.R., Fanin, M., Politano, L., Minetti, C., Ricci, E., Piluso, G., Angelini, C., et al. (2011). Muscular dystrophy with marked Dysferlin deficiency is consistently caused by primary dysferlin gene mutations. Eur. J. Hum. Genet. *19*, 974–980.

Cai, C., Masumiya, H., Weisleder, N., Matsuda, N., Nishi, M., Hwang, M., Ko, J.-K., Lin, P., Thornton, A., Zhao, X., et al. (2009a). MG53 nucleates assembly of cell membrane repair machinery. Nat. Cell Biol. *11*, 56–64.

Cai, C., Weisleder, N., Ko, J.-K., Komazaki, S., Sunada, Y., Nishi, M., Takeshima, H., and Ma, J. (2009b). Membrane Repair Defects in Muscular Dystrophy Are Linked to Altered Interaction between MG53, Caveolin-3, and Dysferlin. J. Biol. Chem. *284*, 15894–15902.

Capanni, C., Sabatelli, P., Mattioli, E., Ognibene, A., Columbaro, M., Lattanzi, G., Merlini, L., Minetti, C., Maraldi, N.M., and Squarzoni, S. (2003). Dysferlin in a hyperCKaemic patient with caveolin 3 mutation and in C2C12 cells after p38 MAP kinase inhibition. Exp. Mol. Med. *35*, 538–544.

Carafoli, E. (2002). Calcium signaling: A tale for all seasons. Proc. Natl. Acad. Sci. *99*, 1115–1122.

Chakrabarti, S., Kobayashi, K.S., Flavell, R.A., Marks, C.B., Miyake, K., Liston, D.R., Fowler, K.T., Gorelick, F.S., and Andrews, N.W. (2003). Impaired membrane resealing and autoimmune myositis in synaptotagmin VII–deficient mice. J. Cell Biol. *162*, 543–549.

Chambers, R., and Chambers, E.L. (1961). Explorations into the Nature of the Living Cell. Acad. Med. *36*, 966.

Cheng, Y., Sequeira, S.M., Malinina, L., Tereshko, V., Söllner, T.H., and Patel, D.J. (2004). Crystallographic identification of Ca2+ and Sr2+ coordination sites in synaptotagmin I C2B domain. Protein Sci. Publ. Protein Soc. *13*, 2665–2672.

Clapham, D.E. (2007). Calcium Signaling. Cell *131*, 1047–1058.

Clark, J.D., Lin, L.-L., Kriz, R.W., Ramesha, C.S., Sultzman, L.A., Lin, A.Y., Milona, N., and Knopf, J.L. (1991). A novel arachidonic acid-selective cytosolic PLA2 contains a Ca2+-dependent translocation domain with homology to PKC and GAP. Cell *65*, 1043–1051.

Clarke Mark S. F., Caldwell Robert W., Chiao Hsi, Miyake Katsuya, and McNeil Paul L. (1995). Contraction-Induced Cell Wounding and Release of Fibroblast Growth Factor in Heart. Circ. Res. *76*, 927–934.

Cocucci, E., Racchetti, G., Podini, P., Rupnik, M., and Meldolesi, J. (2004). Enlargeosome, an Exocytic Vesicle Resistant to Nonionic Detergents, Undergoes Endocytosis via a Nonacidic Route. Mol. Biol. Cell *15*, 5356–5368.

Codding, S.J., Marty, N., Abdullah, N., and Johnson, C.P. (2016). Dysferlin Binds SNAREs (Soluble *N*-Ethylmaleimide-sensitive Factor (NSF) Attachment Protein Receptors) and Stimulates Membrane Fusion in a Calcium-sensitive Manner. J. Biol. Chem. *291*, 14575–14584.

Corbalan-Garcia, S., and Gómez-Fernández, J.C. (2014). Signaling through C2 domains: More than one lipid target. Biochim. Biophys. Acta BBA - Biomembr. *1838*, 1536–1547.

Corbalán-García, S., Rodríguez-Alfaro, J.A., and Gómez-Fernández, J.C. (1999). Determination of the calcium-binding sites of the C2 domain of protein kinase Calpha that are critical for its translocation to the plasma membrane. Biochem. J. *337 (Pt 3)*, 513–521.

Corrotte, M., Almeida, P.E., Tam, C., Castro-Gomes, T., Fernandes, M.C., Millis, B.A., Cortez, M., Miller, H., Song, W., Maugel, T.K., et al. (2013). Caveolae internalization repairs wounded cells and muscle fibers. ELife *2*, e00926.

Davis, D.B., Doherty, K.R., Delmonte, A.J., and McNally, E.M. (2002). Calcium-sensitive Phospholipid Binding Properties of Normal and Mutant Ferlin C2 Domains. J. Biol. Chem. *277*, 22883–22888.

Davletov, B.A., and Sudhof, T.C. (1993). A single C2 domain from synaptotagmin I is sufficient for high affinity Ca2+/phospholipid binding. J. Biol. Chem. *268*, 26386–26390.

De Luna, N., Freixas, A., Gallano, P., Caselles, L., Rojas-García, R., Paradas, C., Nogales, G., Dominguez-Perles, R., Gonzalez-Quereda, L., Vílchez, J.J., et al. (2007). Dysferlin expression in monocytes: A source of mRNA for mutation analysis. Neuromuscul. Disord. *17*, 69–76.

Dempsey, B.R., Rezvanpour, A., Lee, T.-W., Barber, K.R., Junop, M.S., and Shaw, G.S. (2012). Structure of an Asymmetric Ternary Protein Complex Provides Insight for Membrane Interaction. Structure *20*, 1737–1745.

Dessen, A., Tang, J., Schmidt, H., Stahl, M., Clark, J.D., Seehra, J., and Somers, W.S. (1999). Crystal Structure of Human Cytosolic Phospholipase A2 Reveals a Novel Topology and Catalytic Mechanism. Cell *97*, 349–360.

Detrait, E., Eddleman, C.S., Yoo, S., Fukuda, M., Nguyen, M.P., Bittner, G.D., and Fishman, H.M. (2000). Axolemmal repair requires proteins that mediate synaptic vesicle fusion. J. Neurobiol. *44*, 382–391.

Elferink, L.A., Peterson, M.R., and Scheller, R.H. (1993). A role for synaptotagmin (p65) in regulated exocytosis. Cell *72*, 153–159.

Essen, L.-O., Perisic, O., Lynch, D.E., Katan, M., and Williams, R.L. (1997). A Ternary Metal Binding Site in the C2 Domain of Phosphoinositide-Specific Phospholipase C-δ1 [†,‡]. Biochemistry *36*, 2753–2762.

Evesson, F.J., Peat, R.A., Lek, A., Brilot, F., Lo, H.P., Dale, R.C., Parton, R.G., North, K.N., and Cooper, S.T. (2010). Reduced Plasma Membrane Expression of Dysferlin Mutants Is Attributed to Accelerated Endocytosis via a Syntaxin-4-associated Pathway. J. Biol. Chem. *285*, 28529–28539.

Fernandez, I., Araç, D., Ubach, J., Gerber, S.H., Shin, O., Gao, Y., Anderson, R.G.W., Südhof, T.C., and Rizo, J. (2001). Three-Dimensional Structure of the Synaptotagmin 1 C2B-Domain: Synaptotagmin 1 as a Phospholipid Binding Machine. Neuron *32*, 1057–1069.

Fernández-Chacón, R., Königstorfer, A., Gerber, S.H., García, J., Matos, M.F., Stevens, C.F., Brose, N., Rizo, J., Rosenmund, C., and Südhof, T.C. (2001). Synaptotagmin I functions as a calcium regulator of release probability. Nature *410*, 41–49.

Flachenecker, P., Kiefer, R., Naumann, M., Handwerker, M., and Reichmann, H. (1996). Distal muscular dystrophy of Miyoshi type. J. Neurol. *244*, 23–29.

Fukuda, M., Aruga, J., Niinobe, M., Aimoto, S., and Mikoshiba, K. (1994). Inositol-1,3,4,5-tetrakisphosphate binding to C2B domain of IP4BP/synaptotagmin II. J. Biol. Chem. *269*, 29206–29211.

Fukuda, M., Kojima, T., and Mikoshiba, K. (1996). Phospholipid Composition Dependence of Ca-dependent Phospholipid Binding to the C2A Domain of Synaptotagmin IV. J. Biol. Chem. *271*, 8430–8434.

Fuson, K., Rice, A., Mahling, R., Snow, A., Nayak, K., Shanbhogue, P., Meyer, A.G., Redpath, G.M.I., Hinderliter, A., Cooper, S.T., et al. (2014). Alternate Splicing of Dysferlin C2A Confers Ca2+-Dependent and Ca2+-Independent Binding for Membrane Repair. Structure *22*, 104–115.

García-García, J., Corbalán-García, S., and Gómez-Fernández, J.C. (1999). Effect of Calcium and Phosphatidic Acid Binding on the C2 Domain of PKCα As Studied by Fourier Transform Infrared Spectroscopy. Biochemistry *38*, 9667–9675.

Grobler, J.A., Essen, L.-O., Williams, R.L., and Hurley, J.H. (1996). C2 domain conformational changes in phospholipase C-δ1. Nat. Struct. Biol. *3*, 788–795.

Guillen, J., Ferrer-Orta, C., Buxaderas, M., Perez-Sanchez, D., Guerrero-Valero, M., Luengo-Gil, G., Pous, J., Guerra, P., Gomez-Fernandez, J.C., Verdaguer, N., et al. (2013). Structural insights into the Ca2+ and PI(4,5)P2 binding modes of the C2 domains of rabphilin 3A and synaptotagmin 1. Proc. Natl. Acad. Sci. *110*, 20503–20508.

Han, W.-Q., Xia, M., Xu, M., Boini, K.M., Ritter, J.K., Li, N.-J., and Li, P.-L. (2012). Lysosome fusion to the cell membrane is mediated by the dysferlin C2A domain in coronary arterial endothelial cells. J. Cell Sci. *125*, 1225–1234.

Harsini, F.M., Bui, A.A., Rice, A.M., Chebrolu, S., Fuson, K.L., Turtoi, A., Bradberry, M., Chapman, E.R., and Sutton, R.B. (2019). Structural Basis for the Distinct Membrane Binding Activity of the Homologous C2A Domains of Myoferlin and Dysferlin. J. Mol. Biol. *431*, 2112–2126.

Heilbrunn, L.V. (1940). The Action of Calcium on Muscle Protoplasm. Physiol. Zool. *13*, 88–94.

Heilbrunn, L.V. (2013). The Dynamics of Living Protoplasm (Academic Press).

Helfmann, S., Neumann, P., Tittmann, K., Moser, T., Ficner, R., and Reisinger, E. (2011). The Crystal Structure of the C2A Domain of Otoferlin Reveals an Unconventional Top Loop Region. J. Mol. Biol. *406*, 479–490.

Hirano, Y., Gao, Y.-G., Stephenson, D.J., Vu, N.T., Malinina, L., Simanshu, D.K., Chalfant, C.E., Patel, D.J., and Brown, R.E. (2019). Structural basis of phosphatidylcholine recognition by the C2–domain of cytosolic phospholipase A2α. In ELife, p.

Huang, Y., Laval, S.H., van Remoortere, A., Baudier, J., Benaud, C., Anderson, L.V.B., Straub, V., Deelder, A., Frants, R.R., den Dunnen, J.T., et al. (2007). AHNAK, a novel component of the dysferlin protein complex, redistributes to the cytoplasm with dysferlin during skeletal muscle regeneration. FASEB J. *21*, 732–742.

Ikura, M. (1996). Calcium binding and conformational response in EF-hand proteins. Trends Biochem. Sci. *21*, 14–17.

Katz, A.K., Glusker, J.P., Beebe, S.A., and Bock, C.W. (1996). Calcium Ion Coordination: A Comparison with That of Beryllium, Magnesium, and Zinc. J. Am. Chem. Soc. *118*, 5752–5763.

Koerdt, S.N., and Gerke, V. (2017). Annexin A2 is involved in Ca2+-dependent plasma membrane repair in primary human endothelial cells. Biochim. Biophys. Acta BBA - Mol. Cell Res. *1864*, 1046–1053.

Krahn, M., Béroud, C., Labelle, V., Nguyen, K., Bernard, R., Bassez, G., Figarella-Branger, D., Fernandez, C., Bouvenot, J., Richard, I., et al. (2009). Analysis of the *DYSF* mutational spectrum in a large cohort of patients: *DYSF* Mutational Spectrum in a Large Cohort. Hum. Mutat. *30*, E345–E375.

Laval, S.H., and Bushby, K.M.D. (2004). Limb-girdle muscular dystrophies – from genetics to molecular pathology. Neuropathol. Appl. Neurobiol. *30*, 91–105.

Lennon, N.J., Kho, A., Bacskai, B.J., Perlmutter, S.L., Hyman, B.T., and Brown Jr., R.H. (2003). Dysferlin Interacts with Annexins A1 and A2 and Mediates Sarcolemmal Wound-healing. J. Biol. Chem. *278*, 50466–50473.

Leung, C., Utokaparch, S., Sharma, A., Yu, C., Abraham, T., Borchers, C., and Bernatchez, P. (2011). Proteomic identification of dysferlin-interacting protein complexes in human vascular endothelium. Biochem. Biophys. Res. Commun. *415*, 263–269.

Li, C., Ullrich, B., Zhang, J.Z., Anderson, R.G.W., Brose, N., and Südhof, T.C. (1995). Ca 2+ -dependent and -independent activities of neural and non-neural synaptotagmins. Nature *375*, 594–599.

Linse, S., and Forsén, S. (1995). Determinants that govern high-affinity calcium binding. Adv. Second Messenger Phosphoprotein Res. *30*, 89–151.

Liu, J., Aoki, M., Illa, I., Wu, C., Fardeau, M., Angelini, C., Serrano, C., Urtizberea, J.A., Hentati, F., Hamida, M.B., et al. (1998). Dysferlin, a novel skeletal muscle gene, is mutated in Miyoshi myopathy and limb girdle muscular dystrophy. Nat. Genet. *20*, 31–36.

Malmberg, N.J., Van Buskirk, D.R., and Falke, J.J. (2003). Membrane-Docking Loops of the cPLA2 C2 Domain: Detailed Structural Analysis of the Protein−Membrane Interface via Site-Directed Spin-Labeling. Biochemistry *42*, 13227–13240.

Matsuda, C., Hayashi, Y.K., Ogawa, M., Aoki, M., Murayama, K., Nishino, I., Nonaka, I., Arahata, K., and Jr, R.H.B. (2001). The sarcolemmal proteins dysferlin and caveolin-3 interact in skeletal muscle. Hum. Mol. Genet. *10*, 1761–1766.

Matsuda, C., Miyake, K., Kameyama, K., Keduka, E., Takeshima, H., Imamura, T., Araki, N., Nishino, I., and Hayashi, Y. (2012). The C2A domain in dysferlin is important for association with MG53 (TRIM72). PLoS Curr.

McDade, J.R., and Michele, D.E. (2014). Membrane damage-induced vesicle–vesicle fusion of dysferlin-containing vesicles in muscle cells requires microtubules and kinesin. Hum. Mol. Genet. *23*, 1677–1686.

McNeil, P.L., and Ito, S. (1990). Molecular traffic through plasma membrane disruptions of cells in vivo. J. Cell Sci. *96*, 549–556.

McNeil, P.L., and Khakee, R. (1992). Disruptions of muscle fiber plasma membranes. Role in exercise-induced damage. Am. J. Pathol. *140*, 1097–1109.

Medkova, M., and Cho, W. (1998). Differential Membrane-Binding and Activation Mechanisms of Protein Kinase C-α and -ε. Biochemistry *37*, 4892–4900.

Missiaen, L., Robberecht, W., Bosch, L.V.D., Callewaert, G., Parys, J.B., Wuytack, F., Raeymaekers, L., Nilius, B., Eggermont, J., and Smedt, H.D. (2000). Abnormal intracellular Ca2+homeostasis and disease. Cell Calcium *28*, 1–21.

Morrée, A. de, Hensbergen, P.J., Haagen, H.H.H.B.M. van, Dragan, I., Deelder, A.M., Hoen, P.A.C. 't, Frants, R.R., and Maarel, S.M. van der (2010). Proteomic Analysis of the Dysferlin Protein Complex Unveils Its Importance for Sarcolemmal Maintenance and Integrity. PLOS ONE *5*, e13854.

Murray, D., and Honig, B. (2002). Electrostatic Control of the Membrane Targeting of C2 Domains. Mol. Cell *9*, 145–154.

Nalefski, E.A., McDonagh, T., Somers, W., Seehra, J., Falke, J.J., and Clark, J.D. (1998). Independent Folding and Ligand Specificity of the C2 Calciumdependent Lipid Binding Domain of Cytosolic Phospholipase A2. J. Biol. Chem. *273*, 1365–1372.

Nalefski, E.A., Wisner, M.A., Chen, J.Z., Sprang, S.R., Fukuda, M., Mikoshiba, K., and Falke, J.J. (2001). C2 Domains from Different Ca2+ Signaling Pathways Display Functional and Mechanistic Diversity. Biochemistry *40*, 3089–3100.

Nguyen, K., Bassez, G., Bernard, R., Krahn, M., Labelle, V., Figarella-Branger, D., Pouget, J., Hammouda, E.H., Béroud, C., Urtizberea, A., et al. (2005). Dysferlin mutations in LGMD2B, Miyoshi myopathy, and atypical dysferlinopathies. Hum. Mutat. *26*, 165–165.

Ochoa, W.F., Corbalán-Garcia, S., Eritja, R., Rodríguez-Alfaro, J.A., Gómez-Fernández, J.C., Fita, I., and Verdaguer, N. (2002). Additional Binding Sites for Anionic Phospholipids and Calcium Ions in the Crystal Structures of Complexes of the C2 Domain of Protein Kinase Cα. J. Mol. Biol. *320*, 277–291.

Ono, Y., Fujii, T., Igarashi, K., Kuno, T., Tanaka, C., Kikkawa, U., and Nishizuka, Y. (1989). Phorbol ester binding to protein kinase C requires a cysteine-rich zinc-finger-like sequence. Proc. Natl. Acad. Sci. *86*, 4868–4871.

Pappa, H., Murray-Rust, J., Dekker, L.V., Parker, P.J., and McDonald, N.Q. (1998). Crystal structure of the C2 domain from protein kinase C-delta. Struct. Lond. Engl. 1993 *6*, 885–894.

Park, E.Y., Kwon, O.-B., Jeong, B.-C., Yi, J.-S., Lee, C.S., Ko, Y.-G., and Song, H.K. (2010). Crystal structure of PRY-SPRY domain of human TRIM72. Proteins Struct. Funct. Bioinforma. *3*, 790–795.

Perin, M.S., Fried, V.A., Mignery, G.A., Jahn, R., and Südhof, T.C. (1990). Phospholipid binding by a synaptic vesicle protein homologous to the regulatory region of protein kinase C. Nature *345*, 260–263.

Perisic, O., Fong, S., Lynch, D.E., Bycroft, M., and Williams, R.L. (1998a). Crystal structure of a calcium-phospholipid binding domain from cytosolic phospholipase A2. J. Biol. Chem. *273*, 1596–1604.

Perisic, O., Fong, S., Lynch, D.E., Bycroft, M., and Williams, R.L. (1998b). Crystal Structure of a Calcium-Phospholipid Binding Domain from Cytosolic Phospholipase A2. J. Biol. Chem. *273*, 1596–1604.

Permyakov, E. (2009). Metalloproteomics (John Wiley & Sons).

Permyakov, E., and Kretsinger, R.H. (2011). Calcium Binding Proteins (John Wiley & Sons).

Peulen, Rademaker, Anania, Turtoi, Bellahcène, and Castronovo (2019). Ferlin Overview: From Membrane to Cancer Biology. Cells *8*, 954.

Prelle, A., Sciacco, M., Tancredi, L., Fagiolari, G., Comi, G.P., Ciscato, P., Serafini, M., Fortunato, F., Zecca, C., Gallanti, A., et al. (2003). Clinical, morphological and immunological evaluation of six patients with dysferlin deficiency. Acta Neuropathol. (Berl.) *105*, 537–542.

Radhakrishnan, A., Stein, A., Jahn, R., and Fasshauer, D. (2009). The Ca2+ Affinity of Synaptotagmin 1 Is Markedly Increased by a Specific Interaction of Its C2B Domain with Phosphatidylinositol 4,5-Bisphosphate. J. Biol. Chem. *284*, 25749–25760.

Reddy, A., Caler, E.V., and Andrews, N.W. (2001). Plasma Membrane Repair Is Mediated by Ca2+-Regulated Exocytosis of Lysosomes. Cell *106*, 157–169.

Rezvanpour, A., Santamaria-Kisiel, L., and Shaw, G.S. (2011). The S100A10-Annexin A2 Complex Provides a Novel Asymmetric Platform for Membrane Repair. J. Biol. Chem. *286*, 40174–40183.

Ringer, S. (1883). A further Contribution regarding the influence of the different Constituents of the Blood on the Contraction of the Heart. J. Physiol. *4*, 29–42.

Rizo, J., and Südhof, T.C. (1998). C$_2$-domains, Structure and Function of a Universal Ca^{2+}-binding Domain. J. Biol. Chem. *273*, 15879–15882.

Rodríguez, A., Webster, P., Ortego, J., and Andrews, N.W. (1997). Lysosomes Behave as Ca2+-regulated Exocytic Vesicles in Fibroblasts and Epithelial Cells. J. Cell Biol. *137*, 93–104.

Schiavo, G., Gu, Q.-M., Prestwich, G.D., Söllner, T.H., and Rothman, J.E. (1996). Calcium-dependent switching of the specificity of phosphoinositide binding to synaptotagmin. Proc. Natl. Acad. Sci. *93*, 13327–13332.

Schiavo, G., Stenbeck, G., Rothman, J.E., and Söllner, T.H. (1997). Binding of the synaptic vesicle v-SNARE, synaptotagmin, to the plasma membrane t-SNARE, SNAP-25, can explain docked vesicles at neurotoxin-treated synapses. Proc. Natl. Acad. Sci. *94*, 997–1001.

Shao, X., Davletov, B.A., Sutton, R.B., Südhof, T.C., and Rizo, J. (1996). Bipartite Ca2+-binding motif in C2 domains of synaptotagmin and protein kinase C. Science *273*, 248–251.

Shao, X., Li, C., Fernandez, I., Zhang, X., Südhof, T.C., and Rizo, J. (1997). Synaptotagmin–Syntaxin Interaction: The C2 Domain as a Ca2+-Dependent Electrostatic Switch. Neuron *18*, 133–142.

Shao, X., Fernandez, I., Südhof, T.C., and Rizo, J. (1998). Solution Structures of the Ca^{2+}-free and Ca^{2+}-bound C$_2$A Domain of Synaptotagmin I: Does Ca^{2+} Induce a Conformational Change?[†]. Biochemistry *37*, 16106–16115.

Stahelin, R.V., Rafter, J.D., Das, S., and Cho, W. (2003). The Molecular Basis of Differential Subcellular Localization of C2 Domains of Protein Kinase C-α and Group IVa Cytosolic Phospholipase A2. J. Biol. Chem. *278*, 12452–12460.

Steinhardt, R.A., Bi, G., and Alderton, J.M. (1994). Cell Membrane Resealing by a Vesicular Mechanism Similar to Neurotransmitter Release. Science *263*, 390–393.

Stewart, T.A., Yapa, K.T.D.S., and Monteith, G.R. (2015). Altered calcium signaling in cancer cells. Biochim. Biophys. Acta BBA - Biomembr. *1848*, 2502–2511.

Striegel, A.R., Biela, L.M., Evans, C.S., Wang, Z., Delehoy, J.B., Sutton, R.B., Chapman, E.R., and Reist, N.E. (2012). Calcium Binding by Synaptotagmin's C2A Domain is an Essential Element of the Electrostatic Switch That Triggers Synchronous Synaptic Transmission. J. Neurosci. *32*, 1253–1260.

Strynadka, N.C.J., and James, M.N.G. (1989). Crystal structures of the helix-loop-helix calcium-binding proteins. Annu. Rev. Biochem. *58*, 951–998.

Sula, A., Cole, A.R., Yeats, C., Orengo, C., and Keep, N.H. (2014). Crystal structures of the human Dysferlin inner DysF domain. BMC Struct. Biol. *14*, 3.

Terasaki, M., Miyake, K., and McNeil, P.L. (1997). Large Plasma Membrane Disruptions Are Rapidly Resealed by Ca2+-dependent Vesicle–Vesicle Fusion Events. J. Cell Biol. *139*, 63–74.

Therrien, C., Di Fulvio, S., Pickles, S., and Sinnreich, M. (2009). Characterization of Lipid Binding Specificities of Dysferlin C2 Domains Reveals Novel Interactions with Phosphoinositides [†]. Biochemistry *48*, 2377–2384.

Torrecillas, A., Corbalán-García, S., and Gómez-Fernández, J.C. (2003). Structural Study of the C2 Domains of the Classical PKC Isoenzymes Using Infrared Spectroscopy and Two-Dimensional Infrared Correlation Spectroscopy. Biochemistry *42*, 11669–11681.

Torrecillas, A., Laynez, J., Menéndez, M., Corbalán-García, S., and Gómez-Fernández, J.C. (2004). Calorimetric Study of the Interaction of the C2 Domains of Classical Protein Kinase C Isoenzymes with Ca2+ and Phospholipids. Biochemistry *43*, 11727–11739.

Tsien, R.Y. (1981). A non-disruptive technique for loading calcium buffers and indicators into cells. Nature *290*, 527–528.

Tucker, W.C., Weber, T., and Chapman, E.R. (2004). Reconstitution of Ca2+-Regulated Membrane Fusion by Synaptotagmin and SNAREs. Science *304*, 435–438.

Ubach, J., Zhang, X., Shao, X., Südhof, T.C., and Rizo, J. (1998). Ca2+ binding to synaptotagmin: how many Ca2+ ions bind to the tip of a C2-domain? EMBO J. *17*, 3921–3930.

Verdaguer, N., Corbalan-Garcia, S., Ochoa, W.F., Fita, I., and Gómez-Fernández, J.C. (1999). Ca2+ bridges the C2 membrane-binding domain of protein kinase Cα directly to phosphatidylserine. EMBO J. *18*, 6329–6338.

Voleti, R., Tomchick, D.R., Südhof, T.C., and Rizo, J. (2017). Exceptionally tight membrane-binding may explain the key role of the synaptotagmin-7 C_2A domain in asynchronous neurotransmitter release. Proc. Natl. Acad. Sci. *114*, E8518–E8527.

Ward, S., Argon, Y., and Nelson, G.A. (1981). Sperm morphogenesis in wild-type and fertilization-defective mutants of Caenorhabditis elegans. J. Cell Biol. *91*, 26–44.

Wilson, E.B. (1925). The cell in development and heredity. (New York: Macmillan).

Woolger, N., Bournazos, A., Sophocleous, R.A., Evesson, F.J., Lek, A., Driemer, B., Sutton, R.B., and Cooper, S.T. (2017). Limited proteolysis as a tool to probe the tertiary conformation of dysferlin and structural consequences of patient missense variant L344P. J. Biol. Chem. *292*, 18577–18591.

Yagi, H., Conroy, P.J., Leung, E.W.W., Law, R.H.P., Trapani, J.A., Voskoboinik, I., Whisstock, J.C., and Norton, R.S. (2015). Structural Basis for Ca^{2+}-mediated Interaction of the Perforin C2 Domain with Lipid Membranes. J. Biol. Chem. *290*, 25213–25226.

Yasunaga, S., Grati, M., Cohen-Salmon, M., El-Amraoui, A., Mustapha, M., Salem, N., El-Zir, E., Loiselet, J., and Petit, C. (1999). A mutation in OTOF , encoding otoferlin, a FER-1-like protein, causes DFNB9, a nonsyndromic form of deafness. Nat. Genet. *21*, 363–369.

Zhang, D., and Aravind, L. (2010). Identification of novel families and classification of the C2 domain superfamily elucidate the origin and evolution of membrane targeting activities in eukaryotes. Gene *469*, 18–30.

Zheng, L., Krishnamoorthi, R., Zolkiewski, M., and Wang, X. (2000). Distinct Ca2+ Binding Properties of Novel C2 Domains of Plant Phospholipase Dα and β. J. Biol. Chem. *275*, 19700–19706.

Zhou, Y., Frey, T.K., and Yang, J.J. (2009). Viral calciomics: Interplays between Ca2+ and virus. Cell Calcium *46*, 1–17.

Chapter 2

Structure and Dynamics of Dysferlin C2A Domain in the

Apo-state

2.1 Introduction

Dysferlin is a 230 kD cytosolic-facing, membrane bound protein that is a member of the Ferlin family. All Ferlin proteins, including dysferlin, contain a variable number of C2 domains, accessory domains and a single C-terminal transmembrane spanning helix domain (Peulen et al., 2019). For example, dysferlin includes seven C2 domains (C2A-C2G), three Fer domains (FerA, FerB, and FerI) and two DysF domains (Sula et al., 2014). Of these, the N-terminal C2A domain appears to be the most important for membrane repair and is also the location of several substitutions that cause limb-girdle muscular dystrophy type 2B (LGMD2B) or Miyoshi myopathy (MM) (Krahn et al., 2009). The C2A domain demonstrates the strongest interaction with phosphoinositide and phosphotidylserine membrane surfaces and is the only C2 domain in dysferlin that does so in a calcium-dependent manner (Therrien et al., 2009) . Further, the C2A domain in dysferlin has been identified as the main domain responsible for interaction with other proteins (eg. MG53, AHNAK) in response to calcium ion influx to mediate membrane repair (Huang et al., 2007, 2007; Matsuda et al., 2012).

The three-dimensional structure of the calcium-free dysferlin C2A was determined by NMR spectroscopy by previous members of the Shaw lab (Dr. Liliana Santamaria-Kisiel, Dr. Pascal Mercier and Chantal Forristal). The structure displayed an anti-parallel β-sandwich arrangement connected by loops on the top typical of the C2 domain fold (**Figure 2.1 A**). However, the top loops of C2A show remarkably greater flexibility than any other C2 domain that have been structurally characterized (**Figure 2.1 B**). A previously reported crystal structure of the dysferlin C2A domain has shown the similar fold with less flexibility (Fuson et al., 2014) (**Figure 2.1 C**). In this crystal structure, only one of the six molecules in the asymmetric unit coordinated a single divalent cation that was modeled and refined it as a calcium ion. Thus, we consider this structure as apo state. By overlapping the six molecules in a asymmetric unit, variations in positions of loop 1 and 3 were observed (**Figure 2.1 D**). This raised our interest in investigating the difference between the NMR and crystal structures of the C2A domain by probing its dynamics in solution. Although structures of many C2 domains in the apo and calcium bound state have been determined, little is known about the dynamics of these proteins. It is also not clear how calcium-binding to the dysferlin C2A domain alters the structure of this protein and how this might affect its interaction with the inner membrane surface or accessory proteins. In this chapter, I pursued a detailed analysis of the backbone flexibility and dynamics of the dysferlin C2A domain in the calcium-free and calcium-saturated states and the effect of calcium coordination. A combination of methods was applied, including NMR-based heteronuclear NOE and T2 relaxation measurements, and thermal unfolding by circular dichroism. The work provides novel insights into the flexible properties of the dysferlin C2A domain that may be key to its functions in calcium binding and membrane repair.
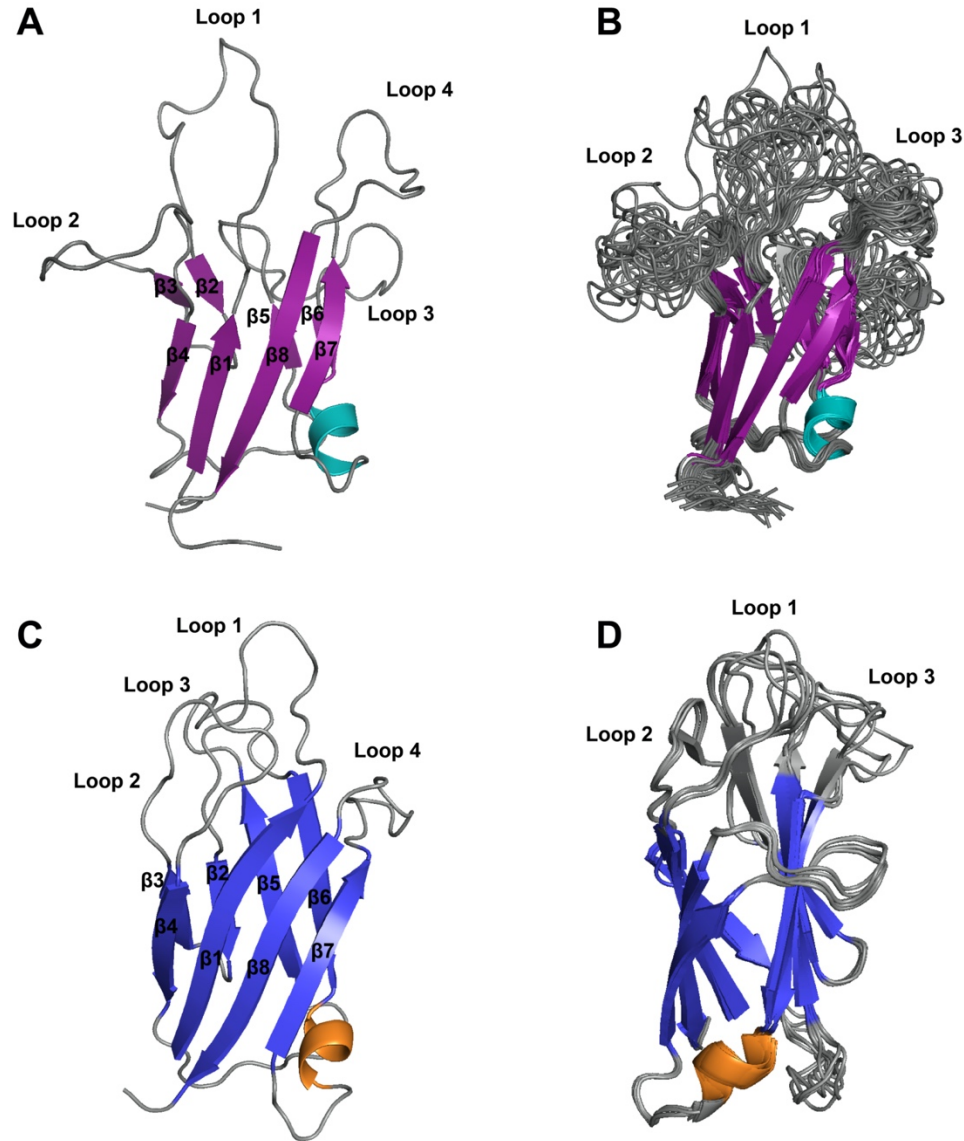
Figure 2. 1 NMR and crystal structures of the C2A domain in the apo state.

(A) Ribbon diagrams of the representative structures of apo-C2A domain of dysferlin show the eight-strand antiparallel β-sandwich assembly in magenta (β1-β8) and single α-helix in cyan. The top loops are shown in gray and labelled by numbers. **(B)** The superposition of the 20 lowest energy structures for the apo-C2A showing the flexibility of the loop region (grey). **(C)** The crystal structure of dysferlin C2A domain (Fuson et al., 2014) (PDB: 4IHB). The eight β sheets are shown in blue, α-helix in orange, and loops in grey. **(D)** The superposition of the structures of the six C2A molecules in a asymmetric unit showing the variation in positions of loop 1 and 3 (grey).

2.2 Materials and Methods

2.2.1 Expression and purification of dysferlin C2A domain

The dysferlin C2A construct was cloned by Chantal Forristal prior to this project. The construct contained dysferlin (DYSF) residues 1-130 and a seven-residue linker (GSGGGGG) at the N-terminus that remained after cleavage of the affinity tag. Unlabeled and uniformly ^{15}N, ^{13}C-labeled wild-type C2A domain of human dysferlin (residues 1-130) were overexpressed in the BL21-CodonPlus (DE3) *Escherichia coli* (*E. coli*) strain in LB or M9 minimal medium supplemented with 30 μg/mL kanamycin and 30 μg/mL chloramphenicol. ^{15}NH$_4$Cl (1 g/L) and ^{13}C$_6$-glucose (2 g/L) were used as the sole nitrogen and carbon sources in the M9 minimal media. The cultures were grown at 37 ºC until an optical density at 600 nm (OD$_{600}$) of 0.6 was reached at which point cells were cooled to 16 °C and induced with 0.5 mM IPTG for 16 hours. Cells were harvested by centrifugation at 6,000 rpm for 15 min and resuspended in lysis buffer (25mM Tris, 300 mM NaCl, 10 mM imidazole, pH 7.5). Cells were lysed by EmulsiFlex-C5 homogenizer (Avestin) and ultracentrifuged at 38,000 rpm for 90 min. The supernatant was filtered through 0.45 micron low protein binding syringe filters (Millipore) and subsequently applied to a 5 mL HisTrap FF column on an AKTA FPLC (GE Healthcare) pre-equilibrated in lysis buffer. The column was washed with lysis buffer plus 50 mM imidazole until the OD$_{280}$ returned to baseline. Bound protein was then eluted with a 250-500 mM imidazole in the elution buffer (25mM Tris, 300 mM NaCl, 250-500 mM imidazole, pH 7.5). Fractions containing the protein were pooled and TEV protease was added to cleave the His$_6$ tag (~1:50 ratio

protease:protein) and dialyzed against cleavage buffer (25 mM Tris, 300 mM NaCl, pH 7.5) overnight at 4 ºC with gentle agitation. Cleaved protein was purified on a 5 mL HisTrap FF column, again in lysis buffer, and flow through was collected containing the protein. A final purification step by size exclusion chromatography was performed on a HiLoad Superdex75 pre-equilibrated with appropriate buffers. Fractions containing the protein were pooled and stored at -80 ºC.

2.2.2 Analytical ultracentrifugation

Sedimentation velocity studies were carried out using a Beckman Optima XL-A Analytical Ultracentrifuge. Two protein samples at 20 µM each were analyzed: apo-C2A in 25 mM MES (pH 7.5), 300 mM NaCl, 3 mM EDTA, and Ca^{2+}-C2A in 25 mM MES (pH 7.5), 300 mM NaCl, 3 mM Ca^{2+}. Samples and matching buffer blanks were prepared in a double sector cell (1.2 cm) with quartz windows. An An60Ti rotor and double-sector cells with Epon charcoal centerpieces were used. Centrifugation was carried out at 4 °C. 60 absorbance measurements at 280 nm were collected at 5-min intervals, in 0.002 cm radial steps. A rotor speed of 50,000 rpm was used. Data were analyzed using non-linear regression in SEDFIT software and fit to a c(s) distribution (Schuck, 2000), to determine sedimentation coefficients corrected to 20 °C in H_2O ($S_{20,w}$).

2.2.3 NMR spectroscopy

All NMR experiments were collected at 25 ˚C on a Varian Inova 600 MHz NMR spectrometer equipped with a triple resonance cryogenic probe and z-field gradients (the Biomolecular NMR Facility, Department of Biochemistry in the Schulich School of

Medicine, The University of Western Ontario). All data were processed using NMRPipe (Delaglio et al., 1995) and analyzed using NMRViewJ (Johnson and Blevins, 1994).

2.2.4 Backbone Chemical Shift Assignment of apo-C2A

The apo-C2A sample was prepared at a concentration of 600 μM in 25 mM MES (pH 4.5), 150 mM NaCl, 1 mM DTT, 5 mM EDTA containing 10% D_2O, 200 μM DSS as an internal reference, and 200 μM imidazole as an internal pH indicator (Baryshnikova et al., 2008). Data for the backbone assignments were obtained from HNCACB (Wittekind and Mueller, 1993) , CBCA(CO)NH (Grzesiek and Bax, 1992) and ^1H-^{15}N HSQC experiments. The ^1H spectral window was 7000 Hz centered on 4.785 ppm. The ^{15}N spectral window was 1944 Hz centered on 116.191 ppm and The ^{13}C spectral window was 8443 Hz centered on 46.000 ppm.

2.2.5 Heteronuclear NOE measurements of apo- and Ca^{2+}-C2A

Heteronuclear NOE experiments (Farrow et al., 1994a) were performed for both apo- and Ca^{2+}-C2A. The ^{15}N-labelled apo-C2A sample was prepared at 700 μM in 25 mM MES (pH 4.5), 150 mM NaCl, 1 mM DTT, 5 mM EDTA and the ^{15}N-labelled Ca^{2+}-C2A was also 700 μM in 25 mM HEPES (pH 7.0), 150 mM NaCl, 250 μM TECP, 10 mM $CaCl_2$. To avoid protein precipitation over time, identical fresh sample was used for each experiment. Spectra were collected first with a recovery delay of 6-s (non-saturated spectrum) and second with a recovery delay of 3-s of proton saturation (saturated spectrum). The ^1H-^{15}N NOE value for each residue was calculated as the ratio of the cross-peak intensity (saturated/non-saturated), and error was estimated from the baseline noise in the two

spectra. Both saturated and non-saturated experiments were conducted in duplicate with fresh protein samples.

2.2.6 T2 relaxation experiment of apo-C2A

T2 relaxation (Bloembergen et al., 1948) data for ^{15}N-labelled apo-C2A (pH 4.5) was collected at a concentration of 170 μM using a 3-s delay. Two dimensional ^{1}H-^{15}N HSQC spectra were recorded with seven different relaxation times: relaxT = 0.01-s, 0.03-s, 0.05-s, 0.07-s, 0.09-s, 0.11-s and 0.15-s. T2 values were determined by fitting the measured peak heights to a two-parameter single-exponential decay function of the form:

$$I(t) = I_0 \exp\left(-\frac{t}{T_2}\right) \qquad (\textbf{Equation 1})$$

where I(t) is the intensity after a delay of time t and I_0 is the intensity at time t = 0.

2.2.7 Circular dichroism

Folding and stability of all proteins was monitored by circular dichroism spectropolarimetry using a Jasco J-810 instrument (Biomolecular Interactions and Conformations Facility, The University of Western Ontario). All proteins were extensively dialyzed in the CD buffer for at least one day with stirring. Samples comprised 20 μM protein in 10 mM MOPS (pH 7.5), 50 mM NaCl, 1 mM EDTA for apo-C2A and 20 mM CaCl$_2$ for Ca^{2+}-C2A. For each protein, 15 scans from 250-200 nm (80 nm/min with

increment of 1 nm) were recorded using a 1 mm path-length cell at 20 °C, averaged and the buffer background was subtracted.

Thermal denaturation studies were performed by exposing the protein to different temperatures within the range of 5-95 °C (1 °C/min with increments of 0.5 °C) by monitoring changes in the ellipticity at 215 nm. A 1 mM path length cuvette was used. The ellipticity was normalized between 0-1 using the function:

$$Y' = (Y-Y_{max})/(Y_{max}-Y_{min}) \qquad \textbf{(Equation 2)}$$

where Y is the observed CD signal at 215 nm, Y_{max} is the signal for the folded protein and Y_{min} is the signal for the unfolded protein.

2.3 Results

2.3.1 Optimized purification of the dysferlin C2A domain

In order to obtain His_6-tagged recombinant C2A protein, the supernatant containing the protein was loaded onto a Ni^{2+}-charged IMAC (HisTrap FF column) following bacterial overexpression and cell lysis. A concentration of 10 mM imidazole was added to both binding and wash buffers to interfere with the weak binding of other proteins. The C2A protein was then eluted with a higher concentration of imidazole. A Coomassie-stained SDS-PAGE gel of the fractions is presented in **Figure 2.2 A** showing that the His_6-tagged
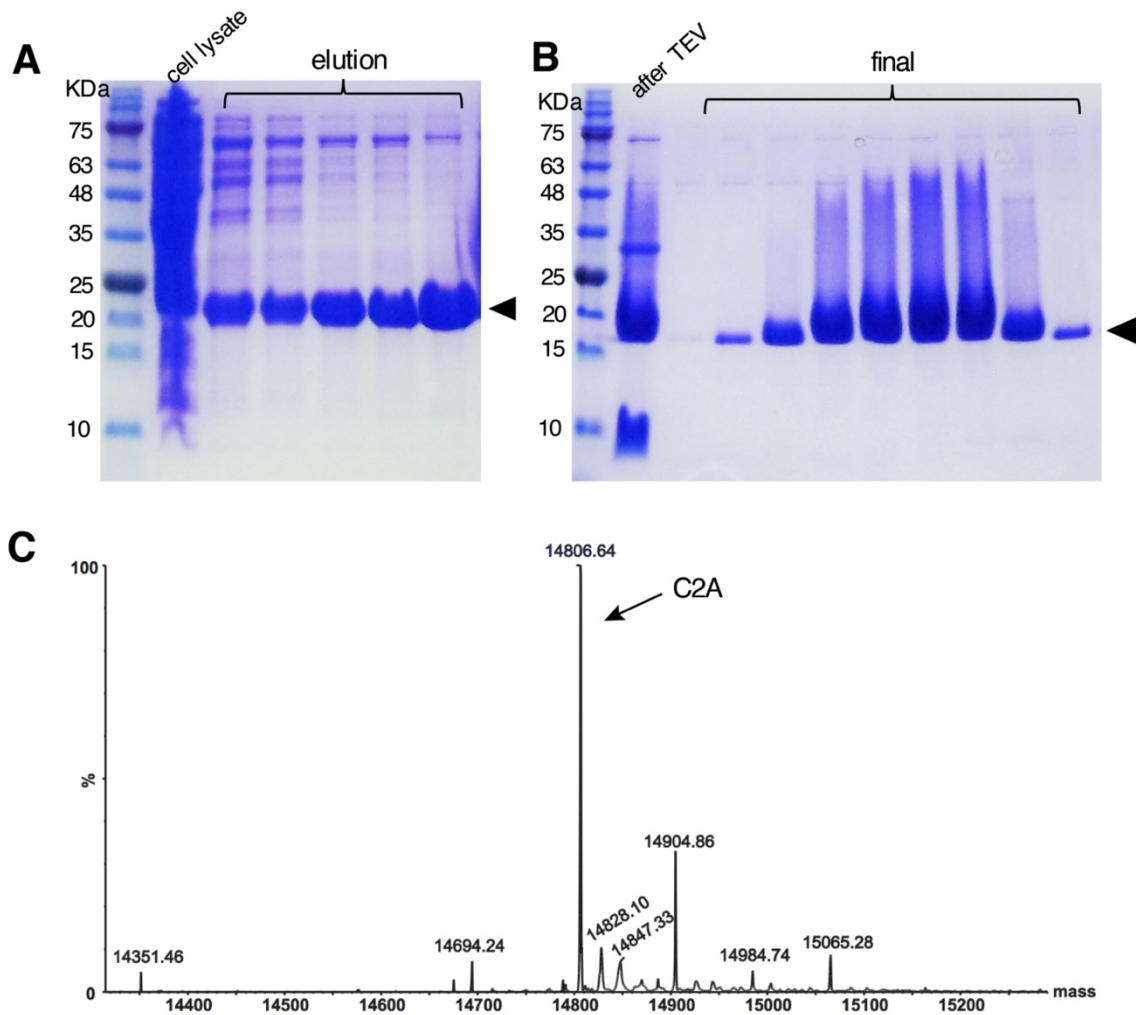
Figure 2. 2 Purification of the dysferlin C2A domain.

(A) Purification of His$_6$-tagged C2A by HisTrap FF chromatography monitored by SDS-PAGE stained with Coomassie blue. Cell lysate was obtained following cell lysis and ultracentrifugation and loaded onto HisTrap FF column. His$_6$-tagged C2A was then eluted by increasing the level of imidazole in the elution buffer (black arrow). **(B)** Purification of cleaved C2A by HisTrap FF chromatography. The eluted His$_6$-tagged C2A was cleaved by TEV protease and loaded onto HisTrap FF column again. Cleaved C2A was eluted in the flow-through fractions (black arrow). **(C)** Mass spectrum confirming the molecular weight of C2A. MW$_{calculated}$: 14805 Da.

C2A protein was successfully purified from the cell lysate. After the first purification step and His$_6$ tag cleavage by TEV protease, a previous method of C2A purification in the lab utilized ion exchange chromatography. This required lower pH conditions (~5.5) and led to significant precipitation of the protein. To solve this issue, nickel affinity purification using a HisTrap FF column was applied again in the second step after cleavage of the His$_6$ tag so that the pH was kept at 7.5 to avoid precipitation. This was followed by gel filtration chromatography. No significant precipitation was observed during this step and the protein yield was greatly increased. The protein was produced at levels of 25-50 mg per liter medium. **Figure 2.2 B** shows successful TEV cleavage and elution of C2A protein from the second HisTrap FF. A sample from one of the fractions was sent for electrospray ionization mass spectrometry (ESI-MS). The mass spectrum clearly shows one main species corresponding to the mass of C2A of 14.8 kDa (**Figure 2.2 C**).

To identify the dimerization/oligomerization state of C2A, analytical ultracentrifugation was used to study its overall shape in solution. Both apo- and Ca^{2+}-C2A samples were analyzed and results showed that, in the absence (+EDTA) and presence of calcium, C2A sediments as a monodisperse sample, fitting well to a single species/peak, corresponding to molecular weights of ~14 kDa and sedimentation coefficients of 1.5 S$_{20,w}$ (**Figure 2.3**). This confirms that C2A is monomeric in both apo- and Ca^{2+}-state with homogeneous conformation in solution.
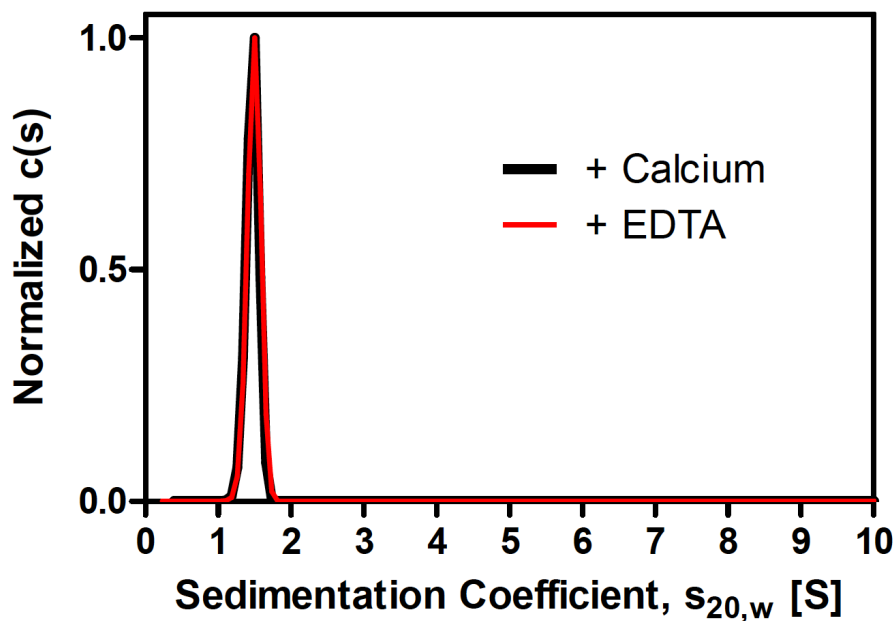
Figure 2. 3 Sedimentation velocity studies of the C2A domain.

Sedimentation velocity experiments of apo-C2A (red) and Ca^{2+}-C2A (black). All data were analyzed using the Lamm equation and fit to a c(s) distribution. Sedimentation coefficients, corrected to 20 °C and in H_2O ($S_{20,w}$), were determined to be 1.472 S for apo-C2A, and 1.493 S for Ca^{2+}-C2A. Fitted molecular weights were calculated to be 14.0 kDa for apo-C2A, and 14.5 kDa for Ca^{2+}-C2A.

2.3.2 Assignment of the NMR spectrum of apo-C2A

Previous work on dysferlin C2A in the lab has solved the solution NMR structure of its calcium free state at pH 7.5. Figure 2.1 B shows the superposition of 20 structures with the lowest combined NOE and dihedral energies as representative of the calculation. The backbone assignment of apo-C2A was also performed by NMR under pH 7.5. However, due to the amide exchange with the bulk H_2O solvent, a large number of amide resonances from the loop regions of the protein were missing. For example, under pH 7.5, many amide resonances from loops L1 (E10, N11, V12, H13, T14, D18, S20, D21, A22, Y23, C24), L2 (T35, K36, V37, S41, V42), L3 (D71, H72, E73, T74, M75, R77, R79) were absent in the ^1H-^{15}N HSQC spectra, which became an obstacle for further investigation of the protein properties.

It was reported previously that the amide hydrogen exchange in proteins is pH-dependent: at pH 4.5, amide hydrogen exchange rate is slowed by ~1000 fold compared to pH 7.5 (Matthew and Richards, 1983). Thus, the ^1H-^{15}N HSQC spectrum of apo-C2A at pH 4.5 was obtained and compared with that at pH 7.5. Many more peaks were observed at lower pH while all the peaks remained well-dispersed, indicating the protein is still properly folded and the amide exchange was significantly slowed (**Figure 2.4**). The backbone assignment (^1H, ^{15}N, and ^{13}C) of the apo-C2A was further completed at pH 4.5 using standard heteronuclear multiple dimensional NMR spectroscopy including ^1H-^{15}N HSQC, HNCACB (Wittekind and Mueller, 1993) and CBCA(CO)NH (Grzesiek and Bax, 1992) (**Figure 2.5** and **Table 2.1**). **Figure 2.6** shows the ^1H-^{15}N HSQC spectrum of apo-C2A (pH 4.5) labeled with newly assigned residues.
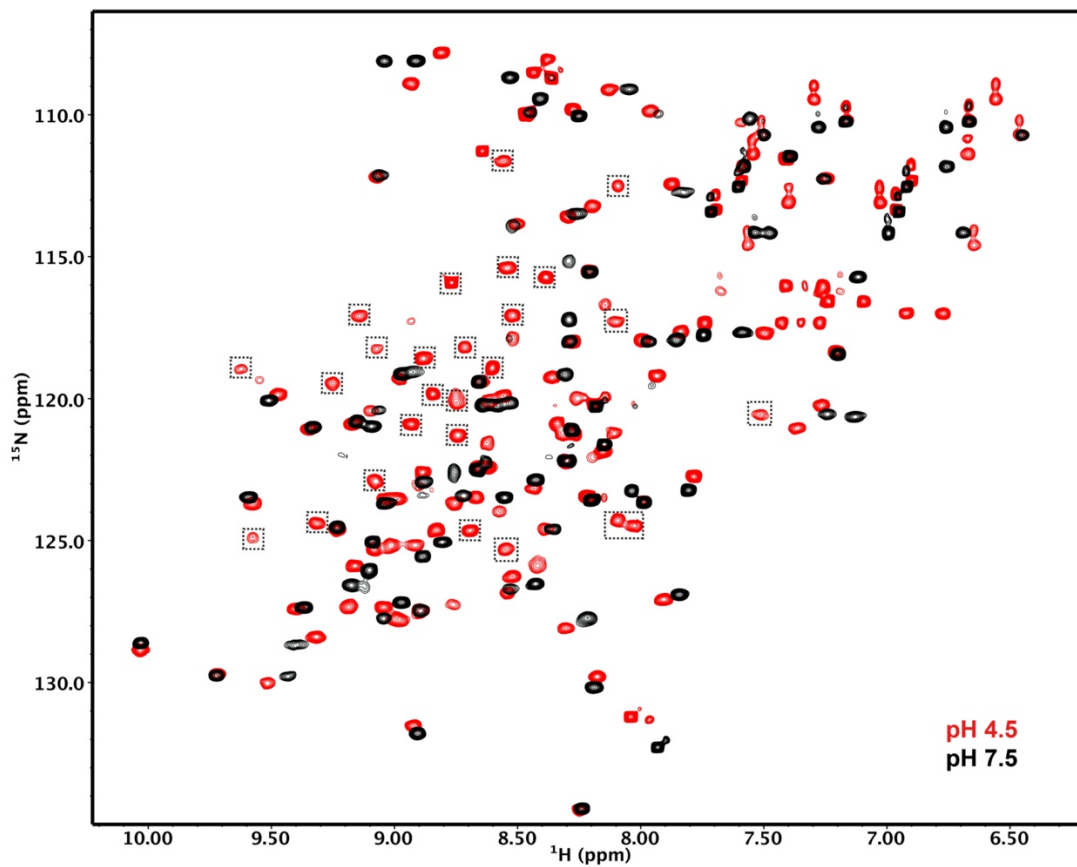
Figure 2. 4 Overlaid ^{1}H-^{15}N HSQC spectra of apo-C2A at pH 4.5 and 7.5.

600 MHz ^{1}H-^{15}N HSQC spectra for the dysferlin C2A in the apo-state at pH 4.5 (red) and 7.5 (black) are shown. Peaks that only appeared at pH 4.5 are indicated in dashed boxes.
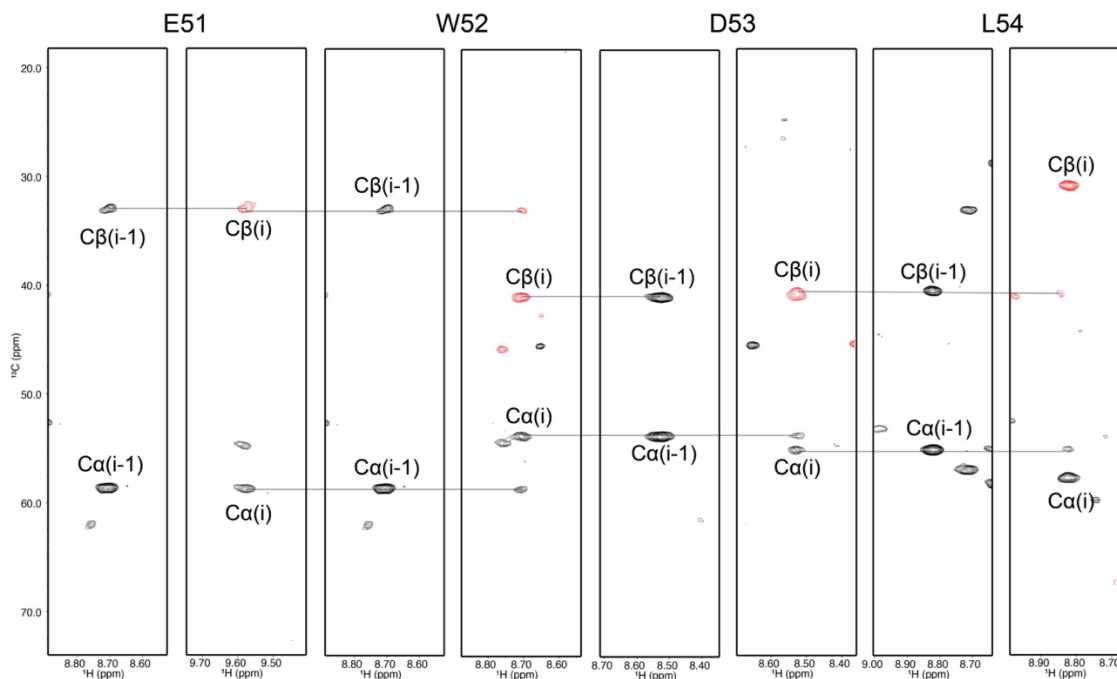
Figure 2. 5 Selected region of sequential backbone assignment of apo-C2A.

The spectra illustrate ^{15}N planes for sequential assignment of residues E51-L54 of the apo-C2A at pH 4.5. For each pair of planes, the CBCA(CO)NH is shown on the left and the HNCACB on the right where the x-axis is the amide proton chemical shift and the y-axis is the ^{13}C plane of the three-dimensional experiments. The $C\alpha$ and $C\beta$ for the intraresidues (indicated as i) are shown on the HNCACB spectra and the corresponding $C\alpha$ and $C\beta$ for the previous residues (i-1) are shown in the CBCA(CO)NH.

Figure 2. 6 Backbone amide assignments of apo-C2A (pH 4.5).

^{1}H-^{15}N HSQC spectrum of 600 μM uniformly ^{15}N, ^{13}C-labelled apo-C2A in 25 mM MES (pH 4.5), 150 mM NaCl, 1 mM DTT, 5 mM EDTA containing 10% D2O. The spectrum was acquired on a Varian INOVA 600 MHz spectrometer. Assigned backbone amide cross peaks are indicated with their one letter amino acid code and number. Pairs of resonances for sidechain amide cross peaks are connected by horizontal lines.

Under pH 4.5, some new signals appeared and were assigned including several in loops L1-L3: E10, N11, V12 and T14 in loop L1, T35, K36, V37, S41 and V42 in loop L2, and T74, M75, R77 in loop L3. This indicates that residues in these loops are exposed to solvent, do not participate in any hydrogen bonding interactions and are subject to amide exchange with the bulk H_2O solvent. It is also worth mentioning that several other residues including A9, H13, D21 and A22 in loop L1, G49 in loop L2, and R79, F80, L81 and G82 in loop L3 were still absent from the ^1H-^{15}N HSQC at pH 4.5, suggesting these regions of the apo-C2A structure may undergo conformational exchange.

2.3.3 pH-dependent dynamics of apo-C2A

The structure of the dysferlin C2A domain in the calcium-free (apo-C2A) state was determined using NMR by previous students. The apo-C2A structure shows anti-parallel β-sandwich arrangement that contains a single short α-helix typical of the C2 domain fold in a classic type II C2 topology. Notably, the loops that connect the β-sheets show very poor definition with large variations in the positions, suggesting that loops L1-L3 are flexible in solution in the absence of calcium (**Figure 2.1 B**). To verify this, various methods were used and the results are stated as follows.

As mentioned above, amide hydrogen exchange in proteins is pH-dependent and the ^1H-^{15}N HSQC spectra of apo-C2A at pH 4.5 and 7.5 showed large differences in the number and position of the peaks. Theoretically, amide protons that undergo faster exchange with the solvent give rise to weaker or unobservable signals from the NMR spectra. Thus, the peak intensities were measured for both pH's and the peak intensity ratios of each residue at pH 7.5 and 4.5 ($I_{7.5}/I_{4.5}$) were calculated. As shown in **Figure 2.7 A**, residues from
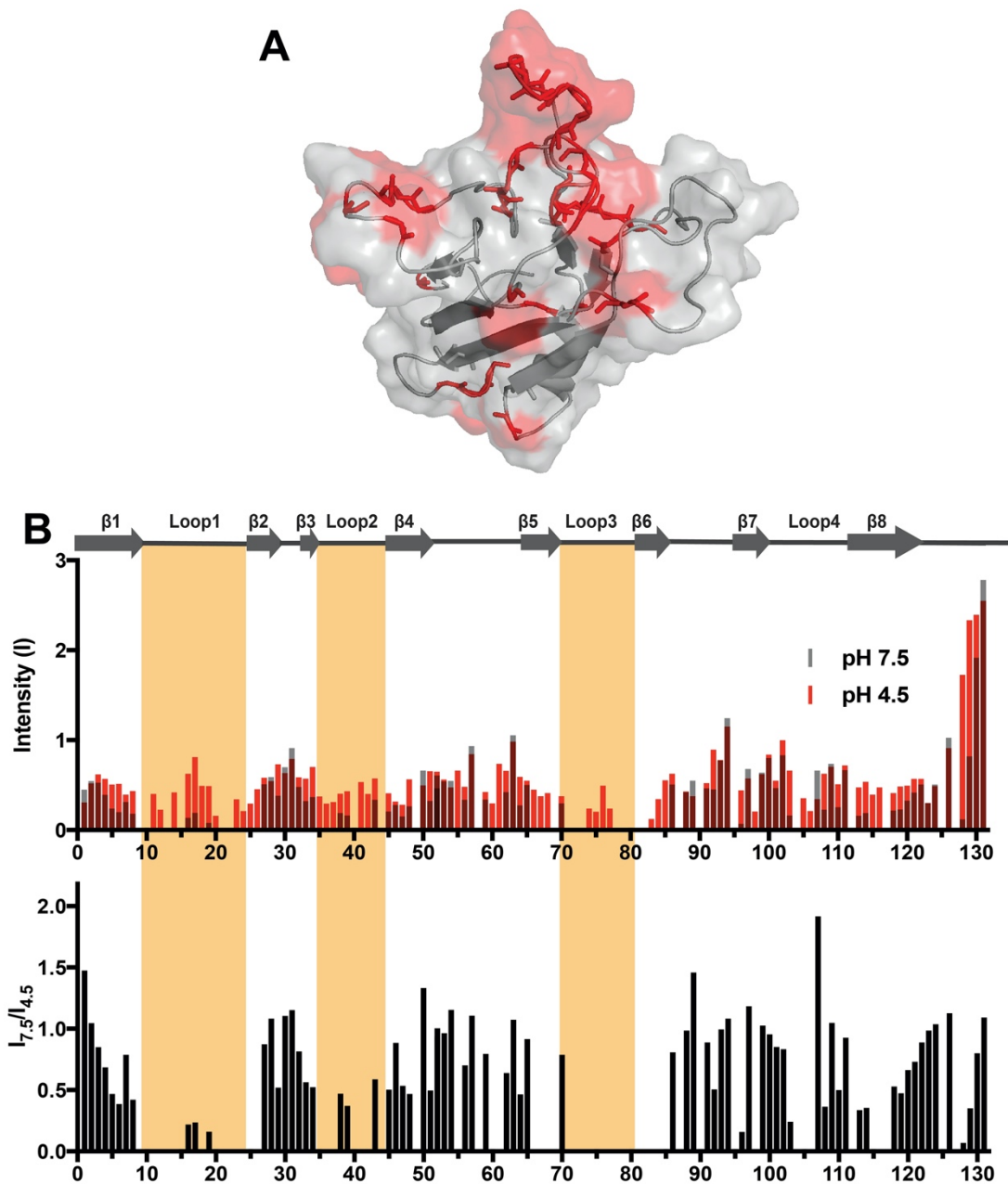
Figure 2. 7 pH-dependent dynamics of apo-C2A.

(A) The residues that were absent in the ^1H-^{15}N HSQC spectrum at pH 7.5 but present at pH 4.5 are shown on the cartoon structure of the apo-C2A structure (red). **(B)** Plot of ^1H-^{15}N HSQC peak intensities (top) and their ratio (bottom). ^1H-^{15}N HSQC peak intensities of each residue of apo-C2A at pH 4.5 (red bars) and pH 7.5 (black bars), and ratio of peak intensities at pH 7.5 and pH 4.5 ($I_{7.5}/I_{4.5}$). A linear schematic of apo-C2A secondary structure is indicated on the top of the figure.

different regions of the protein showed striking differences in peak intensity ratios. Some residues on loops L1 and L2 had the greatest changes including D16, T17, I19, I38, K39, as indicated by the smaller peak intensity ratios at pH 7.5 and pH 4.5 ($I_{7.5}/I_{4.5}$). Some other residues on loop L1-L3 were absent at pH 7.5 (N11, V12, T14, Y23, C24, T35, K36, V37, S41, V42, T74, M75, G76 and R77), shown by blank $I_{7.5}/I_{4.5}$. By contrast, peak intensity within the β-sheet regions showed no major changes with larger $I_{7.5}/I_{4.5}$ values (~1) (**Figure 2.7 B**). These observations indicate that residues on the loop L1-L3 undergo fast amide solvent exchange at physiological pH (7.5), which results in the dramatic flexibility of this region that can be reduced by lowering the pH.

2.3.4 Dynamic properties of C2A monitored by heteronuclear NOE and T2 relaxation

The amide assignments of the apo-C2A at pH 4.5 were used to measure ^{1}H-^{15}N heteronuclear NOE for each residue, which provide valuable information on flexibility and dynamics of the protein backbone (Farrow et al., 1994b). In these experiments, two ^{1}H-^{15}N-correlated spectra are collected where one experiment contains a 3 second proton saturation period prior to the pulse sequence and the other spectrum contains a delay of equivalent length. Amides that undergo fast timescale motions (ps - ns) show decreased signal intensity in the proton-saturated spectrum. In this experiment, the heteronuclear NOE values were measured across the backbone of apo-C2A (pH 4.5) and Ca^{2+}-C2A (pH 7.5). As shown in **Figure 2.8**, in these cases the average observed NOE values were near 0.8, close to that expected for a 15 kDa protein with little flexibility. Close examination reveals that different regions in apo-C2A exhibited different NOE values: loops L1-L3,
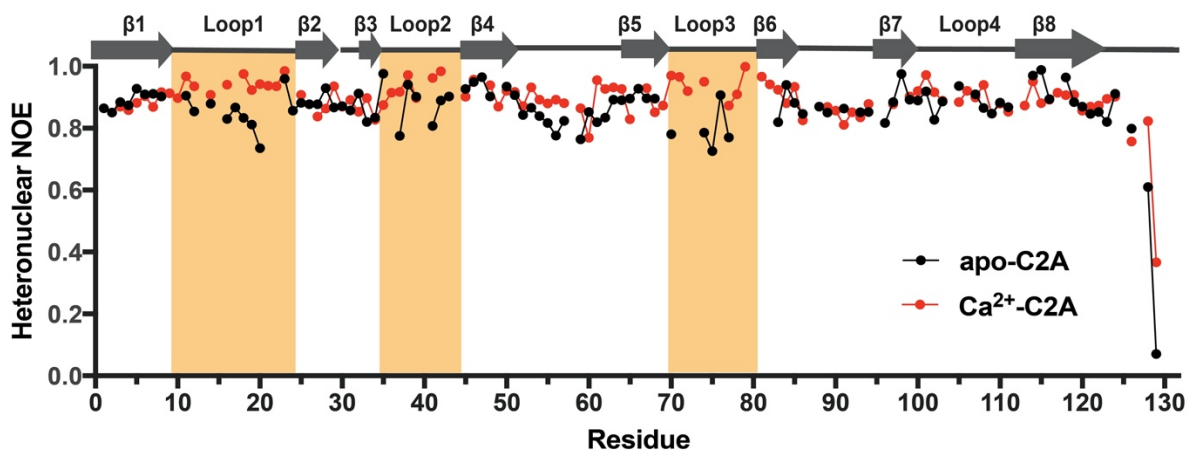
Figure 2. 8 Dynamic properties of C2A measured by heteronuclear NOE.

Heteronuclear NOE analysis of apo-C2A (black) and Ca^{2+}-C2A (red). The values plotted are an average of two independent experiments at 600 MHz. Only assigned resonances in the ^1H-^{15}N HSQC spectra were selected for analysis. The secondary structure domains are indicated on the top of the figure. Resonances that showed decreased NOE values in the apo-state (loops L1-L3) are highlighted in orange.

and the bottom loops that connect β4 - β5, β6 - β7 showed decreased NOE intensities than the rest parts of the protein, indicative of greater flexibility in these regions. Upon calcium addition, little difference for the β-sheet regions for β1-β5 and β7-β8 exists in apo- and Ca^{2+}-C2A domains suggesting the structures and motions of these regions of the protein are similar. In contrast, several residues in loops L1-L3 (D16, T17, D18, I19, S20, V37, S41, K70, T74, M75, R77) and β6 (E83) had smaller NOE values in apo-C2A compared to Ca^{2+}-C2A suggesting these regions in apo-C2A are more flexible than in the calcium-bound state. It is worth mentioning that to measure the NOEs for apo-C2A, pH 4.5 was chosen where the largest number of signals can be observed on the spectra, although some signals are still missing (shown by the gaps between data points in **Figure 2.8**). Based on the previous finding that the protein's motion is restricted at lower pH, it can be predicted that apo-C2A under higher pH would show more significant change in flexibility compared to the calcium-bound state.

In the T2 relaxation experiments, a series of ^1H-^{15}N HSQC spectra of apo-C2A were recorded using seven relaxation periods: 0.01-s, 0.03-s, 0.05-s, 0.07-s, 0.09-s, 0.11-s and 0.15-s. As expected, the overall resonance intensity showed a progressive decrease when T2 relaxation time was increased, resulting in broadened spectra (**Figure 2.9 A**) The corresponding peak intensities of each resonance were fit with a two-parameter exponential function to obtain the T2 values. Shown in **Figure 2.8 B**, data for most residues could be well fit with small SD error and showed an average T2 value of around 0.086-s. Notably, E10, S20, L92 and several C-terminal residues exhibited significantly larger T2 values than the average, indicative of faster molecular tumbling of these residues. In the 3D structure,
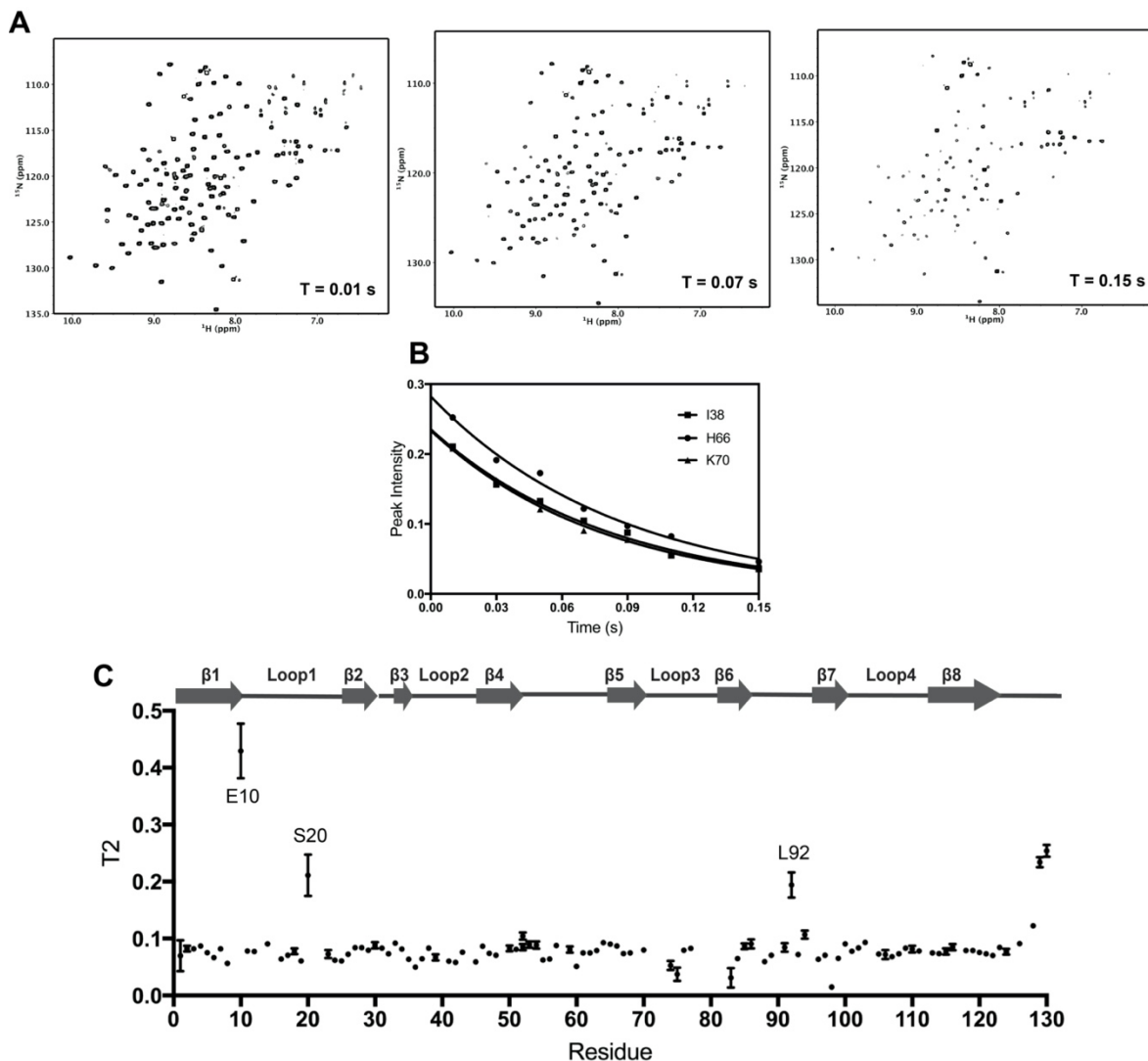
Figure 2. 9 T2 measurements of apo-C2A.

^{1}H-^{15}N NMR T2 relaxation data of 170 μM apo-C2A. **(A)** ^{1}H-^{15}N HSQC spectra recorded with relaxation delay of 0.01-s, 0.07-s and 0.15-s, showing the decrease in signal intensities. **(B)** Plot of peak intensities of I38, H66 and K70 as a function of relaxation delays. The curves represent the non-linear fits of the data using an exponential decay function. T2 data for all the resonances were fitted using the same method. **(C)** Fitted values of T2 as a function of residue number are shown. Residues that were calculated to have larger T2 values are indicated by one-letter residue code and number. The standard deviation error bars from the fit are also indicated.

Table 2. 1 Summary of chemical shifts, ^{15}N T2 relaxation times, heteronuclear NOE values of the backbone amides in apo-C2A.

Residue	^{1}H (ppm)	^{15}N (ppm)	NOE$_{600}$	T2 (s)
M1	8.61	120.1	0.865 ± 0.062	0.0698 ± 0.027
L2	9.03	127.3	0.851 ± 0.026	0.0822 ± 0.0052
R3	9.39	127.4	0.885 ± 0.025	0.0819 ± 0.0029
V4	8.98	123.6	0.874 ± 0.006	0.0869 ± 0.0038
F5	9.71	129.8	0.927 ± 0.054	0.0753 ± 0.004
I6	8.98	127.8	0.909 ± 0.032	0.0666 ± 0.0023
L7	8.29	128.1	0.911 ± 0.045	0.0817 ± 0.0045
Y8	7.24	112.2	0.902 ± 0.029	0.0565 ± 0.0025
E10	8.76	115.9		0.4295 ± 0.0482
N11	8.71	118.2	0.905 ± 0.003	0.078 ± 0.0038
V12	9.06	118.2	0.854 ± 0.049	0.0774 ± 0.0035
T14	8.52	117	0.879 ± 0.007	0.0906 ± 0.0043
D16	8.38	115.7	0.83 ± 0.042	0.0639 ± 0.0019
T17	7.86	112.4	0.867 ± 0.047	0.0706 ± 0.0007
D18	8.33	120.9	0.833 ± 0.044	0.0775 ± 0.005
I19	7.92	119.2	0.812 ± 0.024	0.0607 ± 0.0021
S20	8.13	120	0.736 ± 0.011	0.2112 ± 0.0363
Y23	9.13	117.1	0.959 ± 0.105	0.0729 ± 0.007
C24	8.13	116.7	0.857 ± 0.117	0.0618 ± 0.0047
S25	9.25	119.5	0.882 ± 0.059	0.0608 ± 0.0044
A26	9.18	127.3	0.878 ± 0.041	0.0724 ± 0.003
V27	8.92	120.9	0.878 ± 0.013	0.0838 ± 0.0035
F28	7.9	127.1	0.929 ± 0.052	0.0838 ± 0.0045
A29	8.16	129.8	0.867 ± 0.042	0.0793 ± 0.0039
G30	8.24	134.5	0.871 ± 0.021	0.0881 ± 0.0056
V31	8.21	123.5	0.858 ± 0.015	0.0829 ± 0.0034
K32	8.91	131.5	0.912 ± 0.006	0.0732 ± 0.0033
K33	9.15	125.9	0.82 ± 0.057	0.0919 ± 0.0034
R34	8.26	117.9	0.835 ± 0.04	0.0817 ± 0.0013
T35	8.55	111.6	0.976 ± 0.004	0.0637 ± 0.0047
K36	9.6	119		0.0497 ± 0.0046
V37	8.25	120.1	0.775 ± 0.015	0.0645 ± 0.0028
I38	9.51	130	0.941 ± 0.025	0.0831 ± 0.0044
K39	8.54	126.9	0.902 ± 0.03	0.0669 ± 0.0056
S41	8.29	113.5	0.807 ± 0.031	0.0601 ± 0.0028

V42	8.31	121.3	0.89 ± 0.064	0.0583 ± 0.0034
N43	7.84	117.7	0.903 ± 0.02	0.076 ± 0.0033
V45	7.25	120.2	0.927 ± 0.007	0.059 ± 0.0019
W46	8.38	124.6	0.949 ± 0.082	0.0864 ± 0.003
N47	9.09	120.4	0.965 ± 0.075	0.074 ± 0.0048
E48	7.98	117.9	0.902 ± 0.012	0.0708 ± 0.0016
F50	8.87	118.6	0.934 ± 0.008	0.0827 ± 0.0051
E51	8.35	119.3	0.907 ± 0.087	0.0809 ± 0.0025
W52	10.02	128.9	0.843 ± 0.001	0.1044 ± 0.0063
D53	8.65	123.5	0.866 ± 0.052	0.0893 ± 0.0054
L54	8.5	126.3	0.839 ± 0.039	0.0885 ± 0.0061
K55	8.84	119.7	0.817 ± 0.004	0.0622 ± 0.0029
G56	8.93	108.8	0.776 ± 0.019	0.0639 ± 0.0025
I57	7.77	122.8	0.824 ± 0.008	0.0878 ± 0.0035
L59	7.34	121	0.764 ± 0.033	0.0807 ± 0.0055
D60	8.6	121.6	0.853 ± 0.002	0.0513 ± 0.0025
Q61	8.59	118.9	0.82 ± 0.022	0.0748 ± 0.0026
G62	8.8	107.8	0.834 ± 0.047	0.075 ± 0.0032
S63	7.73	117.4	0.892 ± 0.023	0.0789 ± 0.0024
E64	8.88	122.6	0.891 ± 0.017	0.0926 ± 0.0025
L65	8.42	123.1	0.896 ± 0.017	0.0902 ± 0.0035
H66	8.53	125.3	0.928 ± 0.011	0.0867 ± 0.0047
D67	9.06	122.9	0.897 ± 0.01	0.0734 ± 0.0038
V68	9	125.2	0.896 ± 0.002	0.0746 ± 0.0021
K70	8.1	117.3	0.78 ± 0.06	0.0797 ± 0.0035
T74	8.07	112.5	0.786 ± 0.123	0.0527 ± 0.0081
M75	8.5	117.9	0.726 ± 0.084	0.0373 ± 0.0115
G76	8.37	108.1	0.907 ± 0.004	0.0794 ± 0.0037
R77	7.51	120.6	0.77 ± 0.087	0.0829 ± 0.003
E83	9.54	119.3	0.819 ± 0.074	0.031 ± 0.0172
A84	9.3	124.3	0.94 ± 0.018	0.0649 ± 0.0049
K85	8.73	121.3	0.882 ± 0.035	0.0864 ± 0.005
V86	8.82	124.7	0.846 ± 0.009	0.0906 ± 0.0081
L88	8.08	124.3	0.87 ± 0.01	0.0592 ± 0.0043
R89	8.73	120.2	0.85 ± 0.013	0.0706 ± 0.0036
V91	7.49	117.7	0.864 ± 0.021	0.0846 ± 0.0076
L92	7.25	116.1		0.1941 ± 0.0221
A93	7.2	118.3	0.852 ± 0.038	0.072 ± 0.0028
T94	7.4	111.5	0.852 ± 0.015	0.1068 ± 0.007
S96	7.95	109.9	0.817 ± 0.045	0.0635 ± 0.0015

L97	8.27	121.2	0.885 ± 0.001	0.0706 ± 0.0019
S98	7.58	110.3	0.975 ± 0.013	0.0148
A99	9.07	125.3	0.892 ± 0.006	0.0653 ± 0.004
S100	8.2	115.5	0.89 ± 0.012	0.0905 ± 0.0044
F101	9.16	120.9	0.919 ± 0.021	0.0775 ± 0.0038
N102	8.63	122.4	0.827 ± 0.031	0.0834 ± 0.0042
A103	9.31	128.4	0.886 ± 0.045	0.0931 ± 0.0029
L105	8.09	121.2	0.937 ± 0.003	0.0727 ± 0.0043
L106	9.58	124.9	1.012 ± 0.035	0.0718 ± 0.0081
D107	8.97	119.3	0.91 ± 0.032	0.0681 ± 0.0035
T108	8.12	109.1	0.866 ± 0.03	0.0731 ± 0.0023
K109	8.29	122.2	0.847 ± 0.076	0.083 ± 0.0037
K110	8.19	113.2	0.882 ± 0.03	0.0815 ± 0.0061
Q111	8.64	119.4	0.868 ± 0.019	0.0782 ± 0.0036
T113	8.5	113.9	1.021 ± 0.091	0.0747 ± 0.0038
G114	9.06	112.2	0.97 ± 0.009	0.0737 ± 0.0045
A115	8.02	124.5	0.989 ± 0.045	0.0772 ± 0.0054
S116	8.52	115.4	0.894 ± 0.012	0.085 ± 0.0056
V118	8.88	127.5	0.964 ± 0.034	0.0791 ± 0.0025
L119	8.74	123.7	0.884 ± 0.078	0.079 ± 0.0025
Q120	9.35	121.1	0.87 ± 0.087	0.0754 ± 0.0041
V121	9.22	124.6	0.846 ± 0.027	0.0732 ± 0.0045
S122	9.47	119.9	0.852 ± 0.059	0.0702 ± 0.0031
Y123	8.91	125.2	0.821 ± 0.015	0.0844 ± 0.0035
T124	8.7	124.7	0.911 ± 0.066	0.0768 ± 0.0052
L126	8.15	121.9	0.798 ± 0.02	0.0912 ± 0.0044
G128	8.45	110	0.61 ± 0.006	0.1222 ± 0.0047
A129	7.98	123.6	0.071 ± 0.004	0.2341 ± 0.0089
V130	8.18	120.2		0.2539 ± 0.0107
L131	8.03	131.3		0.2826 ± 0.0122

E10 and S20 are located in loop 1, and L92 in the bottom loop between β6 and β7 suggesting increased flexibilities and faster dynamics occur within these regions. Moreover, the C-terminus of the protein, which is a short random coil, also showed greater flexibility.

The heteronuclear NOE and T2 relaxation data of the apo-C2A showed some agreement: the loop 1 region and bottom loop that connects β6 and β7 of the protein exhibit greater flexibilities in both experiments. However, the NOE data also showed the similar increased dynamics in loop 2 and 3 and the bottom loop between β4 and β5, whereas in T2 relaxation experiment these regions showed little deviation from the average.

2.3.5 Thermal stability study of C2A by circular dichroism

Next, the secondary structure and thermal stability of apo- and Ca^{2+}-C2A were studied by circular dichroism (CD). Far-UV CD spectra from 200-250 nm for C2A in the two states showed they both had a similar spectral signature with a minimum observed around 215 nm, characteristic of a typical β-sheet structure (**Figure 2.10 A**). The spectra between 200-205 nm became noisy and turbulent due to the high tension voltage beyond 600 V. The thermal unfolding experiment was performed over a temperature range of 20-95 °C at a wavelength of 215 nm. It can be clearly observed that Ca^{2+}-C2A had a higher melting temperature than apo-C2A with an almost 10 °C difference, suggesting the addition of calcium stabilizes the protein structure (**Figure 2.10 B**).
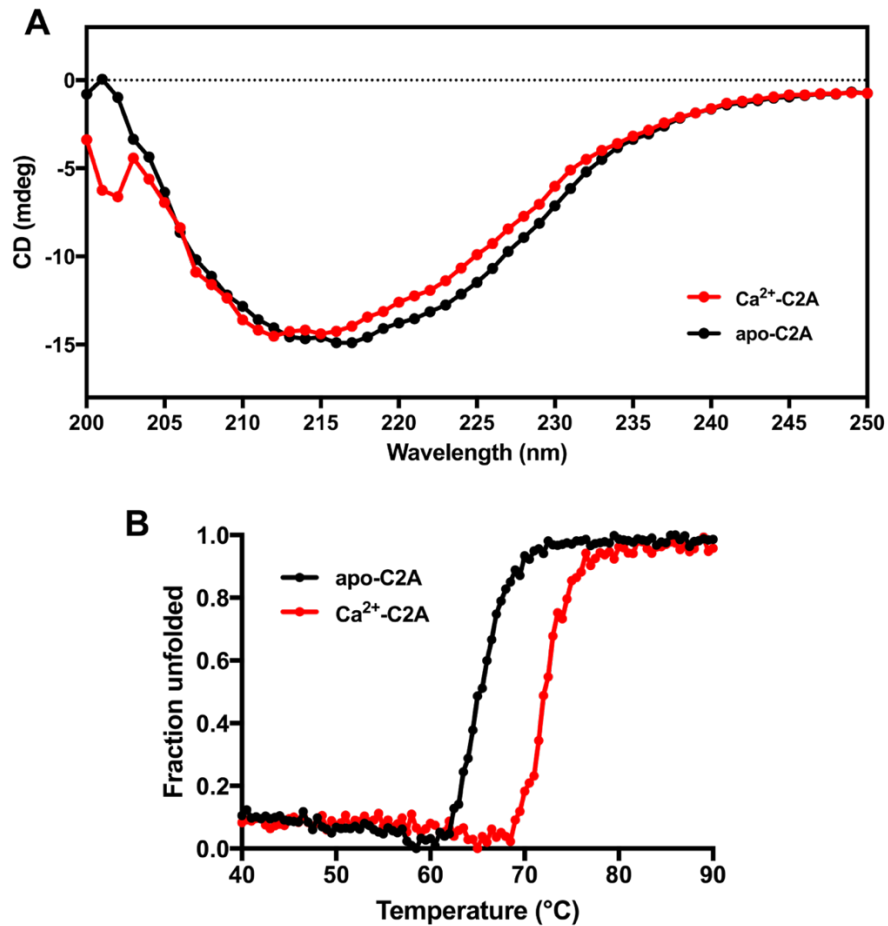
Figure 2. 10 Change in stability of C2A monitored by circular dichroism.

(A) Circular dichroism spectra of apo-C2A (black) and Ca-C2A (red) from 250 – 200 nm. The measurements were taken at 25 °C. The buffer background was subtracted. **(B)** Thermal denaturation apo-C2A (black) and Ca-C2A (red) monitored by circular dichroism within the range of 40 – 90°C in 0.5 °C increments. The unfolding profile as a function of temperature is shown by CD ellipticity at 215 nm.

2.4 Discussion

2.4.1 Flexibility as a novel feature of the dysferlin C2A domain

The structure of dysferlin C2A domain was previously reported with a single Ca^{2+} coordinated to one of the six molecules in the asymmetric unit determined by X-ray crystallography (Fuson et al., 2014) (**Figure 2.11 B**). It is ambiguous from the structure whether the protein is apo or Ca^{2+}-bound. Our work in this chapter focused on the C2A domain in the calcium free state by adding abundant EDTA into the sample solution to completely remove the calcium. Unexpectedly, many resonances corresponding to the residues within the loop region were missing in the ^1H-^{15}N HSQC spectra due to fast exchange of hydrogens between backbone amides and the solvent. Upon solving this solution structure, apo-C2A exhibited shorter β-sheets and more flexible loops compared to the crystal structure (**Figure 2.11 A**). Similar findings were also reported in studies by NMR spectroscopy on the C2 domain of MFG-E (Ye et al., 2013) and synaptotagmin I (Shao et al., 1998). In these cases, several amide resonances of residues in the loop region were missing in the ^1H-^{15}N HSQC spectrum, and a considerable number of long-range NOEs between protons in loop region that were observed for the Ca^{2+}-bound form had substantially smaller intensities or were absent in the data obtained for the Ca^{2+}-free C2A domain. All these data combined with ours suggest a state of Ca^{2+}-free C2 domain with greater flexibility and dynamics in the loops that NMR is competent to probe over X-ray crystallography. This advantage of NMR has also been indicated in studies on other proteins. For instance, the difference between the crystal and solution NMR structures of Ca^{2+}-calmodulin indicates considerable backbone plasticity within the domains of

69

calmodulin, which is critical to their ability to bind a wide range of targets (Chou et al., 2001).

Our work also applied a combination of useful tools to comprehensively examine the protein dynamic behavior including pH titration, heteronuclear NOE, T2 relaxation and thermal denaturation experiments. These experiments confirmed the increased dynamics of Ca^{2+}-free C2A loop region that can be stabilized and rigidified upon calcium binding. Several studies have suggested the similar idea for other C2 domains by using alternative methods including hydrogen/deuterium exchange by mass spectrometry (Hsu et al., 2008), molecular dynamics simulations (Banci et al., 2002) and Carr-Purcell-Meiboom-Gill (CPMG) NMR experiment (Morales et al., 2016). For example, the C2 domain protein kinase Cα showed a similar magnitude of difference with our data in heteronuclear NOE values in response to calcium binding within the loop region (Morales et al., 2016).

However, compared to all the Ca^{2+}-free C2 domains solved by NMR and X-ray crystallography, none of them shows the same level of flexibility as dysferlin C2A domain does. For example, one of the few NMR structures of Ca^{2+}-free C2 domains, piccolo C2A domain, was shown to have a much more rigid structure with longer β-sheets and more refined loops compared to dysferlin C2A (Garcia et al., 2004) (**Figure 2.11 C**). The difference can also be observed from the structure of synaptotagmin I C2A domain in Ca^{2+}-free state (Shao et al., 1998) (**Figure 2.11 D**). Furthermore, the high number of missing amide resonances in the NMR spectra also seems to be an exclusive feature of dysferlin C2A, which does not appear in the cases of other C2 domains such as synaptotagmin I C2A
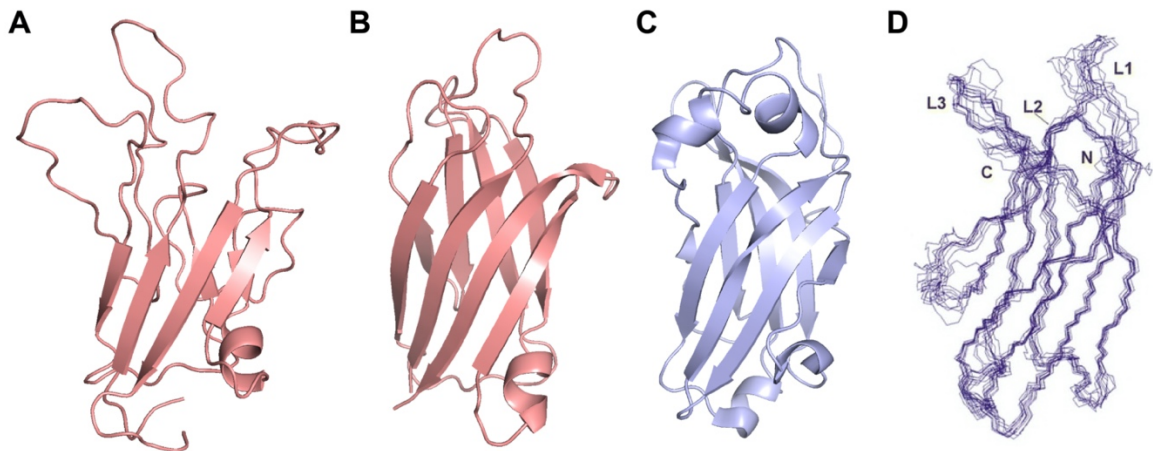
Figure 2. 11 Comparison of C2 domain structures in the calcium free state.

(A) The solution NMR structure of dysferlin C2A domain (solved by Dr. Liliana Santamaria-Kisiel, Dr. Pascal Mercier and Chantal Forristal). **(B)** The crystal structure of dysferlin C2A domain (Fuson et al., 2014) (PDB: 4IHB). **(C)** The solution NMR structure of calcium free piccolo C2A domain (Garcia et al., 2004) (PDB: 1RH8). **(D)** The solution NMR structure of calcium free synaptotagmin I C2A domain. (PDB data missing, figure was taken from the original publication) (Shao et al., 1998).

domain (Ubach et al., 2001) and perforin C2 domain (Yagi et al., 2015). Taken together, our work reveals the flexibility of dysferlin C2A domain in the apo-state as a distinctive characteristic over other C2 domains.

2.4.2 Significance of the flexibility of C2A in calcium and membrane binding

One major function of C2 domains is targeting membrane surfaces as a consequence of calcium binding and specific C2 domains have different phospholipid selectivity. For example, the C2 domains of protein kinase C-α and -ε and synaptotagmins bind to the anionic head group of phosphatidylserine (Corbalán-García et al., 1999; Davletov and Sudhof, 1993; Fukuda et al., 1996; Medkova and Cho, 1998) while the C2 domain of cPLA2 binds to neutral phosphatidylcholine (Nalefski et al., 1998, 2001). It is widely believed that the lipid binding sites of C2 domains are located in the top loops. The dysferlin C2A domain has been identified to bind specifically to phosphoinositide and phosphotidylserine in a calcium-dependent fashione (Therrien et al., 2009). With a low intracellular concentration of $[Ca^{2+}]$ (100 nM) in the resting state of a cell, the dysferlin C2A domain can be considered largely in the apo-state. The high flexible property of C2A may help it avoid the binding to the lipid membrane. Since our work suggests the role of calcium to stabilize the structure of dysferlin C2A, we hypothesize that upon the influx of calcium from the extracellular space due to membrane disruption, the C2A domain adapts a more ordered and rigid conformation, triggering membrane repair through lipid binding. This can also explain why dysferlin-mediated membrane repair is calcium-dependent (Bansal et al., 2003; Han and Campbell, 2007). However, studies of dysferlin's interactions with other proteins indicate a more complicated picture. C2A was shown to associate with MG53 dimers in a Ca^{2+}-dependent manner (Matsuda et al., 2012) but also have calcium-

independent interaction with AHNAK (Huang et al., 2007). It is not clear whether these interactions are linked with the flexibility and dynamics of the protein, which would be an interesting area to explore in the future.

2.5 References

Banci, L., Cavallaro, G., Kheifets, V., and Mochly-Rosen, D. (2002). Molecular Dynamics Characterization of the C2 Domain of Protein Kinase Cβ. J. Biol. Chem. *277*, 12988–12997.

Bansal, D., Miyake, K., Vogel, S.S., Groh, S., Chen, C.-C., Williamson, R., McNeil, P.L., and Campbell, K.P. (2003). Defective membrane repair in dysferlin-deficient muscular dystrophy. Nature *423*, 168–172.

Baryshnikova, O.K., Williams, T.C., and Sykes, B.D. (2008). Internal pH indicators for biomolecular NMR. J. Biomol. NMR *41*, 5–7.

Bloembergen, N., Purcell, E.M., and Pound, R.V. (1948). Relaxation Effects in Nuclear Magnetic Resonance Absorption. Phys. Rev. *73*, 679–712.

Chou, J.J., Li, S., and Klee, C.B. (2001). Solution structure of Ca^{2+}–calmodulin reveals flexible hand-like properties of its domains. Nat. Struct. Biol. *8*, 8.

Corbalán-García, S., Rodríguez-Alfaro, J.A., and Gómez-Fernández, J.C. (1999). Determination of the calcium-binding sites of the C2 domain of protein kinase Cα that are critical for its translocation to the plasma membrane. Biochem. J. *337*, 513–521.

Davletov, B.A., and Sudhof, T.C. (1993). A single C2 domain from synaptotagmin I is sufficient for high affinity Ca^{2+}/phospholipid binding. J. Biol. Chem. *268*, 26386–26390.

Delaglio, F., Grzesiek, S., Vuister, G.W., Zhu, G., Pfeifer, J., and Bax, A. (1995). NMRPipe: A multidimensional spectral processing system based on UNIX pipes. J. Biomol. NMR *6*, 277–293.

Farrow, N.A., Muhandiram, R., Singer, A.U., Pascal, S.M., Kay, C.M., Gish, G., Shoelson, S.E., Pawson, T., Forman-Kay, J.D., and Kay, L.E. (1994a). Backbone Dynamics of a Free and a Phosphopeptide-Complexed Src Homology 2 Domain Studied by 15N NMR Relaxation. Biochemistry *33*, 5984–6003.

Farrow, N.A., Zhang, O., Forman-Kay, J.D., and Kay, L.E. (1994b). A heteronuclear correlation experiment for simultaneous determination of 15N longitudinal decay and chemical exchange rates of systems in slow equilibrium. J. Biomol. NMR *4*, 727–734.

Fukuda, M., Kojima, T., and Mikoshiba, K. (1996). Phospholipid composition dependence of Ca^{2+}-dependent phospholipid binding to the C2A domain of synaptotagmin IV. J. Biol. Chem. *271*, 8430–8434.

Fuson, K., Rice, A., Mahling, R., Snow, A., Nayak, K., Shanbhogue, P., Meyer, A.G., Redpath, G.M.I., Hinderliter, A., Cooper, S.T., et al. (2014). Alternate Splicing of Dysferlin C2A Confers Ca^{2+}-Dependent and Ca^{2+}-Independent Binding for Membrane Repair. Structure *22*, 104–115.

Garcia, J., Gerber, S.H., Sugita, S., Südhof, T.C., and Rizo, J. (2004). A conformational switch in the Piccolo C 2 A domain regulated by alternative splicing. Nat. Struct. Mol. Biol. *11*, 45–53.

Grzesiek, S., and Bax, A. (1992). An efficient experiment for sequential backbone assignment of medium-sized isotopically enriched proteins. J Magn Reson *99*, 201–207.

Han, R., and Campbell, K.P. (2007). Dysferlin and muscle membrane repair. Curr. Opin. Cell Biol. *19*, 409–416.

Hsu, Y.-H., Burke, J.E., Stephens, D.L., Deems, R.A., Li, S., Asmus, K.M., Woods, V.L., and Dennis, E.A. (2008). Calcium Binding Rigidifies the C2 Domain and the Intradomain Interaction of GIVA Phospholipase A $_2$ as Revealed by Hydrogen/Deuterium Exchange Mass Spectrometry. J. Biol. Chem. *283*, 9820–9827.

Huang, Y., Laval, S.H., van Remoortere, A., Baudier, J., Benaud, C., Anderson, L.V.B., Straub, V., Deelder, A., Frants, R.R., den Dunnen, J.T., et al. (2007). AHNAK, a novel component of the dysferlin protein complex, redistributes to the cytoplasm with dysferlin during skeletal muscle regeneration. FASEB J. *21*, 732–742.

Johnson, B.A., and Blevins, R.A. (1994). NMR View: A computer program for the visualization and analysis of NMR data. J. Biomol. NMR *4*, 603–614.

Krahn, M., Béroud, C., Labelle, V., Nguyen, K., Bernard, R., Bassez, G., Figarella-Branger, D., Fernandez, C., Bouvenot, J., Richard, I., et al. (2009). Analysis of the *DYSF* mutational spectrum in a large cohort of patients: *DYSF* Mutational Spectrum in a Large Cohort. Hum. Mutat. *30*, E345–E375.

Matsuda, C., Miyake, K., Kameyama, K., Keduka, E., Takeshima, H., Imamura, T., Araki, N., Nishino, I., and Hayashi, Y. (2012). The C2A domain in dysferlin is important for association with MG53 (TRIM72). PLoS Curr.

Matthew, J.B., and Richards, F.M. (1983). The pH dependence of hydrogen exchange in proteins. J. Biol. Chem. *258*, 3039–3044.

Medkova, M., and Cho, W. (1998). Differential membrane-binding and activation mechanisms of protein kinase C-α and -ε. Biochemistry *37*, 4892–4900.

Morales, K.A., Yang, Y., Cole, T.R., and Igumenova, T.I. (2016). Dynamic Response of the C2 Domain of Protein Kinase Cα to Ca^{2+} Binding. Biophys. J. *111*, 1655–1667.

Nalefski, E.A., McDonagh, T., Somers, W., Seehra, J., Falke, J.J., and Clark, J.D. (1998). Independent Folding and Ligand Specificity of the C2 Calciumdependent Lipid Binding Domain of Cytosolic Phospholipase A2. J. Biol. Chem. *273*, 1365–1372.

Nalefski, E.A., Wisner, M.A., Chen, J.Z., Sprang, S.R., Fukuda, M., Mikoshiba, K., and Falke, J.J. (2001). C2 Domains from Different Ca^{2+} Signaling Pathways Display Functional and Mechanistic Diversity. Biochemistry *40*, 3089–3100.

Peulen, Rademaker, Anania, Turtoi, Bellahcène, and Castronovo (2019). Ferlin Overview: From Membrane to Cancer Biology. Cells *8*, 954.

Schuck, P. (2000). Size-Distribution Analysis of Macromolecules by Sedimentation Velocity Ultracentrifugation and Lamm Equation Modeling. Biophys. J. *78*, 1606–1619.

Shao, X., Fernandez, I., Südhof, T.C., and Rizo, J. (1998). Solution Structures of the Ca^{2+}-free and Ca^{2+}-bound C $_2$ A Domain of Synaptotagmin I: Does Ca^{2+} Induce a Conformational Change? [†]. Biochemistry *37*, 16106–16115.

Sula, A., Cole, A.R., Yeats, C., Orengo, C., and Keep, N.H. (2014). Crystal structures of the human Dysferlin inner DysF domain. BMC Struct. Biol. *14*, 3.

Therrien, C., Di Fulvio, S., Pickles, S., and Sinnreich, M. (2009). Characterization of Lipid Binding Specificities of Dysferlin C2 Domains Reveals Novel Interactions with Phosphoinositides [†]. Biochemistry *48*, 2377–2384.

Ubach, J., Lao, Y., Fernandez, I., Arac, D., Südhof, T.C., and Rizo, J. (2001). The C $_2$ B Domain of Synaptotagmin I Is a Ca^{2+}-Binding Module [†]. Biochemistry *40*, 5854–5860.

Wittekind, M., and Mueller, L. (1993). HNCACB, a High-Sensitivity 3D NMR Experiment to Correlate Amide-Proton and Nitrogen Resonances with the Alpha- and Beta-Carbon Resonances in Proteins. J. Magn. Reson. *101*, 201–205.

Yagi, H., Conroy, P.J., Leung, E.W.W., Law, R.H.P., Trapani, J.A., Voskoboinik, I., Whisstock, J.C., and Norton, R.S. (2015). Structural Basis for Ca^{2+}-mediated Interaction of the Perforin C2 Domain with Lipid Membranes. J. Biol. Chem. *290*, 25213–25226.

Ye, H., Li, B., Subramanian, V., Choi, B.-H., Liang, Y., Harikishore, A., Chakraborty, G., Baek, K., and Yoon, H.S. (2013). NMR solution structure of C2 domain of MFG-E8 and insights into its molecular recognition with phosphatidylserine. Biochim. Biophys. Acta BBA - Biomembr. *1828*, 1083–1093.

Chapter 3

Dissecting the Calcium Binding Mechanisms of the

Dysferlin C2A Domain

3.1 Introduction

As a calcium binding module, it has been shown that many activities of the dysferlin C2A domain are regulated by calcium. Most importantly, the dysferlin C2A domain targets several phospholipids in a calcium-dependent manner, which is consistent with its role in skeletal muscle membrane repair (Bansal et al., 2003; Han and Campbell, 2007; Therrien et al., 2009). Dysferlin rapidly responds to plasma membrane injury by sensing Ca^{2+} influx at the site of damage, and then facilitates Ca^{2+}-dependent patch repair (Davenport et al., 2016). How calcium binds to dysferlin to alter its structure and regulate this process is not known.

To date, more than 100 unique structures of C2 domains have been solved by NMR spectroscopy and X-ray crystallography. The variable loops at the top of the domains are involved in the coordination of Ca^{2+} ions. The Ca^{2+}-binding sites are formed primarily by conserved aspartate residues and the carboxylate or carbonyl group of other residues. Up to four Ca^{2+}-binding sites are possible in a C2 domain depending on the residues that are present on the loops. Although C2 domains share a high degree of structural similarity, the Ca^{2+} binding modes differ significantly, and it is not clear how Ca^{2+} binding affects protein activity (Corbalan-Garcia and Gómez-Fernández, 2014).

Earlier, we solved the crystal structure of the Ca^{2+}-C2A domain which shows two bound calcium ions (Ca1, Ca2) coordinating to residues in loops L1, L2 and L3. One calcium ion (Ca1) is coordinated by side chain oxygen atoms of residues D18, D21 (bidentate) and N40, the backbone carbonyl of I19 and two water molecules. The second ion (Ca2) uses D18, D21, D71 (bidentate) and E73 side chains, the backbone carbonyl from H72 and a single water molecule. Residues D18 and D21 bisect the positions of the two calcium ions and use side chain oxygen atoms to ligate both Ca1 and Ca2 simultaneously (**Figure 3.1**).

In this chapter, we characterized the binding order and affinities of the two Ca^{2+} ions, and investigated the detailed binding mode of dysferlin C2A by using a combination of methods including NMR spectroscopy, ITC, site-directed mutagenesis and circular dichroism spectropolarimetry. The models we proposed provide useful understanding for expanding our knowledge of the calcium and membrane binding mechanisms of C2 domains.

3.2 Materials and Methods

3.2.1 Site-directed mutagenesis of the dysferlin C2A domain

QuikChange site-directed mutagenesis (Wang and Malcolm, 1999) was performed to introduce the following mutations on the dysferlin C2A plasmid: $C2A^{D16K}$, $C2A^{D18N}$, $C2A^{D18K}$, $C2A^{D21N}$, $C2A^{D21K}$, $C2A^{N40A}$, $C2A^{D71N}$, $C2A^{D71K}$. The primers used for making
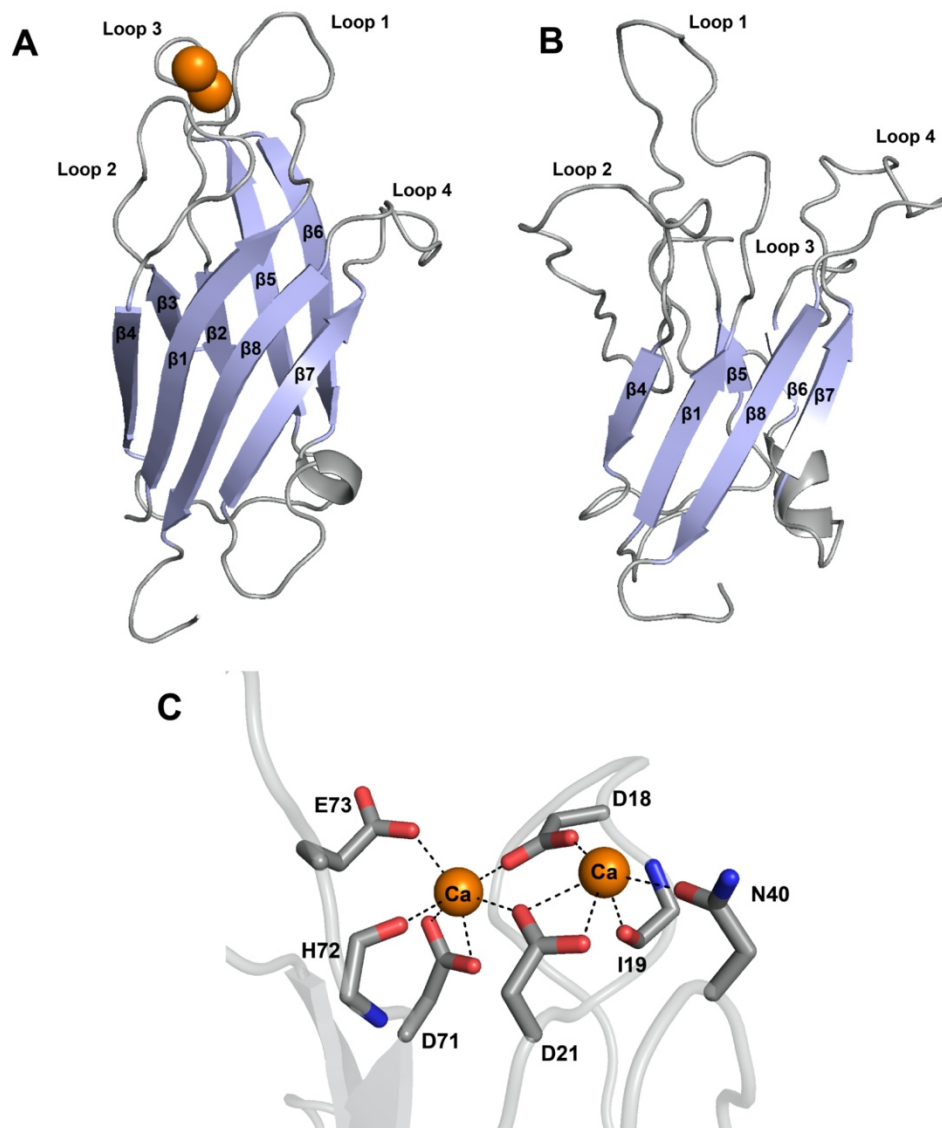
Figure 3. 1 Ca^{2+}-bound and apo Structure of dysferlin C2A domain and the calcium binding site.

(A) Cartoon of the crystal structure of Ca^{2+}-bound C2A. Bound two Ca^{2+} ions are shown as orange spheres. **(B)** The solution NMR structure of apo-C2A. β-sheets are depicted in light blue and loops in gray, labelled by numbers. **(C)** Close-up view of the calcium binding site showing the binding residues D18, I19, D21, N40, D71, H72 and E73. Oxygen atoms are in red and nitrogen atoms in blue.

the mutations are shown in **Table 3.1**. The wild-type C2A plasmid was isolated from harvested BL21 *E. coli* cells using a Bio Basic Inc. EZ-10 spin column miniprep kit. Base pair mutations were incorporated into DNA using the QuikChange Site-Directed Mutagenesis protocol (Agilent) and polymerase chain reaction (PCR). Methylated parental strands that remained in the PCR reaction were digested by Dpn1 overnight at 37°C. The following day, plasmid DNA was purified using a PCR clean-up kit (BioBasic Inc). All PCR products were transformed into competent MM294 cells and incubated on antibiotic-treated LB-agar plates overnight at 37 °C. Multiple colonies were picked and grown in LB. Plasmids were isolated from harvested cells using a Bio Basic Inc. EZ-10 spin column miniprep kit and were sequenced (London Regional Genomics Centre, Canada) to verify that the correct mutations were incorporated. All the substituted proteins were expressed and purified using the same protocol described in **Chapter 2.2.1**.

3.2.2 Ca^{2+} and La^{3+} titrations monitored by NMR Spectroscopy

All NMR experiments were collected at 25˚C on a Varian Inova 600 MHz NMR spectrometer equipped with a triple resonance cryogenic probe and z-field gradients. All data were processed using NMRPipe (Delaglio et al., 1995) and analyzed using NMRViewJ (Johnson and Blevins, 1994). NMR titration experiments were conducted in 25 mM HEPES, 150 mM NaCl, 250 μM TCEP, pH 7.5 with 10% D_2O, 200 μM DSS as an internal reference, and 200 μM imidazole as an internal pH indicator. Uniformly ^{15}N-labeled C2A protein and substituted proteins were incubated with Chelex-100 (Bio-Rad) for 1h to remove residual Ca^{2+} ions before acquiring initial ^1H-^{15}N HSQC spectra by the NMR spectrometer. Protein concentrations were determined from triplicate amino acid

Table 3. 1 Primers used for dysferlin C2A mutagenesis.

Construct	Primer Sequence
D16N	Forward: 5'- CCACACACCCAACACCGACATCAG -3' Reverse: 5'- CTGATGTCGGTGTTGGGTGTGTGG-3'
D16K	Forward: 5'- CCACACACCCAAAACCGACATCAG -3' Reverse: 5'- CTGATGTCGGTTTTGGGTGTGTGG -3'
D18N	Forward: 5'- CACACCCGACACCAACATCAGCG -3' Reverse: 5'- CGCTGATGTTGGTGTCGGGTGTG -3'
D18K	Forward: 5'- CACACCCGACACCAAAATCAGCG -3' Reverse: 5'- CGCTGATTTTGGTGTCGGGTGTG -3'
D21N	Forward: 5'- CACCGACATCAGCAACGCCTACTGCTCCGC -3' Reverse: 5'- GCGGAGCAGTAGGCGTTGCTGATGTCGGTG -3'
D21K	Forward: 5'- CACCGACATCAGCAAAGCCTACTGCTCCGC -3' Reverse: 5'- GCGGAGCAGTAGGCTTTGCTGATGTCGGTG -3'
N40A	Forward: 5'- CATCAAGGCCAGCGTGAAC -3' Reverse: 5'- GTTCACGCTGGCCTTGATG -3'
D71N	Forward: 5'- GGTGGTCAAAAACCATGAGACG -3' Reverse: 5'- CGTCTCATGGTTTTTGACCACC -3'
D71K	Forward: 5'- GGTGGTCAAAAAACATGAGACG -3' Reverse: 5'- CGTCTCATGTTTTTTGACCACC -3'

analysis (Amino Acid Analysis Facility, Hospital for Sick Children, Toronto). The stock solution of $CaCl_2$ was analyzed by deductively coupled plasma - mass spectrometry (ICP-MS) to obtain the accurate concentration (Biotron, Western University). 1-2 μL $CaCl_2$ solution of desired concentration, diluted from the stock $CaCl_2$ solution, was added to the NMR sample at each titration point by a 10 μL Hamilton syringe followed and ^{1}H-^{15}N HSQC spectrum were recorded following each addition at different $[Ca^{2+}]$. **Table 3.2** shows a list of the calcium additions made for the Ca^{2+} titration experiment of the C2A domain. A La^{3+} titration was performed under the same conditions. The stock La^{3+} solution was made by dissolving lanthanum(III) chloride heptahydrate ($LaCl_3 \cdot 7H_2O$) (Sigma-Aldrich) with the NMR buffer. The Ca^{2+} titration was also performed by monitoring the ^{1}H-^{13}C HSQC spectra of C2A using uniformly ^{15}N, ^{13}C -labeled protein under the same conditions. A total number of 19 titration points were added to ^{15}N, ^{13}C-labeled apo-C2A at a concentration of 675 μM. The final concentration of Ca^{2+} added was 22 mM.

The chemical shift change ($\Delta\delta$) or intensity change (ΔI) of selected peaks were measured in the ^{1}H dimension at each titration point. The dissociation constant was obtained by fitting the data in GraphPad Prism according to the following equation:

$$\Delta\delta\ (\Delta I) = N \frac{(P_t + L_t + K_d) - \sqrt{(P_t + L_t + K_d)^2 - 4P_t L_t}}{2P_t} \quad \textbf{(Equation 1)}$$

where P_t is the total C2A concentration, L_t is the total Ca^{2+} concentration at a given titration point, K_d is the dissociation constant, and N is the maximum chemical shift

Table 3. 2 A quantitative demonstration of the NMR titration experiment.

2 µL Ca^{2+} from six different concentrations of stock solutions was added at each titration point to a 600 µL solution containing 432 µM C2A. The titration was completed with the addition of 25 equivalents of Ca^{2+}.

Titration point	Volume of $CaCl_2$ added (µL)	Final volume of the sample (µL)	$[Ca^{2+}]$ added (mM)	Final $[Ca^{2+}]$ (µM)	$[Ca^{2+}]/[C2A]$
0	0	600	0	0	0
1	2	602	26	86	0.2
2	2	604	26	172	0.4
3	2	606	26	257	0.6
4	2	608	26	342	0.8
5	2	610	26	426	1.0
6	2	612	26	510	1.2
7	2	614	26	593	1.37
8	2	616	26	675	1.56
9	2	618	26	757	1.75
10	2	620	26	839	1.94
11	2	622	26	919	2.12
12	2	624	26	998	2.31
13	2	626	26	1080	2.5
14	2	628	55	1253	2.9
15	2	630	124	1642	3.8
16	2	632	139	2073	4.8
17	2	634	139	2506	5.8
18	2	636	538	4190	9.7
19	2	638	2113	10800	25

change ($\Delta\delta$) or peak intensity change (ΔI) that would occur upon saturation of C2A by Ca^{2+}.

3.2.3 Line-shape simulation

The ^{1}H cross-section of selected peaks from the ^{1}H, ^{15}N-HSQC calcium titration spectra were processed for line shape analysis. The ^{1}H dimension traces through peaks at each titration point were extracted using NMRPipe and plotted as the experimental data. The LineShapeKin program was then applied for line-shape simulation (http://lineshapekin.net/index.htm). B model (two site binding to one receptor molecule) was chosen for the simulation. In this model, binding involves two steps with one ligand molecule binding at a time. The conventional description of this model is as follows:

$$P + L \underset{k_{2A1}}{\overset{K_{A1}}{\rightleftarrows}} PL + L \underset{k_{2A2}}{\overset{K_{A2}}{\rightleftarrows}} PL_2 \qquad \textbf{(Equation 2)}$$
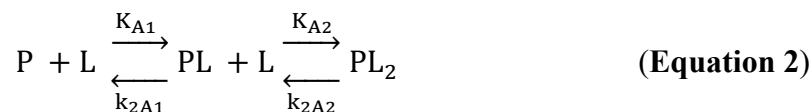
where P is the C2A concentration, L is the Ca^{2+} concentration at a given titration point. The association constants (K) and off-rate constants (k) are macroscopic constants. The two-site-binding model can also be interpreted at the molecular-level with a more detailed scheme of binding reactions making use of microscopic constants as follows (Cantor and Schimmel, 1980):

$$L_aP + L$$

$$K_{A1a} \nearrow \qquad \searrow K_{A2a}$$

$$k_{2A1a} \qquad k_{2A2a}$$

$$P + L \qquad \qquad \qquad PL_2 \qquad \qquad \textbf{(Equation 3)}$$

$$K_{A1b} \qquad K_{A2b} \nearrow$$

$$k_{2A1b} \qquad k_{2A2b}$$

$$PL_b + L$$
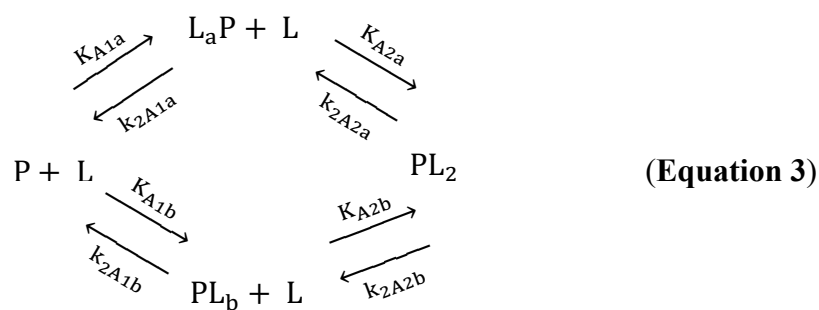
Also, the binding of a second L molecule may have lower or higher affinity due to negative or positive cooperativity between the two binding sites, allowing direct evaluation of allosteric effects between the sites. The microscopic model was used in the LineShapeKin program. Relationships between the micro- and macroscopic association constants (K) in these two schemes are as follows:

$$K_{A1} = K_{A1a} + K_{A1b} \qquad\qquad \textbf{(Equation 4)}$$

$$\frac{1}{K_{A2}} = \frac{1}{K_{A2a}} + \frac{1}{K_{A2b}} \qquad\qquad \textbf{(Equation 5)}$$

The off-rate constants (k) are also related below:

$$k_{2A1} = \frac{K_{A1a}\, k_{2A1a} + K_{A1b}\, k_{2A1b}}{K_{A1}} \qquad\qquad \textbf{(Equation 6)}$$

$$k_{2A2} = k_{2A2a} + k_{2A2b} \qquad\qquad \textbf{(Equation 7)}$$

The simulation was performed in MATLAB Version 9.5. The chemical shifts of peaks, line-widths, LP ratios, rate constants and relaxation rates were adjusted iteratively to achieve consistency with the experimental data and simulated simultaneously for selected

85

peaks. The yielded microscopic association constants and off-rates were then converted to macroscopic constants using **Equation 3 – 6**. The dissociation constants (K_d) can be obtained using its relationship with association constants (K_a) as follows:

$$K_a = \frac{1}{K_d} \qquad\qquad \textbf{(Equation 8)}$$

3.2.4 Isothermal titration calorimetry

All calorimetry experiments were performed using a NanoITC (TA Instruments) at 25°C. All experiments were completed 2–3 times using freshly prepared proteins extensively dialyzed in 25 mM HEPES, 150 mM NaCl, 250 µM TECP, pH 7.5 and pretreated with Chelex-100 (Bio-Rad) to remove residual Ca^{2+} ions for one hour. The optimal concentrations of protein in the experiments were determined to be: 4.75 mM Ca^{2+} titrated into 155 µM wild-type C2A, 35 mM Ca^{2+} titrated into 350 µM C2A^{D16N}, 8 mM Ca^{2+} titrated into 87 µM C2A^{D16K}, 70 mM Ca^{2+} titrated into 350 µM C2A^{D18N}, 20 mM Ca^{2+} titrated into 142 µM C2A^{D18K}, 10 mM Ca^{2+} titrated into 346 µM C2A^{D21K}, 35 mM Ca^{2+} titrated into 525 µM C2A^{D21N}, 20 mM Ca^{2+} titrated into 182 µM C2A^{N40A}, 60 mM Ca^{2+} titrated into 635 µM C2A^{D71N}, 35 mM Ca^{2+} titrated into 400 µM C2A^{D71K}. Proteins and Ca^{2+} solutions were degassed under vacuum prior to each titration. Titrations consisted of 25 injections of 2 µL Ca^{2+} solution into a 146 µL cell containing the proteins with constant stirring. Heats of dilution were measured in a separate experiment in which Ca^{2+} solution was injected into the buffer alone. Ca^{2+} titration to wild-type C2A and C2A^{D16N} were analysed using sequential-two-binding-site model in NanoAnalyze v3.1.2 (TA instruments) to determine best fit values for K_A, ΔH and N. ΔS was calculated according to **Equation 9**.

$$\Delta G = -RTlnK_A = \Delta H - T\Delta S$$

$$\Delta S = RlnK_A + (\Delta H/T) \qquad \textbf{(Equation 9)}$$

3.2.5 Circular dichroism

Folding of all proteins were monitored by circular dichroism spectropolarimetry using a Jasco J-810 instrument (Biomolecular Interactions and Conformations Facility, University of Western Ontario). All proteins were extensively dialyzed in the CD buffer for at least one day with stirring. For proteins in the calcium-free state, samples comprised 20 μM protein were prepared in 20 mM KH_2PO_4 (pH 7.5) in the presence of 1mM EDTA. For Ca^{2+}-bound samples, buffer containing 10 mM MOPS (pH 7.5) and 20 mM $CaCl_2$ was used to avoid precipitation of calcium phosphate. For each sample, 15 scans from 250 –200 nm (80 nm/min with increment of 1 nm) were recorded using a 1 mm path-length cell at 20 °C, averaged, and the buffer background was subtracted. Thermal denaturation studies were performed by exposing the protein to different temperatures within the range of 5 – 95 °C (1 °C/min with increments of 0.5°C) by monitoring changes in the ellipticity at 215 nm. A 1 mM path length cuvette was used. The ellipticity was normalized between 0-1 using the function:

$$Y' = (Y - Y_{max})/(Y_{max} - Y_{min}) \qquad \textbf{(Equation 10)}$$

3.3 Results

3.3.1 Dysferlin C2A contains two classes of calcium-binding sites

3.3.1.1 Crystal structure of Ca²⁺-C2A

Purified dysferlin C2A protein (5 mg/ml) was crystalized in the presence of 20 mM calcium by my colleague Dr. Roya Tadayon and the structure of the C2A domain in the calcium-bound (Ca^{2+}-C2A) state was determined using X-ray crystallography. The structure of the Ca^{2+}-bound dysferlin C2A domain was solved to 2.0 Å resolution and contained four molecules in the asymmetric unit with near identical conformations. The Ca^{2+}-C2A structures shows an anti-parallel β-sandwich arrangement that contains a single short α-helix (**Figure 3.1 A**), similar with the apo-C2A structure. The eight β-strands (β1-β8) are connected by four loops emerging at the top of the structures (L1-L4) where calcium is coordinated (**Figure 3.1 A**). A short α-helix containing residues L88 and V91 packs tightly against residues in the β7 (A99, F101) and β8 (V121) strands. There are significant differences in the lengths of the β-sheets between the apo-C2A and Ca^{2+}-C2A structure, although the arrangement of the β-sheets remains nearly identical. Specifically, the β-sheets for the apo-C2A domain are all 3-5 residues shorter than observed in the Ca^{2+}-C2A structure. In all cases, the loss of β-sheet structure in the apo-C2A domain occurs at the ends of the sheets closest to the calcium-binding loops (**Figure 3.1 A - B**). The loops have very poor definition in apo-C2A structure, as described in **Chapter 2**, whereas the loops in the Ca^{2+}-C2A structure are well-ordered. These observations indicate that calcium rigidifies the Ca^{2+}-C2A structure and stabilizes the β-sheet regions compared to the apo-C2A domain in the NMR structures, which are in good agreement with our results in **Chapter 2**.

The C2A domain in the presence of calcium showed electron density for two calcium ions per molecule for all molecules in the asymmetric unit. Inspection of the structures shows that both calcium ions exhibit classic pentagonal bipyramidal coordination and regular Ca-O distances (2.2-2.7 Å). One calcium ion (Ca1) is coordinated by side chain oxygen atoms of residues D18, D21 (bidentate) and N40, the backbone carbonyl of I19 and two water molecules. The second ion (Ca2) uses D18, D21, D71 (bidentate) and E73 side chains, the backbone carbonyl from H72 and a single water molecule. Residues D18 and D21 bisect the positions of the two calcium ions (Ca1-Ca2 distance 4.3 Å) and use side chain oxygen atoms to ligate both Ca1 and Ca2 simultaneously.

3.3.1.2 Ca^{2+} titration to the C2A domain by ITC

To further characterize the detailed calcium-binding properties, a combination of calcium titration experiments was used by isothermal titration calorimetry (ITC) and NMR spectroscopy. The calcium titration experiment by ITC showed a hook shaped curve with endothermic reaction in the beginning at lower $[Ca^{2+}]/[C2A]$ ratio with positive entropy change (102 J/mol°K) and exothermic at high $[Ca^{2+}]/[C2A]$ ratio with small negative entropy change (-8.6 J/mol°K), indicative of two distinct modes of Ca^{2+} binding **(Figure 3.2)**. Data was fitted using a sequential-two-binding-site model which yielded two dissociation constants (K_d) of 32 and 300 µM. The positive entropy change (ΔS) in the initial step signifies binding of first calcium ion is driven by an increase in disorder in the system, which may result from release of water molecules that surround calcium ions and rearrangement of the loops upon coordinating to C2A (Jelesarov and Bosshard, 1999). Binding of the second calcium gave rise to a fairly small entropy change indicating minimal
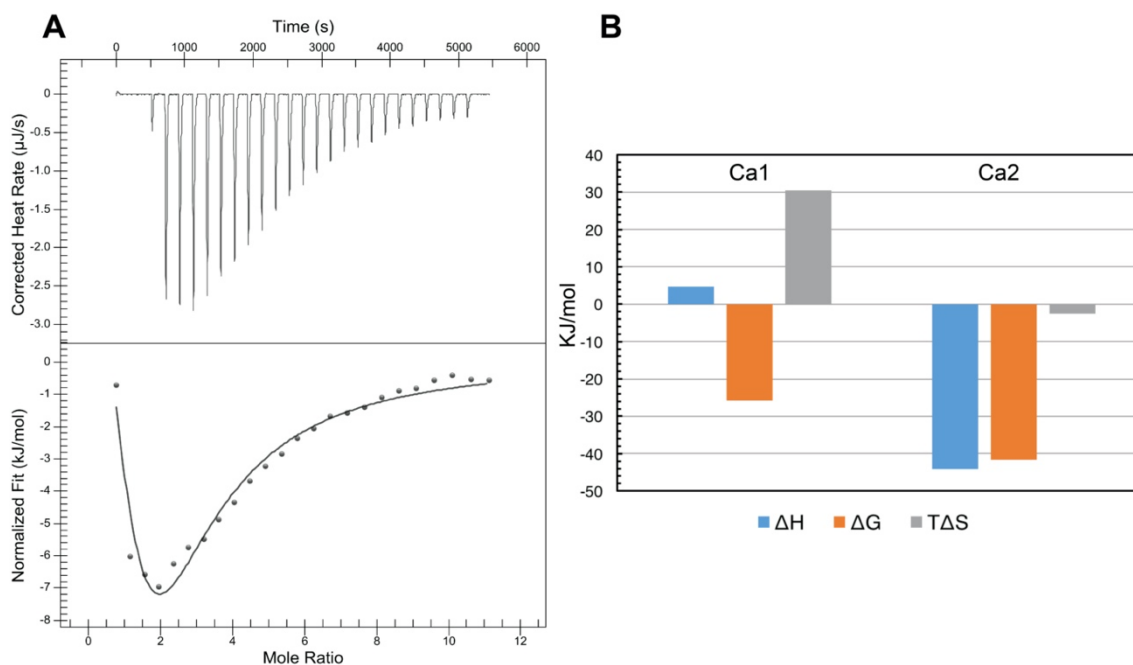
Figure 3. 2 Ca^{2+} titration to dysferlin C2A by ITC.

(A) ITC analysis of calcium binding to the wild-type C2A domain. The data was fit with a sequential two-site binding model that yielded K_d values of 32 μM and 300 μM. Data was collected at 25 °C with 25 mM HEPES, 150 mM NaCl, 250 μM TCEP, pH 7.5 buffer conditions. **(B)** Bar graph showing the thermodynamic properties for the calcium binding to C2A. The data show the first binding is driven by entropy changes (ΔS), indicative of a Ca^{2+}-induced conformational change, while the second binding step gave rise to a small ΔS indicating little overall structural change in C2A.

overall structural change in the C2A structure. This loss in entropy can be attributed to the increased Ca^{2+}-induced conformational rigidity of the loops. Together, the ITC data suggests that the C2A domain contains one tight and one weak calcium-binding site with about 10 times difference in binding affinity. The first binding event has a bigger impact on the reaction system likely through bond breaking and conformational change, whereas the global structure of C2A may remain largely unchanged upon binding to the second calcium.

Some earlier studies have reported the K_d values for the calcium binding sites of the dysferlin C2A measured by ITC (Abdullah et al., 2014; Fuson et al., 2014; Harsini et al., 2019) (**Table 3.3**), which showed similarities but also significant variations compared to our results. All three ITC data sets demonstrated a two-stage profile containing endothermic and exothermic reaction with a transition point. The transition point in our data agrees with one of studies at a $[Ca^{2+}]/[C2A]$ ratio of 2 (Fuson et al., 2014), whereas the other study shows the transition happened earlier when $[Ca^{2+}]/[C2A]$ ratio is less than one(Abdullah et al., 2014). The thermodynamic parameters (K_d, ΔH, and ΔS) yielded also differ from one to another. For example, the K_{d1} and K_{d2} values measured in our study are larger than those in the other two studies. Our K_{d1} value is about 10 and 5000 times larger than the other two studies respectively, and the K_{d2} is a little closer which is 4 and 6 times bigger. These differences may result from different models used to fit the data. One study used a multiple-site model which predicted 5 binding sites (Fuson et al., 2014), whereas we chose a sequential-two-binding-site model based on the two calcium ions observed in our crystal structure.

3.3.1.3 Ca^{2+} titration to the C2A domain monitored by ^{1}H-^{15}N HSQC

In the calcium titration experiment by NMR spectroscopy monitored by ^{1}H-^{15}N HSQC, a total number of 19 titration points were conducted until no further chemical shift changes were observed in the spectra. As noted in **Figure 3.3**, many resonances for calcium-coordinating residues in the loop regions L1-L3 were absent in spectra of the apo-C2A domain and could not be followed during calcium titrations. Nevertheless, the addition of calcium to the apo-C2A domain resulted in many changes in the ^{1}H-^{15}N HSQC spectra, including the appearance of all L1-L3 signals absent in apo-C2A spectra including E10, N11, D16, Y23, T35, S41, R77, D71, H72, A115, etc. (**Figure 3.3 B**). Further, the NMR titration data showed calcium-induced chemical shift changes that occurred in both the slow and fast chemical shift exchange regimes. Several signals including those for loop residues T17, I19, I38 and V45 showed the largest changes and exhibited slow exchange behavior while other residues (L7, F28, W52, A103, T113) showed faster exchange (**Figure 3.3 A**).

Due to the complexity of changes in the ^{1}H-^{15}N HSQC spectra, multiple methods were applied to further understand the detailed binding properties. For peaks that underwent slow exchange (T17, I19, I38 and V45), the peak intensities of both free and bound peaks throughout the process of titration were plotted. As shown in **Figure 3.4 A**, the peaks corresponding to T17 and V45 of Ca^{2+}-free state gradually decreased in intensities with the addition of Ca^{2+} (black panels), and meanwhile a separate signal for Ca^{2+}-bound state appeared and intensified (purple panels). The free-state peaks completely disappeared when [Ca^{2+}]/[C2A] $\approx$ 2 (**Figure 3.4 B**), suggesting the first Ca^{2+}-binding site was mostly
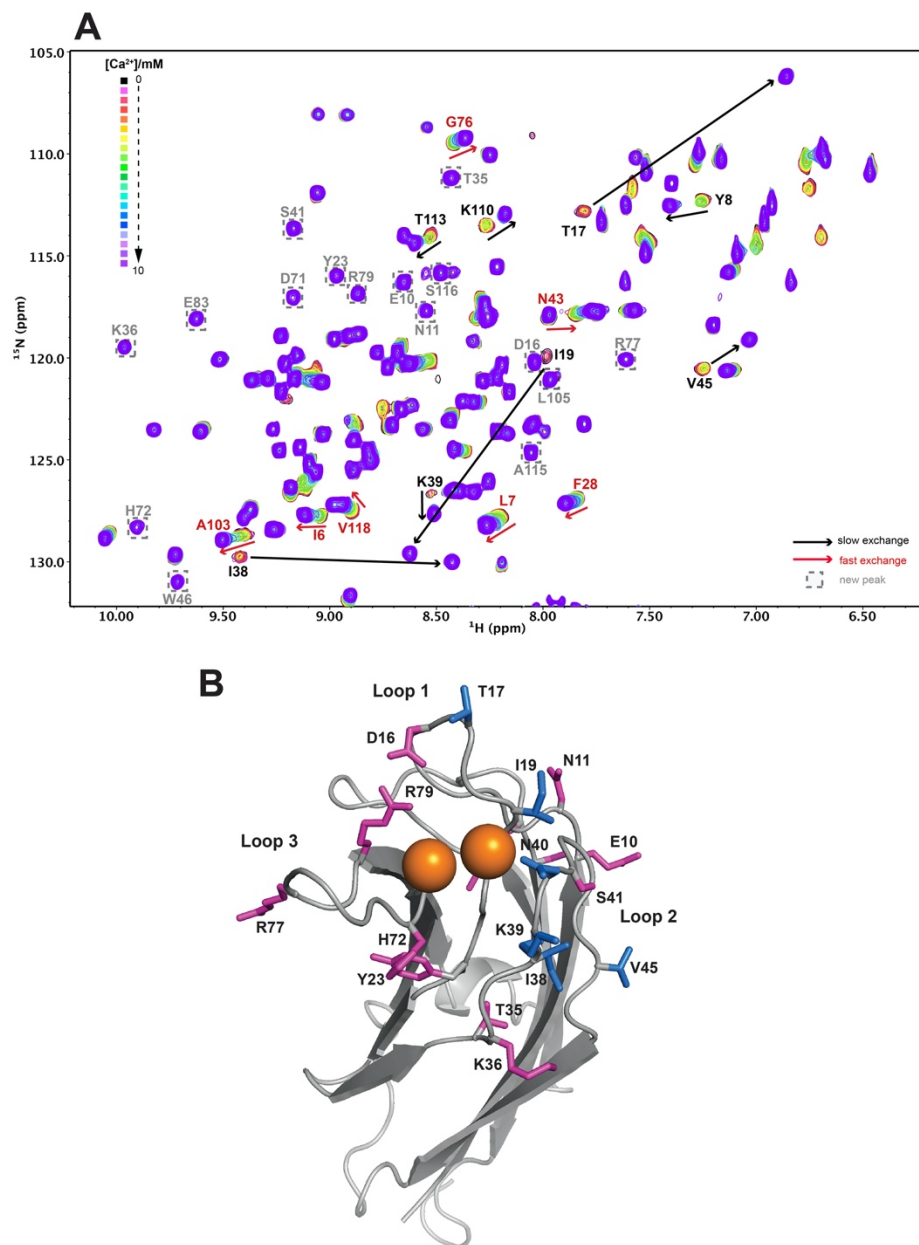
Figure 3. 3 Ca²⁺ titration to dysferlin C2A monitored by ¹H-¹⁵N HSQC NMR.

(A) Overlay of ¹H-¹⁵N HSQC spectra of 432 μM ¹⁵N-labeled C2A recorded with increasing [Ca²⁺]. Slow exchange and fast intermediate exchange were observed during titration and are labeled with black and red arrows respectively. The appearance of new peaks is shown by the grey dashed boxes. **(B)** The residues that showed the largest calcium-induced chemical shifts (blue) and those that appear upon Ca²⁺ binding (magenta) are shown on the cartoon structure of the Ca²⁺-bound dysferlin C2A structure. Most residues reside in loop L1- L3. Calcium ions are shown as orange spheres.
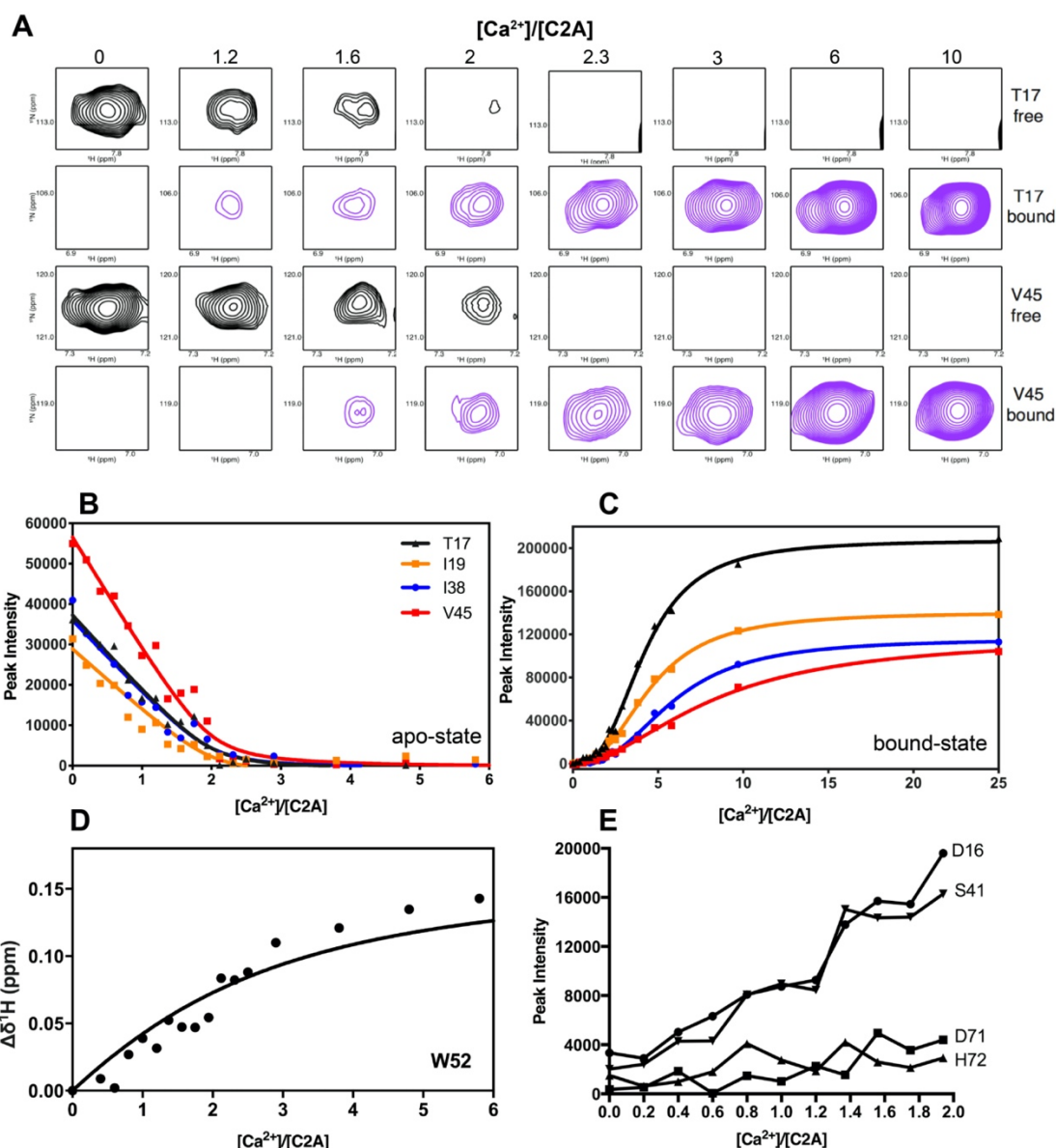
Figure 3. 4 Data analysis from Ca²⁺ titration to dysferlin C2A by NMR.

(A) Track record of the free and Ca²⁺-bound peaks for T17 and V45 along the titration process. (B) Plot of intensities of free peaks corresponding to residues T17, I19, K39 and V45 on 1H dimension at each titration point as a function of [Ca²⁺]/[C2A] ratio. The curves represent the fits of the data to 2:1 binding model. **(C)** Plot of intensities of Ca2+-bound peaks corresponding to residues T17, I19, K39 and V45. The curves represent the fits of the data to Hill function. **(D)** Plot of chemical shift change of W52 peak showing unsuccessful fitting with **Equation 1**. **(E)** Plot of intensities of four new peaks that appeared upon Ca²⁺ addition. Intensities of peaks of D16 and S41 increased within the addition of two equivalents of Ca²⁺, whereas D71 and H72 showed no obvious change in intensities.

saturated at this point. Interestingly, with the addition of more Ca^{2+}, intensities of the bound-state peaks continued increasing and reached a plateau when $[Ca^{2+}]/[C2A] \approx 10$. The plotting showed a hyperbolic binding curve (**Figure 3.4 C**), indicating a second Ca^{2+} ion binds to the protein during this stage, and it has largely rigidified the structure of the C2A domain because the final intensities of the bound-state peaks were remarkably higher than the starting free-state peaks. The data set of the free-state peak intensities were fitted with two-site binding model (**Equation 1**) considering the influence of the second binding (**Figure 2B**) and a K_d of 46 μM was obtained, which is close to the K_d measured by ITC. Unfortunately, it was difficult to measure the K_d of the second binding site from the bound-peak data due to the complexity of the data and lack of suitable model. Another attempt was to obtain K_d from peaks that showed faster exchange by measuring the chemical shift change during the titration. The W52 cross peak was chosen but the data was also difficult to fit using **Equation 1 (Figure 3.4 D)** likely because W52 exhibited a combination of fast and intermediate exchange regime. Indeed, all the above results may not be reliable because the model chosen is best used for pure slow/fast exchange, whereas the NMR signals from our experiments showed significant broadening during the calcium titration and in some cases signals appeared to contain both slow and fast exchange components.

The NMR titration also provides valuable information on the binding order of two calcium ions. During the titration, many resonances that were missing in the apo-C2A spectrum appeared upon the Ca^{2+} addition due to the restriction of amide exchange with the H_2O solvent. By plotting the intensities of the new peaks, we found that residues in loop 1 and 2 (D16, S41) showed a faster increase in intensities than residues in loop 3 (D71, H72)

(**Figure 3.4 E**), suggesting the Ca^{2+} ion that only binds to residues in loop 1 and 2 may be the first binding Ca^{2+} with a higher binding affinity. In fact, D71 and H72 did not show obvious resonances in the spectra until more than 2 equivalents of calcium was titrated, suggesting that they were not affected by the first Ca^{2+} ion. Thus, the other Ca^{2+} ion in the crystal structure that coordinates D71 and E73 in loop 3 may be the second binding Ca^{2+} with a lower affinity.

3.3.1.4 Line shape analysis

To further obtain more accurate information of the calcium binding mode, we applied an on-line program called "LineShapeKin" (http://lineshapekin.net/index.htm) which performs simulation of NMR line shapes for multi-site exchange models. A kinetic model describing a two-site binding mechanism was used (**Equation 1**). Two examples of this are shown for F28 in β-sheet β2 that shows fast intermediate exchange (**Figure 3.5 A, B**) and N40 in loop L2 that shows slow intermediate exchange (**Figure 3.5 D, E**). The chemical shifts of peaks, line-widths, LP ratios, rate constants and relaxation rates were adjusted iteratively to achieve consistency with the experimental data and simulated simultaneously for the F28 and N40 peak. The final simulated data were shown in **Figure 3.5 C, F** and four association constants (K_A) were yielded from the program: $K_{A1a} = 2.00*10^4$ M^{-1}, $K_{A1b} = 1.00*10^4$ M^{-1}, $K_{A2a} = 3.00*10^3$ M^{-1}, $K_{A2b} = 6.00*10^3$ M^{-1}. Using **Equation 3, 4** and **7**, the disassociation constants (K_d) were calculated ($K_{d1} = 33$ μM, $K_{d2} = 500$ μM), which showed very good agreement with results from our ITC data ($K_{d1} = 32$ μM, $K_{d2} = 300$ μM) confirming the presence of a tight and a weak binding site. The simulation also yielded microscopic off-rate constants (k): $k_{2A1a} = 4$ s^{-1}, $k_{2A1b} = 4$ s^{-1}, k_{2A2a}
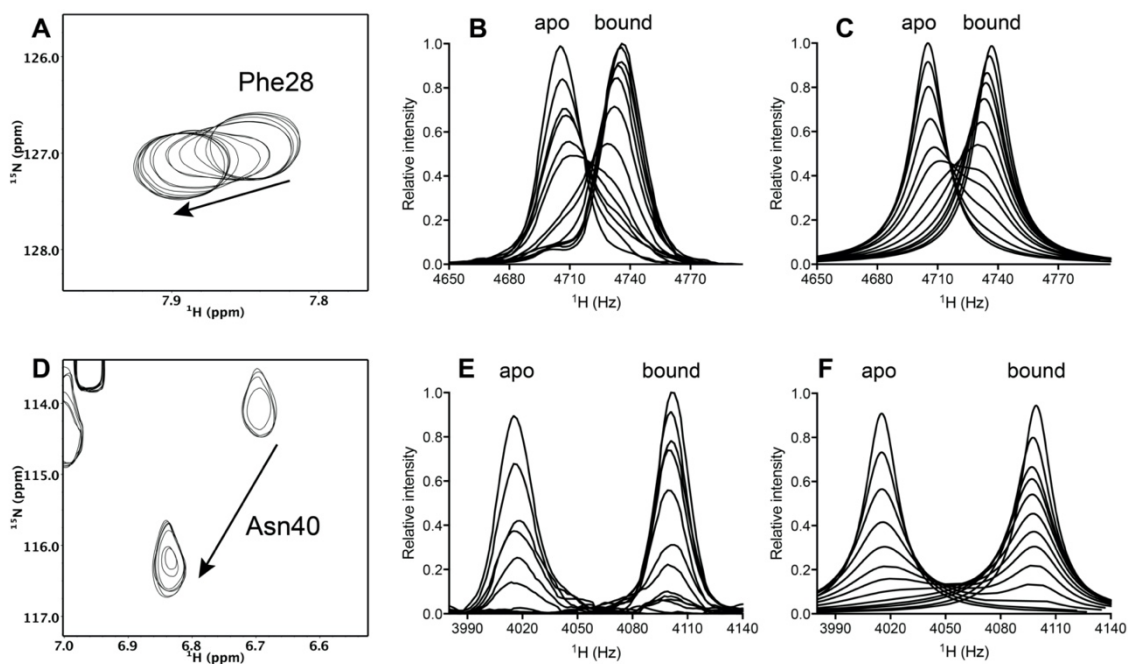
Figure 3. 5 Line-shape simulation of F28 and N40 peaks.

(A, D) Overlays of regions of the ^{1}H-^{15}N HSQC spectra from the Ca^{2+} titration into C2A. In **(A)**, Phe28 undergoes fast intermediate exchange change, where the peak changes in chemical shift during the titration and broadens without completely disappearing. In (D), Asn40 is an example of slow intermediate exchange, where the peak broadens during the titration and reappears in a new position. In both cases the arrow indicates the direction of peak movement at increasing Ca^{2+} concentration. **(B, E)** Experimental data showing one-dimensional ^{1}H traces through the Phe28 and Asn40 peaks at each titration point. **(C, F)** Line-shape simulation using a two-site binding model with LineShapeKin software for F28 and N40 peaks using K_{d1} = 33 µM, $k_{off,1}$ = 4 s^{-1}; K_{d2} = 500 µM, $k_{off,2}$ = 8 s^{-1}.

= 4 s^{-1}, k$_{2A2b}$ = 4 s^{-1}, which could be then converted to macroscopic constants using **Equation 5, 6**. This gave rise to k$_{off,1}$ = 4 s^{-1}, k$_{off,2}$ = 8 s^{-1} for the two calcium binding event. The small k$_{off}$ observed for both sites rationalizes the lack of pure fast exchange changes in the NMR spectra which would only be observed for minute chemical shift changes (ie. << 4 Hz) upon calcium binding and the more apparent slow exchange component for signals that undergo larger changes (i.e. F28, N40 in **Figure 3.5**).

3.3.1.5 Ca^{2+} titration to the C2A domain monitored by ^{1}H-^{13}C HSQC

Calcium titration experiments were also conducted using NMR spectroscopy monitored by ^{1}H-^{13}C HSQC. Using the same method as ^{1}H-^{15}N HSQC, a total number of 19 titration points were added to ^{15}N, ^{13}C-labeled apo-C2A at a concentration of 675 μM. The titration data showed similar calcium-induced chemical shift changes as ^{1}H-^{15}N HSQC. Both slow and fast chemical shift exchange regimes were observed during the titration (**Figure 3.6 A**). Expectedly, no new peaks appeared in the ^{13}C-HSQC titration because aliphatic protons are not affected by amide exchange with the H$_2$O solvent. As shown in **Figure 3.6 A**, the cross peaks corresponding to the γ and δ carbon of residue I19 (I19.CG and I19. CD) exhibited slow exchange, and the intensities their free and bound peaks were plotted against the [Ca^{2+}]/[C2A] ratio shown in **Figure 3.6 B - C.** The trends of the plotted data highly resemble the features of the plots for residues undergoing slow exchange in the ^{1}H-^{15}N HSQC titration data (**Figure 3.4 B, C**), where the free-state peaks completely disappeared when [Ca^{2+}]/[C2A] ≈ 2,while intensities of the bound-state peaks continued increasing and reached a plateau when [Ca^{2+}]/[C2A] ≈ 10. Thus, our ^{1}H-^{13}C HSQC titration data showed good consistency with ^{1}H-^{15}N HSQC data.
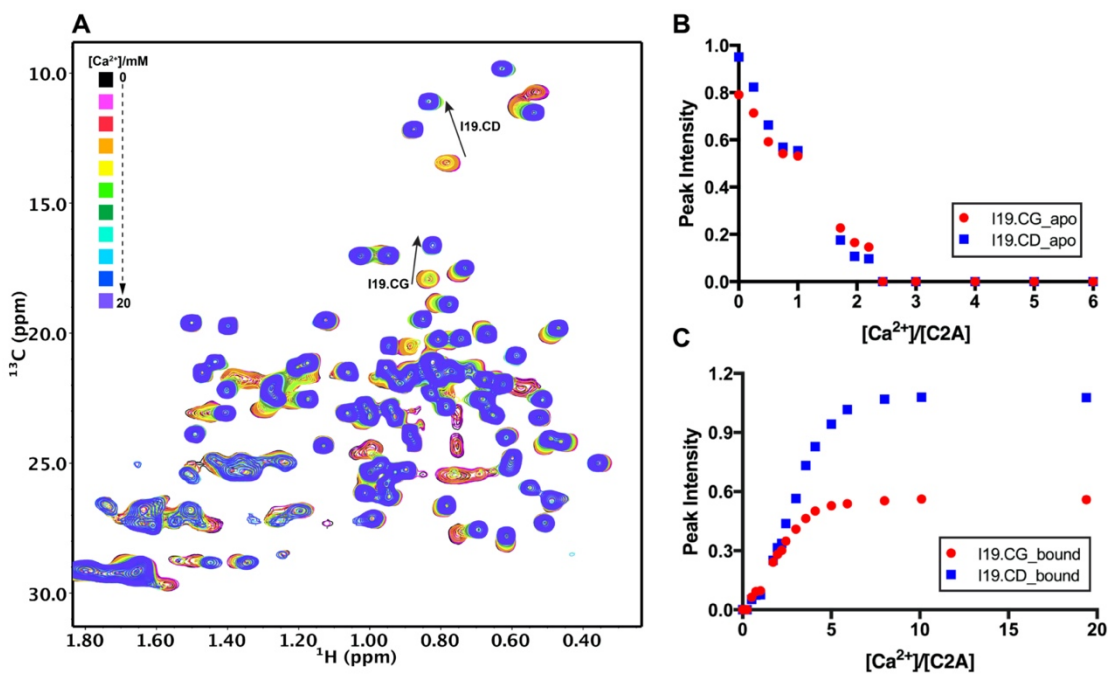
Figure 3. 6 Ca²⁺ titration to dysferlin C2A monitored by ¹H-¹³C HSQC NMR.

(A) Overlay of region of ¹H-¹³C HSQC spectra of 675 μM ¹³C-labeled C2A recorded with increasing [Ca²⁺]. Slow exchange of the cross peaks corresponding to the γ and δ carbon of residue I19 (I19.CG and I19. CD) are labelled. **(B)** Plot of intensities of free peaks of I19.CG and I19. CD on ¹H dimension at each titration point as a function of [Ca²⁺]/[C2A] ratio. **(C)** Plot of intensities of Ca²⁺-bound peaks of I19.CG and I19. CD on ¹H dimension at each titration point.

3.3.1.6 La^{3+} titration to the C2A domain

Lanthanide ions have ionic radii close to that of Ca^{2+} and are widely used as surrogate of Ca^{2+} as they bind to Ca^{2+}-binding sites in proteins (Dudev et al., 2005). To further probe the Ca^{2+}-binding sites in C2A, La^{3+} titration experiment was performed by NMR spectroscopy. The exchange rate between La^{3+}-free and bound state of the resonances were found generally faster compared to those in Ca^{2+} titration. Some of the peaks that showed slow exchange in the Ca^{2+} titration exhibited fast exchange in the La^{3+} titration, including Y8, K39, V45, K110 and T113 (**Figure 3.7 A**). By superimposing the final La^{3+}- and Ca^{2+}-bound spectrum, the peaks were largely overlapped, which suggests that La^{3+} binding brings very similar conformational change as the results from Ca^{2+} binding to the same sites. Notably, movement of some resonances (K39, V45) produced nonlinear curves with a transition point at 742 μM [La^{3+}] (orange peaks in **Figure 3.7 B, C**). This is a sign of two-state binding interaction, as the secondary interaction has a different effect on the chemical shifts than the primary interaction. This finding further verified the conclusion in the Ca^{2+} titration experiment that the C2A domain contains two classes of Ca^{2+}-binding sites. The fact that nonlinear chemical shift changes only appeared in La^{3+} titration may ascribe to the different binding affinities of La^{3+} compared to Ca^{2+}.

Taken together, by combining a variety of methods including X-ray crystallography, ITC, NMR spectroscopy, and line-shape simulation, we characterized two classes of calcium-binding sites in the dysferlin C2A domain and determined the binding affinities with K$_{ds}$ of ~30 μM and 300-500 μM, respectively.
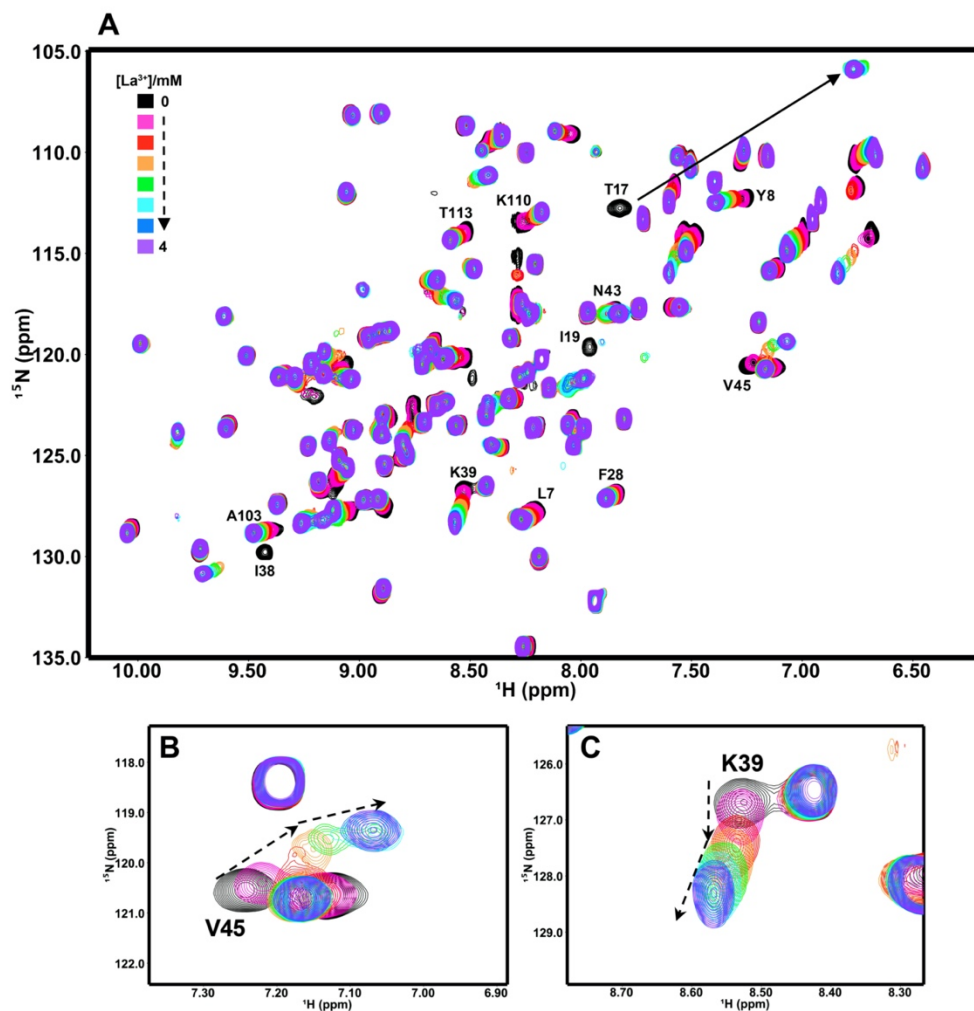
Figure 3. 7 La^{3+} titration to dysferlin C2A by NMR spectroscopy.

(A) Superimposed ^{1}H-^{15}N HSQC spectra of 487 μM ^{15}N-labeled C2A titrated with La^{3+}. Peaks that showed remarkable chemical shift are labeled on the spectra. **(B, C)** Close-up views of the spectra showing the nonlinear movement of the peaks corresponding to residues V45 and K39 upon La^{3+} addition.

3.3.1.7 The C2A domain does not bind to Mg^{2+}

Some Ca^{2+}-binding proteins are shown to bind to Mg^{2+}, such as parvalbumin (Cates et al., 2002). We queried whether the dysferlin C2A domain also binds to Mg^{2+} by monitoring ^{1}H-^{15}N HSQC spectra of apo-C2A and the same sample added with MgCl$_2$ of 66 times the protein concentration. The two ^{1}H-^{15}N HSQC spectra perfectly superimpose (**Figure 3.8**). This indicates that under the conditions used, C2A domain of dysferlin does not interact with the Mg^{2+}.

3.3.2 Calcium binding to dysferlin C2A domain is tightly coupled

In order to further explore the detailed binding mode, site-directed mutagenesis was conducted to the calcium-coordinating residues in the calcium-binding loops L1 (D18, D21), L2 (N40) and L3 (D71). First, substitution to asparagine was made for D18, D21 and D71 (C2A^{D18N}, C2A^{D21N}, and C2A^{D71N}), predicting that the Ca^{2+} binding could still be maintained but weakened. There are multiple other C2 domain structures from cPLA2, perforin and myoferlin (PDB: 1RLW (Perisic et al., 1998), 4Y1T (Yagi et al., 2015), 6EEL (Harsini et al., 2019)) which show that asparagine is an effective residue to coordinate calcium. We repeated the calcium titration experiments by NMR and ITC for the substituted proteins, and in all cases ^{1}H-^{15}N HSQC spectra showed the proteins were properly folded with little perturbation of the calcium-free structures. Calcium titration experiments followed by NMR spectroscopy or ITC both showed that calcium binding was completely eliminated for the C2A^{D18N}, C2A^{D21N} and C2A^{D71N} substitutions (**Figure 3.9 - 3.10**). In the calcium-bound structure of the C2A domain, D18 and D21 provide ligands for both Ca1 and Ca2 ions (**Figure 3.1 C**). However, it was surprising that replacement to
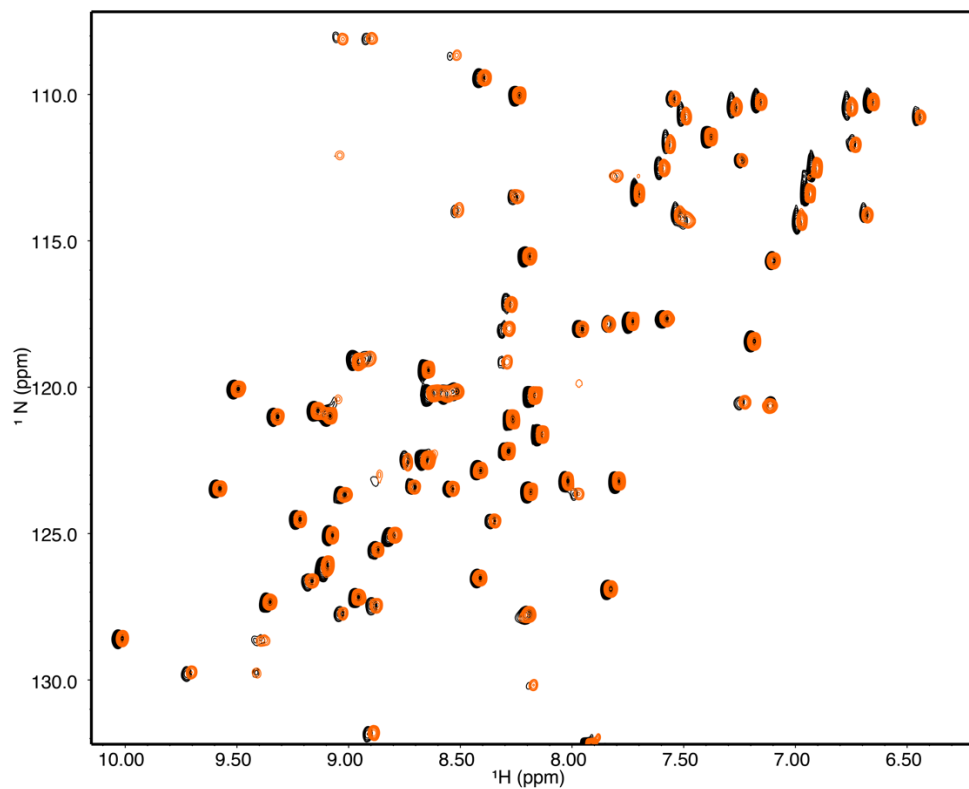
Figure 3. 8 Mg²⁺ titration to dysferlin C2A by NMR spectroscopy.

Superimposed ¹H-¹⁵N HSQC spectra of 300 μM ¹⁵N-labeled apo-C2A (black) and C2A mixed with 20 mM Mg²⁺ (orange). No chemical shift change was observed. Data was collected at 25 °C with 25 mM HEPES, 150 mM NaCl, 250 μM TCEP, pH 7.5 buffer conditions.
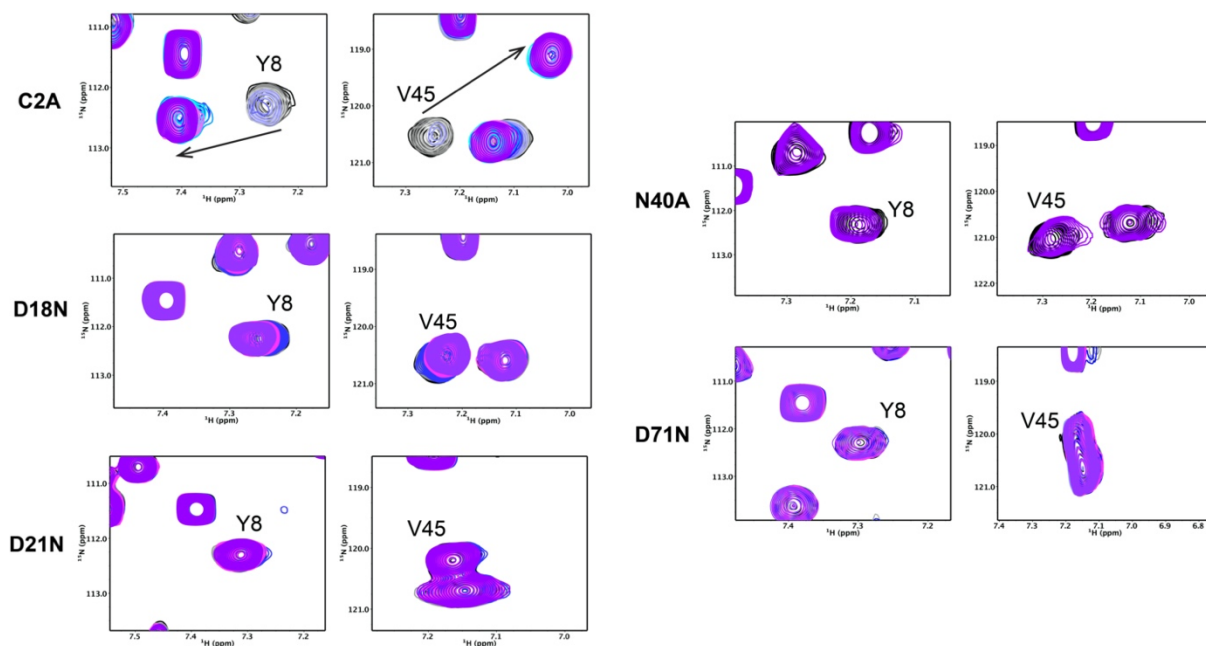
Figure 3. 9 Calcium binding to two sites in the C2A domain is tightly coupled.

Overlay of a portion of ^{1}H-^{15}N HSQC spectra of ^{15}N-labeled C2A, C2A^{D18N}, C2A^{D21N}, C2A^{N40A} and C2A^{D71N} recorded with increasing [Ca^{2+}] showing resonances of residues Y8 and V45. Resonances of residues Y8 and V45 exhibited slow exchange in the titration of wild-type C2A (shown as black arrows), but very little or no chemical shift in C2A^{D18N}, C2A^{D21N}, C2A^{N40A} and C2A^{D71N} indicative of abolished calcium binding.
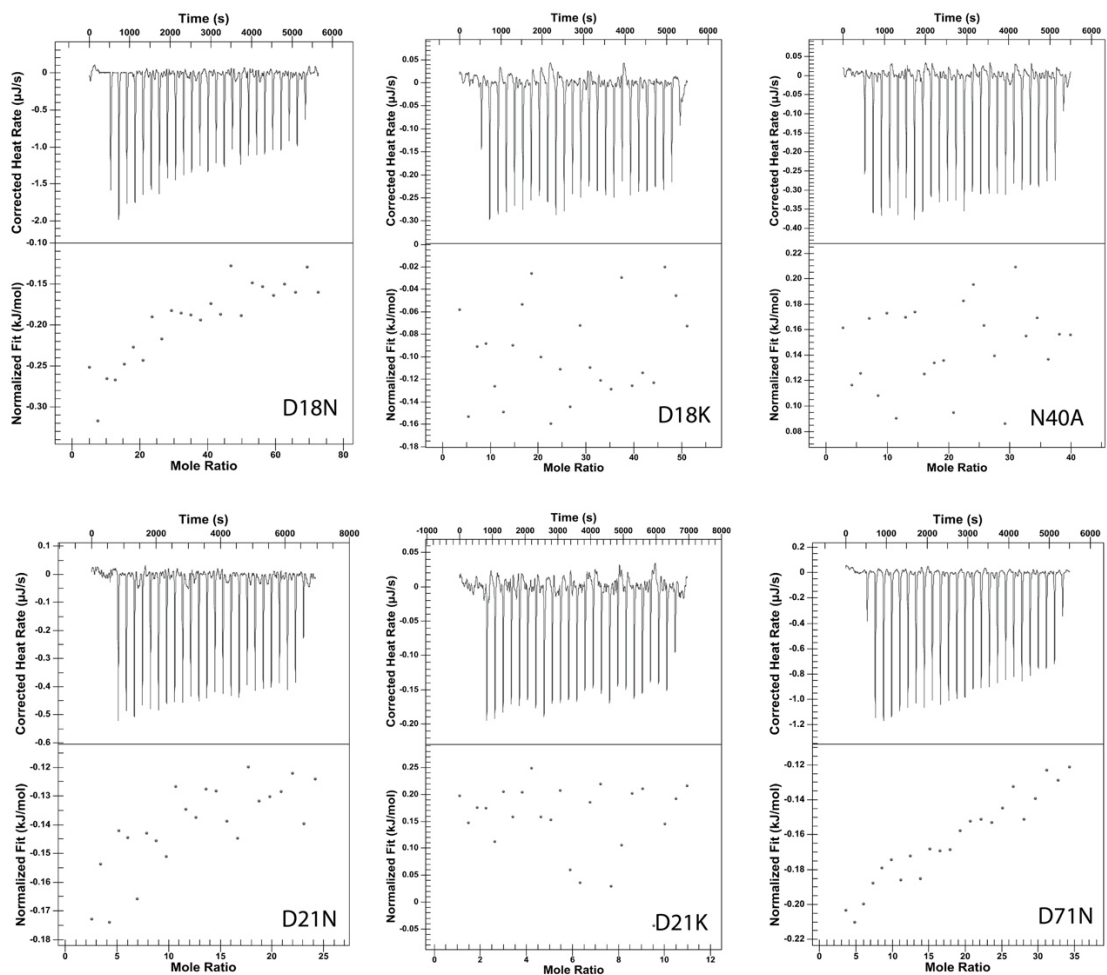
Figure 3. 10 ITC data of Ca^{2+} binding to C2A mutants.

Isotherm graphs of calcium binding to the mutants C2A domain including D18N, D18K, N40A, D21N, D21K, and D71N. All of them showed strongly disrupted Ca^{2+} binding. Data was collected at 25 °C with 25 mM HEPES, 150 mM NaCl, 250 μM TCEP, pH 7.5 buffer conditions.

an asparagine in either D18 or D21 eliminated all calcium binding. In the NMR titration data, compared to the wild-type C2A where peaks Y8 and V45 exhibited slow chemical shift exchange upon calcium addition, the same peaks barely showed any chemical shift changes in the case of C2A^{D18N}, C2A^{D21N} (**Figure 3.9).** The ITC data agreed with the NMR results, shown by the minute heat change upon titration of large amount of calcium (**Figure 3.10**). To further validate our findings, we substituted the D18 and D21 positions with lysine. The resulting proteins (C2A^{D18K}, C2A^{D21K}) showed negligible calcium binding (**Figure 3.10**). These observations suggest that binding of each calcium ion by the dysferlin C2A domain is dependent on the binding of its partner calcium ion.

To test this idea we examined substitutions at N40 and D71 (C2A^{N40A}, C2A^{D71N}). Unlike D18 and D21, these two residues each contribute to the binding of a single calcium ion. N40 in L2 contributes an oxygen ligand to Ca1, while D71 in L3 contributes two oxygen ligands to Ca12 (**Figure 3.1 C**). N40 was substituted to alanine (C2A^{N40A}) and D71 was mutated to asparagine (C2A^{D71N}). Again, substitution of either of these positions completed abolished calcium binding at both sites, shown by the undetectable chemical shift change in NMR and negligible heat change in ITC (**Figure 3.9 – 3.10**). These results support the idea that binding of two Ca^{2+} ions to C2A domain is tightly coupled, and loss of Ca^{2+} binding to one site causes concomitant disruption of the second Ca^{2+} binding site.

3.3.3 Calcium binding is affected by multiple factors

Prior to our crystal structure, it was reported that substitution of residue D16 (C2A^{D16A}) in the L1 loop impairs calcium binding (Abdullah et al., 2014). Yet this residue does not coordinate either of the Ca^{2+} ions in the crystal structure, and the oxygens of its side chain

are 7.6 Å away from the Ca^{2+} ions, beyond the maximum possible distance between ligand oxygen atoms and the calcium ion (~3.5 Å) (**Figure 3.11 D**). Thus, we intended to discover how the calcium binding to C2A protein is affected by residue D16. First, substitution to an asparagine ($C2A^{D16N}$) was made followed by titration experiments by ITC and NMR. The ITC experiments show that $C2A^{D16N}$ maintained the calcium binding property with a similar ITC profile (**Figure 3.11 B**) as the wild-type C2A (**Figure 3.2 A**) indicating two classes of binding sites. Surprisingly, fitting the data using sequential-two-binding-site model yielded two dissociation constants (K_d) of 550 μM and 4.3 mM, suggesting that the binding affinities are about 10 times weaker than the wild type C2A domain. This result was validated from NMR-based calcium titration experiments that showed some resonances that underwent slow exchange binding kinetics for wild-type C2A converted to fast or fast-intermediate exchange kinetics for $C2A^{D16N}$, as exemplified by Y8 and V45 (**Figure 3.11 C**). D16 was then substituted to a positively charged lysine ($C2A^{D16K}$) and the isotherm showed no evidence of binding (**Figure 3.11 A**). This indicates that replacement of a non-calcium coordinating residue in the loop regions of the C2A domain alters its ability to bind calcium, which agreed with an earlier study that showed the same result with the mutation of $C2A^{D16A}$ (Abdullah et al., 2014). This unexpected finding suggests that Ca^{2+} binding to the C2A domain is not determined solely by the ligands that bind Ca^{2+} ions, but is also affected by non-coordinating residues. We hypothesized that the overall electrostatic potential of the loop regions in the C2A domain plays an important role to recruit calcium ions prior to coordination by specific residues. In the apo-state the overall negative charge is dispersed by the flexibility of the loops as shown in our NMR structure, where aspartic (D16, D18, D21, D71) and glutamic acid
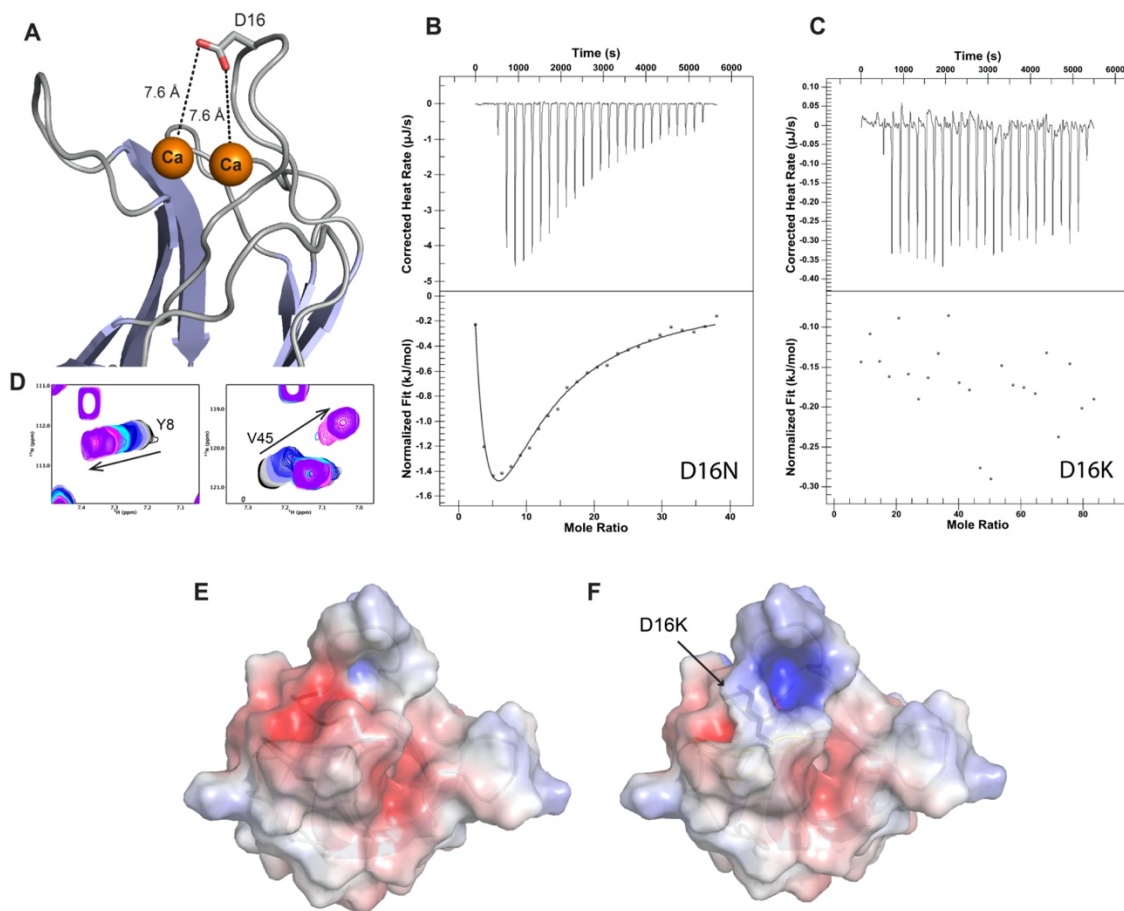
Figure 3. 11 D16 mediates Ca^{2+} binding to dysferlin C2A.

(A) Cartoon of crystal structure of Ca^{2+}-C2A showing the position of D16 and the distance between side chain oxygens and the two calcium ions. **(B, C)** ITC analysis of Ca^{2+} binding to C2A^{D16K} and C2A^{D16N} mutants. Titration to C2A^{D16K} shows abolished Ca^{2+} binding while C2A^{D16N} shows a similar binding curve as wild-type C2A but with binding affinities ~10 times lower (0.55 mM and 4.32 mM). **(D)** Overlay of a portion of ^{1}H-^{15}N HSQC spectra of ^{15}N-labeled C2A^{D16N} with increasing [Ca^{2+}] showing resonances of residues Y8 and V45 which exhibited fast intermediate exchange during the titration. **(E)** The electrostatic surface potential representation of apo-C2A loop region generated by the APBS electrostatic function in PyMOL. **(F)** The electrostatic surface potential representation of C2A^{D16K} loop region showing an electrostatic-switch from negative to positive. The mutation of C2A^{D16K} was modeled using the mutagenesis function in PyMOL.

108

Table 3. 3 Summary of Ca^{2+} binding parameters for the C2A domain

Protein (method)	K_{d1} (µM)	ΔH_1 (KJ/mol)	ΔS_1 (J/mol°K)	K_{d2} (µM)	ΔH_2 (J/mol)	ΔS_2 (J/mol°K)
C2A (ITC)	32	4.661	102.3	300	-44.15	-8.58
C2A (Line shape analysis)	33	-	-	500	-	-
C2A (ITC) (Abdullah et al., 2014)	3.7	0.67	104.25	80	-7.53	52.75
C2A (ITC) (Fuson et al., 2014)[*]	0.006	-1.8	36.09	53.2	-19.25	3.54
C2A^{D16N} (ITC)	553	10.13	9.634	4328	-47.79	-115

* A multiple-site model was used in this study which predicted 5 binding sites (Fuson et al., 2014).

residues (E73) repel each other. Our model suggests that loss of negative charge of any aspartate in the loops will change the electrostatic potential, making calcium recruitment and coordination less favorable. This idea was also proposed in a study of synaptotagmin C2A Domain, where electrostatic repulsion in the Ca^{2+} binding pocket was shown to be important for preventing interactions between the C2 domain and the negatively charged membrane (Striegel et al., 2012). To illustrate this, the electrostatic potential surface of wide-type apo-C2A and C2A^{D16K} was calculated and the loop regions were displayed in **Figure 3.11 E – F**. It is shown that substitution of D16K causes visually dramatic effect on the electrostatic potential of the loops, resulting in a switch from a negative to positive potential, which is a similar effect caused by calcium binding suggested by many studies (Murray and Honig, 2002; Ubach et al., 1998).

Another interesting finding when we examined the ^1H-^{15}N HSQC spectra of calcium-free C2A^{D71N} was that it revealed significant differences in the positions and number of resonances compared to the wild-type protein under identical experimental conditions. There were a few new peaks showing up as well as chemical shift changes of some peaks in the spectrum of C2A^{D71N} (**Figure 3.12 A**). Substitution of D71 to a positively charged lysine (C2A^{D71K}) gave rise to similar changes shown in **Figure 3.12 B**. The spectrum of the calcium-free C2A^{D71N} and C2A^{D71K} contained many new resonances that could mostly be attributed to residues in the loops that are missing in spectra of the wild-type protein based on our observation in **Chapter 2**. This increased number of resonances in ^1H-^{15}N HSQC spectra can be caused by decreased flexibility of the protein structure, so we hypothesized that that replacement of an acidic calcium-binding residue with a basic or
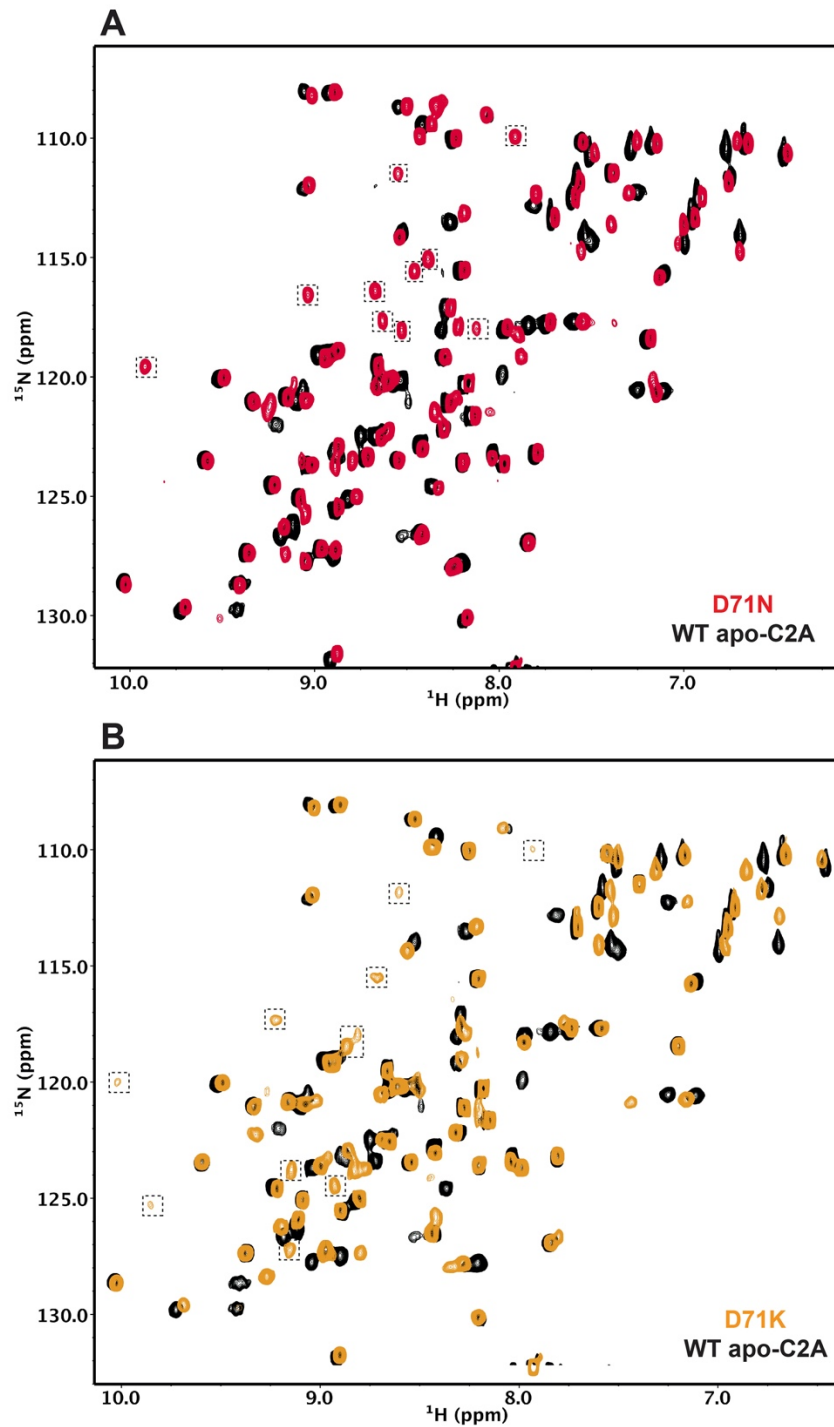
Figure 3. 12 NMR spectra of C2A^{D71N} and C2A^{D71K} compared to wild-type C2A.

Overlaid ^{1}H-^{15}N HSQC spectrum of C2A^{D71N} (red) and apo-C2A (black) **(A)**, C2A^{D71K} (orange) and apo-C2A (black) **(B)**. New peaks that appeared in the spectra of C2A^{D71N} and C2A^{D71K} are labelled in dashed boxes.

neutral residue might stabilize the loop region through neutralizing one of the calcium sites in the same manner as the calcium does. To test this, we further studied the C2A^{D71K} substituted protein as D71 coordinates a single calcium ion (Ca2) using its carboxyl group. As expected, calcium binding to the C2A^{D71K} protein was abolished based on the ITC data (**Figure 3.13 A**). Further, examination of the calcium-free C2A^{D71K} spectrum showed that many of the new signals were located very close to signals in the calcium-bound C2A spectrum. (**Figure 3.13 B**), indicating C2A^{D71K} and calcium-bound C2A may share structural similarities. To examine this possibility, we measured the thermal stability of apo- and Ca^{2+}-C2A domains and compared these to C2A^{D71K} using circular dichroism (**Figure 3.13 C**).

As expected, calcium binding to the apo-C2A domain increased the thermal melting midpoint by about 10˚C, which confirms the stabilizing effect of calcium binding. In comparison, the calcium-free C2A^{D71K} domain had a melting temperature that was very similar to Ca^{2+}-C2A. This observation is consistent with a significant stabilizing effect of the D71K substitution that is similar to calcium binding.

Next, we were curious if mutations of other aspartate residues in the loops would have the same effect as D71K. We examined the ^{1}H-^{15}N HSQC spectra and thermal stability of C2A^{D18K}, C2A^{D21K}, and C2A^{D16K}. As mentioned above, calcium binding is abolished for all these three mutants. Comparisons of the ^{1}H-^{15}N HSQC spectra to the wild-type apo-C2A showed that there were several new resonances appearing in the spectra of C2A^{D18K} and C2A^{D21K}, whereas the spectrum of C2A^{D16K} was almost identical with the wild-type
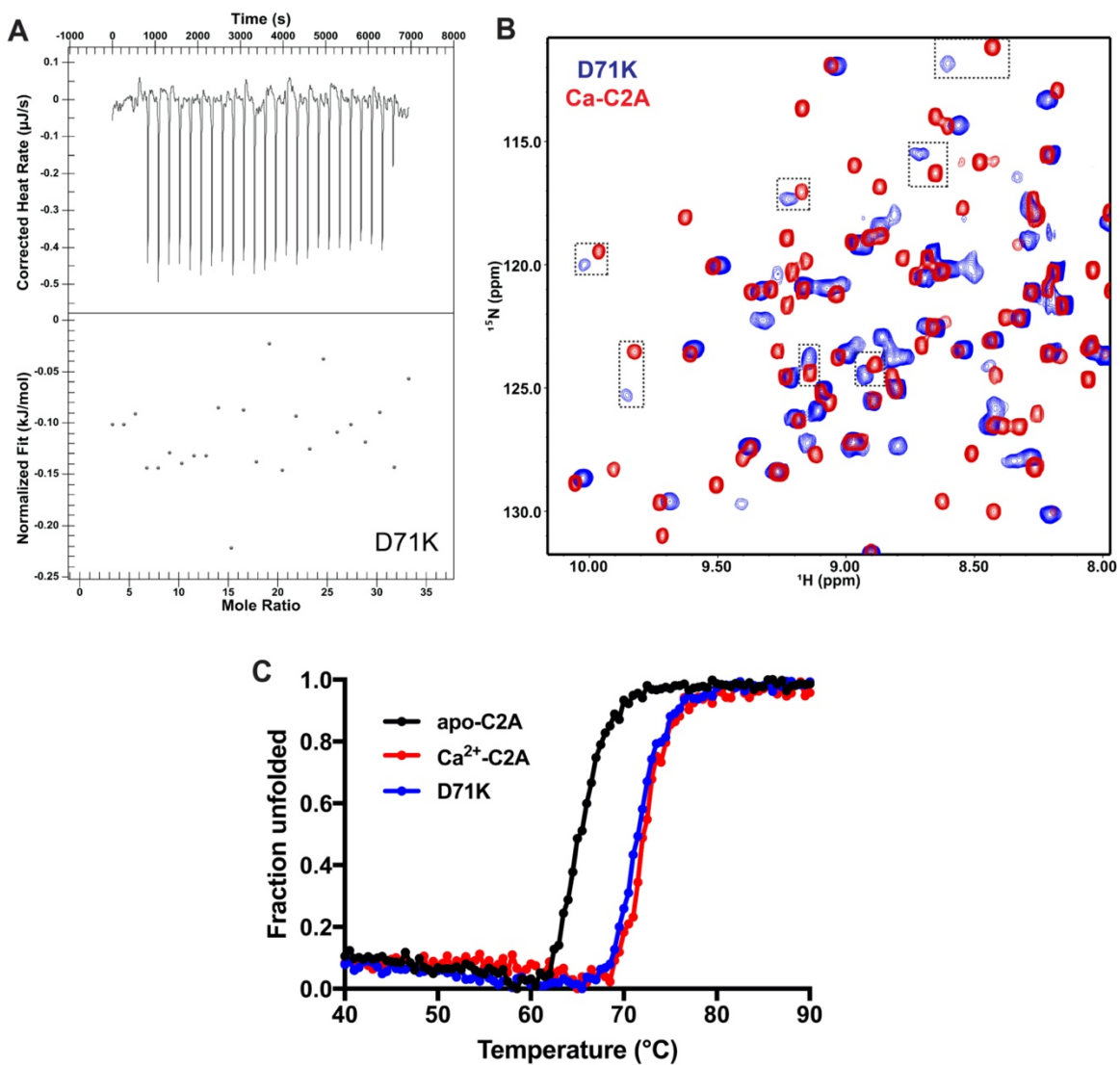
Figure 3. 13 D71K disrupts Ca^{2+} binding to dysferlin C2A.

(A) ITC analysis of Ca^{2+} binding to C2A^{D71K} mutant showed no binding. **(B)** Selected region of overlaid ^{1}H-^{15}N HSQC spectrum of C2A^{D71K} (blue) and Ca-C2A (red). Peaks of D71K and Ca-C2A in close positions are labelled in dashed boxes and residue numbers. **(C)** Thermal denaturation of C2A^{D71K} (blue), apo-C2A (black), Ca-C2A (red) monitored by circular dichroism.

(**Figure 3.14**). The thermal denaturation experiments showed that only the C2A^{D18K} increased the thermal melting midpoint by about 5˚C compared to the apo-C2A, while C2A^{D21K} and C2A^{D16K} had a melting temperature that was almost the same as apo-C2A (**Figure 3.14**). The above observations indicate that C2A^{D18K} likely has an effect of stabilizing the protein in the same manner as C2A^{D71K} does.

We attribute this observation to the ability of the K71/K18 side chain to occupy a similar position as a calcium ion observed in the crystal structure putting the ε-NH$_3^+$ group near the negatively charged side chains for calcium-binding residues. In the case of C2A^{D71K}, the ε-NH$_3^+$ group of K71 interacts closely with the side chains of D18, D21 and E73, and for C2A^{D18k}, K18 is positioned near D21, D71 and E73 (**Figure 3.15**). This proposal indicates that C2A^{D71K}/C2A^{D18k} may mimic the calcium-bound state (at least for Ca2) and have increased stability compared to the wild-type C2A domain and disruption of the flexibility in the loops disables the recruitment and coordination of calcium. Taken together, by examining the impact of substitutions of D16, D18 and D71 on the structure, calcium binding and stability of the C2A protein, we propose that the calcium binding is not solely determined by the coordinating ligands, it can also be affected by other factors including electrostatic potential and flexibility.
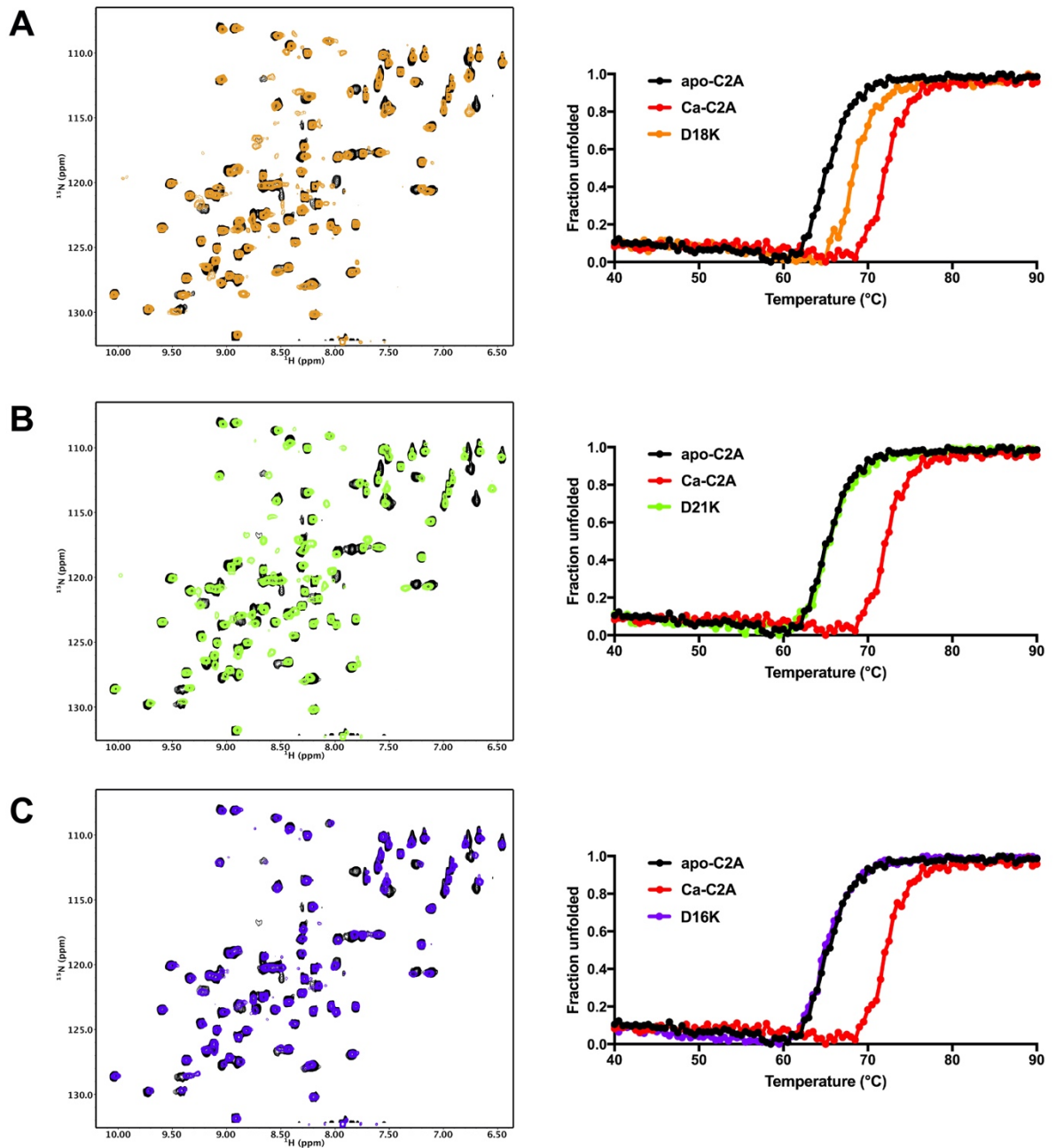
Figure 3. 14 Effects of D18K, D21K and D16K mutations on C2A.

Left panel, ^{1}H-^{15}N HSQC spectrum of C2A^{D18N} (orange) **(A)**, C2A^{D21N} (green) **(B)**, C2A^{D16N} (blue) **(C)** superimposed with apo-C2A (black). Right panel, thermal denaturation results of C2A^{D18N}, C2A^{D21N} and C2A^{D16N} compared to apo-C2A (black) and Ca-C2A (red) monitored by circular dichroism.
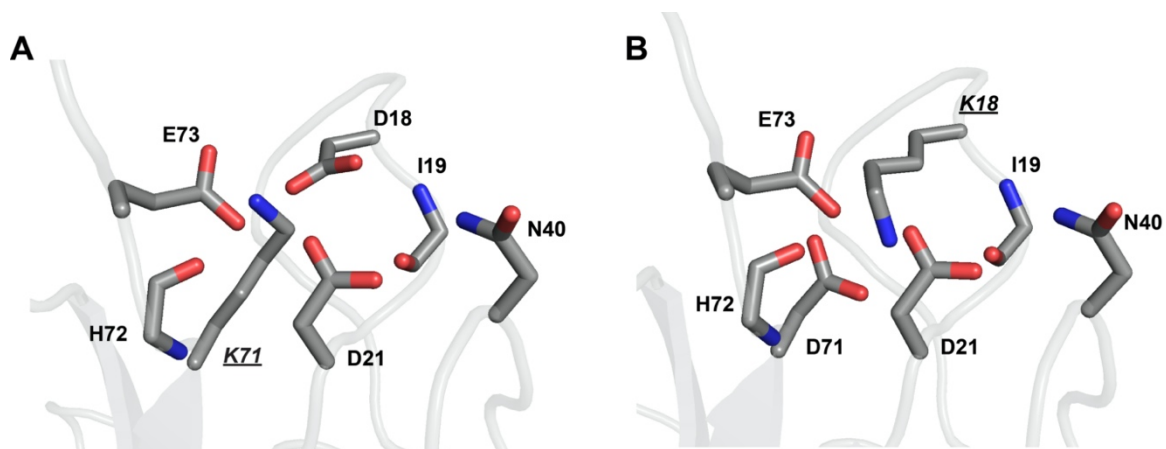
Figure 3. 15 Proposed model of the loop region for C2A^{D71k} and C2A^{D18k}.

3D model of C2A^{D71k} **(A)** and C2A^{D18k} **(B)** showing both K71 and K18 side chain occupies a similar position as a calcium ion (Ca2) putting the ε-NH3$^+$ group near the negatively charged side chains for calcium-binding residues (D18, D21 and E73 for C2A^{D71k}; D21, D71 and E73 for C2A^{D18k}.) The mutagenesis of D71 and D18 was performed in PyMOL.

3.4 Discussion

3.4.1 Calcium binding sites in dysferlin C2A

In this chapter, determination of the structure of dysferlin C2A domain in Ca^{2+}-bound state revealed the β-strands arrangement referred as type II topology that many other C2 domains comprise such as PLC δ1 C2 domain (Essen et al., 1997). More importantly, the Ca^{2+} binding sites are clearly identified from the crystal structure, which are formed primarily by aspartate side chains that serve as bidentate ligands for two Ca^{2+} ions. As previously proposed, a C2 domain has a total of four potential Ca^{2+} binding sites and the occupation of Ca^{2+} ions depends on the side chains present in loops L1-L3 (Rizo and Südhof, 1998). In dysferlin C2A domain, we identified three aspartates coordinating two Ca^{2+} ions in a cooperative manner, as well as four other residues binding via side chain or main chain. **Figure 3.16** shows a structure and sequence comparison of dysferlin C2A with two C2 domains, PLC-δ1 C2 (PDB: 1DJI) and synaptotagmin I C2B (PDB:1UOV), both of which contain two Ca^{2+} ions occupying in the same positions as that in dysferlin C2A. The structure alignment of PLC-δ1 C2 and dysferlin C2A shows the binding residues in each protein are almost identical in positions, except that dysferlin C2A provides one more aspartate (D18) in loop 1. The positions of loop L1-L3 are also very similar, resulting in the same Ca^{2+} occupation manner for the two proteins (**Figure 3.16 A**). The comparison between dysferlin C2A and synaptotagmin I C2B, on the other hand, also shows similar binding sites for the two overlapped Ca^{2+} ions. However, synaptotagmin I C2B provides ligands for an additional Ca^{2+} ion using the side chain of D365 in loop 3 and main chain of M302 in loop 1 (**Figure 3.16 B**). A close examination of the sequence alignment reveals that dysferlin C2A has a few more residues before the first conserved aspartate (D18)
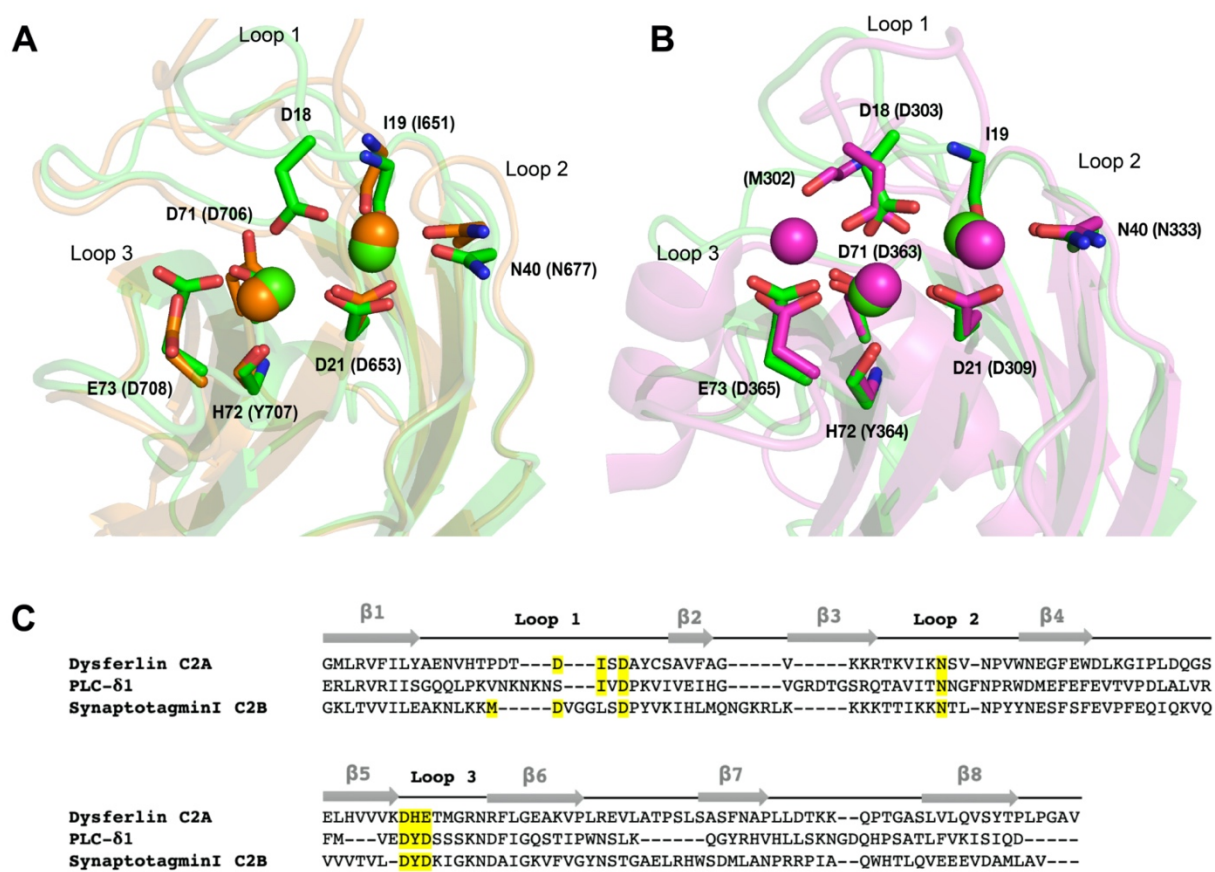
Figure 3. 16 Structure and sequence alignments of C2A with PLC-δ1 C2 and synaptotagmin I C2B.

(A) Structural alignment of Ca^{2+}-bound dysferlin C2A (green) and PLC-δ1 C2 (orange) showing the Ca^{2+} binding residues in loop region. (B) Structural alignment of Ca^{2+}-bound dysferlin C2A (green) and synaptotagmin I C2B (magenta). The spheres correspond to the bound Ca^{2+} ions found in the crystal structures. The residue numbers of dysferlin C2A are labeled near each residue and the residue numbers of PLC-δ1 C2 and synaptotagmin I C2B are in brackets. (C) Sequence alignment of dysferlin C2A versus PLC-δ1 C2 and synaptotagmin I C2B. The arrows above the sequence correspond to residues that possess β strand secondary structure, whereas the lines correspond to the loop region. The Ca^{2+} binding residues are highlight in yellow.

compared to synaptotagmin I C2B (**Figure 3.15 C**). As a result, the first half part of loop 1 in dysferlin C2A projects away from the calcium binding center, whereas that of synaptotagmin I C2B is in closer contact with other loops thus forming an additional Ca^{2+} binding site. The same difference can also be seen between synaptotagmin I C2B and PLC-$\delta1$ C2. The above observations indicate Ca^{2+} occupation in C2 domains is not only determined by the ligands present in loops, subtle difference in the position of loops can also contribute to the different binding manners.

3.4.2 Comparison of calcium binding affinity and binding mode with other C2 domains

Traditional methods such as NMR spectroscopy, ITC, and fluorescence assays are normally used to determine the intrinsic affinity of the Ca^{2+} binding sites for C2 domains. However, accurate measurement has been challenging for researchers due to the natural difficulty in obtaining K_{ds} from multiple binding-site data. For example, fitting the ITC data for synaptotagmin-7 C2B domain yielded results that are ambiguous or even contradictive with the crystal structure, and reliable K_{ds} cannot be obtained because the values are depended strongly on the position chosen for the zero baseline (Voleti et al., 2017). Measurements of binding affinity by NMR spectroscopy for synaptotagmin-7 C2A also only gave an approximate estimate of the affinities (Maximov et al., 2008). Indeed, we experienced the similar obstacle on the analysis of NMR titration data that were mainly composed of intermediate chemical exchange, in which conventional analysis methods have trouble fitting. That is why a combination of other methods were applied in our study

including ITC and line shape simulation, which gave us more reliable results compared to studies that use a single method.

Further, C2-containing proteins bind to calcium with different dissociation constants ranging from nanomolar (nM) to millimolar (mM). In this study, we find dysferlin C2A domain contains two Ca^{2+} binding sites with "middle range" affinities (K_{d1} = 32 μM, K_{d2} = 300 μM). Unlike many other C2 domains that have Ca^{2+} binding sites with quite low affinity such as the weakest site of perforin C2 Domain (K_d > 5 mM) (Yagi et al., 2015) and synaptotagmin 1 C2A (K_d > 20 mM) (Fernández-Chacón et al., 2001), dysferlin C2A domain does not seem to contain such a weak binding site based on our results. However, why these C2 domains exhibit different intrinsic Ca^{2+} affinities is not well understood.

Another interesting finding in our work is the coupled binding mode of the two Ca^{2+} binding sites where residue D18 and D21 coordinate both Ca^{2+} ions simultaneously. This sharing of ligating residues in the dysferlin C2A domain is similar to that observed in structures of rabphilin-3A C2B domain (Montaville et al., 2007), cytosolic phospholipase A2 (cPLA2) C2 domain (Perisic et al., 1998) and synaptotagmin-7 C2B domain (Voleti et al., 2017). Mutagenesis of important ligating residues revealed that binding of each calcium ion by the dysferlin C2A domain is dependent on the binding of its partner calcium ion. Similar finding has also been shown in several studies on other C2 domains. For example, a positive cooperativity binding mode was proposed for cPLA2 C2 domain that the first calcium ion binds to site I, which preorders the side chains of coordinating Asp residues, and partially or fully deprotonates them (Malmberg et al., 2004). The initial binding event

prepares the conformation and protonation state of the remaining site for calcium binding, enabling the second calcium ion to bind with higher affinity than the first as required for positive cooperativity (Malmberg et al., 2004). Also, a study on synaptotagmin 1 C2B domain showed that mutating an Asp residue that coordinates a single calcium ion results in concomitant disruption of the other binding site, suggesting calcium binding to the first site stabilizes the structure of the domain, facilitating calcium binding to the other site (Fernandez et al., 2001). This aligns with the observation of the D71 and N40 mutations in our study.

Our work has also assessed the importance of a non-coordinating residue, D16, on the calcium binding of the C2A protein, which may have been omitted by prior studies. This novel finding suggests the calcium binding of C2A is affected by multiple factors other than the ligands present in the loops. Disruption of the negative electrostatic environment and flexibility of the loops can have a significant influence on its calcium or membrane binding properties. The similar idea has also been proposed in several studies on synaptotagmin C2A domain, where electrostatic repulsion in the loops was shown to be crucial for Ca^{2+} binding and D/N substitutions that disrupt Ca^{2+} binding restored membrane fusion in a manner that the mutations partially mimicked Ca^{2+} binding by decreasing the negative charge of the pocket (Stevens and Sullivan, 2003; Striegel et al., 2012; Yoshihara et al., 2010). Indeed, this idea was further validated by our observation that $C2A^{D71K}$ shares structural similarities with wild-type Ca^{2+}-C2A judging by their NMR spectra and the model we proposed (**Figure 3.14**). It would be interesting to probe the lipid binding properties of wild-type C2A in both apo and Ca^{2+}-bound state as well as $C2A^{D71K}$, as we

predict that $C2A^{D71K}$ would be able to bind negatively charged phospholipids in a similar manner as Ca^{2+}-C2A.

3.4.3 Hypothesis of the membrane binding mechanisms

One important function of C2 domains is targeting membrane, as a result of calcium binding. A number of studies have demonstrated that C2 domains bind to the target membranes by using a combination of electrostatic and hydrophobic interactions, and they display different phospholipid selectivity. The dysferlin C2A domain has been shown to selectively bind to phosphatidylserine (PS) and phosphatidylcholine (PC) in the presence of Ca^{2+} (Therrien et al., 2009). Our work has also suggested that, the switch in electrostatic potential of the top loops from negative to positive upon calcium binding may facilitate the interaction with the phospholipids. A detailed mechanism was proposed in the structural characterization of the C2 domain of PKCα in complex with Ca^{2+} and 1,2-dicaproyl-sn-phosphatidylserine (DCPS) that the phosphoryl group of the phosphoserine completes the coordination sphere of a calcium ion (Verdaguer et al., 1999). In the crystal structure of Ca^{2+}-bound dysferlin C2A, the coordination sphere for both calcium ions are incomplete as one calcium ion (Ca1) binds to two water molecules and the second ion (Ca2) coordinates one water molecule. Thus, we hypothesize that Ca^{2+} acts as a bridge connecting the C2A protein and the phospholipids in the membrane, as the phospholipids fill the incomplete coordination sphere of the Ca^{2+} bound to the domain by replacing the water molecules with phosphoryl groups.

Recently, the X-ray crystal structure of cytosolic PLA2α (cPLA2α) C2 domain bound to 1,2-dihexanoyl-sn-glycero-3-phosphocholine (DHPC) was solved (Hirano et al., 2019). In contrast to the two bound Ca^{2+} ions reported in the lipid-free structure (Dessen et al., 1999; Perisic et al., 1998), an additional Ca^{2+} ion was observed to coordinate in the PC-bound structural complex by bridging residue N65 and the DHPC phosphoryl group. This finding provides novel insights for the possible lipid binding mode of dysferlin C2A as two Ca^{2+} ions occupy in the same positions of the two proteins using many conserved residues as their ligands. Specifically, residue N65 in cPLA2α C2 corresponds to N40 in dysferlin C2A, which may recruit an additional Ca^{2+} ion when binding to phospholipids in the similar manner. We hypothesize that there may be participation of extra Ca^{2+} ions when dysferlin C2A targets phospholipids, possibly by providing bridging interactions between the C2A domain and the phosphate group, which also interacts directly with N40 or other residues in the loop region.

3.5 References

Abdullah, N., Padmanarayana, M., Marty, N.J., and Johnson, C.P. (2014). Quantitation of the Calcium and Membrane Binding Properties of the C2 Domains of Dysferlin. Biophys. J. *106*, 382–389.

Bansal, D., Miyake, K., Vogel, S.S., Groh, S., Chen, C.-C., Williamson, R., McNeil, P.L., and Campbell, K.P. (2003). Defective membrane repair in dysferlin-deficient muscular dystrophy. Nature *423*, 168–172.

Cantor, C.R., and Schimmel, P.R. (1980). Biophysical chemistry: Part III: the behavior of biological macromolecules (Macmillan).

Cates, M.S., Teodoro, M.L., and Phillips, G.N. (2002). Molecular mechanisms of calcium and magnesium binding to parvalbumin. Biophys. J. *82*, 1133–1146.

Corbalan-Garcia, S., and Gómez-Fernández, J.C. (2014). Signaling through C2 domains: More than one lipid target. Biochim. Biophys. Acta BBA - Biomembr. *1838*, 1536–1547.

Davenport, N.R., Sonnemann, K.J., Eliceiri, K.W., and Bement, W.M. (2016). Membrane dynamics during cellular wound repair. Mol. Biol. Cell *27*, 2272–2285.

Delaglio, F., Grzesiek, S., Vuister, G.W., Zhu, G., Pfeifer, J., and Bax, A. (1995). NMRPipe: A multidimensional spectral processing system based on UNIX pipes. J. Biomol. NMR *6*, 277–293.

Dessen, A., Tang, J., Schmidt, H., Stahl, M., Clark, J.D., Seehra, J., and Somers, W.S. (1999). Crystal Structure of Human Cytosolic Phospholipase A2 Reveals a Novel Topology and Catalytic Mechanism. Cell *97*, 349–360.

Dudev, T., Chang, L.-Y., and Lim, C. (2005). Factors Governing the Substitution of La^{3+} for Ca^{2+} and Mg^{2+} in Metalloproteins: A DFT/CDM Study. J. Am. Chem. Soc. *127*, 4091–4103.

Essen, L.-O., Perisic, O., Lynch, D.E., Katan, M., and Williams, R.L. (1997). A Ternary Metal Binding Site in the C2 Domain of Phosphoinositide-Specific Phospholipase C-δ1,. Biochemistry *36*, 2753–2762.

Fernandez, I., Araç, D., Ubach, J., Gerber, S.H., Shin, O., Gao, Y., Anderson, R.G.W., Südhof, T.C., and Rizo, J. (2001). Three-Dimensional Structure of the Synaptotagmin 1 C2B-Domain: Synaptotagmin 1 as a Phospholipid Binding Machine. Neuron *32*, 1057–1069.

Fernández-Chacón, R., Königstorfer, A., Gerber, S.H., García, J., Matos, M.F., Stevens, C.F., Brose, N., Rizo, J., Rosenmund, C., and Südhof, T.C. (2001). Synaptotagmin I functions as a calcium regulator of release probability. Nature *410*, 41–49.

Fuson, K., Rice, A., Mahling, R., Snow, A., Nayak, K., Shanbhogue, P., Meyer, A.G., Redpath, G.M.I., Hinderliter, A., Cooper, S.T., et al. (2014). Alternate Splicing of Dysferlin C2A Confers Ca^{2+}-Dependent and Ca^{2+}-Independent Binding for Membrane Repair. Structure *22*, 104–115.

Han, R., and Campbell, K.P. (2007). Dysferlin and muscle membrane repair. Curr. Opin. Cell Biol. *19*, 409–416.

Harsini, F.M., Bui, A.A., Rice, A.M., Chebrolu, S., Fuson, K.L., Turtoi, A., Bradberry, M., Chapman, E.R., and Sutton, R.B. (2019). Structural Basis for the Distinct Membrane Binding Activity of the Homologous C2A Domains of Myoferlin and Dysferlin. J. Mol. Biol. *431*, 2112–2126.

Hirano, Y., Gao, Y.-G., Stephenson, D.J., Vu, N.T., Malinina, L., Simanshu, D.K., Chalfant, C.E., Patel, D.J., and Brown, R.E. (2019). Structural basis of phosphatidylcholine recognition by the C2–domain of cytosolic phospholipase A2α. In ELife, p.

Jelesarov, I., and Bosshard, H.R. (1999). Isothermal titration calorimetry and differential scanning calorimetry as complementary tools to investigate the energetics of biomolecular recognition. J. Mol. Recognit. *12*, 3–18.

Johnson, B.A., and Blevins, R.A. (1994). NMR View: A computer program for the visualization and analysis of NMR data. J. Biomol. NMR *4*, 603–614.

Malmberg, N.J., Varma, S., Jakobsson, E., and Falke, J.J. (2004). Ca^{2+} Activation of the cPLA $_2$ C2 Domain: Ordered Binding of Two Ca^{2+} Ions with Positive Cooperativity [†]. Biochemistry *43*, 16320–16328.

Maximov, A., Lao, Y., Li, H., Chen, X., Rizo, J., Sorensen, J.B., and Sudhof, T.C. (2008). Genetic analysis of synaptotagmin-7 function in synaptic vesicle exocytosis. Proc. Natl. Acad. Sci. *105*, 3986–3991.

Montaville, P., Schlicker, C., Leonov, A., Zweckstetter, M., Sheldrick, G.M., and Becker, S. (2007). The C2A-C2B Linker Defines the High Affinity Ca^{2+} Binding Mode of Rabphilin-3A. J. Biol. Chem. *282*, 5015–5025.

Murray, D., and Honig, B. (2002). Electrostatic Control of the Membrane Targeting of C2 Domains. Mol. Cell *9*, 145–154.

Perisic, O., Fong, S., Lynch, D.E., Bycroft, M., and Williams, R.L. (1998). Crystal structure of a calcium-phospholipid binding domain from cytosolic phospholipase A2. J. Biol. Chem. *273*, 1596–1604.

Rizo, J., and Südhof, T.C. (1998). C $_2$ -domains, Structure and Function of a Universal Ca^{2+} -binding Domain. J. Biol. Chem. *273*, 15879–15882.

Stevens, C.F., and Sullivan, J.M. (2003). The Synaptotagmin C2A Domain Is Part of the Calcium Sensor Controlling Fast Synaptic Transmission. Neuron *39*, 299–308.

Striegel, A.R., Biela, L.M., Evans, C.S., Wang, Z., Delehoy, J.B., Sutton, R.B., Chapman, E.R., and Reist, N.E. (2012). Calcium Binding by Synaptotagmin's C2A Domain is an Essential Element of the Electrostatic Switch That Triggers Synchronous Synaptic Transmission. J. Neurosci. *32*, 1253–1260.

Therrien, C., Di Fulvio, S., Pickles, S., and Sinnreich, M. (2009). Characterization of Lipid Binding Specificities of Dysferlin C2 Domains Reveals Novel Interactions with Phosphoinositides [†]. Biochemistry *48*, 2377–2384.

Ubach, J., Zhang, X., Shao, X., Südhof, T.C., and Rizo, J. (1998). Ca^{2+} binding to synaptotagmin: how many Ca^{2+} ions bind to the tip of a C2-domain? EMBO J. *17*, 3921–3930.

Verdaguer, N., Corbalan-Garcia, S., Ochoa, W.F., Fita, I., and Gómez-Fernández, J.C. (1999). Ca^{2+} bridges the C2 membrane-binding domain of protein kinase Cα directly to phosphatidylserine. EMBO J. *18*, 6329–6338.

Voleti, R., Tomchick, D.R., Südhof, T.C., and Rizo, J. (2017). Exceptionally tight membrane-binding may explain the key role of the synaptotagmin-7 C_2A domain in asynchronous neurotransmitter release. Proc. Natl. Acad. Sci. *114*, E8518–E8527.

Wang, W., and Malcolm, B.A. (1999). Two-Stage PCR Protocol Allowing Introduction of Multiple Mutations, Deletions and Insertions Using QuikChangeTM Site-Directed Mutagenesis. BioTechniques *26*, 680–682.

Yagi, H., Conroy, P.J., Leung, E.W.W., Law, R.H.P., Trapani, J.A., Voskoboinik, I., Whisstock, J.C., and Norton, R.S. (2015). Structural Basis for Ca^{2+}-mediated Interaction of the Perforin C2 Domain with Lipid Membranes. J. Biol. Chem. *290*, 25213–25226.

Yoshihara, M., Guan, Z., and Littleton, J.T. (2010). Differential regulation of synchronous versus asynchronous neurotransmitter release by the C2 domains of synaptotagmin 1. Proc. Natl. Acad. Sci. *107*, 14869–14874.

Chapter 4

Impacts of Muscular Dystrophy Causing Mutations on Dysferlin C2 Domains

4.1 Introduction

Muscular dystrophy is a degenerative genetic disorder that results in increasing weakness and gradual wasting of skeletal muscles. This muscle wasting occurs because the skeletal muscle cells have weakened plasma or sarcolemma membranes. Muscular dystrophy encompasses a large number of disorders that can be divided into two classes: those caused by defective membrane structure, and those resulting from impaired membrane repair (Rahimov and Kunkel, 2013). Here, emphasis will be placed on the proteins involved in membrane repair deficient muscular dystrophies. Mutations in the dysferlin gene are linked to two clinically distinct muscle diseases, limb-girdle muscular dystrophy type 2B (LGMD2B) and Miyoshi myopathy (MM), but the mechanism that leads to muscle degeneration is unknown (Bashir et al., 1998; Liu et al., 1998). The C2A domain is the major portion of the dysferlin protein responsible for responding to calcium ion influx upon membrane damage and the activation of dysferlin (Matsuda et al., 2012; Therrien et al., 2009). The importance of the C2A domain in dysferlin has been emphasized from a clinical standpoint as substitutions in this region of the protein cause illness.

One mutation, resulting in the substitution of valine for aspartic acid at residue number 67 (V67D) in the C2A domain, has been correlated with two forms of muscular dystrophy (Illarioshkin et al., 2000). The first type, limb-girdle muscular dystrophy type 2B (LGMD2B), affects proximal skeletal muscles, while the second type, Miyoshi myopathy (MM), affects distal skeletal muscles. The dysferlin V67D substitution impedes the membrane repair process because it diminishes calcium-dependent phospholipid binding (Davis et al., 2002). Furthermore, wild-type dysferlin usually binds to and stabilizes AHNAK, a large protein also implicated in membrane repair, but the V67D mutation prevents this interaction (Huang et al., 2007). Another substitution on the C2A domain, W52R, leads to Miyoshi myopathy (MM) (De Luna et al., 2007) and also inhibits the association with MG53 (Matsuda et al., 2012). Furthermore, pathogenic mutations have been identified throughout the dysferlin gene including all the other C2 domains (Krahn et al., 2009). For example, seven mutations (G234E, R253W, L266P, I284T, G299R, S340R, L344P) have been characterized on the C2B domain leading to muscular dystrophy diseases. Therefore, an understanding of the effects of these substitutions on the structure of the C2 domain may provide insight into how and why these mutations disrupt the protein activities and ultimately inhibit membrane repair. In this chapter the impacts of several pathogenic substitution on the structure, stability and calcium binding ability of the C2A domain were investigated. The work provides important evidence that explains the mechanisms of some inherited muscular dystrophy diseases.

4.2 Materials and Methods

4.2.1 Site-directed mutagenesis of the dysferlin C2A domain

QuikChange site-directed mutagenesis (Wang and Malcolm, 1999) was performed to introduce the following mutations on the dysferlin C2A plasmid: $C2A^{W52R}$, $C2A^{W52A}$, $C2A^{W52M}$, $C2A^{W52T}$, $C2A^{K36W}$ and $C2A^{K36A}$. The primers used for making the mutations are shown in **Table 4.1**. The mutagenesis was performed using the same protocol describe in **Chapter 3.2.1**. The mutagenesis of $C2A^{V67D}$, $C2A^{V67A}$, $C2A^{V67T}$, and $C2A^{V67N}$ was made by previous students.

4.2.2 Test expression of the pathogenic mutants of C2A

Small-scale test expression experiments were performed for the following C2A mutants: $C2A^{V67D}$, $C2A^{V67A}$, $C2A^{V67T}$, $C2A^{V67N}$, $C2A^{W52R}$, $C2A^{W52A}$, $C2A^{W52M}$, $C2A^{W52T}$ $C2A^{K36W}$ and $C2A^{K36A}$. Plasmids containing the mutant DNA were transformed BL21-CodonPlus (DE3) E. coli strain. Isolated colonies were picked and grown in 5 mL LB overnight as starters. The following day 250 μL starters were inoculated into 25 ml LB with 30 μg/mL kanamycin and 30 μg/mL chloramphenicol. The cultures were grown at 37 ℃ until an OD600 of 0.6 was reached at which point cells were cooled to 16 °C and induced with 0.5 mM IPTG for 16 hours. Cells were harvested by centrifugation at 4,000 rpm for 20 min and resuspended in lysis buffer (25mM Tris, 300 mM NaCl, pH 7.5). Cells were lysed by EmulsiFlex-C5 homogenizer (Avestin). Gel sample was taken at this point as total protein (i.e. 30 μL + 15 μL 3 × SDS loading buffer). Then 1 mL cell lysate was centrifuged for 10 - 15 minutes at 14,000 rpm in tabletop centrifuge. The supernatant was taken as gel sample (soluble fraction). Cell pellet was resuspended in 1 ml of 2% SDS with vortexing and taken

Table 4. 1 Primers used for dysferlin C2A mutagenesis.

Construct	Primer Sequence
K36W	Forward: 5'- GTGAAGAAGAGAACCTGGGTCATCAAGAAC -3' Reverse: 5'- GTTCTTGATGACCCAGGTTCTCTTCTTCAC -3'
K36A	Forward: 5'- GTGAAGAAGAGAACCGCAGTCATCAAGAAC -3' Reverse: 5'- GTTCTTGATGACTGCGGTTCTCTTCTTCAC -3'
W52R	Forward: 5'- GGATTTGAACGTGACCTCAAGG -3' Reverse: 5'- CCTTGAGGTCACGTTCAAATCC -3'
W52A	Forward: 5'- GAGGGATTTGAAGCGGACCTCAAGGGC -3' Reverse: 5'- GCCCTTGAGGTCCGCTTCAAATCCCTC -3'
W52M	Forward: 5'- GAGGGATTTGAAATGGACCTCAAGGGC -3' Reverse: 5'- GCCCTTGAGGTCCATTTCAAATCCCTC -3'
W52T	Forward: 5'- GAGGGATTTGAAACCGACCTCAAGGGC -3' Reverse: 5'- GCCCTTGAGGTCGGTTTCAAATCCCTC -3'

as gel sample (insoluble fraction). The total protein, soluble and insoluble fractions were checked by SDS-PAGE. All the mutant proteins were expressed and purified using the same protocol described in **Chapter 2.2.1**.

4.2.3 Circular dichroism

Folding of all proteins were monitored by circular dichroism spectropolarimetry using a Jasco J-810 instrument (Biomolecular Interactions and Conformations Facility, University of Western Ontario). All proteins were extensively dialyzed in the CD buffer for at least one day with stirring. For proteins in the calcium-free state, samples comprised 20 μM protein were prepared in 20 mM KH_2PO_4 (pH 7.5) in the presence of 1mM EDTA. For Ca^{2+}-bound samples, buffer containing 10 mM MOPS (pH 7.5) and 20 mM $CaCl_2$ was used to avoid precipitation of calcium phosphate. For each sample, 15 scans from 250 –200 nm (80 nm/min with increment of 1 nm) were recorded using a 1 mm path-length cell at 20 °C, averaged and the buffer background was subtracted.

Thermal denaturation studies were performed by exposing the protein to different temperatures within the range of 5 – 95 °C (1 °C/min with increments of 0.5°C) by monitoring changes in the ellipticity at 215 nm. A 1 mM path length cuvette was used. The ellipticity was normalized between 0 - 1 using the function:

$$Y' = (Y-Y_{max})/(Y_{max}-Y_{min}) \qquad \textbf{(Equation 1)}$$

where Y is the observed CD signal at 215 nm, Y_{max} is the signal for the folded protein and Y_{min} is the signal for the unfolded protein. A two-state unfolding curve was used to fit the data as a function of temperature and fitting for the melting point transition (T_m) and the enthalpy (ΔH_m) according to **Equation 2**. During the fitting process a heat capacity (ΔC_p) of 0 kJ/(mol K) was used.

$$\Delta G = \Delta H_m \left(1 - \frac{T}{T_m}\right) + \Delta C_p(T - T_m) - Tln\left(\frac{T}{T_m}\right) \quad \textbf{(Equation 2)}$$

The differences in stability ($\Delta\Delta G$) between substituted dysferlin proteins and the wild-type protein were calculated using $\Delta H_m(wt)$, $T_m(wt)$, and the differences in melting temperatures (ΔT_m) between the wild type and the appropriate substituted proteins according to **Equation 3**:

$$\Delta\Delta G = \Delta T_m \left(\frac{\Delta H_m(wt)}{T_m(wt)}\right) \quad \textbf{(Equation 3)}$$

4.2.4 Isothermal titration calorimetry

All calorimetry experiments were performed using a NanoITC (TA Instruments) at 25°C. All experiments were completed 2–3 times using freshly prepared proteins extensively dialyzed in 25 mM HEPES, 150 mM NaCl, 250 μM TECP, pH 7.5 and pretreated with Chelex-100 (Bio-Rad) to remove residual Ca^{2+} ions for one hour. The optimal concentrations of protein in the experiments were determined to be: 5 mM Ca^{2+} titrated into 85 μM C2A^{V67A}, 3 mM Ca^{2+} titrated into 52 μM C2A^{W52M}, 3 mM Ca^{2+} titrated into 77 μM C2A^{K36W} . Proteins and Ca^{2+} solutions were degassed under vacuum prior to each titration.

Titrations consisted of 25 injections of 2 µL Ca^{2+} solution into a 146 µL cell containing the proteins with constant stirring. Heats of dilution were measured in a separate experiment in which Ca^{2+} solution was injected into the buffer alone. The titration data were analysed using sequential-two-binding-site model in NanoAnalyze v3.1.2 (TA instruments) to determine best fit values for K_A, ΔH and N. ΔS was calculated according to **Equation 4**.

$$\Delta G = -RT\ln K_A = \Delta H - T\Delta S$$

$$\Delta S = R\ln K_A + (\Delta H/T) \qquad \qquad (\textbf{Equation 4})$$

4.2.5 NMR spectroscopy

All NMR experiments were collected at 25˚C on a Varian Inova 600 MHz NMR spectrometer equipped with a triple resonance cryogenic probe and z-field gradients. All data were processed using NMRPipe (Delaglio et al., 1995) and analyzed using NMRViewJ (Johnson and Blevins, 1994). The ^1H, ^{15}N-HSQC NMR experiments were conducted in 25 mM HEPES, 150 mM NaCl, 250 µM TECP, pH 7.5 with 10% D_2O, 200 µM DSS as an internal reference, and 200 µM imidazole as an internal pH indicator. A sample of 200 µM uniformly ^{15}N-labeled $C2A^{V67A}$ protein was incubated with Chelex-100 (Bio-Rad) for one hour to remove residual Ca^{2+} ions before acquiring the ^1H-^{15}N HSQC spectra by the NMR spectrometer. Subsequently, 2 µL $CaCl_2$ solution was added to the sample to make a final $[Ca^{2+}]$ of 20 mM and $^1H^{15}N$-HSQC spectrum was recorded again using the same method. The stock solution of $CaCl_2$ was analyzed by Inductively Coupled Plasma - Mass Spectrometry (ICP-MS) to obtain the precise concentration (Biotron, Western University).

4.3 Results

4.3.1 Mapping pathogenic mutations in the C2A domain

The point substitutions $C2A^{V67D}$ and $C2A^{W52R}$ in the dysferlin C2A domain are associated with the development of Limb Girdle muscular dystrophy 2B (LGMD2B) and Miyoshi myopathy (MM) (Krahn et al., 2009). In the structure of the C2A domain V67 lies on sheet β5 tucked between two alanine residues (A26, A84) on β2 and β6 and across from a series of hydrophobic residues on β1 (V4, I6) and β8 (L117, L119). The W52 residue is located on sheet β4, the side chain of which is buried inside the β sheet sandwich, projecting towards β2 and β3 (**Figure 4.1**). Sequence comparison of other C2A domain proteins show that despite the fact that V67 and W52 are not well-conserved residues there is a strong preference for hydrophobic amino acids at these two positions.

Since the seven C2 domains of dysferlin are expected to share similar β -sandwich structures, pathogenic substitutions on other C2 domains can be theoretically mapped to the C2A domain through structural and sequence alignments. For example, the C2B domain carries a more extensive distribution of substitutions, with seven substitutions (G234E, R253W, L266P, I284T, G299R, S340R, L344P) identified and located on five different β sheets and two loops. By substituting the corresponding residues in the C2A domain, it will be possible to characterize how those substitutions might affect the conformation and activity of the other C2 domains. This will help understand how pathogenic mechanisms of substitutions that cause dysferlinopathy. Since the $C2A^{V67D}$ and $C2A^{W52R}$ substitutions in the C2A domain are both located in the β sheets, we also

134

A

	β1	Loop 1	β2	β3

Dysferlin-C2A GSPEFMLRVFILYAENVHTPDTDIS-DAYCSAVFAGVKKR
Dysferlin-C2B KPQDFQIRVQV----IEGRQLPGVNIKPVVKVTAAGQTKR

Loop 2	β4		β5

Dysferlin-C2A TKVIKNSVNPVWNEGFEWDLKGIPLDQ-GSELHVVVK
Dysferlin-C2B TRIHKG-NSPLFNETLFFNLFDSPGELFDEPIFITVV

Loop 3	β6	β7

Dysferlin-C2A DHETMGRNRFLGEAKVPLREVLATPSLS-ASFNAP
Dysferlin-C2B DSRSLRTDALLGEFRMDVGTIYREPRHAYLRKWLL

	β8

Dysferlin-C2A LLDTKKQPTGASLVLQVSYTAAAS--
Dysferlin-C2B LSDPDDFSAGARGYLKTSLCVLGPGD

Figure 4. 1 Pathogenic mutations in dysferlin C2A and C2B domain.

(A) Sequence alignment of dysferlin C2A and C2B domain. The arrows above the sequence correspond to residues that possess β strand secondary structure, whereas the lines corresponds to the loop region. Pathogenic mutated residue V67 and W52 in C2A and R253 in C2B are highlighted in red and the corresponding conserved residue in the other C2 are highlighted in yellow. **(B)** Cartoon of the crystal structure of Ca^{2+}-bound C2A showing the location of mutated residue V67, W52 and K36. Residue V67 and W52 both lie on β sheet and K36 is on one of the loops. The binding Ca^{2+} ions are shown by orange spheres.

attempted to investigate a pathogenic substitution in the loop region. Based on the sequence alignment of the C2A and C2B domains, we found the substitution at R253 in C2B could be mapped to K36 in C2A as the two basic residues in loop 2 are highly conserved between two hydrophobic residues (**Figure 4.1 A**). Making a substitution at K36 in C2A will mimic the effect of R253W in C2B, hence we will be able to assess the impact of this substitution on the structure and function of the C2 domain.

4.3.2 Impact of pathogenic mutations on the expression and solubility

The mutations of C2A^{V67D}, C2A^{W52R} and C2A^{K36W} were initially generated to assess the impact of substitutions on protein folding and stability. In the test expression experiments, *E. coli* cells containing C2A^{V67D}, C2A^{W52R} and C2A^{K36W} plasmids were grown and induced in the same conditions used for the wild type C2A. However, unlike wild type C2A domain that was found mostly in the soluble fraction on the gel, C2A^{V67D} and C2A^{W52R} were almost completely located in inclusion bodies, and a majority of C2A^{K36W} protein was in the precipitate as well (**Figure 4.2**). Repeated attempts to refold the proteins were unsuccessful indicating that these substitutions in the dysferlin C2A domain cause instability or misfolding in the domain leading to aggregation. Examining the position of each residue in the structure of C2A has helped us understand how the aggregation happened. The central location of V67 puts it in a hydrophobic environment at the core of the protein. The region surrounding the V67 residue is composed entirely of hydrophobic residues. On the same β-sheet, the highly conserved residues, L65 and V69, are also pointed inward enhancing the hydrophobic environment at the core of the protein. Additionally, two residues on adjacent β-sheets, A26 and A85 are in close distance with V67 (**Figure 4.3 A**).
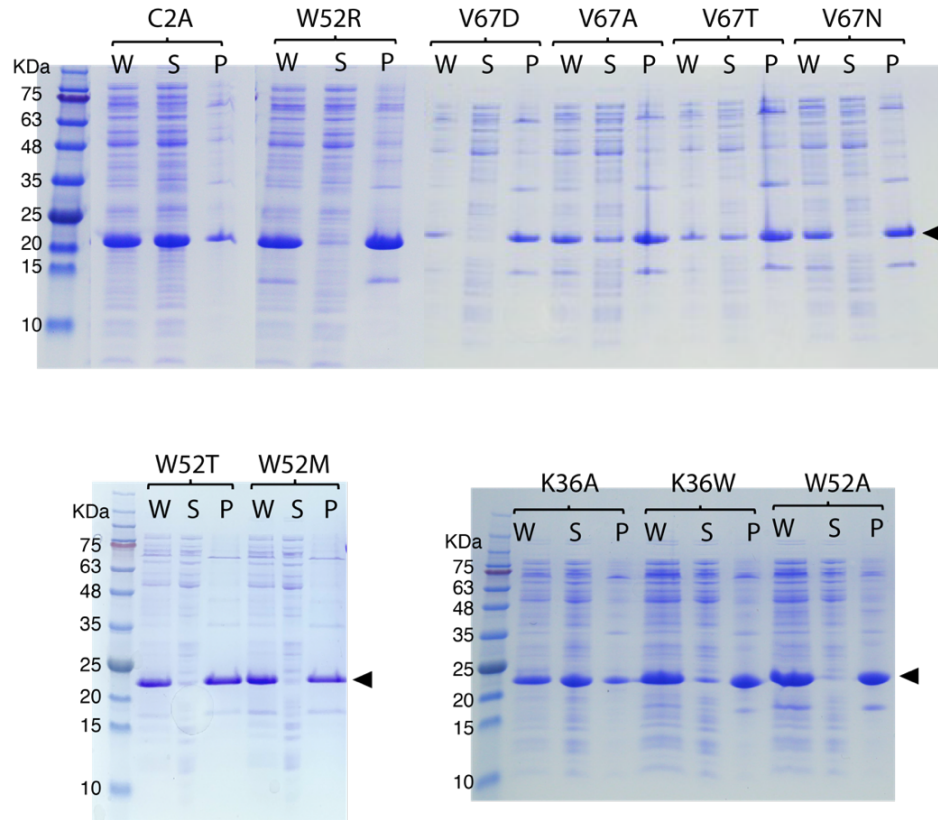
Figure 4. 2 Test expression of C2A mutants.

Wild-type C2A, C2A^{V67D}, C2A^{V67A}, C2A^{V67T}, C2A^{V67N}, C2A^{W52R}, C2A^{W52A}, C2A^{W52M}, C2A^{W52T} C2A^{K36W} and C2A^{K36A} were expressed in *E. coli* cells and the total protein (W), supernatant (S) and pellet (P) were checked by SDS-PAGE gel.
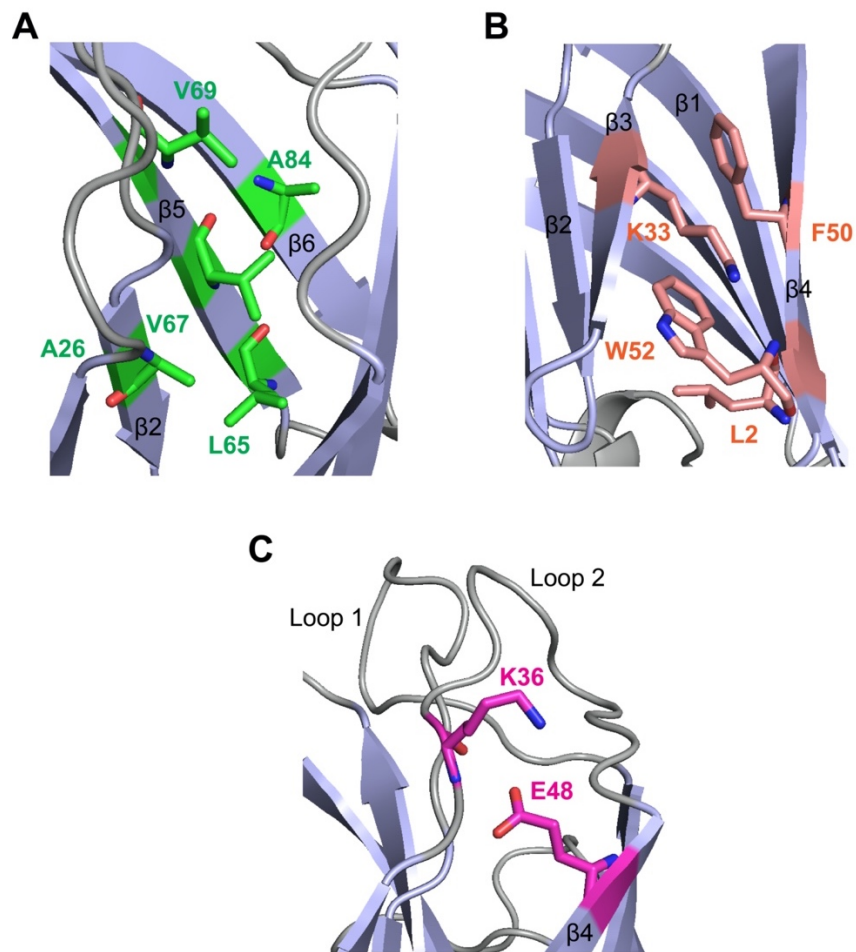
Figure 4. 3 Close-up views of the location of residue V67, W52 and K36 in the C2A structure.

Residue V67 (**A**), W52 (**B**), and K36 (**C**) as well as their neighbouring residues are shown in sticks and labeled by residue numbers in the cartoon structure of Ca^{2+}-bound C2A.

Once again the neighbouring residues are all hydrophobic, which suggests that hydrophobic interactions may play a role in the structure's stability in this region and that maintenance of hydrophobicity at residue number 67 could be crucial for protein stability. The introduction of a charged acidic residue in this position is a energetically costly event and likely disrupts the hydrophobic interactions forming the core of the protein. A similar structural environment can be seen for W52, as it directs inward at the core of the β-sheet sandwich likewise, together with two neighbouring hydrophobic residues, F50 on the same β-sheet and L2 on adjacent β-sheet. Further, a basic residue K33 on the opposite side is also within close distance, pointing inward between the side chains of W52 and F50 (**Figure 4.3 B**). Substitution of W52 to an arginine would likely trigger a charge-charge repelling effect with K33, resulting in the disruption of the protein conformation. For K36, which is located at one end of loop 2, we found it points towards β4, bonding with E48 on β4 via electrostatic interaction (**Figure 4.3 C**). This interaction may be important for bringing the two sides of the protein together, thus substitution to a hydrophobic residue causes a destabilization effect.

In an attempt to better characterize the mechanism of this instability we incorporated several other substitutions at V67, W52 and K36. For V67, we introduced two less hydrophobic substitutions ($C2A^{V67A}$, $C2A^{V67T}$) and a less acidic one ($C2A^{V67N}$). In the test expression, $C2A^{V67N}$ was found completely in inclusion bodies. Although a large amount of $C2A^{V67A}$ and $C2A^{V67T}$ were still located in the insoluble fraction, some protein was found in the soluble fractions. For W52, two less hydrophobic substitutions ($C2A^{W52A}$, $C2A^{W52M}$), and a polar one with a methyl group ($C2A^{W52T}$) were generated. However, all of them

showed serious aggregation on the test expression gel so we chose C2A^{W52M} as the subject for the following studies. For K36, we incorporated a less hydrophobic substitution (C2A^{K36A}) and C2A^{K36A} showed increased level of solubility than C2A^{K36W} (**Figure 4.2**). In general, the levels of protein expression and solubility for all these proteins were much lower compared to wild type dysferlin C2A. However, sufficient amounts of C2A^{V67A}, C2A^{V67T}, C2A^{W52M} and C2A^{K36A} proteins were obtained to compare their stabilities to the wild-type protein.

4.3.3 Protein purification

Using the same protocol described in **Chapter 2.2.**1, the C2A^{V67A}, C2A^{V67T}, C2A^{W52M}, C2A^{K36W} and C2A^{K36A} mutant proteins were purified using nickel-charged HisTrap FF column followed by gel filtration chromatography. Coomassie-stained SDS-PAGE gels of the fractions for each protein are presented in **Figure 4.4** and show the expected band of molecular weight around 14 kDa for the C2A^{V67A}, C2A^{V67T}, C2A^{K36W} and C2A^{K36A} proteins following His$_6$-tagged cleavage by TEV protease. For the C2A^{W52M} protein, in particular, the His$_6$-tagged was kept due to the serious precipitation of the protein. The SDS-PAGE gel of C2A^{W52M} shows bands of around 19 kDa, corresponding to the calculated molecular weight of the His$_6$-C2A^{W52M} protein. ^{15}N-labelled C2A^{V67A} used for NMR studies was purified using the same method. For each experiment, the proteins were freshly made.
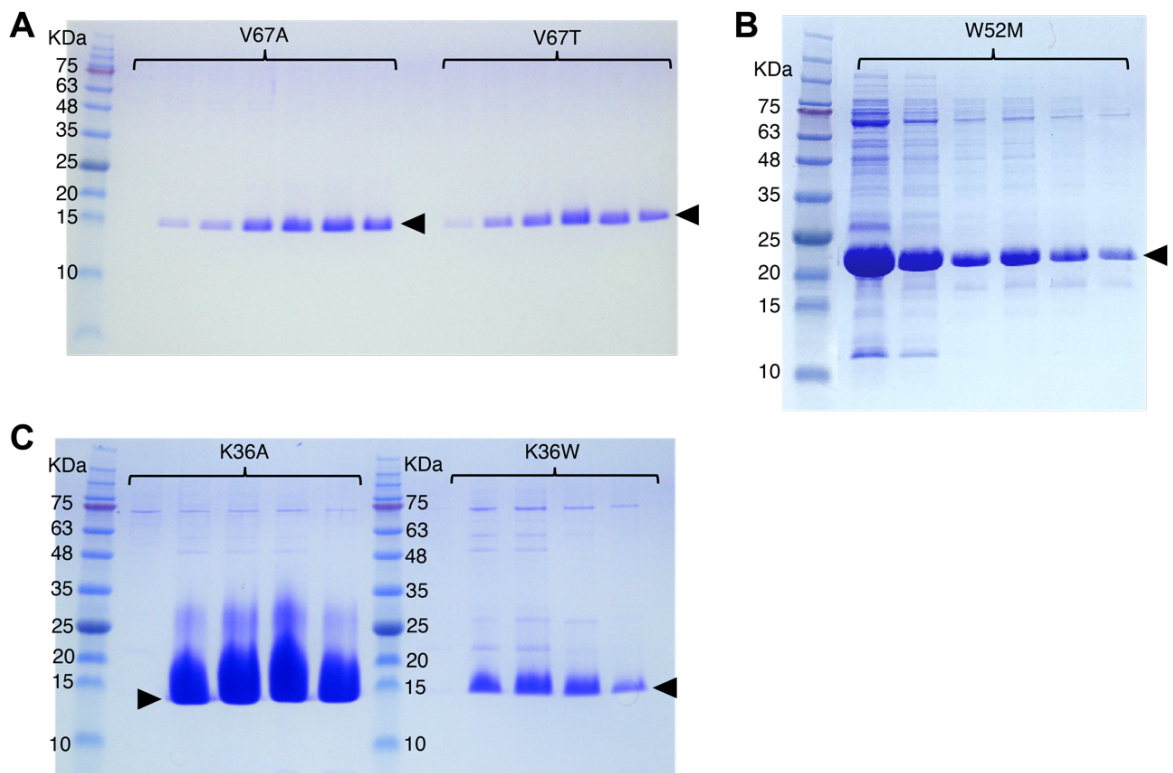
Figure 4. 4 Purification of the C2A^{V67A}, C2A^{V67T}, C2A^{W52M} , C2A^{K36A} and C2A^{K36W} mutant proteins.

Purification of C2A mutants by HisTrap FF chromatography monitored by SDS-PAGE stained with Coomassie blue. Cleaved C2A^{V67A} and C2A^{V67T} (**A**), C2A^{K36A} and C2A^{K36W} (**C**) and His$_6$-tagged C2A^{W52M} (**B**) are indicated by black arrows.

4.3.4 Pathogenic substitutions cause loss of stability for the C2A domain

The secondary structure and thermal stability of each substituted protein was studied by circular dichroism (CD) as a comparison to the wild-type C2A. First, the secondary structure for each protein was examined without attempts to control the levels of calcium. That being said, the proteins used were obtained directly from the purification of *E.coli* cells with no manipulation of Ca^{2+} ions. As mentioned in **Chapter 2.3.4,** the CD spectrum of the dysferlin C2A domain at 25 ˚C had a negative band near 215 nm consistent with the well-defined antiparallel β-sheet structure of the protein. As presented in **Figure 4.5 A, 4.6 A**, and **4.7 A**, the CD spectra of C2A^{V67A}, C2A^{V67T} C2A^{W52M}, C2A^{K36W}, and C2A^{K36A} all showed a similar profile, indicating that most of the β-sheet structure is preserved with these substitutions. However, the spectra of the substituted proteins (especially C2A^{W52M}) were fairly noisy between 200 – 210 nm due to the high tension voltage beyond 600 V. This might be a consequence of the protein aggregation at 25 ˚C although very low concentration (20 μM) was used.

Thermal denaturation experiments measured by CD spectropolarimetry examined changes in molar ellipticity at 215 nm as a function of temperature (5 - 95 ˚C). The melting curve for native C2A in apo and Ca^{2+}-bound state both showed a smooth sigmoidal transition between folded and unfolded species that follows a two-state unfolding pathway (Freire, 1995), with a melting temperate (T_m) at 61 ˚C and 73 ˚C, and enthalpy change (ΔH_m) of 147 and 236 KJ/mol, respectively (**Figure 4.5 A, Table 4.2**).

Figure 4. 5 Folding and thermal stability of C2A^{V67A} and C2A^{V67T} monitored by circular dichroism.

(A) Circular dichroism spectra of wild type C2A (black), C2A^{V67A} (red) and C2A^{V67T} (blue) from 250 – 195 nm. The measurements were taken at 25 °C. The buffer background was subtracted. **(B) (C)** Thermal denaturation of C2A (black), C2A^{V67A} (red) and C2A^{V67T} (blue) in apo- and Ca^{2+}-bound state within the range of 5 – 95°C in 0.5 °C increments. The unfolding profile as a function of temperature is shown by CD ellipticity at 215 nm. The relative change in ellipticity at 215 nm was plotted as a fraction unfolded and fitted according to **Equation 2-3** in experimental section.

For C2A^{V67A} and C2A^{V67T}, the unfolding curves shifted to lower transition temperatures in apo and Ca^{2+}-bound state. The unfolding profiles of C2A^{V67A} and C2A^{V67T} almost completely overlapped, indicating two proteins underwent similar unfolding process. The melting temperate (T$_m$) for apo-C2A^{V67A} (49.67 ˚C) and apo-C2A^{V67T} (48.2 ˚C) was over 10˚C lower than the native apo-C2A. Also Ca^{2+}-C2A^{V67A} and Ca^{2+}-C2A^{V67T} had a T$_m$ that is 7˚C lower than the wild-type Ca^{2+}-C2A (**Figure 4.5 B – C, Table 4.2**). Notably, C2A^{V67A} and C2A^{V67T} showed a further gradual transition following melting perhaps indicative of a less cooperative unfolding process or the presence of aggregated species in solution. Further, denaturation of both C2A^{V67A} and C2A^{V67T} yielded smaller enthalpy change (ΔH$_m$) compared to the wild-type, which resulted from decreased thermal stabilities. These results suggest that substitution of V67 causes large instabilities in the C2A domain and that the V67D substitution likely causes its unfolding and aggregation.

Fitting of the unfolding data of apo-C2A^{W52M} yielded a higher melting temperate (T$_m$) (79˚C) than the wild-type apo-C2A (**Table 4.2**). however, the slope of the plot of apo-C2A^{W52M} was remarkably decreased compared to that of the native C2A, resulting in an exceptionally smaller enthalpy change (ΔH$_m$) (**Figure 4. 6 B, Table 4.2**). The unfolding profile of apo-C2A^{W52M} showed a non-cooperative unfolding manner, indicative of significant accumulation of intermediates likely due to the protein aggregation. In the case of Ca^{2+}-C2A^{W52M}, the unfolding curves showed a melting temperature almost 18˚C lower than the native Ca^{2+}-C2A, accompanied with a decreased slope and smaller enthalpy change (ΔH$_m$) (**Figure 4.6 C, Table 4.2**). All these observations suggest that substitution of W52 causes even more significant instabilities than V67 that leads to severe aggregation.
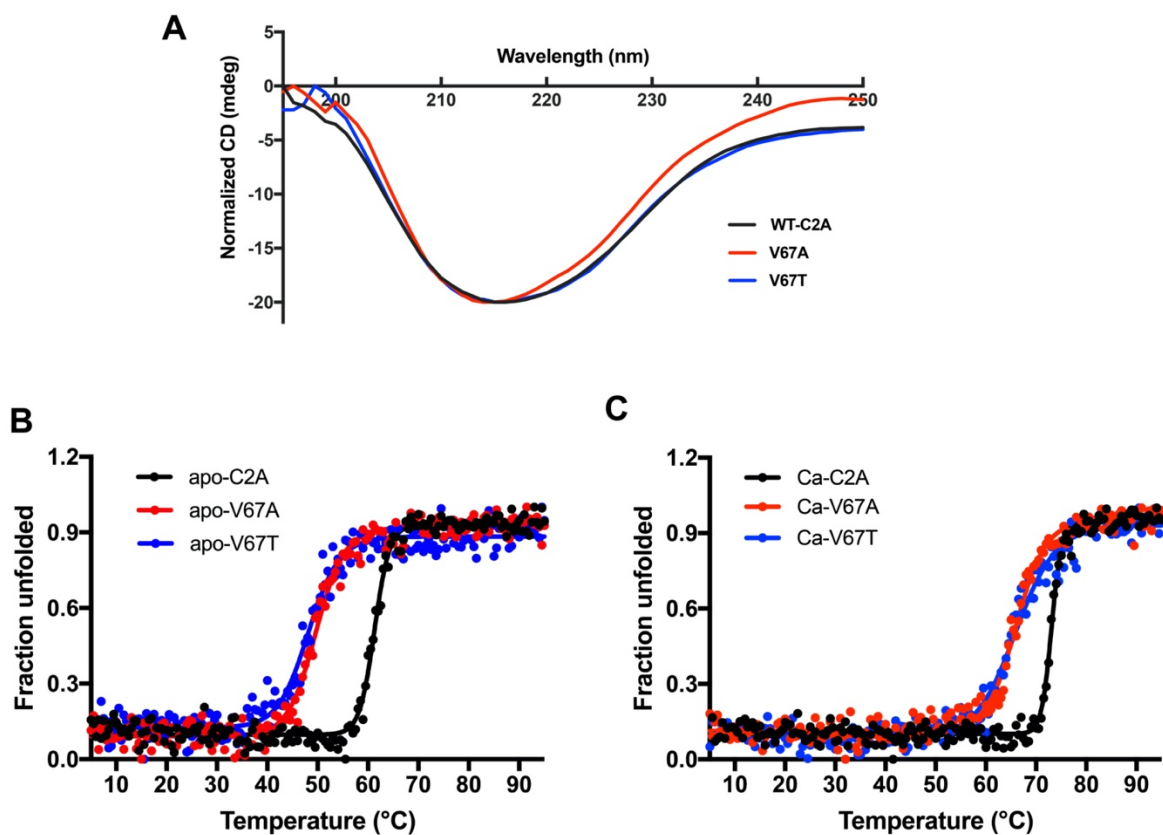
144
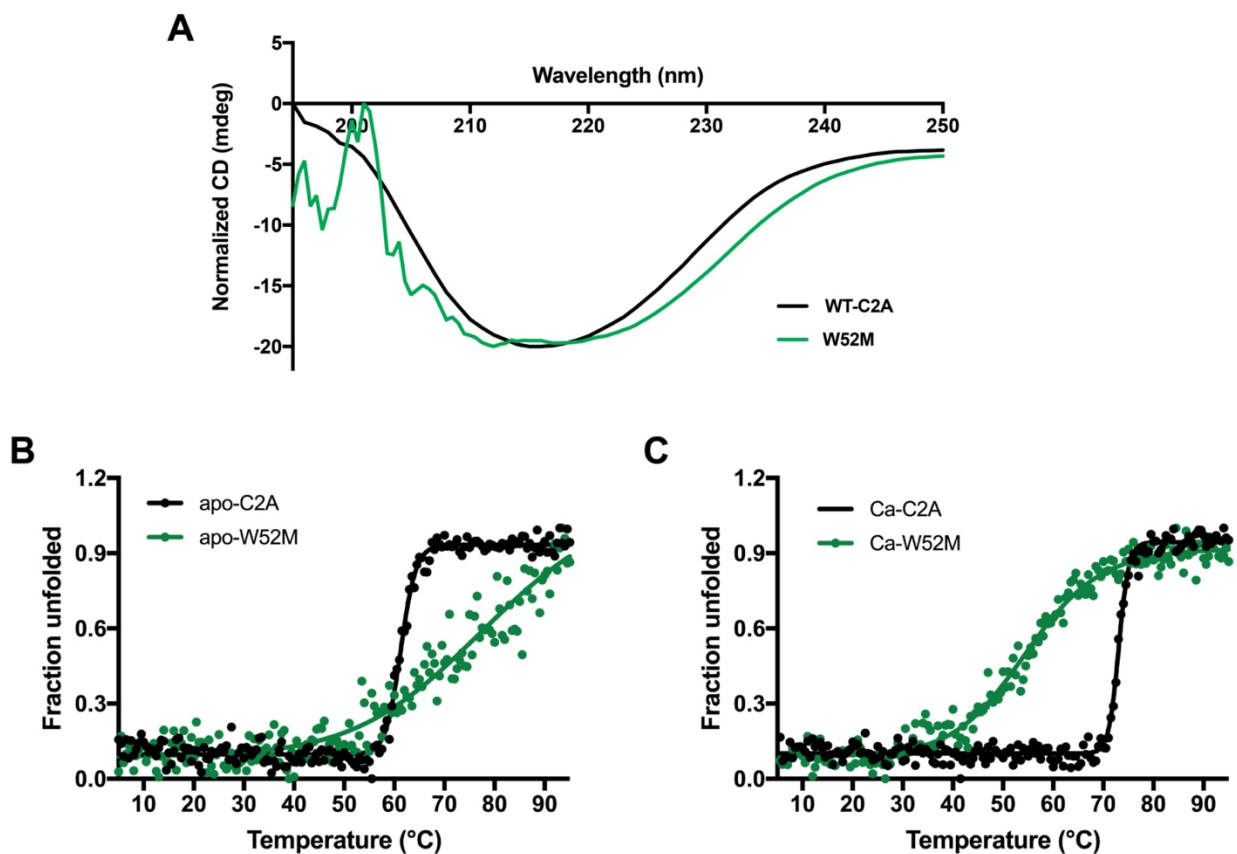
Figure 4. 6 Folding and thermal stability of C2A^{W52M} monitored by circular dichroism.

(A) Circular dichroism spectra of wild type C2A (black) and C2A^{W52M} (green) from 250 – 195 nm. The measurements were taken at 25 °C. The buffer background was subtracted. **(B) (C)** Thermal denaturation of C2A (black) and C2A^{W52M} (green) in apo- and Ca^{2+}-bound state within the range of 5 – 95°C in 0.5 °C increments. The unfolding profile as a function of temperature is shown by CD ellipticity at 215 nm. The relative change in ellipticity at 215 nm was plotted as a fraction unfolded and fitted according to **Equation 2-3** in experimental section.
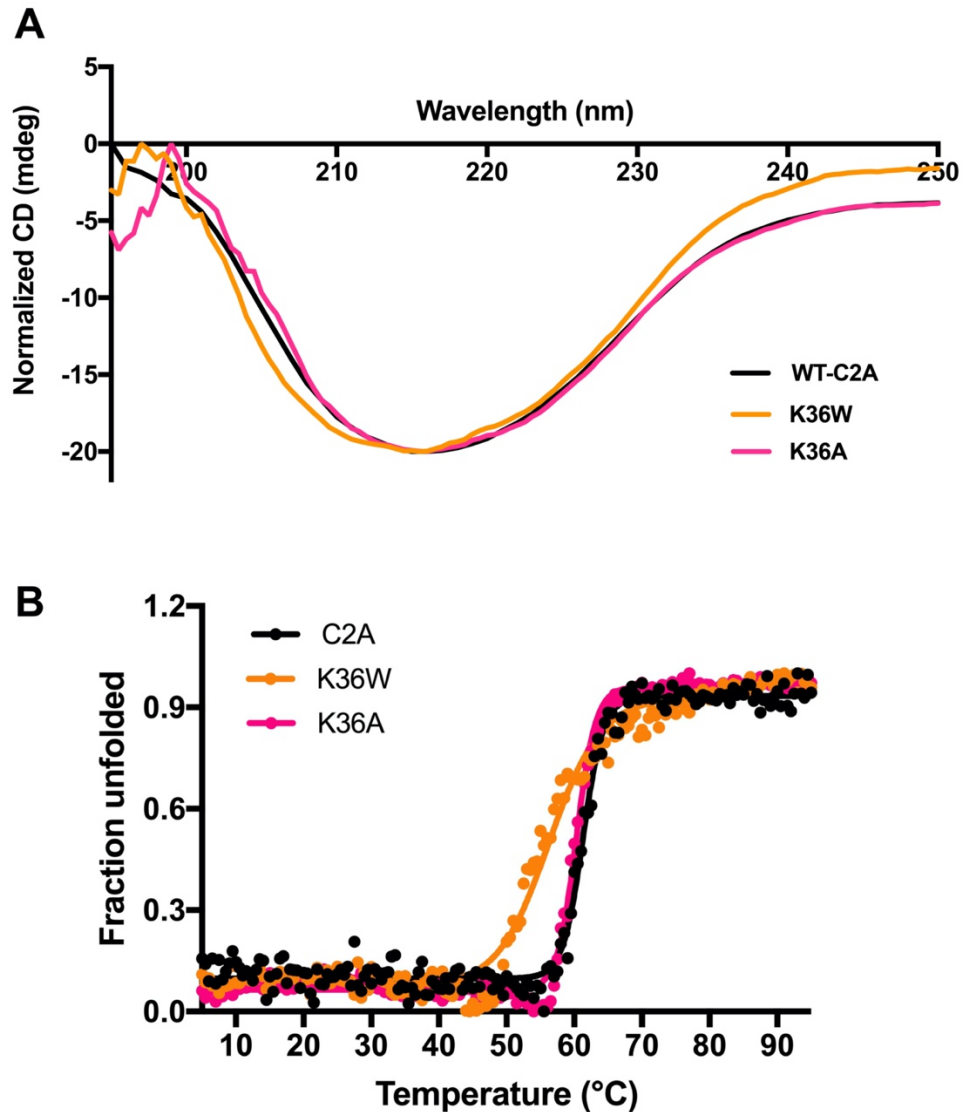
Figure 4. 7 Folding and thermal stability of C2A^{K36A} and C2A^{K36W} monitored by circular dichroism.

(A) Circular dichroism spectra of wild type C2A (black), C2A^{K36A} (pink) and C2A^{K36W} (orange) from 250 – 195 nm. The measurements were taken at 25 °C. The buffer background was subtracted. **(B) (C)** Thermal denaturation of C2A (black), C2A^{K36A} (pink) and C2A^{K36W} (orange) within the range of 5 – 95°C in 0.5 °C increments. The unfolding profile as a function of temperature is shown by CD ellipticity at 215 nm. The relative change in ellipticity at 215 nm was plotted as a fraction unfolded and fitted according to **Equation 2-3** in experimental section.

146

Table 4. 2 Summary of parameters calculated for the thermal unfolding of the C2A domain and its substitutions.

Protein	T_m (°C)	ΔH_m (KJ/mol)
apo-C2A	61.31	147
Ca^{2+}-C2A	73.08	236.1
apo-V67A	49.67	72.86
Ca^{2+}-V67A	66.03	78.18
apo-V67T	48.2	66.95
Ca^{2+}-V67T	66.04	57.6
apo-W52M	79.09	18
Ca^{2+}-W52M	54.73	28.79
K36W	56.37	56.2
K36A	60.33	155.3

Furthermore, the C2A^{K36A} mutant showed almost the same unfolding profile as wild-type C2A with similar T$_m$ and ΔH$_m$, while C2A^{K36W} had a melting temperature about 5 ˚C lower with a slightly reduced slope and much lower T$_m$ (**Figure 4.7 B – C, Table 4.2**). These results indicate that substitution of K36 with an alanine does not seem to affect the folding and stability of the protein, whereas a tryptophan causes destabilization likely due to its hydrophobic exposure effect.

Taken together, although V67D and W52R proteins were unobtainable, we were able to assess the importance and function of residue V67 and W52 by introducing other substitutions at these positions. We found disruption of hydrophobic properties at these positions causes severe instabilities to the overall structure of C2A domain leading to aggregation. Substitution of K36W causes similar destabilization effect, but possibly through introducing hydrophobic residue to the loop region where is more exposed to the solvent, resulting in misfolding of the domain.

4.3.5 Impact of pathogenic mutations on the calcium binding

Next, calcium titration experiments by ITC were conducted to probe the calcium binding properties of each protein. As shown in **Figure 4.8**, the ITC data of C2A^{V67A}, C2A^{W52M}, and C2A^{K36W} all demonstrated endothermic reactions in the beginning and exothermic binding after the mole ratio of [Ca^{2+}]/[C2A] reached 2, indicative of two distinct Ca^{2+} binding modes. This two-stage titration profile resembles that of wild-type C2A observed in **Chapter 3.3.1** (**Figure 3.2**), indicating the Ca^{2+} binding property of C2A domain is maintained for the mutants. Data was fitted using sequential-two-binding-site model and
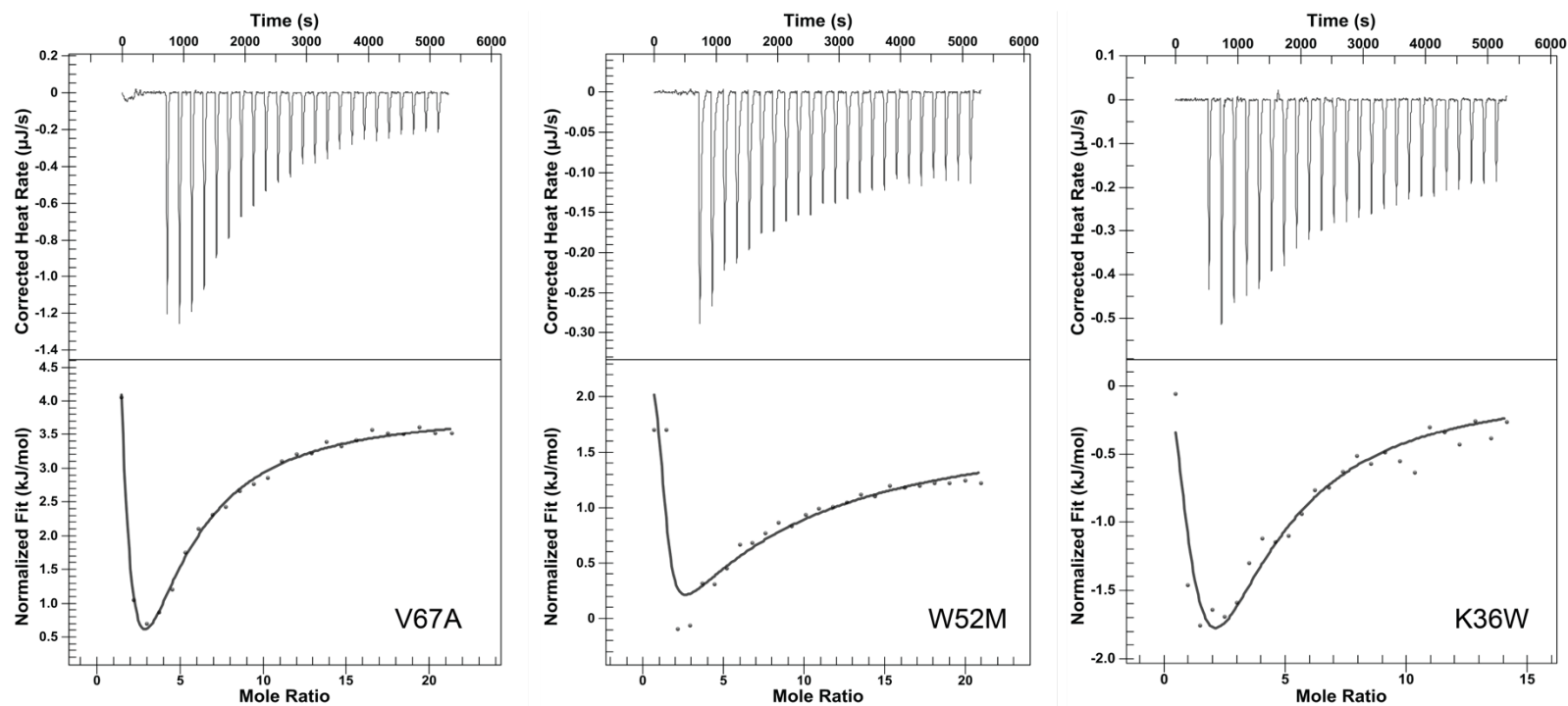
Figure 4. 8 ITC data of Ca^{2+} binding to C2A^{V67A}, C2A^{W52M}, and C2A^{K36W}.

Isotherm graphs of calcium binding to the mutants C2A^{V67A}, C2A^{W52M}, and C2A^{K36W}. Data were collected at 25 °C with 25 mM HEPES, 150 mM NaCl, 250 μM TCEP, pH 7.5 buffer conditions. The data were all fitted with a sequential two-site binding model and the yielded thermodynamic parameters are shown in **Table 4.2**.

Table 4. 3 Summary of Ca^{2+} binding parameters for the C2A domain and its substitutions measured by ITC.

Protein	K_{d1} (μM)	ΔH_1 (KJ/mol)	ΔS_1 (J/mol°K)	K_{d2} (μM)	ΔH_2 (J/mol)	ΔS_2 (J/mol°K)
C2A	32	4.661	102.3	300	-44.15	-8.58
C2A^{V67A}	19	10.78	126.7	342	-35.58	-5.30
C2A^{W52M}	5.4	0.664	103.1	1082	-41.68	-8.30
C2A^{K36W}	27	0.045	8.761	335	-16.54	1.10

thermodynamic parameters yielded are shown in **Table 4.3**. Firstly, the K_d values for the two binding sites of C2A^{V67A} and C2A^{K36W} are within the same order of magnitude as those for the wild-type C2A. The K_{d2} values, particularly, are all about 300 μM, suggesting these substitutions barely affect the Ca^{2+} binding affinities of the domain. The C2A^{W52M} protein showed a little divergent Ca^{2+} binding affinities with a smaller K_{D1} and larger K_{D2} compared to the others. However, it is difficult to assess the accuracy of the ITC data for a large amount of precipitate was observed during the titration which might affect the result. Secondly, by examining the ΔH and ΔS values, all of them show large positive entropy change in the initial step (ΔS$_1$) and a fairly small entropy change (ΔS$_2$) for the second binding step, indicating binding of the first calcium ion results in larger overall structural change of the domain than the second calcium ion. Taken together, the ITC titrations for the C2A^{V67A}, C2A^{W52M}, and C2A^{K36W} proteins demonstrate that substitutions at position V67, W52 and K36 do not affect the Ca^{2+} binding property of the C2A domain.

4.3.6 NMR studies

To further examine the impact of the substitutions on protein folding, NMR spectroscopy was used. Due to severe precipitation of the mutant protein, only adequate C2A^{V67A} protein was obtained to for NMR studies. The ^{1}H-^{15}N-HSQC spectra of apo-C2A^{V67A} compared to wild-type apo-C2A showed apo-C2A^{V67A} displayed a population of well-dispersed peaks and the two spectra demonstrated significant overlap (**Figure 4.9 A**), indicating the V67A substitution does not change the fold and the secondary structure of C2A domain in the apo-state. Subsequently, a large amount of Ca^{2+} was added into the sample and ^{1}H-^{15}N-HSQC spectra was recorded using the identical parameters. However, the spectrum of

C2A^{V67A} protein in Ca^{2+}-bound state showed large variations in peak number and positions compared to the wild-type Ca^{2+}-C2A (**Figure 4.9 B**). It can be observed from the superposition of the two spectra that there was an increased number of signals in the C2A^{V67A} domain, including a series of signals between 8.0 – 9.0 ppm in ^{1}H dimension and 115 – 120 ppm in ^{15}N dimension. This might result from proteolysis and degradation of the protein. Further, the two spectra do not show high level of overlap regarding peak positions, indicating the Ca^{2+}-C2A^{V67A} takes on a conformation different than the wild-type. In addition, based on the fact that the signals of Ca^{2+}-C2A^{V67A} are significantly weaker than the apo-C2A and large amount of precipitate was observed in the final sample, we conclude that protein aggregation occurred during spectral acquisition at room temperature. It is difficult to confirm whether this aggregation resulted from Ca^{2+} binding or the long period of time (more than 8 hours) near room temperature. According to the ITC result that C2A^{V67A} has very similar Ca^{2+} binding properties to the wild-type C2A, it is speculated that the different spectrum of Ca^{2+}-C2A^{V67A} is likely a consequence of protein proteolysis and aggregation, suggesting V67 substitution impairs the long term stability of the C2A domain at room temperature, which further agrees with our previous results.
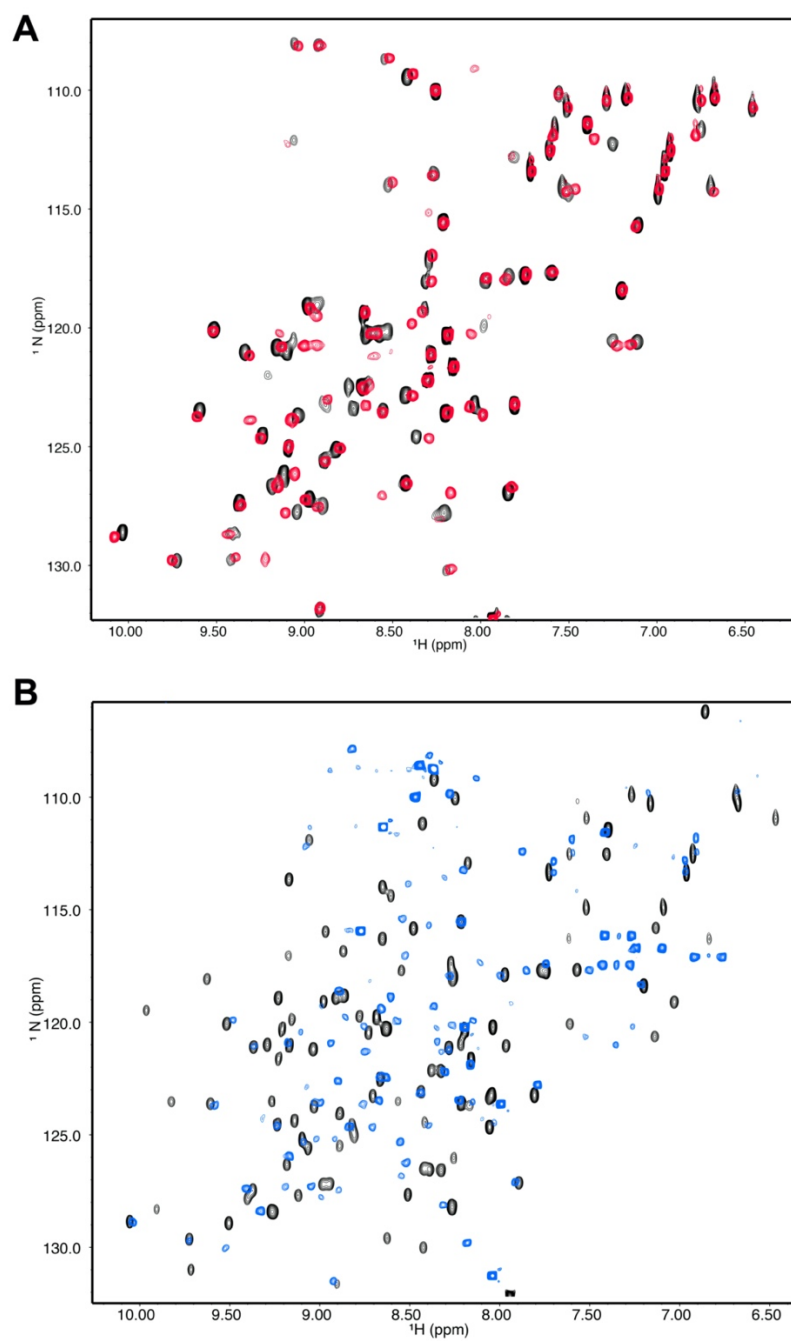
Figure 4. 9 NMR spectra of C2A^{V67A} overlapped with wild-type C2A.

Overlaid ^{1}H-^{15}N HSQC spectrum of apo-C2A^{V67A} (red) and apo-C2A (black) **(A)**, Ca^{2+}-C2A^{V67A} (blue) and Ca^{2+}-C2A (black) **(B)**.

4.4 Discussion

In dysferlin, about half of the missense mutations leading to muscular dystrophy are found within the C2 or the DysF domains. Most of the C2 domain substitutions are found within the predicted β sheet structures and only rarely in the intervening loops. Missense mutations often affect those structures as well as residues that were highly conserved in the C2 domains (Therrien et al., 2006). This can also be seen from the sequence alignment of C2A and C2B domain, where W52 and V67 on C2A and K36 on C2B are all highly conserved residues (**Figure 4.1 A**). We were able to investigate the impact of a pathogenic mutation in the loop region through mapping it from C2B (R253) to C2A (K36) domain based on the sequence homology. This method can be useful to predict the possible consequences of affected residues in different regions of other C2 domains might have on the structure or function of the dysferlin protein.

Clinical data have reported that the pathogenic dysferlin mutations affect the protein expression level in skeletal muscle, characterized by severely decreased or absence of dysferlin expression (Krahn et al., 2009; Nguyen et al., 2005). An amount of dysferlin $\leq$ 20% has been shown to be pathogenic and always caused by primary dysferlin gene mutations (Cacciottolo et al., 2011). Further characterization of dysferlin on a molecular level is needed to better understand the structure and the function of this protein in normal and pathological conditions. Our work investigated three pathogenic mutations on C2A domain that cause limb-girdle muscular dystrophy type 2B (LGMD2B) and Miyoshi myopathy (MM) and show all three substitutions significantly decrease the stability of the C2A domain. In the previous chapter we have shown that wild-type dysferlin C2A domain

takes on an eight β-sheet structure, with multiple calcium- and phospholipid-binding sites. Maintenance of this structure is essential for dysferlin to function in the membrane repair process and V67, W52 and K36 are identified to be structurally important. Unfolding or improper folding of the C2A domain of dysferlin encompassing the V67D, W52R and K36W substitutions is predicted to be responsible for impaired dysferlin function in the membrane repair process, and consequently the wasting of skeletal muscles in muscular dystrophy patients.

4.5 References

Bashir, R., Britton, S., Strachan, T., Keers, S., Vafiadaki, E., Lako, M., Richard, I., Marchand, S., Bourg, N., Argov, Z., et al. (1998). A gene related to Caenorhabditis elegans spermatogenesis factor fer-1 is mutated in limb-girdle muscular dystrophy type 2B. Nat. Genet. *20*, 37–42.

Cacciottolo, M., Numitone, G., Aurino, S., Caserta, I.R., Fanin, M., Politano, L., Minetti, C., Ricci, E., Piluso, G., Angelini, C., et al. (2011). Muscular dystrophy with marked Dysferlin deficiency is consistently caused by primary dysferlin gene mutations. Eur. J. Hum. Genet. *19*, 974–980.

Davis, D.B., Doherty, K.R., Delmonte, A.J., and McNally, E.M. (2002). Calcium-sensitive Phospholipid Binding Properties of Normal and Mutant Ferlin C2 Domains. J. Biol. Chem. *277*, 22883–22888.

De Luna, N., Freixas, A., Gallano, P., Caselles, L., Rojas-García, R., Paradas, C., Nogales, G., Dominguez-Perles, R., Gonzalez-Quereda, L., Vílchez, J.J., et al. (2007). Dysferlin expression in monocytes: A source of mRNA for mutation analysis. Neuromuscul. Disord. *17*, 69–76.

Delaglio, F., Grzesiek, S., Vuister, G.W., Zhu, G., Pfeifer, J., and Bax, A. (1995). NMRPipe: A multidimensional spectral processing system based on UNIX pipes. J. Biomol. NMR *6*, 277–293.

Freire, E. (1995). [6] Thermal denaturation methods in the study of protein folding. In Methods in Enzymology, (Academic Press), pp. 144–168.

Huang, Y., Laval, S.H., van Remoortere, A., Baudier, J., Benaud, C., Anderson, L.V.B., Straub, V., Deelder, A., Frants, R.R., den Dunnen, J.T., et al. (2007). AHNAK, a novel component of the dysferlin protein complex, redistributes to the cytoplasm with dysferlin during skeletal muscle regeneration. FASEB J. *21*, 732–742.

Illarioshkin, S.N., Ivanova-Smolenskaya, I.A., Greenberg, C.R., Nylen, E., Sukhorukov, V.S., Poleshchuk, V.V., Markova, E.D., and Wrogemann, K. (2000). Identical dysferlin mutation in limb-girdle muscular dystrophy type 2B and distal myopathy. Neurology *55*, 1931–1933.

Johnson, B.A., and Blevins, R.A. (1994). NMR View: A computer program for the visualization and analysis of NMR data. J. Biomol. NMR *4*, 603–614.

Krahn, M., Béroud, C., Labelle, V., Nguyen, K., Bernard, R., Bassez, G., Figarella-Branger, D., Fernandez, C., Bouvenot, J., Richard, I., et al. (2009). Analysis of the *DYSF* mutational spectrum in a large cohort of patients: *DYSF* Mutational Spectrum in a Large Cohort. Hum. Mutat. *30*, E345–E375.

Liu, J., Aoki, M., Illa, I., Wu, C., Fardeau, M., Angelini, C., Serrano, C., Urtizberea, J.A., Hentati, F., Hamida, M.B., et al. (1998). Dysferlin, a novel skeletal muscle gene, is

mutated in Miyoshi myopathy and limb girdle muscular dystrophy. Nat. Genet. *20*, 31–36.

Matsuda, C., Miyake, K., Kameyama, K., Keduka, E., Takeshima, H., Imamura, T., Araki, N., Nishino, I., and Hayashi, Y. (2012). The C2A domain in dysferlin is important for association with MG53 (TRIM72). PLoS Curr.

Nguyen, K., Bassez, G., Bernard, R., Krahn, M., Labelle, V., Figarella-Branger, D., Pouget, J., Hammouda, E.H., Béroud, C., Urtizberea, A., et al. (2005). Dysferlin mutations in LGMD2B, Miyoshi myopathy, and atypical dysferlinopathies. Hum. Mutat. *26*, 165–165.

Rahimov, F., and Kunkel, L.M. (2013). Cellular and molecular mechanisms underlying muscular dystrophy. J. Cell Biol. *201*, 499–510.

Therrien, C., Dodig, D., Karpati, G., and Sinnreich, M. (2006). Mutation impact on dysferlin inferred from database analysis and computer-based structural predictions. J. Neurol. Sci. *250*, 71–78.

Therrien, C., Di Fulvio, S., Pickles, S., and Sinnreich, M. (2009). Characterization of Lipid Binding Specificities of Dysferlin C2 Domains Reveals Novel Interactions with Phosphoinositides [†]. Biochemistry *48*, 2377–2384.

Wang, W., and Malcolm, B.A. (1999). Two-Stage PCR Protocol Allowing Introduction of Multiple Mutations, Deletions and Insertions Using QuikChangeTM Site-Directed Mutagenesis. BioTechniques *26*, 680–682.

Chapter 5

Design and Characterization of Dysferlin C2B and C2C Domain

5.1 Introduction

Dysferlin is a large protein containing 2080 amino acids with a short C-terminal transmembrane domain. Within the cytosolic region of dysferlin, it possess a rare feature consisting of seven tandem C2 domains (C2A – C2G) separated by linkers, together with two Fer domains and one DysF domain. The tertiary structure of dysferlin has not been characterized, only DysF domains has been solved by crystallography (Sula et al., 2014), and the C2A domain has been comprehensively investigated in the previous chapters of this thesis. Dysferlinopathy is characterized by absence or marked reduction of dysferlin protein, with 43% of reported pathogenic variants being missense mutations that span the length of the dysferlin protein including all the C2 domains (Cacciottolo et al., 2011; Krahn et al., 2009). This suggests that all seven C2 domains are structurally or functionally important for maintaining dysferlin's activities. Although it was previously predicted that the C2A, C2B, and C2E domains adopted the type II topology, whereas the remainder of the C2 domains were expected to adopt the type I topology (Therrien et al., 2006), it is still unclear what the specific structure and role of each C2 domain is and the interplay between them and other domains.

A limited number of studies have focused on the C2 domains of dysferlin individually. By using isolated proteins, one study demonstrated that all seven dysferlin C2 domains interact with Ca^{2+} with various binding affinities ranging from micromolar (C2A and C2C) to millimolar (C2D), as well as with different stoichiometry (Abdullah et al., 2014). A lipid binding assay showed that the C2A domains of dysferlin exhibited binding to phosphatidylserine (PS) and several phosphoinositides in a Ca^{2+}-dependent manner, whereas all of the other dysferlin C2 domains exhibited weaker and Ca^{2+}-independent binding to PS and no detectable binding to phosphoinositides. Although these studies laid some ground for investigations into dysferlin C2 domains, some issues are implicit in them. Firstly, different studies have used constructs of C2 domains that include different regions of the protein, which vary considerably in some cases: the domain boundaries have not been defined clearly yet. Secondly, the secondary structure of each C2 domain was almost never analyzed to confirm the proper folding of the domains, which could be problematic when drawing conclusions regarding any features of the C2 domains. To address the above issue, I pursued my studies on characterizing the C2B and C2C domains of dysferlin. The work in this chapter aimed to define the accurate domain boundaries of the two domains and to investigate the structural properties of them.

5.2 Materials and Methods

5.2.1 Restriction-free (RF) cloning of the dysferlin C2B and C2C domain

All the dysferlin C2B and C2C constructs were cloned using restriction-free cloning technique (van den Ent and Löwe, 2006). Plasmid encoding the full length human dysferlin

gene (DYSF) was purchased from Addgene plasmid repository (#60216). DNA fragments encoding C2B and C2C domains from the full length DYSF gene were inserted into the following vectors containing different affinity tags: pET28a (His$_6$ tag), pET-SUMO (His-SUMO tag), pGEX (GST tag). Primers were designed using the online program (https://www.rf-cloning.org) and are shown in **Table 5.1**. The DYSF plasmid was isolated from harvested MM294 *E. coli* cells using the Bio Basic Inc. EZ-10 spin column miniprep kit. The restriction-free cloning was conducted using Polymerase chain reaction (PCR). Methylated parental strands that remained in the PCR reaction were digested by Dpn1 overnight at 37°C. The following day, plasmid DNA was purified using a PCR clean-up kit (BioBasic Inc). All PCR products were transformed into competent MM294 cells and incubated on antibiotic-treated LB-agar plates overnight at 37 °C. Multiple colonies were picked and grown in LB. Plasmids were isolated from harvested cells using the Bio Basic Inc. EZ-10 spin column miniprep kit and were sequenced (London Regional Genomics Centre, Canada) to verify that the correct mutations were incorporated.

5.2.2 Test expression and solubility test

Small-scale test expression experiment was performed for the following constructs: His-C2B, His-SUMO-C2B, GST-C2B, His-C2C, His-SUMO-C2C, GST-C2C, His-C2BC, His-SUMO-C2BC, GST-C2BC, His-C2BC-DysF, His-SUMO-C2BC-DysF, GST-C2BC-DysF (also shown in **Figure 5.3 B**). Plasmids containing the DNA were transformed BL21-CodonPlus (DE3) E. coli strain. Isolated colonies were picked and grown in 5 mL LB/DYT overnight as starters. The following day 250 μL starters were inoculated into 25 ml LB/DYT with appropriate antibiotics. The cultures were grown at 37 °C until an OD600 of

Table 5. 1 Primers used for restriction-free cloning for generating dysferlin C2B and C2C constructs.

Construct	Primer Sequence
His-C2B	Forward: 5'- AGGATCCGGCGGCGGCGGCGGCAAACCGCAGGATTTCCAGA -3' Reverse: 5'- AGTGGTGGTGGTGGTGGTGCTAGTCCCCAGGCCCCAGCAC -3'
His-SUMO-C2B	Forward: 5'- GGCTCACAGAGAACAGATTGGTGGTAAACCGCAGGATTTCCAGATCA -3' Reverse: 5'- CGCCGAATAAATACCTAAGCTTGTCTCTAGTCCCCAGGCCCCAGCAC -3'
GST-C2B	Forward: 5'- GTTCCAGGGGCCCCTGGGATCCAAACCGCAGGATTTCCAGA -3' Reverse: 5'- CACGATGCGGCCGCTCGAGTCAGTCCCCAGGCCCCAGCAC -3'
His-C2C	Forward: 5'- AGGATCCGGCGGCGGCGGCGGCGGAGCCCACTTCTGCCTGAAGG -3' Reverse: 5'- CAGTGGTGGTGGTGGTGGTGCTAACTGCCATAGAGGTTGATGTAGC -3'
His-SUMO-C2C	Forward: 5'- GGCTCACAGAGAACAGATTGGTGGTGGAGCCCACTTCTGCCTGAAG -3' Reverse: 5'- CGAATAAATACCTAAGCTTGTCTCTAACTGCCATAGAGGTTGATGTAGC -3'
GST-C2C	Forward: 5'- GTTCCAGGGGCCCCTGGGATCCGGAGCCCACTTCTGCCTGAAG -3' Reverse: 5'- CACGATGCGGCCGCTCGAGTCAACTGCCATAGAGGTTGATGTAGC -3'
His-C2BC	Forward: 5'- CAAGGATCCGGCGGCGGCGGCGGCAAACCGCAGGATTTCCAGATC -3' Reverse: 5'- GTGGTGGTGGTGGTGGTGCTAACTGCCATAGAGGTTGATGTAGC -3'
His-SUMO-C2BC	Forward: 5'- GGCTCACAGAGAACAGATTGGTGGTAAACCGCAGGATTTCCAGATC -3' Reverse: 5'- CGAATAAATACCTAAGCTTGTCTCTAACTGCCATAGAGGTTGATGTAGC -3'
GST-C2BC	Forward: 5'- GTTCCAGGGGCCCCTGGGATCCAAACCGCAGGATTTCCAGATC -3' Reverse: 5'- CACGATGCGGCCGCTCGAGTCAACTGCCATAGAGGTTGATGTAGC -3'
His-C2BC-DysF	Forward: 5'- CAAGGATCCGGCGGCGGCGGCGGCAAACCGCAGGATTTCCAGATC -3' Reverse: 5'- CTCAGTGGTGGTGGTGGTGGTGCTACTCGCCCTCCGCCTCCGCC -3'
His-SUMO-C2BC-DysF	Forward: 5'- CCTCCCCACTTTTGGGCCCTGCACTAAGTTGGCCCTTGTTGG -3' Reverse: 5'- GTGGTGGTGGTGGTGGTGCTACTCGCCCTCCGCCTCCGCCTGC -3'
GST-C2BC-DysF	Forward: 5'- GTTCCAGGGGCCCCTGGGATCCAAACCGCAGGATTTCCAGATC -3' Reverse: 5'- GTCACGATGCGGCCGCTCGAGTCACTCGCCCTCCGCCTCCGCC -3'

0.6 was reached and were induced with 0.05 – 0.5 mM IPTG, followed by continued growth at 37 ˚C for 5 hours or at 16 ˚C for 20 hours. Cells were harvested by centrifugation at 4,000 rpm for 20 min and resuspended in various lysis buffers. Cells were lysed by EmulsiFlex-C5 homogenizer (Avestin). Gel sample was taken at this point as total protein (i.e. 30 μL + 15 μL 3 × SDS loading buffer). Then 1 mL cell lysate was centrifuged for 10 - 15 minutes at 14,000 rpm in tabletop centrifuge. The supernatant was taken as gel sample (soluble fraction). Cell pellet was resuspended in 1 ml of 2% SDS with vortexing and taken as gel sample (insoluble fraction). The total protein (W), soluble (S) and insoluble fractions (P) were checked by SDS-PAGE along with the relevant negative and positive controls.

5.2.3 Expression and purification of His-SUMO-C2B and His-SUMO

The dysferlin C2B domain (residues 216-348) that was inserted into a pET SUMO expression system vector (Invitrogen) is referred to as His-SUMO-C2B. Unlabeled or uniformly ^{15}N-labeled His-SUMO-C2B were overexpressed in the BL21-CodonPlus (DE3) *E. coli* strain in LB or M9 minimal medium supplemented with 30 μg/mL kanamycin and 30 μg/mL chloramphenicol. ^{15}NH$_4$Cl (1 g/L) and ^{13}C$_6$-glucose (2 g/L) were used as the sole nitrogen and carbon sources in the M9 minimal media. The cultures were grown at 37 ºC until an OD600 of 0.6 was reached at which point cells were cooled to 16 °C and induced with 0.5 mM IPTG for 20 hours. Cells were harvested by centrifugation at 6,000 rpm for 15 min and resuspended in lysis buffer (50 mM Tris, 300 mM NaCl, 10 mM imidazole, 0.1 % Triton X-100, 5% glycerol, pH 9.5). Cells were lysed by EmulsiFlex-C5 homogenizer (Avestin) and centrifuged at 20,000 g for 40 min. The supernatant was filtered through 0.45 micron low protein binding Millipore syringe filters and subsequently applied

to a 5 mL HisTrap FF column on an AKTA FPLC (GE Healthcare) pre-equilibrated in binding buffer (50 mM Tris, 300 mM NaCl, 10 mM imidazole, 0.1 % Triton X-100, 5% glycerol, pH 7.5). The column was washed with the binding buffer with 50 mM imidazole until the OD280 returned to baseline. Bound protein was then eluted with a 250-500 mM imidazole in the elution buffer (50 mM Tris, 300 mM NaCl, 250-500 mM imidazole, 0.1 % Triton X-100, 5% glycerol, pH 7.5). A final purification step by gel filtration was performed on a HiLoad Superdex75 pre-equilibrated with appropriate buffers. Fractions containing the protein were pooled and stored at -80 ºC.

Uniformly ^{15}N-labeled His-SUMO (Invitrogen) was overexpressed in the BL21-CodonPlus (DE3) *E. coli* strain in M9 minimal medium supplemented with 30 µg/mL kanamycin. The cultures were grown at 37 ºC until an OD600 of 0.6 was reached at which point cells were cooled to 16 °C and induced with 0.5 mM IPTG for 20 hours. Cells were harvested by centrifugation at 6,000 rpm for 15 min and resuspended in lysis buffer (25 mM Tris, 300 mM NaCl, 10 mM imidazole, pH 7.5). Cells were lysed by EmulsiFlex-C5 homogenizer (Avestin) and centrifuged at 38,000 rpm for 90 min. The supernatant was filtered through 0.45 micron low protein binding Millipore syringe filters and subsequently applied to a 5 mL HisTrap FF column on an AKTA FPLC (GE Healthcare) pre-equilibrated in lysis buffer. The column was washed with the binding buffer with 50 mM imidazole until the OD280 returned to baseline. Bound protein was then eluted with a 250-500 mM imidazole in the elution buffer (25 mM Tris, 300 mM NaCl, 250-500 mM imidazole, pH 7.5). Fractions containing the His-SUMO protein were verified by SDS-PAGE.

5.2.3 Expression and purification of GST-C2BC-DysF

The dysferlin C2BC domain (216-521) and DysF domain (886-1067) were linked together by cloning and incorporated into the pGEX (GST tag) expression vector (referred to as GST-C2BC-DysF). Unlabeled GST-C2BC-DysF was over-expressed in the BL21 (DE3) Codon Plus *E. coli* strain. The cultures were grown at 37 ºC in the presence of ampicillin (50 µg/mL) to a density of (A600) 0.6 AU, then induced by adding 0.5 mM IPTG. Induction continued for another 20 h with constant shaking at 16 ºC. Cells were harvested by centrifugation at 6,000 rpm for 15 min and resuspended in PBS buffer (140 mM NaCl, 2.7 mM KCl, 10 mM Na_2HPO_4, 1.8 mM KH_2PO_4, pH 7.3). Cells were lysed by EmulsiFlex-C5 homogenizer (Avestin) and centrifuged at 30,000 rpm for 90 min. All fractionation steps were performed at 4 °C. The supernatant was applied to a 5 mL glutathione-linked sepharose column (GSTrap FF) on an AKTA FPLC (GE Healthcare) pre-equilibrated in PBS buffer. The column was then washed with the PBS buffer until the OD280 returned to baseline. The bound GST-C2BC-DysF protein was eluted in elution buffer (50 mM Tris-HCl, 20 mM reduced glutathione, , pH 8.0). Fractions containing the GST-C2BC-DysF protein were verified by SDS-PAGE.

5.2.4 NMR spectroscopy

All NMR experiments were collected at 25˚C on a Varian Inova 600 MHz NMR spectrometer equipped with a triple resonance cryogenic probe and z-field gradients. All data were processed using NMRPipe (Delaglio et al., 1995) and analyzed using NMRViewJ (Johnson and Blevins, 1994). The ^{1}H-^{15}N HSQC NMR experiments were conducted in 25 mM HEPES, 150 mM NaCl, 250 µM TECP, pH 7.5 with 10% D_2O, 200

μM DSS as an internal reference, and 200 μM imidazole as an internal pH indicator. The ^{1}H-^{15}N HSQC NMR spectra was collected using a sample of 200 μM uniformly ^{15}N-labeled His-SUMO, and a sample of 150 μM ^{15}N-labeled His-SUMO-C2B. Spectral windows were 7000.0 Hz centered on 4.773 ppm for ^{1}H and 1944.3 Hz centered on 121.2 ppm for ^{15}N. For the interaction study of dysferlin C2A and C2B domain, the apo and Ca^{2+}-bound ^{15}N-labeled C2A samples were prepared as described in **Chapter 3.3.2**, with a concentration of 200 μM. A ^{1}H-^{15}N HSQC NMR spectrum was recorded for each. Then 100 μM unlabeled His-SUMO-C2B was added into the sample followed by collection of another ^{1}H-^{15}N HSQC spectrum.

5.2.5 Circular dichroism

Folding of all proteins were monitored by circular dichroism spectropolarimetry using a Jasco J-810 instrument (Biomolecular Interactions and Conformations Facility, University of Western Ontario). Proteins were extensively dialyzed in the CD buffer (20 mM KH$_2$PO$_4$, pH 7.5) for at least one day with stirring. For each sample, 15 scans from 250 –200 nm (80 nm/min with increment of 1 nm) were recorded using a 1 mm path-length cell at 20 °C and 95 °C, averaged and the buffer background was subtracted.

5.2.6 Isothermal titration calorimetry

All calorimetry experiments were performed using a NanoITC (TA Instruments) at 25°C. All experiments were completed 2–3 times using freshly prepared proteins extensively dialyzed in 25 mM HEPES, 150 mM NaCl, 250 μM TECP, pH 7.5 and pretreated with Chelex-100 (Bio-Rad) to remove residual Ca^{2+} ions for one hour. The optimal concentrations of protein and Ca^{2+} in the experiments were determined to be: 1.5 mM Ca^{2+}

titrated into 57 µM His-SUMO-C2B. Protein and Ca^{2+} solution were degassed under vacuum prior to each titration. Titrations consisted of 25 injections of 2 µL Ca^{2+} solution into a 146 µL cell containing the proteins with constant stirring. Heats of dilution were measured in a separate experiment in which Ca^{2+} solution was injected into the buffer alone.

5.3 Results

5.3.1 Design of the dysferlin C2B and C2C constructs

As mentioned earlier, dysferlin has been identified to possess a unique structure consisting of seven tandem cytosolic C2 domains (C2A – C2G) separated by linkers, together with two Fer domains and one DysF domain in the middle of the protein (**Figure 5.3 A**). However, in the existing studies on dysferlin, different domain boundaries have been predicted. For example, three dysferlin studies were conducted using the C2C domain spanning three different regions (residue 345 – 574, 378 – 528 and 366 – 515, respectively (Abdullah et al., 2014; Llanga et al., 2017; Therrien et al., 2009). For our study which requires properly folded protein and pursues structural characterization, accurate boundary identification of dysferlin C2 domains is needed.

First, we carried out secondary structure prediction and sequence alignment. We used the online program JPred (http://www.compbio.dundee.ac.uk/jpred4) and YASPIN (http://www.ibi.vu.nl/programs/yaspinwww) for secondary structure predication of the dysferlin C2B and C2C domains. In the prediction for C2B domain from residue K216 to

D348, the first six β strands were predicted by the two programs consistently and the β-strands were shown to be connected by random coils (**Figure 5.1 A**). In contrast, in the prediction by YASPIN, there were sequence preferences for one more β strand element at the end of the sequence and three α helix structures between β4 -5 and β6 -7. In the prediction of C2C domain from residue G378 to C521, there were also six β strands predicted by both programs and YASPIN identified two more β strands. Further, two programs each predicted one α helix in different positions (**Figure 5.1 B**). In principle, the C2 domains are expected to present eight β sheets, so the predictions do not give high reliabilities. Nonetheless, the above results helped us to locate the approximate segments of the C2B and C2C domains. Meanwhile, a sequence alignment of the C2B and C2C domains was performed along with secondary structure information obtained from dysferlin C2A and PLC-δ1 (Essen et al., 1997) crystal structures to map the putative calcium binding residues and structurally conserved residues. Residues important for the structure of β-strands and intervening loops of the domains were aligned according to an amino acid consensus obtained from the structural alignment of dysferlin C2A and PLC-δ1. As shown in **Figure 5.1 C**, there is a lot of sequence conservativity within the region encompassing the first six β strands. For example, a number of hydrophobic residues were aligned well in the β sheet regions and several aspartate and asparagine residues were indicated to be analogous in loop 1 – 3 which likely correspond to the calcium binding sites. In comparison, the regions after β6 showed weaker sequence preservation with fewer conserved amino acid residues. This aligns closely with the secondary structure prediction results that these regions demonstrated prominent structural discrepancy in the two
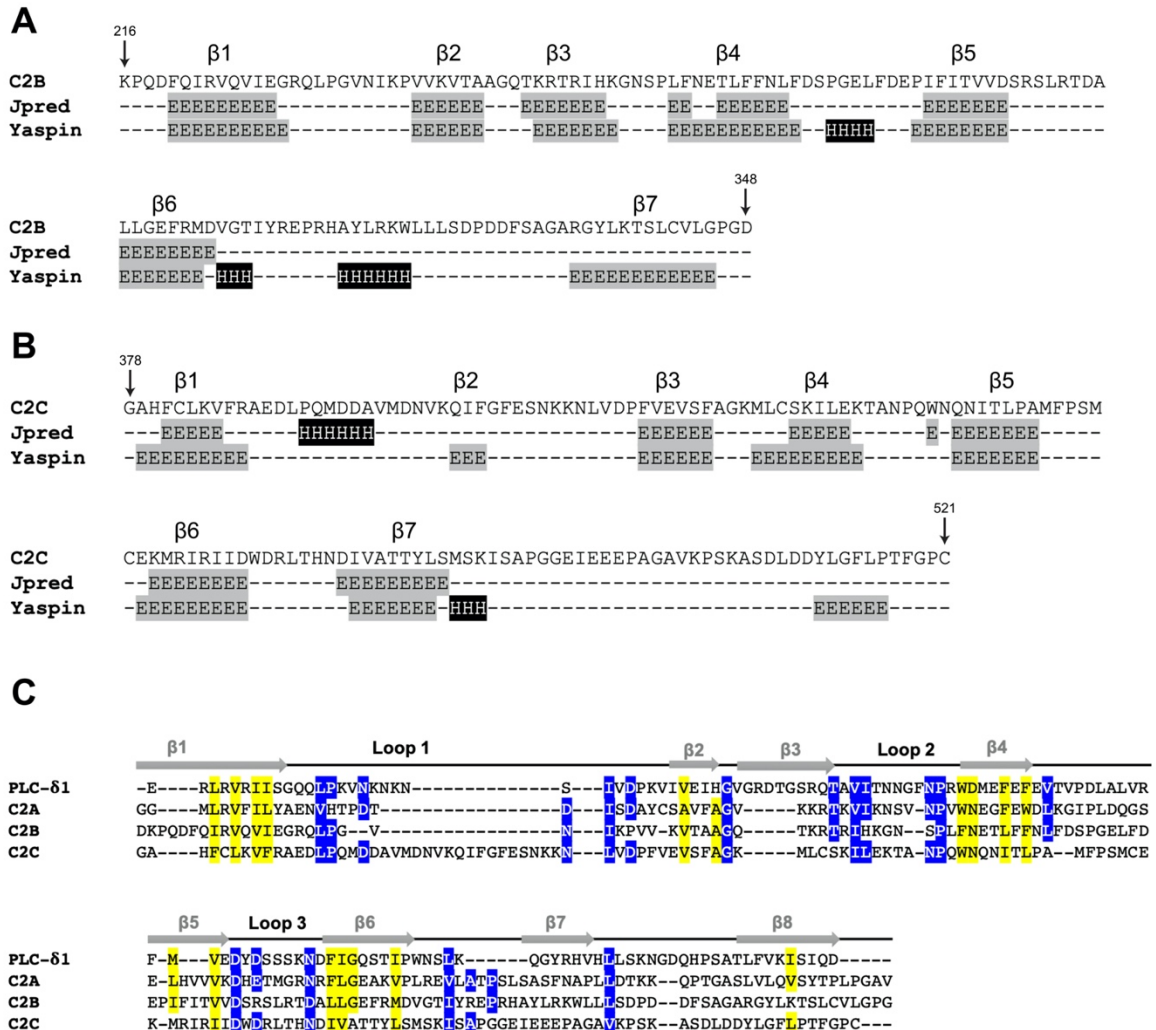
Figure 5. 1 Secondary structure prediction and sequence alignment of dysferlin C2B and C2C domain.

(A) (B) Secondary structure prediction of amino acid sequences corresponding to dysferlin C2B **(A)** and C2C **(B)** domain using online prediction program Jpred (http://www.compbio.dundee.ac.uk/jpred/) and Yaspin (http://www.ibi.vu.nl/programs/yaspinwww/). The secondary structure elements are shown: H, α helix; E, β sheet; -, disorder/loop. Putative β sheets are marked on the top of the sequences. **(C)** Alignment of dysferlin C2B and C2C domain with C2A and PLC-δ1C2 domain. Hydrophobic residues that are highly conserved in β sheet regions are highlighted in yellow. Conserved residues in the loop regions are highlighted in white with a blue background. The arrows above the sequence correspond to residues that possess β strand secondary structure, whereas the lines correspond to the loop region.

programs (**Figure 5.1 A - B**). We suspect that there might be larger structural variations between the C2 domains' sequences within this region, which causes difficulty to identify the accurate boundaries.

To attain more insights into designing the C2B and C2C constructs, we combined the above results with a computational model performed by our collaborator (Dr. Lance Stewart and Dr. David Baker, University of Washington, U.S.). The model simulated the 3D structure of the entire dysferlin protein. The C2B and C2C domains modeled both show an anti-parallel β-sandwich arrangement connected by four loops at the top of the structures, typical of the C2 domain fold (**Figure 5.2 A - B**). The domain boundaries are identified to be K216 to D348, and G378 to C521, respectively. Of note, the C2C domain model demonstrates a much longer loop region comprising an α-helix fold. This explains the extra residues in the C2C loop 1 observed in the sequence alignment (**Figure 5.1 C**). Together, the starting residue of the C2B and C2C domains align perfectly in the three methods described above, and the computational simulation helped us determining the end points of the domains.

More importantly, the simulated model also shows that C2B and C2C domain together adopt an arched-shaped arrangement joined by a linker sequence that forms an α-helix and packs against the two domains. The N and C termini of both domains are located at the bottom of the overall structure, whereas the putative calcium binding loops on the top (**Figure 5.2 C**). This proposed model is supported by a few studies. In a limited proteolysis study on dysferlin, C2B-C2C was found to be excised as an intact module and exist in a
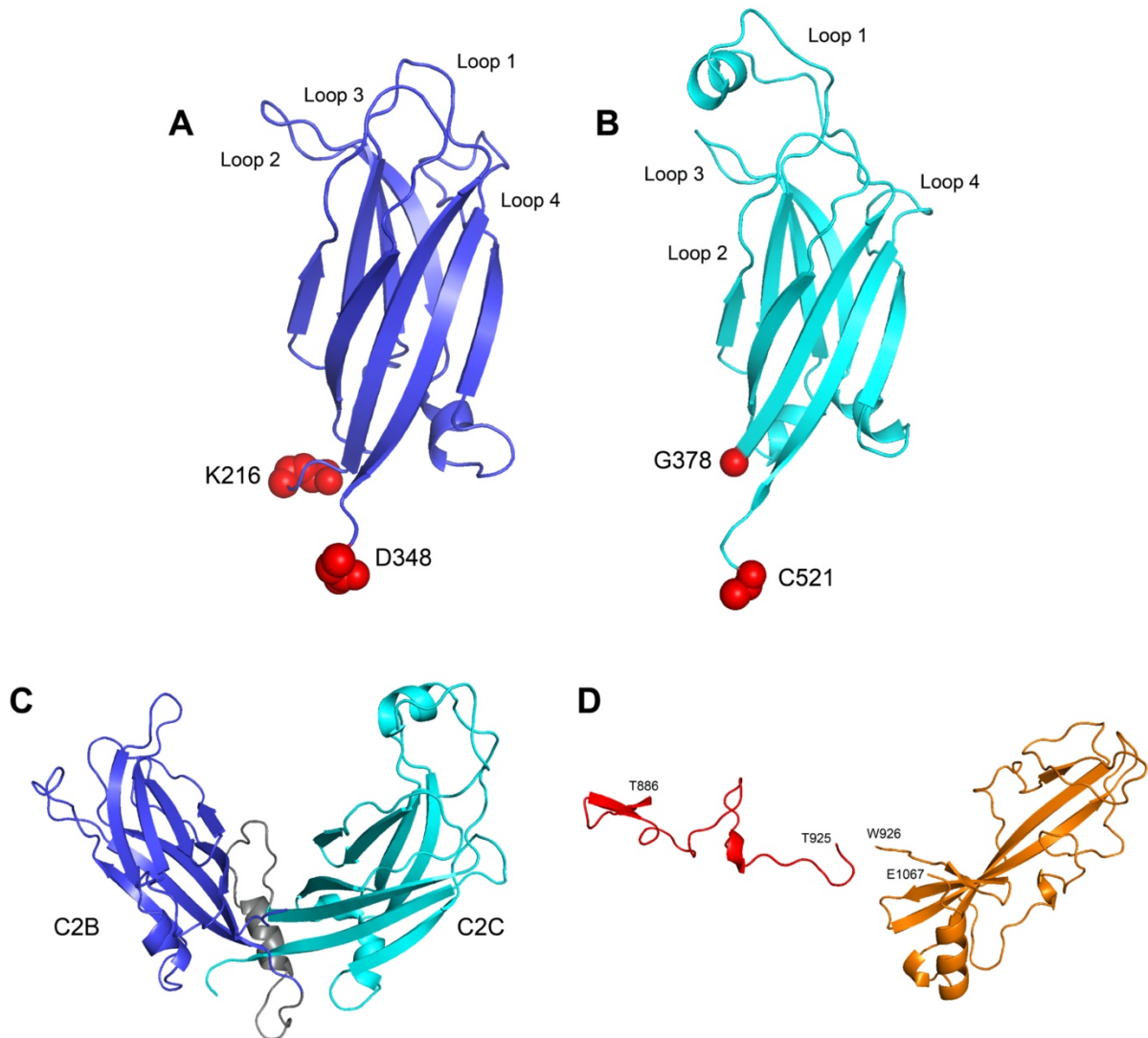
Figure 5. 2 Modeling of dysferlin C2B, C2C, and DysF domains.

Predicted structures of dysferlin C2B domain **(A)** and C2C domain **(B)** by collaborator's modeling. The N- and C-terminal residues are labeled red dots and residue numbers. **(C)** Modeling of the C2B-C2C module showing C2B and C2C domains together adopt an arched-shaped arrangement joined by a linker sequence (gray) that forms an α-helix and packs against the two domains. **(D)** Modeled DysF domain, containing a β-sheet motif encompassing residue W926 to E1067 (orange) with an extension of a second "DysF" like domain from T886 to T925 (red).

170

closed conformation (Woolger et al., 2017), consistent with the cellular function of the C2B-C2C motif in regulating dysferlin plasma membrane expression (Evesson et al., 2010). Further, the modeled C2B-C2C conformation is similar in structure to the tandem C2 domains (C2A-C2B) of extended synaptotagmin (Schauder et al., 2014; Xu et al., 2014), which is evolutionarily conserved to dysferlin. Thus, C2B-C2C could be regarded as a single domain and the folding of each domain may be dependent on the other.

Additionally, the DysF domain, encompassing residue W926 to E1067, was predicted to be associated with the C2B-C2C module by our collaborator. It is proposed that the DysF domain resembles the SMP domain of extended synaptotagmin that makes contact with the C2A-C2B motif and mediates lipid binding. The crystal structure of DysF domain shows it consists of two long antiparallel β-strands, one at each terminus, connected with a long loop (Sula et al., 2014) (**Figure 5.2 D**), which is similar to parts of the β-barrel structure of the SMP domain of extended synaptotagmin (Schauder et al., 2014). It is also suggested that the fragment covering residue T886 – T925 could be an extension of the structure of DysF domain or a second "DysF" like domain, and interacts with C2B-C2C module together with DysF domain (**Figure 5.2 D**).

On the basis of all the above information, by utilizing restriction-free cloning method using the full-length DYSF gene and vectors containing different affinity tags, the following constructs were generated (**Figure 5.3 B**):
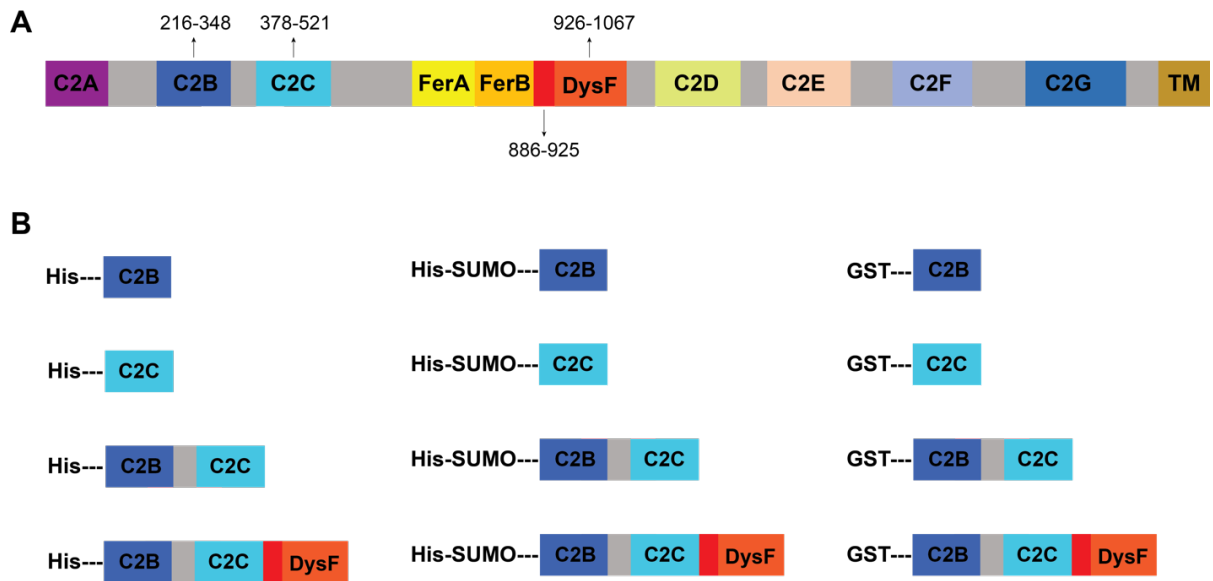
(i) C2B domain (216 - 348).

(ii) C2C domain (378 - 521).

Figure 5. 3 Overview of dysferlin C2B and C2C constructs generated by RF cloning.

(A) Domain architecture of full-length dysferlin demonstrating the domain boundaries of C2B, C2C and DysF domains. **(B)** Schematic representation of the constructs generated in this study. Three different affinity tags were incorporated at N terminus for each construct, including His6 tag, His-SUMO (small ubiquitin-like modifying protein) tag and GST (Glutathione S-transferase) tag.

(iii) C2BC (216 - 521).

(iv) C2BC-DysF (216 - 521+ 886 - 1067).

For each fragment, three different affinity tags were incorporated at N terminus, including His$_6$ tag, His-SUMO (small ubiquitin-like modifying protein) tag and GST (Glutathione S-transferase) tag. All twelve constructs were successfully cloned and transformed into BL21-CodonPlus (DE3) *E. coli* expressing cell line.

5.3.2 Dysferlin C2B and C2C domains show low solubilities

Initially, all the constructs were tested for expression and solubility using the same conditions for the wild-type C2A domain described in **Chapter 2.2.1**. However, though expressed well, all proteins were found to be completely insoluble. Therefore, small-scale expression screening was performed for each construct by varying multiple conditions as follows:

(i) Culture condition: LB and DYT medium were used as the culture for cell growth.

(ii) Induction condition: Different concentrations of IPTG (0.05 to 0.5 mM) were used to induce protein expression.

(iii) Growth temperature: Cells were grown at 37 ˚C and 16 ˚C following IPTG induction for 5 hours and 20 hours, respectively.

(iv) Buffer conditions: Buffers containing different salt concentrations, w/o addition of detergents, and at different pH were used to resuspend the harvested cells prior to lysis.

The cell lysate was separated, by centrifugation, into soluble fractions (supernatant) and insoluble fractions (pellet). Some test results are presented in **Figure 5.4**, including His-
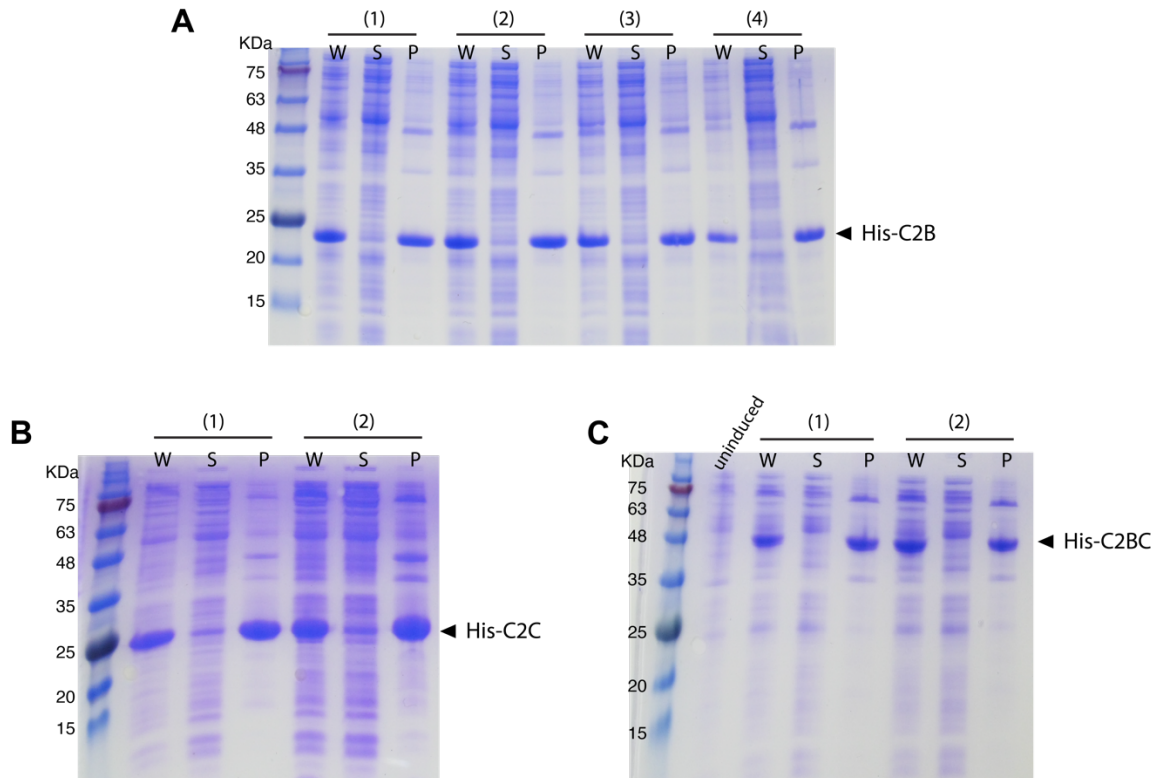
Figure 5. 4 Representative experiments of test expression and soluble expression showing insolubility of the dysferlin C2B and C2C domains.

His-C2B, His-C2C and His-C2BC were expressed in E. coli cells and the total protein (W), supernatant (S) and pellet (P) were checked by SDS-PAGE gel. For each protein, variable conditions were tested. **(A)** Different buffer conditions: (1) 25 mM Tris, 1 mM DTT, 5 mM NaCl, pH 7.5. (2) 25 mM Tris, 1 mM DTT, 3 mM $CaCl_2$, pH 7.5. (3) 25 mM Tris, 1 mM DTT, 100 mM NaCl, 5% glycerol, pH 7.5. (4) 25 mM Tris, 1 mM DTT, 100 mM NaCl, 2% Triton X-100, pH 7.5. **(B)** Different growth temperatures: (1) 37 ˚C following IPTG induction for 5 hours. (2) 16 ˚C following IPTG induction for 20 hours. **(C)** Different IPTG concentrations: (1) Induced by 0.5 mM ITPG. (2) Induced by 1 mM IPTG. All of them showed great degree of insolubility.

C2B, His-C2C and His-C2BC. **Figure 5.4 A** shows results of four buffer conditions tested for His-C2B consisted of various NaCl concentrations added with different types of detergents (e.g. Triton X-100). The SDS-PAGE gels of His-C2C and His-C2BC demonstrate the expression and solubility of the proteins grown under different temperatures and induced by different concentrations of IPTG, respectively (**Figure 5.4 B - C**). It can be clearly seen that all the three proteins showed high levels of overexpression with heavy bands of expected molecular weight (MW) on SDS-PAGE gels. However, none of the constructs produced soluble protein, as almost the entire portion was found to precipitate in the cell pellet as insoluble fractions, and we barely detected any protein in the supernatant.

Extensive tests were also carried out for the same proteins employed with SUMO and GST tag, as well as all the other constructs including C2BC-DysF. Unfortunately, most of the constructs exhibited severe insolubility issue similar to the ones discussed above, which hindered further purification. Nonetheless, by performing expression screening, two candidates, His-SUMO-C2B and GST-C2BC-DysF, showed promising possibilities for solubilization among the twelve, which are described below.

5.3.3 Solubilization and purification of His-SUMO-C2B

In attempt to test the expression and solubility of His-SUMO-C2B, we discovered that the pH of lysis buffer had a significant influence on the protein solubility. Using a buffer at physiological pH (7.5), no evident protein could be observed in the supernatant. In contrast, by increasing the pH (9.5), a clearly visible band corresponding to the expected MW

appeared in the soluble fraction (**Figure 5.5 A**). Next, LB and M9 minimal medium were tested as the growth culture using the buffer condition at pH 9.5. Both beautifully showed specific bands in the soluble fractions, suggesting that it is promising in attaining labeled His-SUMO-C2B protein from minimal media for NMR studies (**Figure 5.5 B**). Interestingly, we also discovered that once the protein has been partially solubilized from the cell lysate using higher pH buffer, it stays soluble safely at pH 7.5 in the subsequent purification steps. To explain this, we reasoned that as a putative membrane binding protein, C2B domain associates with the bacterial cell membrane, thus precipitates along with the membrane as the cell debris by centrifugation. High pH contributes to the disruption of the association and extraction the protein off the membrane. This strategy has also been suggested by past studies (Smith, 2011).

In order to obtain His-tagged recombinant His-SUMO-C2B protein, the supernatant containing the protein was loaded onto a Ni^{2+}-charged IMAC (HisTrap FF column) following bacterial overexpression and cell lysis. A concentration of 10 mM imidazole was added to both binding and wash buffers to interfere with the weak binding of other proteins. Before elution, wash with a gradient concentration of imidazole was conducted to remove more background impurity. The His-SUMO-C2B protein was then eluted with a higher concentration of imidazole. A Coomassie-stained SDS-PAGE gel of the fractions is presented in **Figure 5.5 C** showing that the His-SUMO-C2B protein was successfully isolated from the cell lysate with high purity.
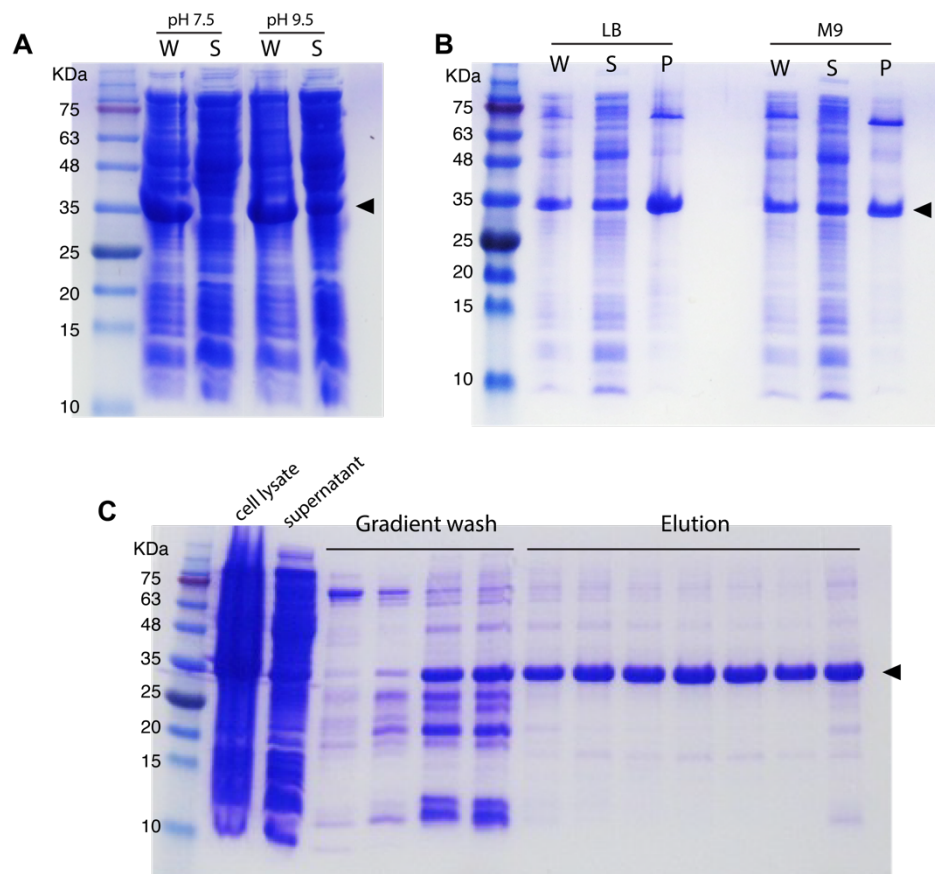
Figure 5. 5 Solubilization and purification of His-SUMO-C2B

(A) Test expression of His-SUMO-C2B and the total protein (W), supernatant (S) were checked by SDS-PAGE gel. Buffers containing 50 mM Tris, 300 mM NaCl, 10 mM imidazole, 0.1 % Triton X-100, 5% glycerol at pH 7.5 and 9.5 were respectively used. A visible band corresponding to the expected MW appeared in the soluble fraction at pH 9.5. **(B)** LB and M9 minimal medium were tested as the growth culture using the buffer condition at pH 9.5. **(C)** Purification of His-SUMO-C2B by HisTrap FF chromatography monitored by SDSPAGE stained with Coomassie blue. Cell lysate was obtained following cell lysis and ultracentrifugation and loaded onto HisTrap FF column. His-SUMO-C2B was then eluted by increasing the level of imidazole in the elution buffer (black arrow).

After the first purification step, Ulp1 protease was added attempting to cleave the SUMO tag. Ulp1 is known as SUMO protease, highly specific for the SUMO protein fusion, recognizing the tertiary structure of SUMO and removing it from recombinant proteins. Severe precipitation was seen immediately after the addition of Ulp1 protease. The precipitate was discarded following centrifugation and the supernatant was analyzed by SDS-PAGE. As shown **Figure 5.6 A**, before centrifugation, three main bands could be recognized which presumably correspond to Ulp1, His-SUMO and C2B, indicating the SUMO-tag was successfully cleaved by Ulp1. After the elimination of insoluble fraction, the lowest band disappeared from the supernatant due to precipitation. A HisTrap FF column was then applied and two proteins were eluted by imidazole (**Figure 5.6 A**). Since the molecular weights of SUMO tag and C2B are fairly close (13.3 and 14.9 kDa), a sample from one of the elution fractions was sent for electrospray ionization mass spectrometry (ESI-MS). The mass spectrum showed the main species corresponds to the mass of His-SUMO tag (13.3 kDa); no peak indicative of cleaved C2B protein was found in the spectrum (**Figure 5.6 B**). Different buffer conditions were tested for the cleavage reaction, however, no soluble C2B protein could be attained. This issue is seemingly due to the fact that the protein is either not properly folded or exists as soluble aggregates in partially folded forms (Raran-Kurussi and Waugh, 2016). Therefore, the SUMO tag was kept for the subsequent experiments.

5.3.3 Folding of dysferlin C2B domain

To examine the folding of His-SUMO-C2B, the ^{1}H^{15}N-HSQC spectrum was recorded by NMR spectroscopy. Large spectral dispersion is expected for a well-folded protein. The
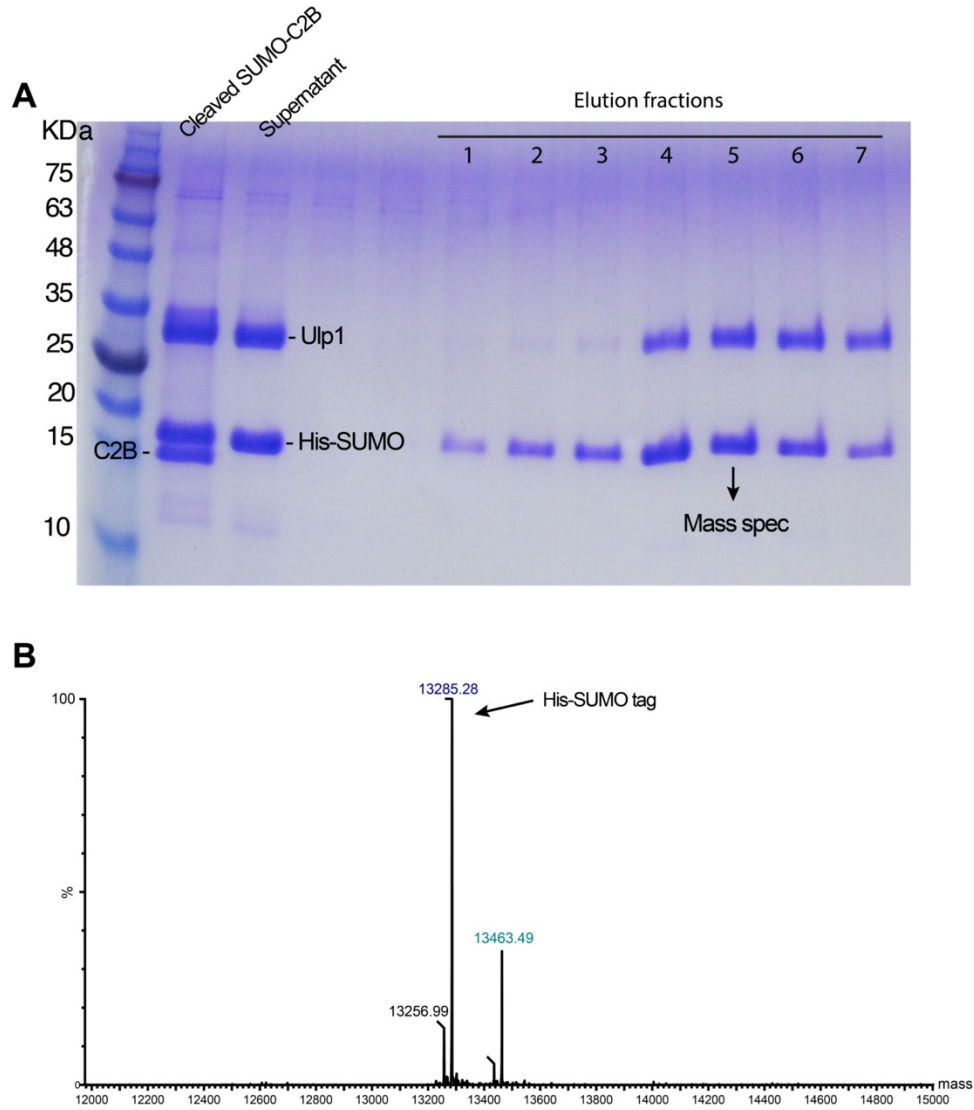
Figure 5. 6 Ulp1 cleavage of His-SUMO-C2B.

(A) Ulp1 protease was added to purified His-SUMO-C2B (first lane) and the precipitate was discarded following centrifugation and the supernatant was analyzed (second lane). A HisTrap FF column was then applied and two proteins were eluted by imidazole. Fraction 5 was taken for mass spectrometry. **(B)** Mass spectrum showing the main species corresponds to the mass of His-SUMO tag (13.3 kDa).

spectrum of His-SUMO-C2B demonstrated a mixture of well-dispersed strong signals and resonances with very low intensities (**Figure 5.7 A**). Then His-SUMO empty vector was expressed and uniformly ^{15}N-labeled. The ^{15}N-labeled His-SUMO protein was purified and ^{1}H^{15}N-HSQC spectrum was collected. By superimposing the spectrum of His-SUMO-C2B and His-SUMO, it can be clearly seen that a majority of strong signals from His-SUMO-C2B overlapped with those of His-SUMO (**Figure 5.7 A**), indicating the SUMO tag is properly folded with no structural change linked with C2B domain. On the other hand, a few resonances can be observed in the spectrum of His-SUMO-C2B that do not derive from His-SUMO. These signals are centralized from 7.00 to 8.25 ppm over ^{1}H dimension and the signal intensities are strikingly lower than those of His-SUMO. In addition, the number of resonances in the spectrum (~30) is much smaller than the number of amides in the C2B domain (133 residues). These observations suggest that the C2B domain may be largely unfolded or aggregated without stable secondary structures.

The folding state of His-SUMO-C2B was also checked by circular dichroism. Unlike the CD spectra of dysferlin C2A domain that exhibits a prominent negative peak at 215 nm, indicative of β sheet structure, the spectra of His-SUMO-C2B showed maximal negative signal around 205 nm (**Figure 5.8 A**). SUMO contains secondary structures of β strands and α helices, which likely contribute to the small negative peak at 225 nm. Therefore, the negative peak at 205 nm represents predominant existence of unstructured components which presumably belongs to the C2B domain. The CD data demonstrates good agreement with the NMR results, as well as the fact that C2B domain precipitates after the cleavage of His-SUMO tag. As described in **Chapter 5.3.1**, the dysferlin C2B and C2C domains are
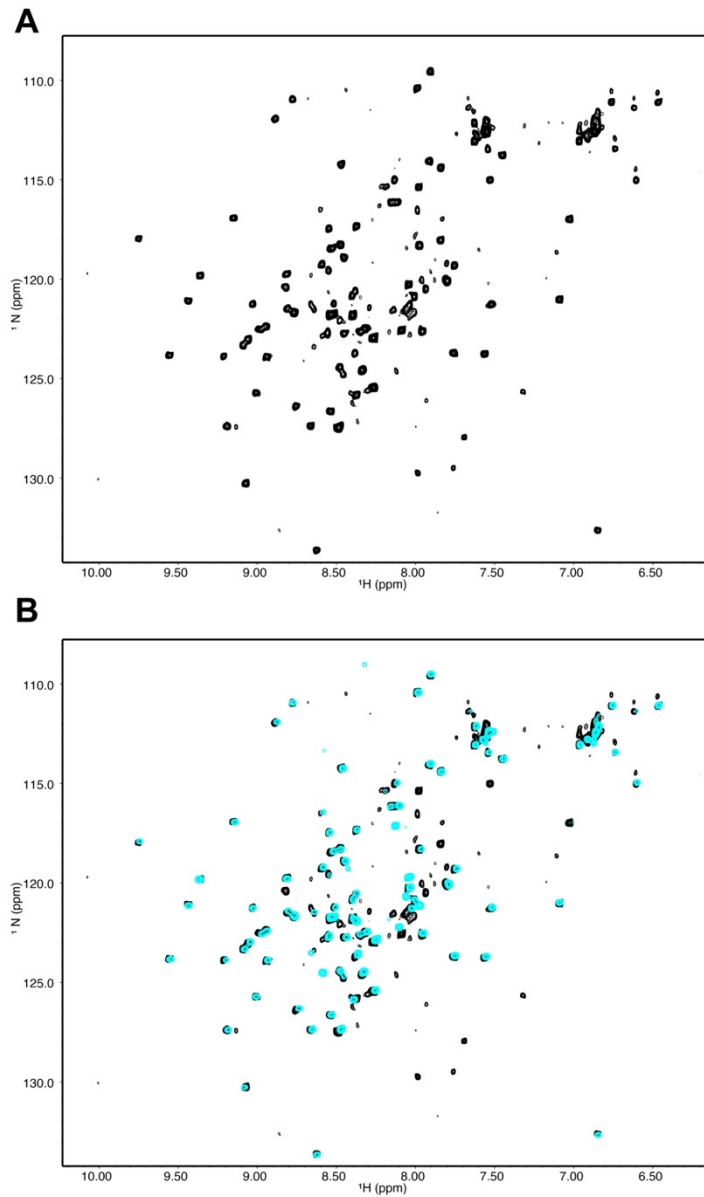
Figure 5. 7 ^{1}H-^{15}N HSQC spectra of His-SUMO-C2B and His-SUMO.

(A) ^{1}H-^{15}N HSQC spectrum of uniformly ^{15}N-labeled His-SUMO-C2B. **(B)** Overlaid HSQC spectra of His-SUMO-C2B (black) and His-SUMO (cyan). The buffer conditions are: 25 mM HEPES, 150 mM NaCl, 250 μM TECP, pH 7.5.
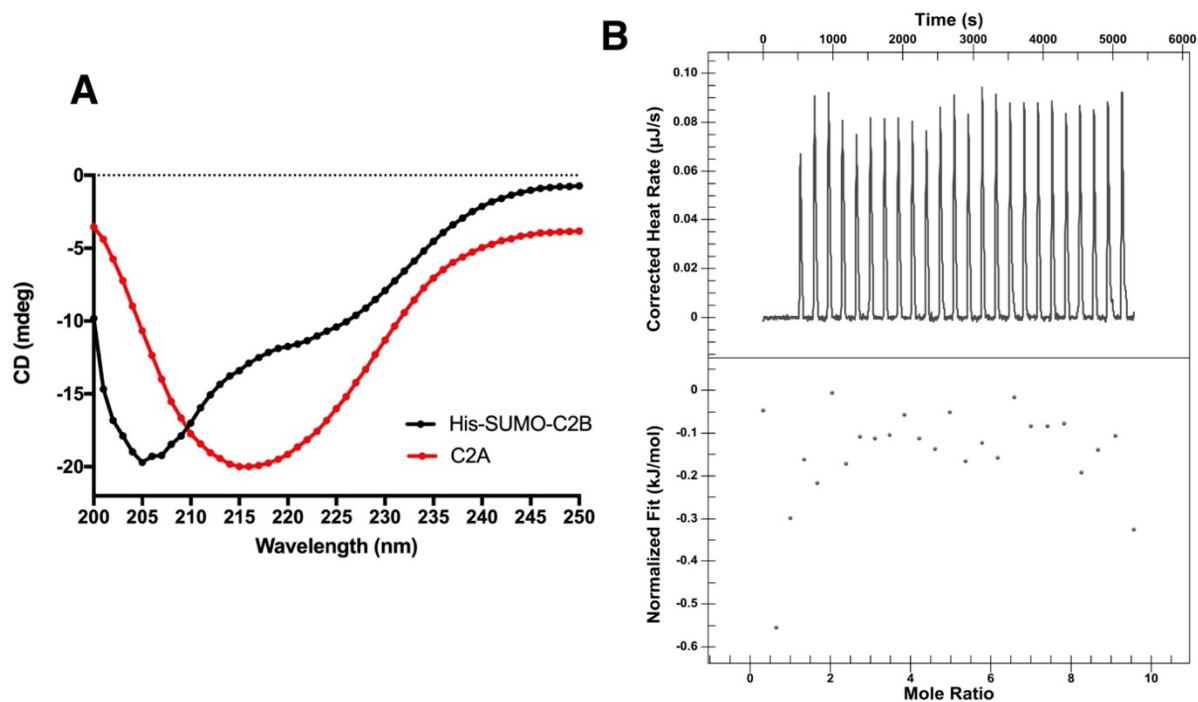
Figure 5. 8 Secondary structure and Ca^{2+}-binding of His-SUMO-C2B.

(A) Circular dichroism spectra of His-SUMO-C2B (black) and dysferlin C2A domain (red) from 250 – 200 nm. The measurements were taken at 25 °C in the buffer conditions of 20 mM KH$_2$PO$_4$, pH 7.5. The buffer background was subtracted. **(B)** ITC analysis of Ca^{2+} binding to His-SUMO-C2B showing no binding. Data was collected at 25 °C with 25 mM HEPES, 150 mM NaCl, 250 μM TCEP, pH 7.5 buffer conditions.

predicted to adopt an arched-shaped arrangement as an intact module through interdomain interactions (**Figure 5.2 C**). Thus, we reasoned that folding of the C2B domain might require connection with C2C domain or other binding partners within dysferlin.

Previous study reported that dysferlin C2B domain binds to one Ca^{2+} ion (Abdullah et al., 2014). Here Ca^{2+} titration to His-SUMO-C2B was performed by ITC. The ITC data showed minute heat change upon titration of large amount of calcium (**Figure 5.8 B**), suggesting His-SUMO-C2B is Ca^{2+} insensitive. Nevertheless, this result should be considered with caution for the unfolded state of C2B domain might affect its Ca^{2+} binding property.

5.3.4 Interaction study between dysferlin C2A and C2B domain

Interaction between C2 domains has been revealed for the C2A and C2B domain of synaptotagmin 1 and the association was shown to play an important role in regulating exocytosis (Evans et al., 2016; Fuson et al., 2007). Till now, cooperation between dysferlin C2 domains has not been examined yet. We queried whether there is interdomain interaction between the C2A and C2B domain of dysferlin since both domains have been generated. Although the C2B domain was found to remain largely unfolded, it is possible that it folds upon association with its binding partner, which is a common feature of many intrinsically disordered proteins (Wright and Dyson, 2009).

A preliminary interaction study was performed by NMR spectroscopy. First, $^{1}H^{15}N$-HSQC spectra of ^{15}N-labeled apo-C2A alone, and apo-C2A in the presence of 0.5 equivalents of unlabeled His-SUMO-C2B were collected. Upon addition of His-SUMO-C2B, chemical

shift changes were clearly seen for peaks corresponding to residues T14, I19, A26 and K32, while most of other peaks remained unchanged (**Figure 5.9**). Subsequently, $^1H^{15}N$-HSQC spectra of ^{15}N-labeled Ca^{2+}-C2A in the absence and presence of 0.5 equivalents of unlabeled His-SUMO-C2B were recorded. Superimposition of two spectra showed changes of many peaks, including chemical shift change of I19, H72, R77, R79, K32, T35 and K36 (**Figure 5.10**). Moreover, some peaks in the spectrum of Ca^{2+}-C2A disappeared, accompanied with appearance of new peaks upon addition of His-SUMO-C2B. All these findings suggest that His-SUMO-C2B interacts with the C2A domain in both apo and Ca^{2+}-bound state. By mapping the residues that showed the largest chemical shift changes on the structure of dysferlin C2A domain, it was found that almost all the residues are located on the one side of the β sandwich (**Figure 5.11**). Specifically, the β sheet groove formed by β2, 3, and 5, and the Ca^{2+}-binding loops (loop 1-3) are where these residues lay on and are likely to be the binding interface. Therefore, it is tempting to propose that His-SUMO-C2B binds to C2A domain and the binding results in conformational changes of the β strands on one side, as well as the Ca^{2+}-binding loops.

Again, these results should be interpreted with caution for two reasons: (1) Although there is no evidence showing interaction between C2 domains and SUMO protein, this possibility cannot be ruled out. A control experiment examining interaction between the SUMO tag and C2A domain is necessary. (2) In our study, only 0.5 equivalents of His-SUMO-C2B was added into the C2A sample due to the difficulty of obtaining concentrated C2B protein. The chemical shift changes of peaks were putatively identified based on their
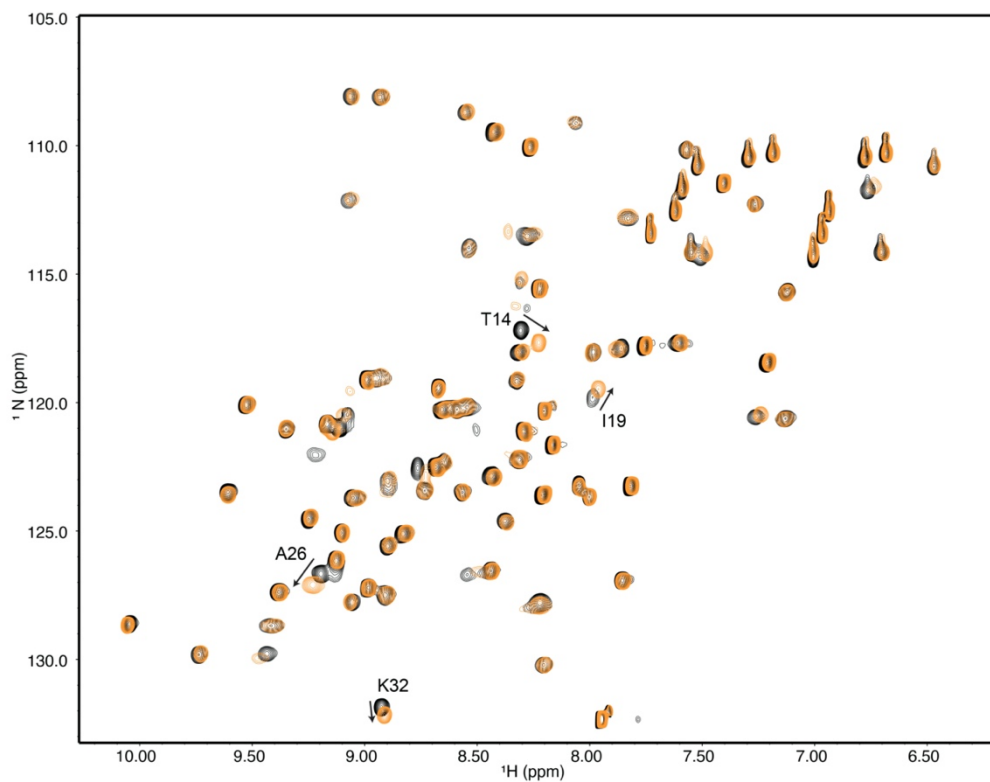
Figure 5. 9 NMR spectra showing interaction of apo-C2A with SUMO-C2B.

Overlaid ^{1}H-^{15}N HSQC spectrum of apo-C2A (black) and apo-C2A mixed with His-SUMO-C2B (orange). Chemical shift changes of peaks corresponding to T14, I19, A26 and K32 are indicated with arrows.
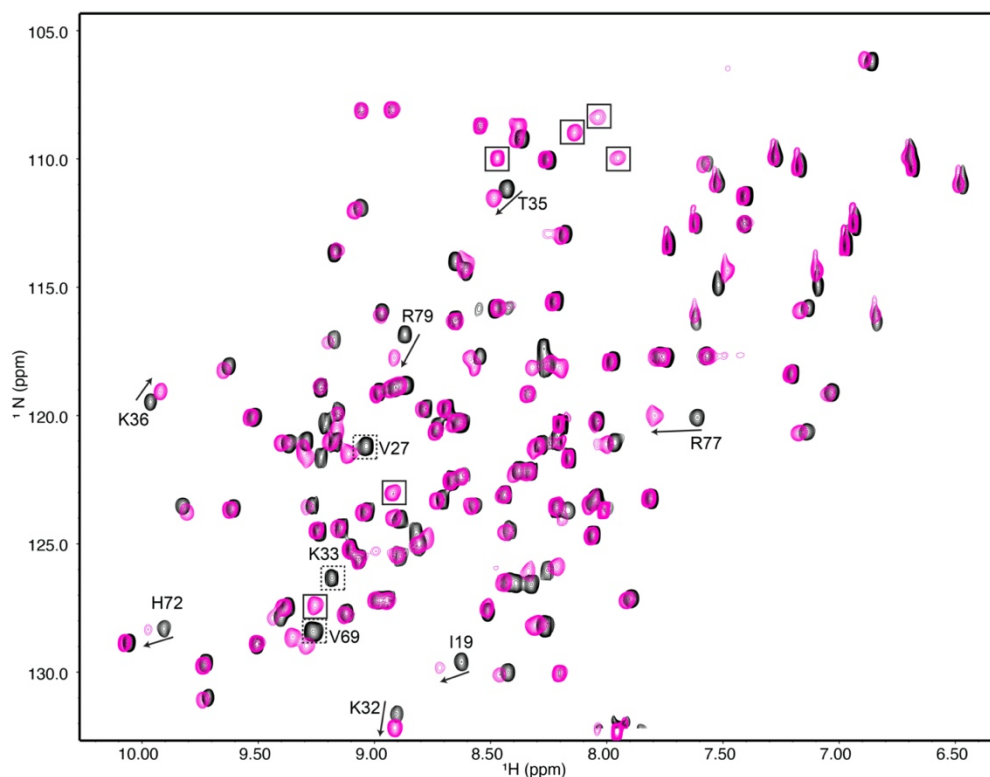
Figure 5. 10 NMR spectra showing interaction of Ca²⁺-C2A with SUMO-C2B.

Overlaid ¹H-¹⁵N HSQC spectrum of Ca²⁺-C2A (black) and Ca²⁺-C2A mixed with His-SUMO-C2B (pink). Chemical shift changes of peaks corresponding to I19, K32, T35, K36, H72, R77 and R79 are indicated with arrows. Peaks that disappeared upon addition of His-SUMO-C2B are labeled in dashed boxes (V69, V27 and K33). New peaks that are yet to be identified are labeled in black boxes.
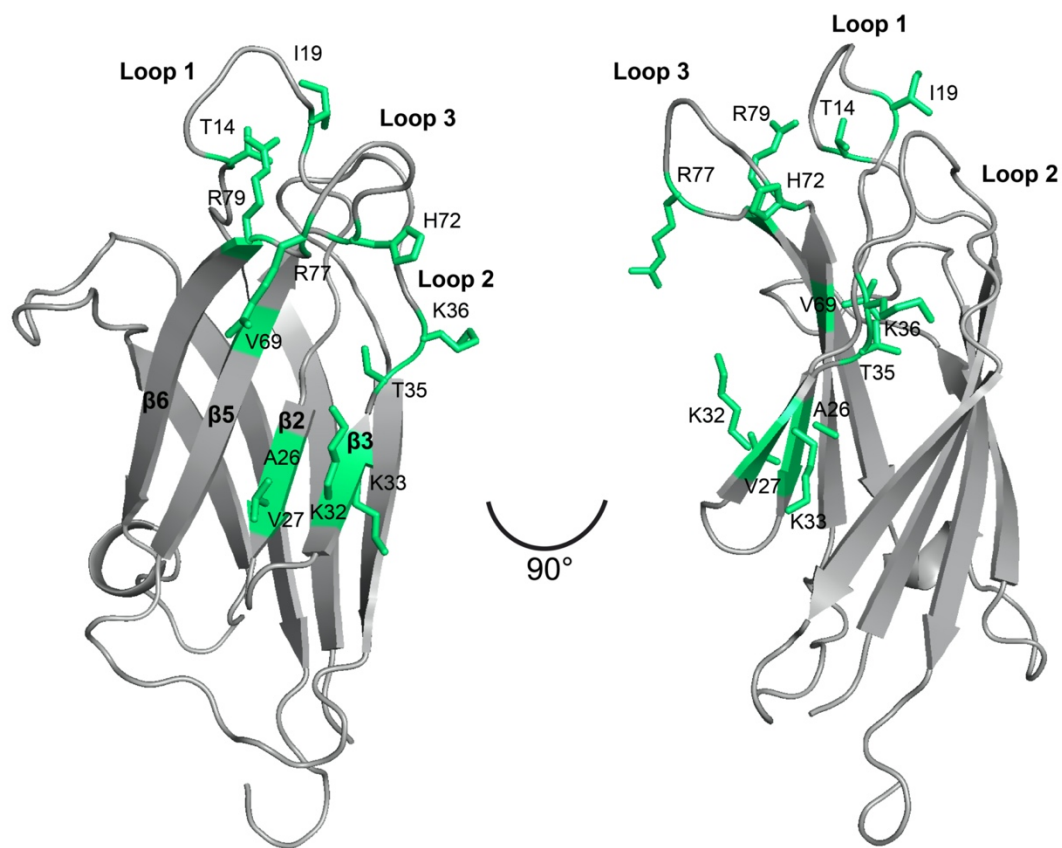
Figure 5. 11 Identification of the His-SUMO-C2B binding region on dysferlin C2A.

Residues experiencing significant chemical shift changes in the NMR spectra upon His-SUMO-C2B binding are mapped on the C2A domain structure, and represented in sticks and explicitly labeled. All the residues are located on the one side of the β sandwich. In particular, A26, V27, K32, K33, and V69 are on the β sheet groove formed by β2, 3, and 5. The other residues are in the Ca^{2+}-binding loops (loop 1-3).

positions (**Figure 5.9 - 5.10**). In the future, a titration experiment needs to be performed which allows us to follow the peak movements for pursuing accurate results.

5.3.5 Expression and purification of GST-C2BC-DysF

Extensive test expression was carried out for GST-C2BC-DysF, and growth at 37 °C and 16 °C following IPTG induction was found to yield most soluble protein. Different buffer conditions were also tested and one example is demonstrated in **Figure 5.12 A**. Generally, at physiological pH (7.5), although a large portion of the protein precipitated, some could be seen in the soluble fraction. The solubility of GST-C2BC-DysF does not seem to be salt-dependent, the amounts of soluble protein were similar on SDS-PAGE gel in all the buffer conditions. PBS buffer was then used as the lysis buffer for protein purification.

In the large-scale purification, using a glutathione-linked sepharose column (GSTrap FF), one protein showing a molecular weight approximate to GST-C2BC-DysF (82 kDa) was eluted (**Figure 5.12 B**). To examine whether it was the desired protein, Prescission protease was added to the eluted protein. Prescission protease is widely used for specifically cleavage of GST tag. Results are shown in **Figure 5.12 C**: In addition to the bands indicative of GST-C2BC-DysF (82 kDa) and Prescission protease (50 kDa), two new bands were shown on the gel, corresponding to the molecular weight of C2BC-DysF (56 kDa) and GST tag (26 kDa). These preliminary tests indicate that GST-C2BC-DysF could be successfully purified and cleaved.
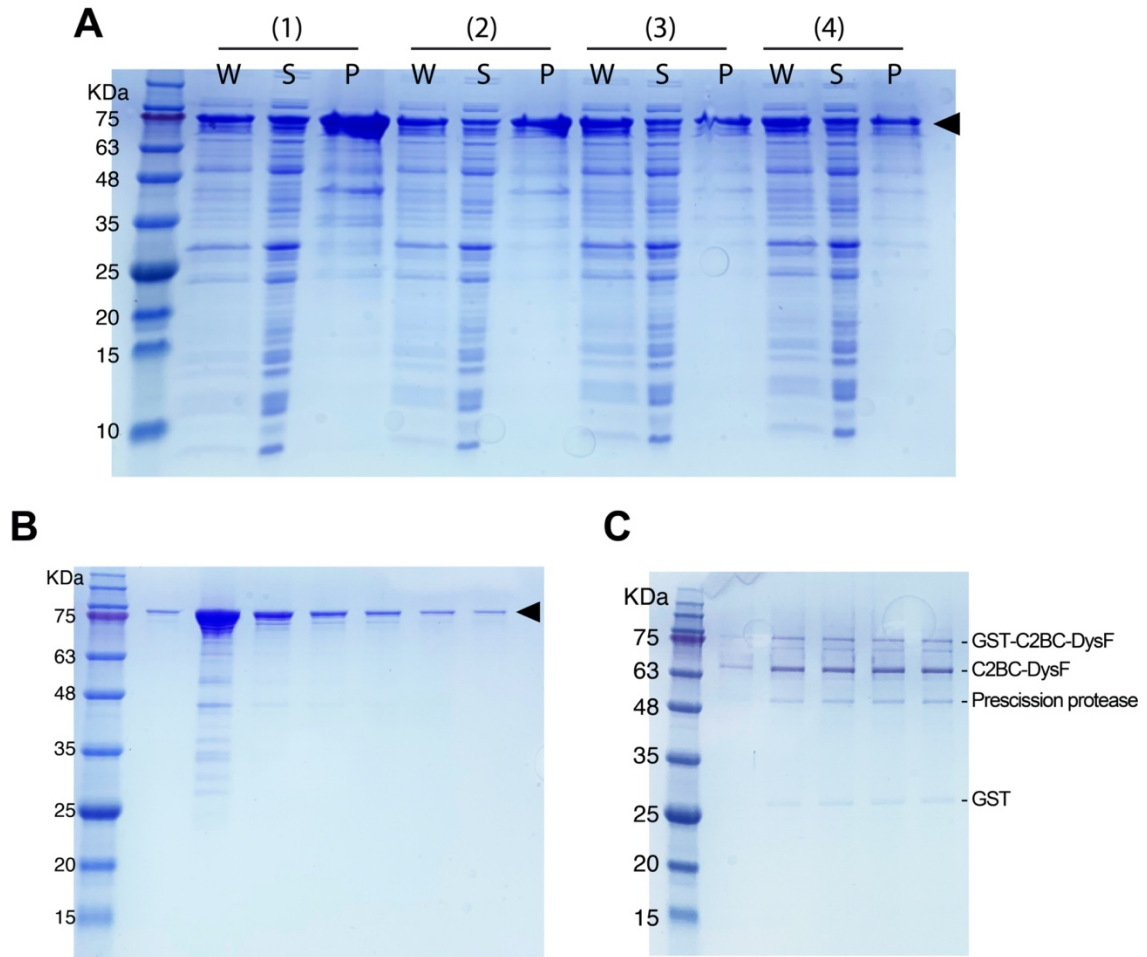
Figure 5. 12 Solubilization and purification of GST-C2BC-DysF

(A) Test expression of GST-C2BC-DysF in different buffer conditions. The cells were grown at 37 ˚C and 16 ˚C following IPTG induction. The total protein (W), supernatant (S) were checked by SDS-PAGE gel. The buffer used are as follows: (1) 20 mM KH_2PO_4, pH 7.5. (2) 25 mM HEPES, 150 mM NaCl, pH 7.5. (3) 25 mM Tris, 300 mM NaCl, pH 7.5. (4) PBS (140 mM NaCl, 2.7 mM KCl, 10 mM Na_2HPO_4, 1.8 mM KH_2PO_4, pH 7.3). Band corresponding to the expected MW (82 kDa) is indicated with the black arrow. **(B)** Purification of GST-C2BC-DysF using a glutathione-linked sepharose column (GSTrap FF). One protein showing a molecular weight approximate to GST-C2BC-DysF was eluted. **(C)** Prescission protease cleavage of GST-C2BC-DysF showing the protein was mostly cleaved. Bands indicative of uncleaved GST-C2BC-DysF (82 kDa), Prescission protease (50 kDa), C2BC-DysF (56 kDa) and GST tag (26 kDa) are labeled on the right.

However, a workable concentration of C2BC-DysF has not been attained yet, as the protein precipitated at much low concentrations. Further optimization for more production needs to be done in the future.

5.4 Discussion

5.4.1 Insolubility issue of C2B and C2C domains

In this chapter, I pursued study on the dysferlin C2B and C2C domains by combining experimental and computational approaches. A considerable amount of effort was made and the major bottleneck this study encountered was the insolubility of the proteins. As a structure predominantly composed of β sheets with hydrophobic residues, it is not surprising for a C2 domain to be insoluble in solution. In addition, the lipid binding properties of C2 domains can possibly drive association with *E. coli* membranes during protein expression, causing difficulty in extracting the protein. Although we were not able to produce enough soluble proteins required for structural characterization, this work represents an important step forward in designing the C2B and C2C proteins with more precise domain boundaries. The two workable constructs that were generated, His-SUMO-C2B and GST-C2BC-DysF, looked promising for future study if optimization is made.

Further directions are suggested as follows: (1) In the process of protein purification, unfolding and subsequent refolding could be carried out. For example, previous studies on

the C2 domains of cytosolic phospholipase A2 (cPLA$_2$) and plant phospholipase D (PLD) used 6 M guanidine HCl (GndHCl) and 8 M urea to successfully extract the proteins from inclusion bodies and refolded the proteins with gel filtration column (Nalefski et al., 1998; Zheng et al., 2000). Mild denaturation is also recommended (e.g. extreme pH, low concentrations of GndHCl or urea), as we noticed significantly increased solubility of C2B and C2C domains under pH 11 (data not shown). (2) Methods to disrupt the association of C2 domains with *E. coli* membranes could be developed. In our work, we found that a combination of detergent and high pH led to release of the C2B domain from the bacterial membrane. A study on perforin C2 domain obtained properly folded protein by mutating four hydrophobic aromatic residues in the loops (Trp427, Tyr430, Tyr486, and Trp488) that were assumed to contribute to the interaction with *E. coli* membranes (Yagi et al., 2015). The computational models of dysferlin C2B and C2C domains both show the presence of hydrophobic aromatic residues on the loops. Thus, the above approach could be worthwhile to conduct in the future.

5.4.2 Interplay between C2 domains

In addition to the Ca^{2+} and lipid binding properties, there has been a number of studies providing evidence for the interdomain interactions between C2 domains, such as the C2A and C2B domain of synaptotagmin 1 (Evans et al., 2016; Fuson et al., 2007). Besides, the C2 domains dimerization has been reported for RIM1α C2B domain (Guan et al., 2007), Munc 13-1 C2A domain (Lu et al., 2006), and dysferlin C2 domains (Xu et al., 2011).

Our preliminary NMR data suggested a possible interaction between the dysferlin C2A and C2B domains and identified the binding region on the C2A domain (**Figure 5.11**). Interestingly, the binding site on dysferlin C2A domain shows high resemblance to that of the Munc 13-1 C2A homodimer (Lu et al., 2006). The Munc13–1 C2A domain forms a stable homodimer and the X-ray crystal structure shows that the dimerization is mediated by the concave surfaces of the β-sheets formed by strands 3, 2, 5, and 6 of each monomer. These surfaces pack in an antiparallel orientation, twisting around each other. The binding interface arises from the formation of multiple hydrophobic, ionic, and hydrogen-bonding interactions between side chains of both monomers (**Figure 5.13 A**). By overlapping the structures of Munc13–1 C2A monomer with the dysferlin C2A domain, the binding sites on the two domains were found in the same region: the concave surfaces formed by β2, 3, 5 and 6 (**Figure 5.13 B**). More particularly, some residues on the dysferlin C2A domain, that were identified to be important for binding to the C2B domain, aligned well with the binding residues in Munc13–1 C2A homodimer. This finding indicates that the ability of the C2 domains to homodimerize/heterodimerize is possibly shared in a wide variety of proteins. We hypothesize that the dysferlin C2A domain dimerizes with C2B domain in a Ca^{2+}-independent manner. The functional significance of this dimerization is not clear. One guess is that it may compete with the C2B-C2C module in response to Ca^{2+}, or with other protein interactions of the C2A domain. Also, the concave surfaces formed by β2, 3, 5 and 6 may serve as the target site for protein interactions.
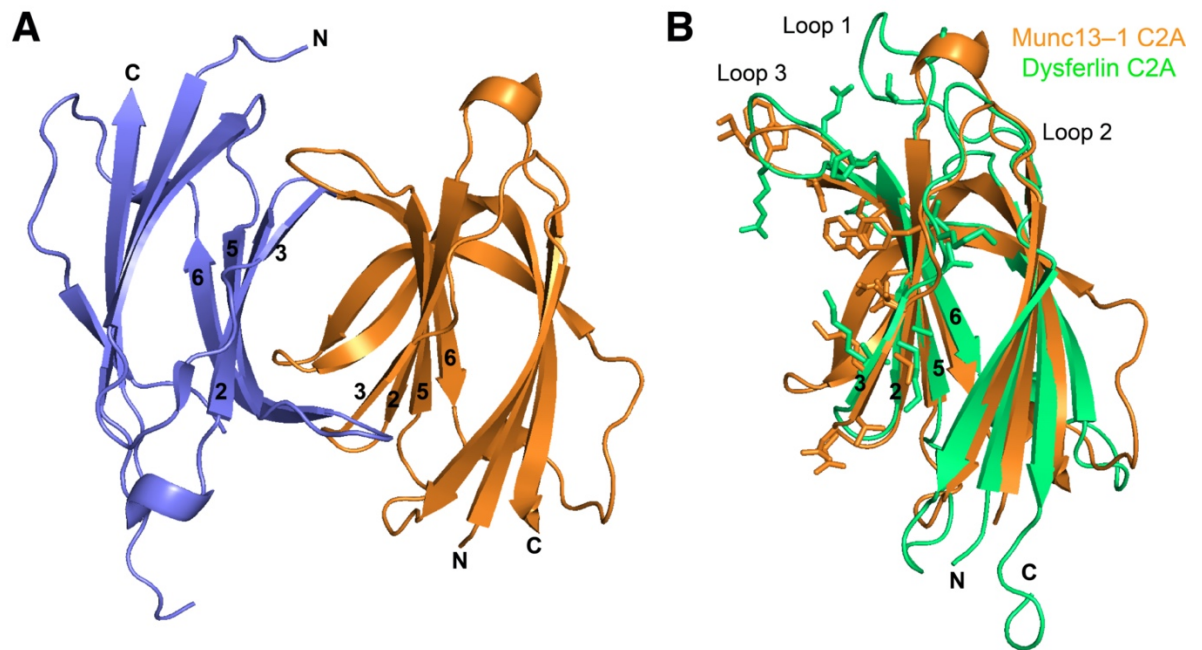
Figure 5. 13 Munc 13-1 C2A homodimer and superposition of Munc 13-1 C2A monomer and dysferlin C2A domain.

(A) Ribbon diagram of the Munc13–1 C2A domain homodimer formed by two monomers (blue and orange) showing a top view of the β-barrel like structure. The β-strands are labeled with numbers, and the N- and C-termini are indicated with N and C, respectively. (PDB: 2CJT) **(B)** Superposition of the structures of Munc 13-1 C2A monomer (orange) and dysferlin C2A domain (green). The side chains of residues involved in intermolecular contacts of Munc13–1 C2A domain homodimerization and dysferlin C2A-C2B interaction are shown as sticks.

5.5 References

Abdullah, N., Padmanarayana, M., Marty, N.J., and Johnson, C.P. (2014). Quantitation of the Calcium and Membrane Binding Properties of the C2 Domains of Dysferlin. Biophys. J. *106*, 382–389.

Cacciottolo, M., Numitone, G., Aurino, S., Caserta, I.R., Fanin, M., Politano, L., Minetti, C., Ricci, E., Piluso, G., Angelini, C., et al. (2011). Muscular dystrophy with marked Dysferlin deficiency is consistently caused by primary dysferlin gene mutations. Eur. J. Hum. Genet. *19*, 974–980.

Chapman, E.R., An, S., Edwardson, J.M., and Jahn, R. (1996). A Novel Function for the Second C2 Domain of Synaptotagmin Ca-TRIGGERED DIMERIZATION. J. Biol. Chem. *271*, 5844–5849.

Delaglio, F., Grzesiek, S., Vuister, G.W., Zhu, G., Pfeifer, J., and Bax, A. (1995). NMRPipe: A multidimensional spectral processing system based on UNIX pipes. J. Biomol. NMR *6*, 277–293.

van den Ent, F., and Löwe, J. (2006). RF cloning: a restriction-free method for inserting target genes into plasmids. J. Biochem. Biophys. Methods *67*, 67–74.

Essen, L.-O., Perisic, O., Lynch, D.E., Katan, M., and Williams, R.L. (1997). A Ternary Metal Binding Site in the C2 Domain of Phosphoinositide-Specific Phospholipase C-δ1 [†], [‡]. Biochemistry *36*, 2753–2762.

Evans, C.S., He, Z., Bai, H., Lou, X., Jeggle, P., Sutton, R.B., Edwardson, J.M., and Chapman, E.R. (2016). Functional analysis of the interface between the tandem C2 domains of synaptotagmin-1. Mol. Biol. Cell *27*, 979–989.

Evesson, F.J., Peat, R.A., Lek, A., Brilot, F., Lo, H.P., Dale, R.C., Parton, R.G., North, K.N., and Cooper, S.T. (2010). Reduced Plasma Membrane Expression of Dysferlin Mutants Is Attributed to Accelerated Endocytosis via a Syntaxin-4-associated Pathway. J. Biol. Chem. *285*, 28529–28539.

Fuson, K.L., Montes, M., Robert, J.J., and Sutton, R.B. (2007). Structure of Human Synaptotagmin 1 C2AB in the Absence of Ca^{2+} Reveals a Novel Domain Association,. Biochemistry *46*, 13041–13048.

Guan, R., Dai, H., Tomchick, D.R., Dulubova, I., Machius, M., Südhof, T.C., and Rizo, J. (2007). Crystal Structure of the RIM1α C2B Domain at 1.7 Å Resolution,. Biochemistry *46*, 8988–8998.

Johnson, B.A., and Blevins, R.A. (1994). NMR View: A computer program for the visualization and analysis of NMR data. J. Biomol. NMR *4*, 603–614.

Krahn, M., Béroud, C., Labelle, V., Nguyen, K., Bernard, R., Bassez, G., Figarella-Branger, D., Fernandez, C., Bouvenot, J., Richard, I., et al. (2009). Analysis of the *DYSF* mutational

spectrum in a large cohort of patients: *DYSF* Mutational Spectrum in a Large Cohort. Hum. Mutat. *30*, E345–E375.

Llanga, T., Nagy, N., Conatser, L., Dial, C., Sutton, R.B., and Hirsch, M.L. (2017). Structure-Based Designed Nano-Dysferlin Significantly Improves Dysferlinopathy in BLA/J Mice. Mol. Ther. *25*, 2150–2162.

Lu, J., Machius, M., Dulubova, I., Dai, H., Südhof, T.C., Tomchick, D.R., and Rizo, J. (2006). Structural Basis for a Munc13–1 Homodimer to Munc13–1/RIM Heterodimer Switch. PLOS Biol. *4*, e192.

Nalefski, E.A., McDonagh, T., Somers, W., Seehra, J., Falke, J.J., and Clark, J.D. (1998). Independent Folding and Ligand Specificity of the C2 Calciumdependent Lipid Binding Domain of Cytosolic Phospholipase A2. J. Biol. Chem. *273*, 1365–1372.

Raran-Kurussi, S., and Waugh, D.S. (2016). A Dual Protease Approach for Expression and Affinity Purification of Recombinant Proteins. Anal. Biochem. *504*, 30–37.

Schauder, C.M., Wu, X., Saheki, Y., Narayanaswamy, P., Torta, F., Wenk, M.R., De Camilli, P., and Reinisch, K.M. (2014). Structure of a lipid-bound extended synaptotagmin indicates a role in lipid transfer. Nature *510*, 552–555.

Smith, S.M. (2011). Strategies for the Purification of Membrane Proteins. In Protein Chromatography: Methods and Protocols, D. Walls, and S.T. Loughran, eds. (Totowa, NJ: Humana Press), pp. 485–496.

Sula, A., Cole, A.R., Yeats, C., Orengo, C., and Keep, N.H. (2014). Crystal structures of the human Dysferlin inner DysF domain. BMC Struct. Biol. *14*, 3.

Therrien, C., Dodig, D., Karpati, G., and Sinnreich, M. (2006). Mutation impact on dysferlin inferred from database analysis and computer-based structural predictions. J. Neurol. Sci. *250*, 71–78.

Therrien, C., Di Fulvio, S., Pickles, S., and Sinnreich, M. (2009). Characterization of Lipid Binding Specificities of Dysferlin C2 Domains Reveals Novel Interactions with Phosphoinositides [†]. Biochemistry *48*, 2377–2384.

Woolger, N., Bournazos, A., Sophocleous, R.A., Evesson, F.J., Lek, A., Driemer, B., Sutton, R.B., and Cooper, S.T. (2017). Limited proteolysis as a tool to probe the tertiary conformation of dysferlin and structural consequences of patient missense variant L344P. J. Biol. Chem. *292*, 18577–18591.

Wright, P.E., and Dyson, H.J. (2009). Linking folding and binding. Curr. Opin. Struct. Biol. *19*, 31–38.

Xu, J., Bacaj, T., Zhou, A., Tomchick, D.R., Südhof, T.C., and Rizo, J. (2014). Structure and Ca^{2+}-Binding Properties of the Tandem C2 Domains of E-Syt2. Structure *22*, 269–280.

Xu, L., Pallikkuth, S., Hou, Z., Mignery, G.A., Robia, S.L., and Han, R. (2011). Dysferlin Forms a Dimer Mediated by the C2 Domains and the Transmembrane Domain In Vitro and in Living Cells. PLOS ONE *6*, e27884.

Yagi, H., Conroy, P.J., Leung, E.W.W., Law, R.H.P., Trapani, J.A., Voskoboinik, I., Whisstock, J.C., and Norton, R.S. (2015). Structural Basis for Ca^{2+}-mediated Interaction of the Perforin C2 Domain with Lipid Membranes. J. Biol. Chem. *290*, 25213–25226.

Zheng, L., Krishnamoorthi, R., Zolkiewski, M., and Wang, X. (2000). Distinct Ca^{2+} Binding Properties of Novel C2 Domains of Plant Phospholipase Dα and β. J. Biol. Chem. *275*, 19700–19706.

Chapter 6

Summary

6.1 Background

Dysferlin is a 230 kDa cytosolic-facing, membrane bound protein that includes seven C2 domains (C2A-C2G), three Fer domains (FerA, FerB, and FerI) and two DysF domains (Sula et al., 2014). It is a membrane repair protein involved in the trafficking of proteins and vesicles around injured membranes in skeletal muscle cells. Failure to repair injured sarcolemmal membranes leads to muscular dystrophy, a degenerative disorder that results in increasing weakness and gradual wasting of skeletal muscles.

The N-terminal C2A domain of dysferlin appears to be the major portion responsible for responding to calcium influx upon membrane damage and the activation of dysferlin. The C2A domain was identified to bind phospholipids in a Ca^{2+}-dependent fashion, mediating the fusion of lysosomes with the plasma membrane (Han et al., 2012; Therrien et al., 2009). The C2A domain also plays a regulatory role in interaction with other membrane repair proteins, such as AHNAK and MG53 (Huang et al., 2007; Matsuda et al., 2012). A crystal structure of the C2A domain was reported (**Figure 2.11 B**) (Fuson et al., 2014), yet there is much to be learned about the Ca^{2+} binding properties of the domain. Further, the importance of the C2A domain in dysferlin has been emphasized from a clinical standpoint as substitutions (e.g. W52R, V67D) in this region lead to limb-girdle muscular dystrophy

type 2B (LGMD2B) or Miyoshi myopathy (MM) (Krahn et al., 2009). However the molecular basis of pathogenic mechanisms still remains unclear.

Additionally, little information is available about the other C2 domains of dysferlin as well as the interdomain interactions. A limited proteolysis study suggested that C2B-C2C may function as an intact module and exist in a closed conformation (Woolger et al., 2017), consistent with the cellular function of the C2B-C2C motif in regulating dysferlin plasma membrane expression (Evesson et al., 2010). Another study demonstrated that all seven dysferlin C2 domains interact with Ca^{2+} with various binding affinities and stoichiometries (Abdullah et al., 2014). However, a comprehensive study on the structures and interactions of the other C2 domains with precise domain boundary determination is required .

6.2 New insights into dynamics and Ca^{2+} binding of the dysferlin C2A domain

In chapter 2, the work focused on the dynamics of the C2A domain on the basis of its NMR structure in the Ca^{2+}-free state. By employing a series of NMR methods, high flexibility within the loop region was identified to be a remarkable feature of the dysferlin C2A domain, which is rarely seen in other C2 domain containing proteins. A comparison is shown in **Figure 2.11**, which also highlights the powerful applications of NMR spectroscopy over other methods in probing protein dynamics. It was also proved that a striking decrease in the flexibility occurs upon calcium binding, in line with the finding that calcium stabilizes the structure of the C2A domain.

For EF-hand proteins, binding of calcium leads to a dramatic conformational change from "closed" to "open" (Ikura, 1996). In comparison, the mechanism of Ca^{2+} binding to C2 domains has for long been recognized to be different. Ca^{2+} immobilizes the structure of C2 domains but does not produce a significant structural change from a well-defined conformation to another (Shao et al., 1998). The main effect of Ca^{2+} binding on the C2 domain is to change the electrostatic potential of loop region rather than its structure. Our data further confirmed this knowledge and also suggested new pictures of calcium-dependent membrane repair process. The high flexibility in the apo-state may be functionally significant considering the major function of the C2A domain, which is calcium-sensitive membrane binding (Bansal et al., 2003; Han and Campbell, 2007). In the resting state of a cell when the dysferlin C2A domain is Ca^{2+}-free, the dynamics of the C2A domain may prevent it from binding to the lipid membrane. Unlike exocytosis, which occurs when the local $[Ca^{2+}]$ rises into the 10-100 μM range (Hille et al., 1999), membrane repair process is activated at a higher $[Ca^{2+}]$ concentration due to the millimolar range of $[Ca^{2+}]$ in the extracellular space. The remarkable flexible property of dysferlin C2A may be important for maintaining its exclusive function of membrane repair, so that it is not as readily triggered by low $[Ca^{2+}]$ as proteins involved in exocytosis (e.g. synaptotagmin). It is hypothesized that only upon the influx of calcium from the extracellular space as a result of membrane disruption, the C2A domain binds calcium and adapts a more ordered and rigid conformation, triggering membrane repair through lipid binding.

In chapter 3, the detailed Ca^{2+} binding properties of the dysferlin C2A domain was studied. Comparison of the binding sites, affinities and binding modes with other C2 domains was

discussed in **Chapter 3.4**. It is indeed fascinating that C2 domains exhibit a diverse array of Ca^{2+} binding properties that serve for the specific biological function. This work pursued a thorough characterization on the molecular mechanisms of Ca^{2+} binding to the C2A domain. Here, I would like to expand the discussion on the two striking findings.

In the previous crystal structure of the C2A domain (Fuson et al., 2014), there is a single Ca^{2+} coordinated to one of the six domains in the asymmetric unit and D16 was modeled to be a coordinating residue for another Ca^{2+} ion. Further, an ITC study showed that D16A substitution caused elimination of Ca^{2+} binding (Abdullah et al., 2014), which seems to support the postulation that D16 is a ligand for Ca^{2+}-binding. However, in our crystal structure of the Ca^{2+}-bound dysferlin C2A domain which contained four molecules in the asymmetric unit with two Ca^{2+} ion bound to each molecule, D16 does not bind to either of the Ca^{2+} ion. The oxygens of its side chain are beyond the maximum possible distance between ligand oxygen atoms and the calcium ion (**Figure 3.11 A**). This work for the first time identified the importance of the non-coordinating residue of C2 domains. Subsequent mutagenesis study showed consistent results with the previous literature. We attributed this observation to the change of the electrostatic potential of the loop region (**Figure 3.11 E - F**). By examining the sequence of dysferlin C2A with other C2 domain, it can be seen that the dysferlin C2A domain contains an additional aspartic acid in loop 1 compared to most of other C2 domains (D16, D18 and D21) (**Figure 1.4**). Our work has helped clarify the contribution of each aspartic acid and recognized "electrostatic potential" as a critical factor for calcium binding.

Another interesting finding was how substitution of a single residue can mimic the effect of Ca^{2+} ion. This was validated by our observation that C2A^{D71K} shares structural similarities with wild-type Ca^{2+}-C2A judging by their NMR spectra and the model we proposed (**Figure 3.14**). In fact, several previous studies on synaptotagmin have suggested the similar idea by testing the protein function in synaptic transmission (Stevens and Sullivan, 2003; Striegel et al., 2012; Yoshihara et al., 2010). Our work here provides strong supporting evidence for this idea on the molecular basis. It would be interesting to probe the lipid binding properties of wild-type C2A in both apo and Ca^{2+}-bound state as well as C2A^{D71K}, C2A^{D18K}, C2A^{D21K} and C2A^{D16K}. We predict that some of the substituted proteins would have the ability to bind negatively charged phospholipids in a similar manner as Ca^{2+}-C2A. Moreover, for some substitutions, the membrane repair activity of dysferlin might be preserved even the Ca^{2+}-binding for the C2A domain is abolished.

In summary, our work has provided novel insights for understanding the mechanisms of dysferlin-mediated membrane repair. In the resting state when the intracellular Ca^{2+} concentration is extremely low, the electrostatic repulsion caused by negative charged residues in the loops (D16, D18, D21, D71 and E73) inhibits the interaction between the C2A domain and membrane. Ca^{2+} influx due to membrane disruption results in an electrostatic switch of the loops from negative to positive, targeting the protein to the membrane, thus facilitates membrane fusion.

6.3 The tertiary folding of dysferlin C2A, C2B and C2C domains

In chapter 5, the research delved into the other parts of dysferlin attempting to characterize the structure and folding of the C2B and C2C domain. Unlike most of the C2 domain-containing proteins usually consist of one or two C2 domains such as synaptotagmins, the ferlin family proteins harbour five to seven C2 domains (Peulen et al., 2019). The tertiary folding of these domains is poorly understood: whether they are in linear arrangement or folded together through interdomain interactions?

Our NMR data provided the first evidence for the possible interaction between the C2A and C2B domain (**Figure 5.9 – 5.11**). Interestingly, the binding region on the dysferlin C2A domain was found to highly overlap with the binding interface of the Munc 13-1 C2A homodimer (Lu et al., 2006). Furthermore, although we have not been able to generate workable C2B-C2C construct, the computational model performed by our collaborator simulated the 3D structure of the C2B-C2C module on the basis of the C2A-C2B structure of extended synaptotagmin (**Figure 5.2**) (Schauder et al., 2014). The simulated model shows that C2B and C2C domain together adopt an arched-shaped arrangement joined by a linker sequence that forms an α-helix and packs against the two domains. The N and C termini of both domains are located at the bottom of the overall structure, whereas the putative calcium binding loops on the top. This C2B-C2C module was additionally supported by a limited proteolysis study on dysferlin, where C2B-C2C was found to exist in a closed conformation (Woolger et al., 2017).

Based on all the above knowledge, a model that depicts the tertiary folding and interdomain association between C2A, C2B and C2C domain is proposed. In this model, the crystal structure of dysferlin C2A domain was aligned with one of the monomer in the Munc 13-1 C2A homodimer. The dysferlin C2B-C2C structure was taken from the computational simulation and the C2B domain was aligned with the other monomer of the Munc 13-1 C2A homodimer. **Figure 6.1** demonstrates the result generated by PyMOL, showing the tertiary folding of the C2A, C2B and C2C domain. The C2A domain forms a heterodimer with C2B and the dimerization is mediated by the concave surfaces of the β-sheets of each domain. The two domains pack in an antiparallel orientation, twisting around each other. In this way, the C2A domain falls into the groove formed by the C2B-C2C module with the Ca^{2+}-binding loops faced inward to the bottom of the groove. **Figure 6.1 B** clearly shows that the three C2 domains overall adopt a compact closed conformation.

The closed conformation formed by the C2A, C2B and C2C domains indicates that the three domains may function in an autoinhibitory manner. Autoinhibition of protein activities mediated by C2 domains have been identified in some proteins including Nedd4, protein kinase C (PKC), and Smurf2 (Antal et al., 2015; Wang et al., 2010; Wiesner et al., 2007). For example, it was shown that the C2 domain mediates the autoinhibition of Nedd4-1 and Nedd4-2 through association with the HECT domain. Calcium disrupts binding of the C2 domain to the HECT domain and activates the E3 ubiquitin ligase activity of Nedd4 by releasing the autoinhibition. Here, we hypothesize that in the resting state of a cell when dysferlin is Ca^{2+}-free, the C2A, C2B and C2C domains form a closed conformation that autoinhibits the activity of C2A. This autoinhibition prevents the C2A
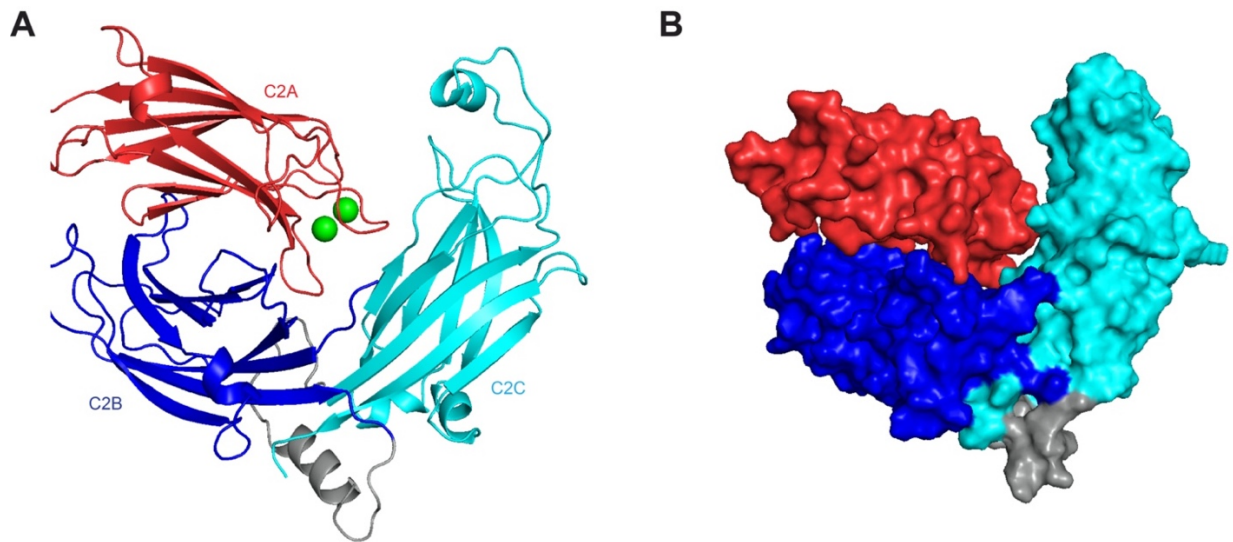
Figure 6. 1 Proposed model of the tertiary folding of the C2A, C2B and C2C domains of dysferlin.

(A) Cartoon representation of the tertiary structure formed by the dysferlin C2A (red), C2B (blue), and C2C (cyan) domain. The bound Ca^{2+} ions of the C2A domain are shown as green spheres. The linker between the C2A and C2B domain is not shown in the figure. The C2B and C2C domain is joined by a linker sequence shown in grey. **(B)** Surface representation of the structure demonstrating a closed conformation.

domain from binding to the lipid membrane. When cell membrane disruption occurs with Ca^{2+} entry into the cytoplasm, the C2A, C2B and C2C domains changes the conformation from "closed" to "open", releasing the C2A domain. Meanwhile, Ca^{2+} binding to the C2A domain targets it to the membrane of the cell or repair vesicles. Membrane anchoring in both N- and C-terminus of dysferlin "drags" the lipids close to each other, thereby mediating membrane fusion between vesicles as well as with plasma membrane (**Figure 6.2**). Additionally, since the apo-C2A is highly flexible and more unstructured, the autoinhibition mechanism may also protect it from degradation in cells. This model revealed an activation mechanism of dysferlin and established a connection of intracellular calcium signaling to regulation of membrane repair. Hopefully the model could be further examined by more experiments in the future in both molecular and cellular levels.

6.4 Conclusion

The work in this thesis has greatly achieved the four objectives raised in **Chapter 1.7** and contributed valuable information regarding the membrane repair mechanisms mediated by dysferlin. The calcium binding of the dysferlin C2A domain and the details on the stoichiometry, affinities, binding mode as well as structural information provided novel insights into the Ca^{2+} binding of C2 domains. Assessment of dysferlin C2A domain under pathological conditions has helped better understand the pathogenesis of muscular dystrophy on a molecular level. Finally, investigation of the C2B and C2C domains laid important groundwork for the subsequent studies of dysferlin structure and its function. In all, structural and mechanistic research here will have a significant impact on the understanding of related diseases and the development of drug therapeutics in the future.
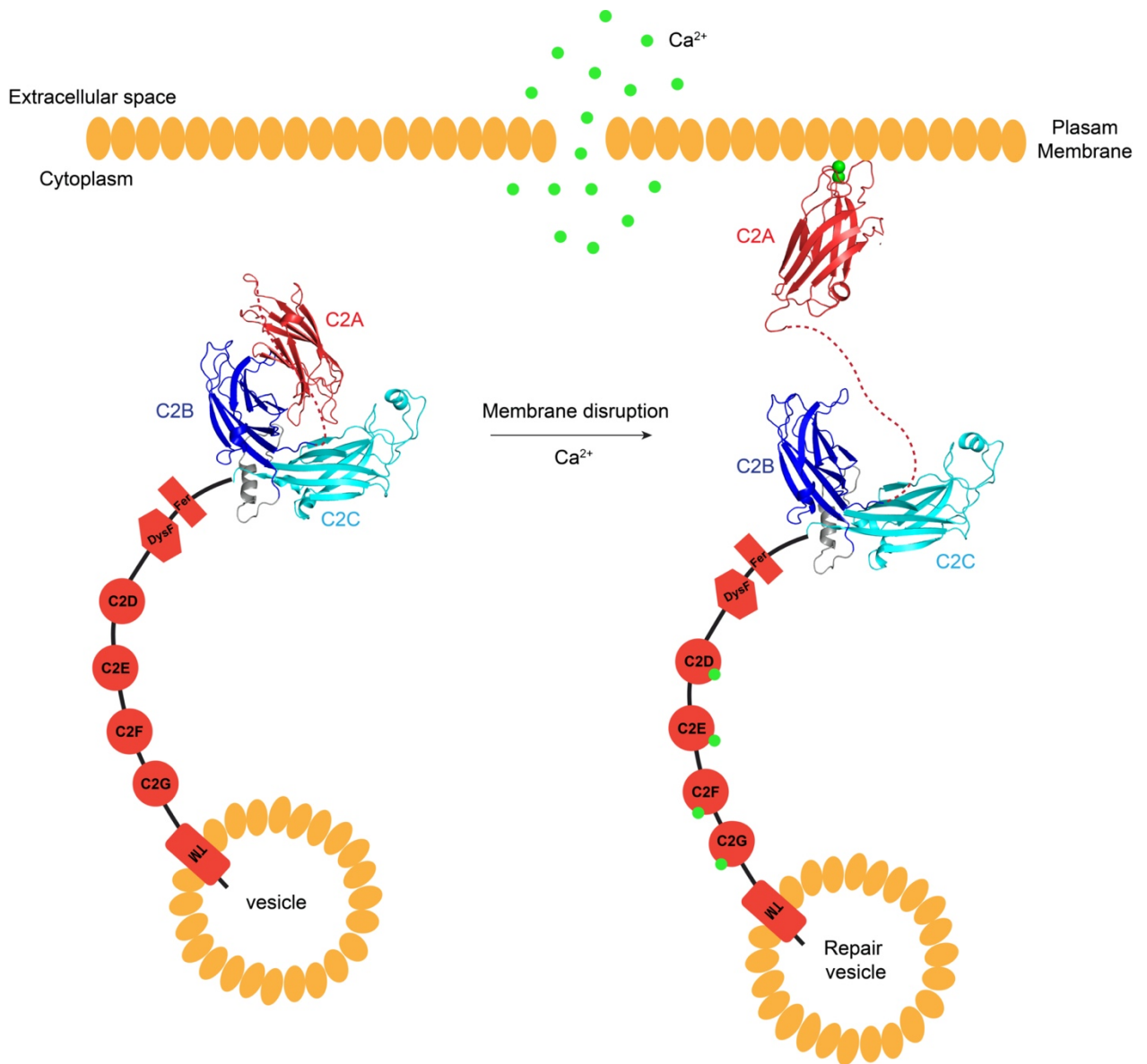
Figure 6. 2 Proposed model for autoinhibition and activation of dysferlin through releasing the C2A domain from C2B-C2C domain.

Dysferlin is localized by its C-terminal transmembrane domain to cytoplasmic vesicles and the plasma membrane. In the resting state of a cell when dysferlin is Ca^{2+}-free, the C2A (red), C2B (blue) and C2C (cyan) domains form a closed conformation which prevents the C2A domain from binding to the membrane. On injury of the membrane, Ca^{2+} influx raises the intracellular Ca^{2+} concentration, which leads to a conformational change from "closed" to "open", releasing the C2A domain. Ca^{2+}-binding to the C2A domain targets it to the lipid membrane, thereby "dragging" lipids together and ultimately mediating membrane fusion.

6.5 References

Abdullah, N., Padmanarayana, M., Marty, N.J., and Johnson, C.P. (2014). Quantitation of the Calcium and Membrane Binding Properties of the C2 Domains of Dysferlin. Biophys. J. *106*, 382–389.

Antal, C.E., Callender, J.A., Kornev, A.P., Taylor, S.S., and Newton, A.C. (2015). Intramolecular C2 Domain-Mediated Autoinhibition of Protein Kinase C βII. Cell Rep. *12*, 1252–1260.

Bansal, D., Miyake, K., Vogel, S.S., Groh, S., Chen, C.-C., Williamson, R., McNeil, P.L., and Campbell, K.P. (2003). Defective membrane repair in dysferlin-deficient muscular dystrophy. Nature *423*, 168–172.

Evesson, F.J., Peat, R.A., Lek, A., Brilot, F., Lo, H.P., Dale, R.C., Parton, R.G., North, K.N., and Cooper, S.T. (2010). Reduced Plasma Membrane Expression of Dysferlin Mutants Is Attributed to Accelerated Endocytosis via a Syntaxin-4-associated Pathway. J. Biol. Chem. *285*, 28529–28539.

Fuson, K., Rice, A., Mahling, R., Snow, A., Nayak, K., Shanbhogue, P., Meyer, A.G., Redpath, G.M.I., Hinderliter, A., Cooper, S.T., et al. (2014). Alternate Splicing of Dysferlin C2A Confers Ca^{2+}-Dependent and Ca^{2+}-Independent Binding for Membrane Repair. Structure *22*, 104–115.

Han, R., and Campbell, K.P. (2007). Dysferlin and muscle membrane repair. Curr. Opin. Cell Biol. *19*, 409–416.

Han, W.-Q., Xia, M., Xu, M., Boini, K.M., Ritter, J.K., Li, N.-J., and Li, P.-L. (2012). Lysosome fusion to the cell membrane is mediated by the dysferlin C2A domain in coronary arterial endothelial cells. J. Cell Sci. *125*, 1225–1234.

Hille, B., Billiard, J., Babcock, D.F., Nguyen, T., and Koh, D.-S. (1999). Stimulation of exocytosis without a calcium signal. J. Physiol. *520*, 23–31.

Huang, Y., Laval, S.H., van Remoortere, A., Baudier, J., Benaud, C., Anderson, L.V.B., Straub, V., Deelder, A., Frants, R.R., den Dunnen, J.T., et al. (2007). AHNAK, a novel component of the dysferlin protein complex, redistributes to the cytoplasm with dysferlin during skeletal muscle regeneration. FASEB J. *21*, 732–742.

Ikura, M. (1996). Calcium binding and conformational response in EF-hand proteins. Trends Biochem. Sci. *21*, 14–17.

Krahn, M., Béroud, C., Labelle, V., Nguyen, K., Bernard, R., Bassez, G., Figarella-Branger, D., Fernandez, C., Bouvenot, J., Richard, I., et al. (2009). Analysis of the *DYSF* mutational spectrum in a large cohort of patients: *DYSF* Mutational Spectrum in a Large Cohort. Hum. Mutat. *30*, E345–E375.

Lu, J., Machius, M., Dulubova, I., Dai, H., Südhof, T.C., Tomchick, D.R., and Rizo, J. (2006). Structural Basis for a Munc13–1 Homodimer to Munc13–1/RIM Heterodimer Switch. PLOS Biol. *4*, e192.

Matsuda, C., Miyake, K., Kameyama, K., Keduka, E., Takeshima, H., Imamura, T., Araki, N., Nishino, I., and Hayashi, Y. (2012). The C2A domain in dysferlin is important for association with MG53 (TRIM72). PLoS Curr.

Peulen, Rademaker, Anania, Turtoi, Bellahcène, and Castronovo (2019). Ferlin Overview: From Membrane to Cancer Biology. Cells *8*, 954.

Schauder, C.M., Wu, X., Saheki, Y., Narayanaswamy, P., Torta, F., Wenk, M.R., De Camilli, P., and Reinisch, K.M. (2014). Structure of a lipid-bound extended synaptotagmin indicates a role in lipid transfer. Nature *510*, 552–555.

Shao, X., Fernandez, I., Südhof, T.C., and Rizo, J. (1998). Solution Structures of the Ca^{2+}-free and Ca^{2+}-bound C_2A Domain of Synaptotagmin I: Does Ca^{2+} Induce a Conformational Change? [†]. Biochemistry *37*, 16106–16115.

Stevens, C.F., and Sullivan, J.M. (2003). The Synaptotagmin C2A Domain Is Part of the Calcium Sensor Controlling Fast Synaptic Transmission. Neuron *39*, 299–308.

Striegel, A.R., Biela, L.M., Evans, C.S., Wang, Z., Delehoy, J.B., Sutton, R.B., Chapman, E.R., and Reist, N.E. (2012). Calcium Binding by Synaptotagmin's C2A Domain is an Essential Element of the Electrostatic Switch That Triggers Synchronous Synaptic Transmission. J. Neurosci. *32*, 1253–1260.

Sula, A., Cole, A.R., Yeats, C., Orengo, C., and Keep, N.H. (2014). Crystal structures of the human Dysferlin inner DysF domain. BMC Struct. Biol. *14*, 3.

Therrien, C., Di Fulvio, S., Pickles, S., and Sinnreich, M. (2009). Characterization of Lipid Binding Specificities of Dysferlin C2 Domains Reveals Novel Interactions with Phosphoinositides [†]. Biochemistry *48*, 2377–2384.

Wang, J., Peng, Q., Lin, Q., Childress, C., Carey, D., and Yang, W. (2010). Calcium Activates Nedd4 E3 Ubiquitin Ligases by Releasing the C2 Domain-mediated Auto-inhibition. J. Biol. Chem. *285*, 12279–12288.

Wiesner, S., Ogunjimi, A.A., Wang, H.-R., Rotin, D., Sicheri, F., Wrana, J.L., and Forman-Kay, J.D. (2007). Autoinhibition of the HECT-Type Ubiquitin Ligase Smurf2 through Its C2 Domain. Cell *130*, 651–662.

Woolger, N., Bournazos, A., Sophocleous, R.A., Evesson, F.J., Lek, A., Driemer, B., Sutton, R.B., and Cooper, S.T. (2017). Limited proteolysis as a tool to probe the tertiary conformation of dysferlin and structural consequences of patient missense variant L344P. J. Biol. Chem. *292*, 18577–18591.

Yoshihara, M., Guan, Z., and Littleton, J.T. (2010). Differential regulation of synchronous versus asynchronous neurotransmitter release by the C2 domains of synaptotagmin 1. Proc. Natl. Acad. Sci. *107*, 14869–14874.

CURRICULUM VITAE

Yuning Wang

EDUCATION

PhD candidate in Biochemistry September 2015 - present
Department of Biochemistry, The University of Western Ontario
Supervisor: Dr. Gary Shaw
• Structural mechanisms of calcium signaling in dysferlin-mediated membrane repair

MSc in Biochemistry and Molecular Biology September 2011 – December 2013
Department of Biochemistry and Biochemistry, Wuhan University, China
Supervisor: Dr. Yi Liang
• Regulation of fibril formation of human Tau fragment by zinc
• Post-translational modification of degenerative disease-related proteins

BSc in Biological Sciences September 2007 - June 2011
Wuhan University, China
• 4th-year Thesis: The expression and purification of human β2-microglobulin and the effect of macromolecular crowding on its formation of amyloid fibrils

---

PUBLICATIONS

Wang Y, Tadayon R, and Shaw GS. Monitoring Interactions Between S100B and the Dopamine D2 Receptor Using NMR Spectroscopy. in Calcium-Binding Proteins of the EF-Hand Superfamily: From Basics to Medical Applications (ed. Heizmann, C. W.) 311–324 (Springer, 2019).

Wang Y, Tadayon R, Santamaria-Kisiel L, Mercier P, J. Forristal C, and Shaw GS. (2020) Structural insights into calcium binding to the dysferlin C2A domain. In preparation.

Wang Y, and Shaw GS. (2020) Impacts of muscular dystrophy causing mutations on dysferlin C2 Domains. In preparation.

CONFERENCES & PRESENTATIONS

Poster presentation: "Membrane Repair and Trafficking by Dysferlin Complex". Harold B. Stewart Research Symposium. London, Ontario, Canada. January 2016.

Oral presentation: "Calcium signaling in dysferlin-mediated membrane repair". Graduate Seminar Series- Western University. London, Ontario, Canada. May 2017.

Poster presentation (**Best poster award**): "Calcium binding to the dysferlin C2A domain".

30th Moot NMR Symposium. London, Ontario, Canada. September, 2017

Poster presentation: "Calcium Binding to the Dysferlin C2A Domain." London Health Research Day. London, Ontario, Canada. May 10, 2018.

Oral presentation: "Calcium Signaling in Dysferlin-mediated Membrane Repair". Fall Biochemistry Symposium, London, Ontario, Canada. October 2018

Poster presentation: "Structural insights into calcium-binding to the dysferlin C2A domain". International Meeting of the European Calcium Society (**Junior travel award: 400 €**), Hamburg, Germany, September 2018.

Poster presentation: "Impact of muscular dystrophy causing mutations on the folding and stability of dysferlin C2A domain." Annual Meeting of The Biophysical Society of Canada, Mississauga, Ontario, Canada. May 2019

Oral presentation: "Mutations of Dysferlin C2A Domain Associated with Calcium Binding and Muscular Dystrophy"
Maud L. Menten Fall Symposium, London, Ontario, Canada. September 2019

Oral presentation: "Using NMR to investigate the dynamics and calcium-binding mechanisms of dysferlin C2A domain"
32th Moot NMR Symposium, Ottawa, Ontario, Canada. October 2019

WORK & VOLUNTEER EXPERIENCE

Research Intern AvocadoCore (EdTech Startup)**.** September 2017 - present
•Conduct marketing research for the private sector.
•Write and implement new research proposals in collaboration with the business and development team.

Teaching assistant (Biochemistry 2280, 3380 - The University of Western Ontario)
• Answered questions of lecture topics on the OWL forum.
• Conducted tutorial lectures for 2rd year undergraduate students.
• Evaluated and critiqued essays and lab reports.
•Taught in laboratory classes on topics of biochemistry and post-lab tutoring in close communication with a group of 10 students.

Presentation Moderator London Health Research Day. April 2019
•Moderated the featured platform presentations by introducing platform speakers and moderating question and answer period after each talk.

Event assistant TAP Centre for Creativity. March 2017 - September 2017
•Volunteered in organizing and participating 5 local arts and cultural performances.